Novel aspects of the dynamics of binary black-hole mergers

Dissertation

Zur Erlangung des wissenschaftlichen Grades

Doktor der Naturwissenschaften

Dr. rer. nat.

eingereicht an der

Mathematisch-Naturwissenschaftlichen Fakultät

der Universität Potsdam

von

Philipp Mösta

Oktober 2011

Published online at the
Institutional Repository of the University of Potsdam:
URL http://opus.kobv.de/ubp/volltexte/2012/5982/
URN urn:nbn:de:kobv:517-opus-59820
http://nbn-resolving.de/urn:nbn:de:kobv:517-opus-59820

Novel aspects of the dynamics of binary black-hole mergers

Philipp Mösta

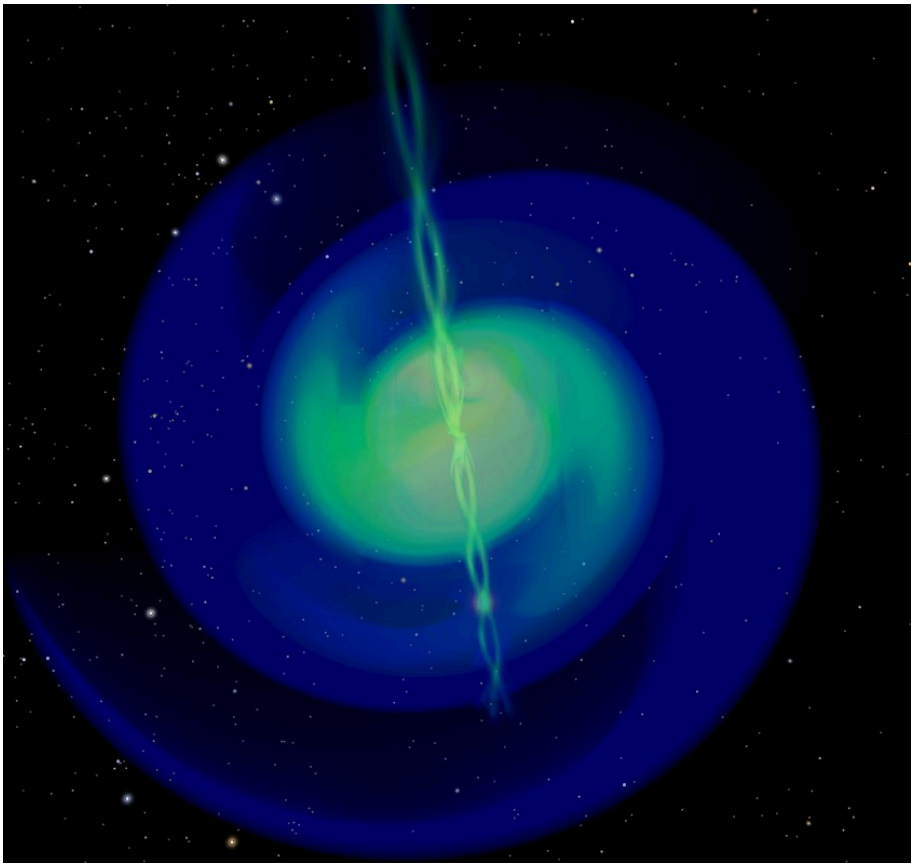

Dissertation

Albert-Einstein-Institut
Max-Planck-Institut für Gravitationsphysik

and

Mathematisch-Naturwissenschaftliche Fakultät
Universität Potsdam

2011

Cover figure: Isosurface volume rendering of the electromagnetic energy flux in geometric units of a equal-mass, non-spinning binary black-hole system at time $t = 300.8M$ during the late inspiral. The color map ranges from 0 to $10^{-12}1/M$.

Abstract

The inspiral and merger of two black holes is among the most exciting and extreme events in our universe. Being one of the loudest sources of gravitational waves, they provide a unique dynamical probe of strong-field general relativity and a fertile ground for the observation of fundamental physics. While the detection of gravitational waves alone will allow us to observe our universe through an entirely new window, combining the information obtained from both gravitational wave and electro-magnetic observations will allow us to gain even greater insight in some of the most exciting astrophysical phenomena. In addition, binary black-hole mergers serve as an intriguing tool to study the geometry of space-time itself.

In this dissertation we study the merger process of binary black-holes in a variety of conditions. Our results show that asymmetries in the curvature distribution on the common apparent horizon are correlated to the linear momentum acquired by the merger remnant. We propose useful tools for the analysis of black holes in the dynamical and isolated horizon frameworks and shed light on how the final merger of apparent horizons proceeds after a common horizon has already formed. We connect mathematical theorems with data obtained from numerical simulations and provide a first glimpse on the behavior of these surfaces in situations not accessible to analytical tools.

We study electro-magnetic counterparts of super-massive binary black-hole mergers with fully 3D general relativistic simulations of binary black-holes immersed both in a uniform magnetic field in vacuum and in a tenuous plasma. We find that while a direct detection of merger signatures with current electro-magnetic telescopes is unlikely, secondary emission, either by altering the accretion rate of the circumbinary disk or by synchrotron radiation from accelerated charges, may be detectable. We propose a novel approach to measure the electro-magnetic radiation in these simulations and find a non-collimated emission that dominates over the collimated one appearing in the form of dual jets associated with each of the black holes.

Finally, we provide an optimized gravitational wave detection pipeline using phenomenological waveforms for signals from compact binary coalescence and show that by including spin effects in the waveform templates, the detection efficiency is drastically improved as well as the bias on recovered source parameters reduced.

On the whole, this disseration provides evidence that a multi-messenger approach to binary black-hole merger observations provides an exciting prospect to understand these sources and, ultimately, our universe.

Acknowledgements

First and foremost I would like to thank my parents and family for their love and support that put me in the position to pursue this work.

I am deeply thankful to Luciano Rezzolla for enabling me to carry out this work at the Albert-Einstein-Institut, for being an always helpful supervisor and for providing useful insights and comments from beginning to end of this work. I am additionally indebted to Badri Krishnan for providing the opportunity to participate in the work that finally formed the data analysis part of this dissertation, and specifically for being patient and understanding of the difficulties that come with working in parallel on two practically often unrelated topics.

I am thankful to my many close collaborators: To Jeffrey Winicour and Bela Szilágyi for their inspiration and endurance to assist in following the not-so-standard geometrical work presented in parts of this thesis. To Jose-Luis Jaramillo and Rodrigo Pannoso Macedo for forming "team anti-kick". To Carlos Palenzuela and Luis Lehner for providing the opportunity to collaborate on the projects regarding the interaction of space-time dynamics with electromagnetic fields and for being always able to provide answers to my many questions and to Emma Robinson for assisting my every step in learning how the CBC data analysis pipeline works.

I am grateful to Michael Koppitz for his help with visualizing simulation data using the Amira package and Thomas Radke for being an invaluable source of help and support for programming and computer infrastructure related questions.

Additionally, I thank Erik Schnetter, Peter Diener, Harald Pfeiffer, Ulrich Sperhake, Mark Hannam, Christian D. Ott, Kyriaki Dyonosopolous, Filippo Galeazzi, Eloisa Bentivegna, Ian Hinder, Barry Wardell, Alexander Beck-Ratzka, Erik Schnetter, Bernard Schutz, Sascha Husa, Christian Reisswig, Lucia Santamaria Lara, Jennifer Seiler, Bruno Giacomazzo, David Radice, Kentaro Takami, Cecilia Chirenti, Stanislav Babak, Pau Amaro-Seoane, Constanze Rödig, Antoine Petitaeu, Andreas Donath and Nico Budewitz for many interesting discussions.

I thank my colleagues and most importantly friends Frank Ohme, Francesco Pannarale, Argelia Bernal, Juan Barranco, Daniela Alic, Jose-Luis Jaramillo and Rodrigo Panosso Macedo for their support and presence during parts of the time I have spent at the Albert-Einstein-Institute. You have made the time here the most pleasant one.

I acknowledge the Albert-Einstein-Institut and the Max-Planck-Gesellschaft for financial support. I thank the California Institute of Technology, the Canadian Institute for Theoretical Astrophysics, the Center for Computation and Technology at Louisiana State University and the University of the Balearic Islands for hospitality in my numerous visits.

Finally, I would like to thank Chao-Fen Wang for her love, support and simply being there during the final write-up of this thesis.

Computations were performed at the Peyote, Belladonna, Damiana, Datura and atlas clusters at the AEI, at QueenBee on LONI and at Kraken and Ranger on the Teragrid.

Contents

Preface

Binary black-hole mergers

Binary black-hole mergers are among the most extreme and fascinating events in our universe. The observation of such process would enable us to probe gravitational physics in the strong field regime as well as study the properties and dynamics of some of the most fundamental objects that exist in our universe, black-holes. The inspiral and merger of a binary black-hole system provides an excellent candidate for the detection of gravitational waves. Gravitational waves have been predicted by Einstein in his theory of General Relativity (GR) and while indirectly measured already through the accurate timing of pulsars, a direct detection of a gravitational wave has not yet been achieved. In the case of a binary black-hole merger, up to 10% of the total system mass may be radiated in gravitational waves. For supermassive black holes with masses up to $10^8 M_\odot$ this corresponds to a luminoity of 10^{57}erg/s. The successful direct measurement of gravitational waves would not only verify GR in this fundamental aspect but also would open a completely new window to observing our universe. Gravitational waves constitute an ideal tool for the observation of events which are not visible to other observational tools. In the case of supermassive black-hole binaries another highly interesting possibility of observation arises. As the binary forms as a result of a galaxy merger, the two black-holes inspiral towards each other on ever shrinking orbits. During the inspiral both black-holes are surrounded by their own accretion disc. However, as gravitational wave emission becomes the driving mechanism of the orbital evolution, a circumbinary disc is formed. The binary will be embedded in a low density gas and/or plasma and the the magnetic field anchored at the magnetized circumbinary disk will reach the region containing the black-holes. This environment provides a fertile ground for fundamental physics as the black-holes orbit towards their ultimate coalescence. One interesting possibility is offered by the interaction of the binary with the surrounding electromagnetic (EM) fields and the plasma. The dynamics of the black-holes distort the EM fields and perturb the plasma generating EM radiation in a direct way as well as through secondary emission processes like synchrotron radiation from accelerated charges. This EM radiation provides an alternative way of observing a binary black-hole merger and a coincident detection of gravitational waves with an EM counterpart signature would significantly increase our insight into the source as well as allow the measuremnent of the redshift of the source enabling us to also determine the cosmological setting of the event. Binary black-hole mergers also provide an excellent system to study the geometry of space-time in the strong field regime. The formation and interaction of black-hole horizons is a truly fascinating aspect of black-hole mergers and their connection to the geometry of space-time opens the possibility of correlating the dynamics of strong-field effects to observable signatures at large distances measured

in terms of gravitational waves. On the whole, binary black-hole mergers are an ideal probe of GR in the strong-field regime and provide an excellent candidate for testing fundamental physics in our universe.

New Results achieved in this thesis

This thesis is concerned with novel aspects of binary black-hole mergers and their observational signatures. The results presented in this dissertation are in part reported in [1, 2, 3, 4, 5, 6, 7, 8] and are the author's genuine contribution. They have been obtained through numerical simulations of binary black-hole space-times as well as using a modified data analysis pipeline used for the search of gravitational waves from compact binary inspirals. We acknowledge collaboration with Daniela Alic, Lars Anderson, Jose-Luis Jaramillo, Badri Krishnan, Luis Lehner, Jan Metzger, Carlos Palenzuela, Rodrigo Panosso Macedo, Luciano Rezzolla, Emma Robinson, Bela Szilágyi, Jeffrey Winicour, and Olindo Zanotti. In what follows we briefly describe the describe the results presented in this thesis.

We start with the anti-kick in binary black-hole mergers describes a phenomenon where the linear momentum acquired by the remnant of the merger decreases before settling down to a constant value. In this thesis we provide a thorough analysis of this process for unequal-mass head-on binary black-hole simulations. We construct an effective curvature parameter on the dynamical horizon of the merger remnant and correlate it with the linear momentum carried away by gravitational waves measured at infinity. In an additional step we investigate the relation of the effective curvature parameter to other geometric quantities, e.g. the Bondi-flux at the inner horizon and at infinity and introduce a number of meaningful geometric quantities that are of importance in the analysis of black-hole space-times.
In a similar but distinct work we have performed numerical simulations of head-on unequal-mass binary black-hole mergers using a generalized harmonic formulation of Einstein's equations with the emphasis of monitoring the evolution of the individual apparent horizons in the very final moments of the merger after a common outer horizon has already formed. Our results verify that apparent horizons can intersect in the final moments of a binary black-hole merger and we were able to track the individual apparent horizons to a stage when an overlap of up to 1/2 of the smaller apparent horizon's coordinate area is achieved. We find that as they approach each other the small black hole produces a strong tidal effect on the larger black hole as indicated by a localized growth of the mean curvature. As the two surfaces touch their mean curvature is the same at the point of osculation. As the two horizons continue to interact, the time evolution of the larger black hole shows discrete jumps in its coordinate shape and area evolution.
Furthermore, we have performed the first simulations of binary black-mergers immersed in a uniform magnetic field and when the two black holes are spinning. The space-time dynamics impact the EM fields and our results show that spin effects introduce an extra component of this distortion. The radiated energy becomes a function of the spin magnitude as well as of the orientation angle and we find a close correlation between the radiation in gravitational waves and the EM one. This is most evident for the $l = 2 = m$-mode of the spherical harmonic decomposition where we show that both phase and amplitude of the two kinds of emission are scaled by a simple factor only.

While we find that it is unlikely that the radiation signatures can be detected directly, they might be observable through indirect processes by altering the accretion rate of the circumbinary disc.
As a step towards a more realistic modeling, we have also performed simulations of the above scenario including the effects of a tenuous plasma. We have introduced a more consistent approach of measuring the radiation content in models where the magnetic field has non-compact support. More specifically, we find that this new measure changes the angular distribution of EM signatures from binary black-hole coalescence, as well as improves the overall emission efficiency by factors up to 100. The emission in the form of jets associated with both black-hole is dominated by a non-collimated one in the final orbits and through the merger and may restrict their detectability.
Finally, for the part of this thesis devoted to data analysis, we have developed a modified and extended compact-binary-coalescence data analysis pipeline that includes the corrections introduced by the of the spin compact object. Our results show that the inclusion of spin effects greatly improves the detection statistics of binary black-hole inspiral signals. Systematic biases in the physical parameters of the recovered signals are reduced or even eliminated.

Layout of this thesis

This is thesis is organized in four parts. Part one introduces the basic theoretical concepts related to the presentation of the results in this thesis. More specifically, chapter 1 reviews Einstein's equations and binary black-hole space-times, while chapter 2 reviews the basic aspects of black-holes. Chapter 3 presents an overview of Cauchy evolution in GR while chapter 4 highlights key aspects of the Einstein-Maxwell evolution system. Chapter 5 reviews the basic concepts behind the extraction of gravitational wave and EM signatures from binary black-hole simulations.

Part two reviews the computational methods that have been used to obtain the results presented. Chapter 6 presents the discretization of partial differential equations and the stability analysis of these systems, while chapter 7 reviews the computational infrastructure used. Finally, chapter 8 presents the implementation of Einstein's equations for Numerical Relativity simulations.

Part three contains a discussion of the core results obtained from the simulation of binary-black hole mergers. Chapter 9 presents results explaining the 'anti-kick' in binary black-hole mergers and introduces useful tools to analyze the geometry of black-holes. Chapter 10 discusses the time evolution of trapped surfaces in unequal-mass head-on binary black-hole mergers and chapter 11 presents results for binary black-hole mergers immersed in a magnetic field, and plasma, and discusses the astrophysical relevance of the different emission processes evident in our simulations.

Finally, part four is devoted to searches for gravitational waves in simulated detector data. Chapter 12 reviews the basic principles of matched-filtering in data analysis, while chapter 13 gives an overview of an analysis pipeline and its implementation. Chapter 14 points out the importance of using templates including spin effects in searches for spinning binary black-hole inspiral and merger signals.

Notation and Conventions

The system of untis used in is fixed by assuming $c = G = M_\odot = 1$. For convenience, we list conversion factors to CGS and geometric units ($c = G = 1$) and values of physical constants in appendix A. We choose Greek indices running from 0 to 3 to indicate 4-vectors and 4-tensors. Latin indices running from 1 to 3 indicate spatial components. We adopt the abstract index notation with sum convention. Unless noted otherwise, we assume a space-like signature $(-, +, +, +)$ and indicate 4-vectors and 4-tensors i in abstract notation in bold letters. On the other hand abstract 3-vectors are indicated by the standard vector symbol.

Part I

GR: Foundations and Mathematical Theory

1

Binary black-hole space-times

1.1 The Einstein equations

In his theory of Special Relativity [1] Einstein joined the concepts of space and time to provide a description for the electro-dynamical effects of moving bodies. Instead of viewing space and time as separate entities he suggested to view space and time as one, a four-dimensional structure called space-time. To incorporate the effects of gravity into his space-time picture Einstein proposed that the geometry of space-time itself may be curved. He related the geometry of space-time to the presence of matter and energy. Einstein's field equations describe the interaction of matter, energy and geometry and present the core component of his theory of GR [2, 3, 4].

$$G_{\mu\nu} = 8\pi T_{\mu\nu}. \tag{1.1}$$

$G_{\mu\nu}$ is the Einstein tensor, defined as

$$G_{\mu\nu} = R_{\mu\nu} - \frac{1}{2} g_{\mu\nu} R, \tag{1.2}$$

and $T_{\mu\nu}$ is the stress-energy tensor describing all forms of matter and energy. $R_{\mu\nu} = R^{\rho}{}_{\mu\rho\nu}$ is the Ricci-tensor and $R = R^{\rho}{}_{\rho}$ the Ricci-scalar, both contractions of the Riemann tensor $R^{\mu}{}_{\nu\rho\sigma}$, which provides a description for the curvature of space-time. Space-time itself is described as a set $(\mathcal{M}, g)$, $\mathcal{M}$ being a four-dimensional manifold and g a pseudo-Riemannian metric. The metric tensor provides a measure of proper distances on $\mathcal{M}$ given by the invariant differential line element.

$$ds^2 = g_{\mu\nu} dx^{\mu} dx^{\nu}. \tag{1.3}$$

The Riemann-tensor is constructed as

$$R^{\mu}{}_{\nu\rho\sigma} = \Gamma^{\mu}{}_{\nu\sigma,\rho} = \Gamma^{\mu}{}_{\nu\rho,\sigma} + \Gamma^{\mu}{}_{\tau\rho}\Gamma^{\tau}{}_{\nu\sigma} - \Gamma^{\mu}{}_{\tau\sigma}\Gamma^{\tau}{}_{\nu\rho}, \tag{1.4}$$

where $\Gamma^{\mu}{}_{\nu\rho}$ are the connection coefficients of the metric, the Christoffel-symbols

$$\Gamma^{\mu}{}_{\nu\rho} = \frac{1}{2} g^{\mu\tau} \left(g_{\rho\tau,\nu} + g_{\nu\tau,\rho} - g_{\nu\rho,\tau} \right). \tag{1.5}$$

Einstein's equations, while looking simple at first glance in tensorial notation, form a set of ten coupled non-linear partial differential equations. Analytical solutions are known only for the most idealized physical systems [5, 6]. For any scenario of interest in astrophysics solutions are found by perturbation theory or obtained numerically.

1.2 Black holes

Black-hole space-times arise as a family of solutions to Einstein's equations. The term black hole describes a region of space-time containing a singularity, i.e. a point of space-time, where the curvature tensor becomes infinite. Assuming space-time to be globally hyperbolic, and keeping aside the possibility of the existence of naked singularities, a singularity is surrounded by a part of space-time where all light-cones are directed inwards, preventing any light-ray to escape from the region containing the singularity. In a more technical definition no future directed null geodesic can escape to null infinity if originating in this region of space-time. The region inside is called a trapped region, it is causally disconnected from the rest of the space-time manifold. The region forming the boundary between inward and outward directed light-cones is called an event-horizon. It practically "shields" the singularity from the rest of space-time. The simplest black-hole space-time is the Schwarzschild space-time, a spherical symmetric solution first obtained by Karl Schwarzschild [6]. It's line element reads

$$ds^2 = -(1 - 2M/r)dt^2 + \frac{dr^2}{1 - 2M/r} + r^2(d\theta^2 + \sin^2\theta d\phi^2), \tag{1.6}$$

written in the standard spherical coordinates r, θ and ϕ. The Schwarzschild solution is static, possesses a physical singularity at $r = 0$ and is asymptotically flat as it approaches Minkowksi space-time for $r \to \infty$. The event horizon is a sphere with $r = 2M$ and the the Schwarzschild solution is unique for static black holes, i.e. any spherical symmetric solution to the Einstein field equations in vacuum is isometric to the Schwarzschild solution locally. A more general black-hole solution is the Kerr space-time, first obtained by Kerr [5], which is stationary, rotating and axisymmetric. It is unique in describing stationary solutions to Einstein's equations. It was later generalized to include charge by Newman [7] and the Kerr-Newman line element in Boyer-Lindquist coordinates is described by

$$ds^2 = \frac{\Delta}{\rho^2}\left(dt - \alpha\sin^2\theta d\phi\right)^2 + \frac{\sin^2\theta}{\rho^2}\left(\left(r^2 + \alpha^2\right)d\phi - \alpha dt\right)^2 + \frac{\rho^2}{\Delta}dr^2 + \rho^2 d\theta^2, \tag{1.7}$$

with

$$\Delta = r^2 - 2Mr + \alpha^2 + Q^2 \tag{1.8}$$

$$\rho^2 = r^2 + \alpha^2\cos^2\theta \tag{1.9}$$

$$\alpha = S/M. \tag{1.10}$$

Here α denotes the angular momentum of the space-time S per unit mass M as measured by an observer at infinity and Q the electric charge. An additional quantity that is often used is the dimensionless spin parameter $a = \alpha/M = S/M^2$. Assuming the cosmic censorship conjecture [8] holds, one can put limits on the parameters of the Kerr solution,

$$M^2 \geq Q^2 + \alpha^2. \tag{1.11}$$

It is very likely that for any astrophysically realistic black hole Q vanishes and thus useful to explore those bounds for $Q = 0$. This yields $-M \leq \alpha \leq M$ or in terms of the dimensionless spin parameter $-1 \leq a \leq 1$. This is a generic condition on the spin parameter for any axisymmetric space-time and the case $|a| = 1$ can only be achieved

in the case of a Kerr-slice of space-time [9]. It is possible to characterize any classical stationary black-hole space-time using the three parameters introduced above, the mass M, the dimensionless spin-parameter a and the electric charge Q. Any realistic black hole in nature would be surrounded by either an accretion disk or dust and thus would not be able to carry a non-neglectable amount of charge Q since it would immediately neutralize by interaction with the surrounding matter. Therefore the charge parameter Q is often dropped in describing black-hole space-times. Turning to how black holes are created in astrophysical scenarios one can restrict the mass-range they exist in. Stellar-mass black-holes are formed by collapsing stars, which to form a black hole have to at least have a mass of about $20M_\odot$. Stellar mass black-holes typically range in order of magnitude from $10M_\odot$ to $100M_\odot$. They typically are formed in globular clusters containing many old stars and collapsed objects [10, 11]. Intermediate mass black-holes are characterized by a mass of $100M_\odot \leq M \leq 10^5 M_\odot$ and are expected to exist in stellar clusters [12, 13]. Only recently proposed by theoretical considerations there is very little observational evidence for intermediate mass black-holes to exist, hinting that these objects may be very rare. Supermassive black-holes have masses ranging from $10^5 M_\odot$ to $10^9 M_\odot$ and are expected to exist at the center of most major galaxies, i.e. there is strong observational evidence that the center of our own galaxy, the milky-way, is host of a supermassive black-hole of about $M = 4.1\ 10^6 M_\odot$ [14, 15, 16]. Theoretical models suggest that they are the outcome of hierarchical galaxy-mergers, which are accompanied by a merger of their central black holes. Thus the maximum mass of a black hole being formed by this mechanism is bound by the number of merger-events in a Hubble-time [16, 17, 18, 19, 20]. Currently these models do not support masses of above $10^9 M_\odot$. In summary the parameters of a black hole in vacuum are the mass M and the spin a. The mass is constrained in its minimum by the mass a collapsing star needs to have in order to form a black-hole remnant, and in its maximum by the number of hierarchical merger events a galaxy can undergo during a Hubble time. This leads to a possible mass range of $1.5M_\odot \leq M \leq 10^9 M_\odot$. The dimensionless spin parameter in turn is constrained by assuming the cosmic censorship conjecture to hold and is thereby limited to $-1 \leq a \leq 1$. Black-holes in general and especially in dynamical situations are complex in their geometry but nonetheless some properties about black holes in general can be stated. A black hole undergoing interaction with its environment will return to a stationary state if no further interaction takes place. This is commonly described as a black-hole ring-down. Any perturbation against spherical or axisymmetry is radiated away in gravitational waves. A black hole of mass M and spin a rings down with unique frequencies, the quasi-normal mode frequencies. It is therefore possible to accurately determine a black hole's mass and spin if one can measure its quasi-normal mode ring-down [21, 22, 23]. In general the geometry of a black hole in a dynamic situation can be very complex, so that it might be very difficult to define quantities like the black-hole mass and spin parameters. In those situations quasi-local definitions of mass and spin measured on the apparent or isolated horizon (these concepts will be discussed in more detail in chapter 2) are often introduced which turn out to be very helpful in obtaining the mass and spin of a very dynamical black hole.

1.3 Asymptotic properties of space-times

In GR one cannot generally define global integral conservation laws unless space-time possesses Killing-symmetries. For any global integral conservation law to be formu-

lated one would typically need vanishing divergence of some flux-tensor related to the quantity one is interested in. Typically this involves vector-valued tensorial equations, e.g. conservation of momentum locally reads $\nabla_\mu T^{\mu\nu} = 0$. Now in calculus on Riemannian manifolds the addition of vectors at different points is not defined so that it is impossible to construct a general global conservation law since one cannot define an integral sum for expressing the integral. It is therefore often impossible to define global properties like the mass of space-time or the energy carried away by gravitational waves. Unfortunately this poses a fundamental problem since these are often the very quantities one is interested in the most. It therefore would be ideal to look at space-times that have the required symmetries. Although that is unlikely the case for realistic systems of interest in astrophysics there is a way to circumvent missing symmetries by imposing that space-time is asymptotically flat. This idea goes back to work by Newman and Penrose [24, 25, 26] , and consists of representing the system of interest as an isolated self-gravitating system. One basically assumes to have flat Minkowski space-time at spatial infinity and therefore nearly Minkoswki far from the region containing the gravitational source and therefore can characterize far-fields of isolated systems by their conformal structure. Using this one now can make use of the symmetries of Minkowski and in this way at least globally measure the quantities one is interested in. We will discuss the asymptotic properties of space-times in detail in chapter 5.

1.4 Gravitational waves

Gravitational waves can be thought of as ripples in space-time. They locally distort space-time and travel at the speed of light, as will become clear later in this chapter. The local distortions created by gravitational waves can be measured by detectors, i.e. via laser interferometers. Gravitational waves carry energy, angular and linear momentum away from their source. Thus the source of a gravitational wave is not preserved, since it loses mass through the gravitational waves carrying away energy [27, 28]. This is in contrast to electromagnetism, where i.e. the charge q as a source of EM radiation is preserved. Additionally due to the highly non-linear dynamics of gravity it is very difficult to distinguish near-field from far-field effects like in electromagnetism. Actually gravitational radiation is only well defined at future null-infinity where space-time is asymptotically flat, since only here it is possible to clearly distinguish the gravitational wave signal as a perturbation on a flat background space-time metric. Gravitational waves arise from accelerated masses, as EM waves arise from accelerated charges. However gravitational waves are quadrupolar in nature in contrast to the dipolar nature of EM waves. This follows mainly from Birkhoff's theorem which prevents radiation from spherically symmetric space-times and thus prevent $l = 0$-modes, and from conservation of momentum which prohibits $l = 1$-modes. Given the very weak nature of gravity compared to the other fundamental forces it is not surprising that the local distortions in space-time caused by gravitational waves are very weak. Good sources of gravitational radiation are therefore events that are highly relativistic in their dynamics and involve very compact and heavy objects, like binary black-hole or binary neutron star mergers. These systems form some of the most extreme events in the universe as they radiated away tremendous amounts of energy ($E_{rad} \approx 10^{55} erg/s$ for some systems) and are therefore ideal candidates for sources of strong gravitational radiation. However, the gravitational wave distortion (or strain) of even these extreme events caused in a

region far away from the source is very small, i.e. of the order of $h \approx 10^{-21}m$ for a $100M_{\odot}$-mass binary black-hole system observed at a distance of $100Mpc$. It is these very small distortions that make the detection of gravitational waves a major experimental challenge. While being indirectly measured and verified for the Hulse-Taylor and other pulsars [29, 30] no direct detection of a gravitational wave has been claimed so far. Once detected, gravitational waves however will open a new window to the universe, allowing a exciting new perspective on some of the most fundamental events in our universe. Observations of gravitational waves will not only allow direct measurements of the gravitational interaction of stellar and galactic objects [31] but may also shed light on the big-bang itself or help in choosing alternative candidate theories of classical or non-classical gravity [32]. In this section we will introduce the basic concepts of gravitational waves.

1.4.1 Gravitational waves in linearized theory

Given their weak nature gravitational waves can be described as perturbations on top of a background metric. Furthermore assuming the background metric to be flat for now (we later can extend this to metrics describing curved space-times) the metric can be written in the form

$$g_{\mu\nu} = \eta_{\mu\nu} + h_{\mu\nu}, \qquad |h_{\mu\nu}| \ll 1. \tag{1.12}$$

Here $\eta_{\mu\nu}$ denotes the flat Minkowski metric and $h_{\mu\nu}$ is a linear small perturbation on top of the background metric. The connection coefficients of the metric can now be expressed as

$$\begin{aligned} \Gamma^{\mu}{}_{\nu\sigma} &= \frac{1}{2}\eta^{\mu\rho}\left(\partial_\sigma h_{\rho\nu} + \partial_\nu h_{\rho\sigma} - \partial_\rho h_{\nu\sigma}\right) \\ &= \frac{1}{2}\left(\partial_\sigma h^{\mu}{}_{\nu} + \partial_\nu h^{\mu}{}_{\sigma} - \partial^\mu h_{\nu\sigma}\right), \end{aligned} \tag{1.13}$$

and using this the Riemann-tensor reads

$$\begin{aligned} R^{\mu}{}_{\nu\sigma\rho} &= \partial_\sigma \Gamma^{\mu}{}_{\nu\rho} - \partial_\rho \Gamma^{\mu}{}_{\nu\sigma} \\ &= \frac{1}{2}\left(\partial_\sigma\partial_\nu h^{\mu}{}_{\rho} + \partial_\sigma\partial^\mu h_{\nu\rho} - \partial_\rho\partial_\nu h^{\mu}{}_{\sigma}\right). \end{aligned} \tag{1.14}$$

From this the Ricci-tensor is constructed as

$$R_{\mu\nu} = R^{\sigma}{}_{\mu\sigma\nu} = \frac{1}{2}\left(\partial_\sigma\partial_\nu h^{\sigma}{}_{\mu} + \partial^\sigma\partial_\mu h_{\nu\sigma} - \Box h_{\mu\nu} - \partial_\mu\partial_\nu h\right), \tag{1.15}$$

where $\Box = \nabla^2 - \partial_t^2$ is the usual wave operator and $h = h^{\mu}{}_{\mu}$ is the trace of the metric perturbation. Another contraction on the Ricci-tensor leads to an expression for the Ricci-scalar, which reads

$$R = R^{\mu}{}_{\mu} = \partial_\sigma\partial^\mu h^{\sigma}{}_{\mu} - \Box h, \tag{1.16}$$

which now can be used to construct the Einstein tensor

$$\begin{aligned} G_{\mu\nu} &= R_{\mu\nu} - \frac{1}{2}h_{\mu\nu}R \\ &= \frac{1}{2}(\partial_\sigma\partial_\nu h^{\sigma}{}_{\mu} + \partial^\sigma\partial_\mu h_{\nu\sigma} - \Box h_{\mu\nu} - \partial_\mu\partial_\nu h \\ &\quad -\eta_{\mu\nu}\partial_\sigma\partial^\rho h^{\sigma}{}_{\rho} + \eta_{\mu\nu}\Box h). \end{aligned} \tag{1.17}$$

Recasting the metric perturbations in a *trace-reversed* form

$$\bar{h}_{\mu\nu} = h_{\mu\nu} - \frac{1}{2}\eta_{\mu\nu}h \tag{1.18}$$

we can simplify the expression for the Einstein tensor

$$G_{\mu\nu} = \frac{1}{2}\left(\partial_\sigma\partial_\nu\bar{h}^\sigma{}_\mu + \partial^\sigma\partial_\mu\bar{h}_{\nu\sigma} - \Box\bar{h}_{\mu\nu} - \eta_{\mu\nu}\partial_\sigma\partial^\rho\bar{h}^\sigma{}_\rho\right). \tag{1.19}$$

Additionally using our gauge-freedom by choosing the Lorentz gauge

$$\partial^\mu\bar{h}_{\mu\nu} = 0, \tag{1.20}$$

simplifies the expressions even further, yielding

$$G_{\mu\nu} = -\frac{1}{2}\Box\bar{h}_{\mu\nu}. \tag{1.21}$$

In a vacuum space-time this results in

$$\Box\bar{h}_{\mu\nu} = 0. \tag{1.22}$$

Now (1.22) is just an ordinary wave equation for the metric perturbations $\bar{h}_{\mu\nu}$ and we can find solutions to it in the form of

$$\bar{h}_{\mu\nu}(x,t) = \mathrm{Re}\int d^3k A_{\mu\nu}(\mathbf{k}\mathbf{e}^{\mathbf{i}(\mathbf{k}\cdot\mathbf{x}-\omega\mathbf{t})}. \tag{1.23}$$

Here k is the wave-vector, $\omega = |\mathbf{k}|$ and the amplitude coefficients $A_{\mu\nu}(\mathbf{k})$ are a function of $\mathbf{k}$. The Lorentz gauge, that we have chosen leads to the additional constraint $k^\mu A_{\mu\nu} = 0$ with $k^\mu = (\omega, \mathbf{k})$. We already call the solutions $\bar{h}_{\mu\nu}(x,t)$ gravitational waves but can further restrict their form. Imposing asymptotic flatness, we can restrict the perturbations to be being purely spatial,

$$h_{tt} = 0 = h_{ti}, \tag{1.24}$$

and traceless,

$$h = h^i{}_i = 0. \tag{1.25}$$

Now the Lorentz gauge condition implies

$$\partial_i h_{ij} = 0, \tag{1.26}$$

which leads to our metric perturbation h being purely transverse. We call the gauge-conditions chosen to cast the metric perturbation into this form the
transverse − traceless(TT) gauge. By choosing the TT gauge we have now used all our gauge-freedom so that the metric perturbations h^{TT} (sometimes quantities in the TT gauge are written in the form A^{TT}) are fixed in their form and contain purely physical information about the gravitational waves. One feature that becomes obvious in the

TT gauge is that gravitational wave can have two polarizations. Considering a plane gravitational wave which is a solution to $\Box h_{ij}^{TT} = 0$ and travels along the z-direction ($h_{ij}^{TT} = h_{ij}^{TT}(t-z)$) the Lorentz gauge $\partial_z h_{ij}^{TT} = 0$ leads to h_{zj} being constant. Asymptotic flatness implies that the only non-zero components of the metric perturbation are h_{xx},h_{xy},h_{yx} and h_{yy}. Taking into account the trace-free and symmetry conditions we can furthermore reduce this to only two independent components

$$h_+ = h_{xx}^{TT} = -h_{yy}^{TT} \tag{1.27}$$

$$h_\times = h_{xy}^{TT} = h_{yx}^{TT}. \tag{1.28}$$

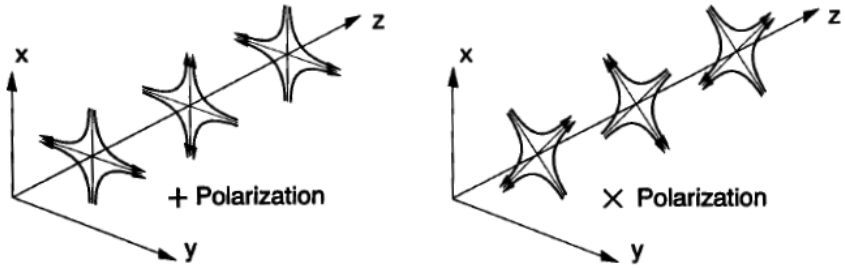

Figure 1.1: The two polarization states h_+ (left) and $h_\times$ (right) of gravitational waves represent by their lines of force in affecting particles. Figure taken from [33].

As shown in [34] the metric components h_+ and $h_\times$ are the only pure radiative degrees of freedom. They are the only components that obey a wave equation in all gauges. All other components can be shown to form a set that obeys Poisson's equations. The fact that the non-TT part of the metric also satisfies a wave-equation is an artifact in the TT-gauge. Figure 1.1 illustrates the differences between the two polarization states h_+ and $h_\times$. We can construct linear waves by superposing h_+ and $h_\times$ in phase and circular or elliptical waves by superposing the two polarizations with a phase shift of $\pi/2$.

1.4.2 Energy linear and angular momentum carried by gravitational waves

Gravitational waves carry energy, linear and angular momentum. While in general it is not possible to define energy and momentum in a global fashion in GR we can however find approximations that work well under certain conditions. One such quantity in this context is the Isaacson stress-energy-tensor [35, 36] which assumes the weak-field nature of the gravitational field. Expanding the metric to second-order perturbations

$$g_{\mu\nu} = g_{\mu\nu}^B + \epsilon h_{\mu\nu} + \epsilon^2 j_{\mu\nu} + \mathcal{O}(\epsilon^3), \tag{1.29}$$

where $g^B_{\mu\nu}$ is the background-metric, $h_{\mu\nu}$ and $j_{\mu\nu}$ are perturbations to linear and second order and ϵ is an expansion parameter with $\epsilon \ll 1$. We now can equivalently expand the Ricci- and Einstein-tensor and derive the Einstein equations in the same way as done for the first-oder perturbations around a flat space-time metric as outlined in 1.4.1 to linear order,

$$\frac{1}{2}\Box^B h_{\nu\rho} + R^B_{\mu\rho\nu\lambda} h^{\mu\lambda} = 0. \tag{1.30}$$

The solutions to this set of equations can again be interpreted as gravitational waves, but in contrast to the perturbations derived around a flat space-time in 1.4.1 there exists a coupling to the Riemann tensor of the background metric and in addition the wave-operator in respect to the background metric induces another coupling also to the connections coefficients of the background metric. Now to identify the 'true' gravitational waves from the background space-time we can use the fact that the length-scales involved are very different. The wavelength of the gravitational waves λ_{GW} is typically very small compared to the length-scale L over which the background metric changes. We can therefore use the fact $\lambda_{GW} \ll L$ and by averaging over a region covering which covers a large amount of wavelength λ_{GW} but is still small compared to the length-scale L of the background metric. This procedure (well known as the *short-wavelength approximation* or *geometric optics regime*) [35, 36, 37] leads to the gravitational wave perturbation being to first oder

$$\epsilon h_{\mu\nu} = g_{\mu\nu} - g^B_{\mu\nu}. \tag{1.31}$$

Now including also the second-order perturbation we can derive an effective stress-energy for gravitational waves. Inserting the metric perturbation to second order into Einstein's equations we get

$$G_{\mu\nu} = \frac{1}{4}\langle \partial_\mu h^{TT}_{ij} - \partial_\nu h^{TT}_{ij} \rangle + \mathcal{O}(\epsilon^3) \tag{1.32}$$

, where $\langle\rangle$ denotes an averaging procedure over multiple wavelengths. We can now identify the effective stress-energy tensor of gravitational waves in the TT-gauge as

$$T^{GW,eff}_{\mu\nu} = \frac{1}{32\pi}\langle \partial_\mu h^{TT}_{ij} - \partial_\nu h^{TT}_{ij} \rangle. \tag{1.33}$$

Due to the averaging over multiple wavelengths the first oder perturbations have disappeared in (1.33) and all quantities in (1.33) except the effective gravitational wave stress-energy tensor vary on length-scales related to the background metric $g^B_{\mu\nu}$. Thus for when averaging over long length-scales the energy and momentum of gravitational waves can now be computed from $T^{GW,eff}_{\mu\nu}$.

1.4.3 Detector response to gravitational waves

Recently, it has become technically feasible to construct and operate gravitational wave detectors whose sensitivity is high enough to possibly measure gravitational waves from

distant sources on Earth [38, 39]. As shown in the previous section gravitational waves appear as a perturbation around an asymptotically flat space-time. In order to measure those perturbations here on earth we need to determine the effect the gravitational wave perturbations have on our instrument. For simplicity assuming we are in a flat region of space-time (i.e. neglecting the gravitational field of the source of the gravitational waves and also neglecting the gravitational field of the earth itself) the only change induced on top of our flat background metric can be caused by gravitational waves. Typical modern gravitational wave detectors are laser-interferometers that measure changes in the distance between two points with very high accuracy. The proper distance between two points at $x = 0$ and $x = L_p$ located at $z = 0$ is given by

$$L = \int_0^{L_p} dx \sqrt{g_{xx}}, \tag{1.34}$$

and a gravitational wave traveling along the z-axis passing the detector will change the proper distance to

$$\begin{aligned} L = & \int_0^{L_p} dx \sqrt{g_{xx} + h^{TT}_{xx}(t, z = 0)} \\ = & \int_0^{L_p} dx \sqrt{1 + h^{TT}_{xx}(t, z = 0)} \\ \simeq & L_p \left(1 + \frac{1}{2} h^{TT}_{xx}(t, z = 0)\right). \end{aligned} \tag{1.35}$$

The change in proper distance as a result of the gravitational wave interacting with the detector therefore is

$$\frac{\delta L}{L} \simeq \frac{1}{2} h^{TT}_{xx}(t, z = 0). \tag{1.36}$$

A photon traveling between two mirrors in one arm of a laser interferometer interacting with this gravitational wave would now require a phase shift of $\delta\phi = 4\pi\delta L/\lambda$ with λ being the wavelength of the photon. A photon traveling in the other perpendicular arm of the laser interferometer would not acquire any phase shift and the resulting difference in phase can be measured by interference patterns when the two photons are in the end super-positioned again. In practice however it turns out to be very complicated and technically challenging to measure gravitational waves for a multitude of reasons. First, the assumption that we are in an entirely flat region of space-time is not true due to the gravitational field of the earth and other near-zone effects introducing noise into the detector. Due to that it is not anymore possible to genuinely distinguish a gravitational wave from the background space-time. Second, the detector itself introduces extra sources of noise, that need to be taken into account. *Seismic* noise, i.e. noise transmitted through ground vibrations from objects moving more or less in the vicinity of the detectors (people walking around, trains passing by), needs to be isolated by suspending the detector mirrors on very-advanced multi-stage pendula. *Thermal* noise is noise generated by thermal fluctuations in the mirrors and other parts of the interferometer itself. *Photon-shot* noise is due to the quantum nature of light itself and leads

to statistical distribution of the interference pattern measured when combining the two laser-beams. To minimize its effect we can increase the power in the laser-beam and achieve a higher accuracy in the measurement of the position of the photons but on the other hand introduce a higher uncertainty into the momentum measure which will lead to higher fluctuations in the momentum transferred to the mirrors and in addition a higher thermal noise. This however can be in turn minimized by using squeezed states of light. One other source of noise possibly affecting the sensitivity of the detector is *gravity gradient* noise which is cause by local fluctuations in the near-zone gravitational field. This set serious limitations on the frequency range for earth-based gravitational wave detectors and limits them to frequencies of above $1Hz$. To circumvent this limitation space-based missions and underground detectors are proposed which would have access to this astrophysically highly interesting range of frequency. As we will discuss in more detail in the next section we expect many supermassive black-hole systems to generate gravitational waves in this frequency range. As a result of all these noise-sources each detector has a unique sensitivity curve which is tuned to give maximum sensitivity for a specific frequency range. This frequency range typically is chosen to match the frequency range of the designated sources (i.e. binary black-hole or binary neutron-star systems with chosen parameters). One such sensitivity curve for the current and planned advanced laser interferometer gravitational-wave observatory (LIGO) detector is shown in figure 1.2.

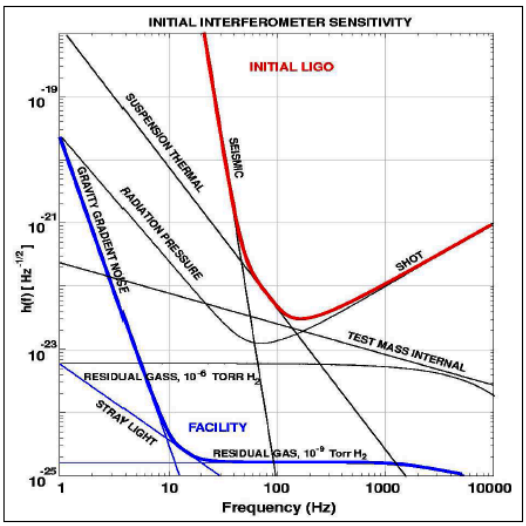

Figure 1.2: Initial LIGO interferometer sensitivity curve (in red) together with potentially contributing noise curves. Seismic, thermal, and photo-shot noise mainly contribute limit the sensitivity in the different frequency regions. In blue is shown the theoretically best possible sensitivity curve achievable for a ground-based detector, limited by gravity gradient noise and residual gas noise. Figure taken from [40].

Although one detector would be enough to measure a gravitational wave, to eliminate as much as possible the uncertainty of false-alarms related to noise affecting the

measurement of the detector, one would like to achieve a coincidence detection between at least two detectors located far away from each other. Additionally, two detectors with different orientations would allow to measure both polarizations of a gravitational wave. It should be noted that so far no gravitational wave has been measured. In a next step current earth-based detector are receiving a technology upgrade to increase their sensitivity and in addition multiple next-generation detectors (space- or earth-based) are proposed.

1.5 Binary black-hole mergers and their astrophysical environment

The evolution of a black-hole binary system can be described in three stages: After the formation of a binary system at some point the two black holes orbit each other on nearly circular orbits [41]. This stage can last for multiple millions of years, depending on the mass of the system and at first very little energy is radiated away from the system in the form of gravitational waves. However as the separation becomes closer and closer, the amplitude and frequency of the emitted gravitational waves increases and thus the system looses energy more rapidly. At some point in the evolution this effect becomes so strong, that a separation is reached after which no stable quasi-circular orbit is possible anymore (the inner-most stable orbit (ISCO)). Hereafter the two black holes first plunge and finally merge to form a single, excited black hole as a result of the merger. This remnant first is deformed and after radiating away perturbations which are present as a result of the recent merger, it evolves to an isolated, single black hole. This process is called a ring-down as the excited black hole radiates away all perturbations from axial- or spherical symmetry in the form of quasi-normal modes, exponentially damped gravitational radiation. These quasi-normal modes have specific frequency that can be identified with the mass and spin of the black hole and can therefore if detectable be used to measure mass and spin of the remnant black hole. The remnant is expected to evolve to a Kerr space-time [42, 43, 44, 45], however this has not been proven mathematically yet. Detailed aspects of the ring-down process and it's signature in the linear momentum carried away by the gravitational waves are illustrated in chapter 9.

While the orbits of the binary initially may be highly eccentric (depending on the circumstances of its formation), it can be shown that due to radiation reaction damping the eccentricity will be removed on a rather short time-scale of a few hundreds of orbits. While the binary inspirals the emitted gravitational radiation is essentially sinusoidal in nature, but with monotonically increasing amplitude and frequency. Current binary black-hole simulations typically evolve 10-15 orbits before merger and therefore take initial data with circular orbits for both black holes. This is justified by mentioned eccentricity removal over the millions of orbits in the early inspiral phase. however recent simulations of accretion disks have suggested that due to interaction of the binary with an accretion disk in the late inspiral it may be possible to have highly eccentric orbits also in the very late inspiral which so far has not been taken into account by

most numerical simulations. Eccentricity will add an additional modulation to the gravitational wave signal emitted by the binary.

The parameter space of binary black-hole systems consists of the the mass-ratio and the two spin-vectors and is therefore 7-dimensional. All the results scale trivially with the total system mass. In practice however since we start our simulation at a finite separation of the two black holes, we have to introduce as initial parameters also the initial momenta of both black holes. While these 6 additional parameters effectively increase our parameter space they are introduced only to mimic the behavior of the binary at the chosen initial separation and such our results must be independent of the chosen separation. One can therefore think of a binary black-hole merger simulation as a mapping of the initial 7 parameters of the two individual black holes two the properties of the final black-hole space-time,

$$(\eta, \mathbf{S}_1, \mathbf{S}_2) \rightarrow (\mathbf{v}_{kick}, \mathbf{S}_F, M_F) \tag{1.37}$$

where η is the mass-ratio of the binary, $\mathbf{S}_1$ and $\mathbf{S}_2$ are the spin vectors of both individual black holes, and $\mathbf{v}_{kick}$ is the boost velocity, $\mathbf{S}_F$ the final spin and M_F the final mass of the remnant black hole. The parameters of the remnant are another interesting field that can be explored by numerical simulations. As already obvious from (1.37) the final black hole in general obtains a boost-velocity, the so-called *kick* due to asymmetries in the emitted gravitational radiation. This kick depends on the initial parameters of the binary and can be so large [46] that the remnant may escape its host galaxy. In addition the time evolution of the kick velocities reveals a feature commonly referred to as the *'anti-kick'*, a decrease in the the kick-velocity around the formation of the common horizon of the remnant which will in detail describe in chapter 9. In addition to the boost-velocity, the remaining parameters are the spin-vector and mass of the remnant black hole. Since it is computationally very expensive to cover the whole parameter space of binary black-hole mergers numerically it is desirable to have effective analytical mappings of the initial parameters into the parameters of remnant, as presented *i.e.,* in [47, 48].

2

Black hole geometry

Black holes play a crucial role in theory of GR as already seen in chapter 1. The concept of a horizon can be used to determine the existence and characterize black holes in a space-time. Horizons form the boundary of two regions of space-time which are causally disconnected. Since the hyperbolic nature of GR implies causal relations between events, horizons play a crucial role which events in a space-time can influence others. Black-hole properties can be uniquely described by its *event horizon* (EH). The EH is defined as the surface where null geodesics are neither in-going or outgoing, but have null expansion. It therefore divides space-time into a region where all outwards directed null geodesics will necessarily fall back into the black hole and a region where outwards directed null rays can escape to infinity. Since the existence of an EH is a global property of space-time we need to know the full evolution of our space-time before being able to determine whether an EH has been formed or not during a typical simulation. It can therefore not be used to find horizons during the course of a simulation, which however is a highly interesting aspect of binary black-hole simulations. It is therefore useful to introduce a local definition of horizons, the concept of an *apparent horizon*. An apparent horizon can be found locally, as in on a single spatial hypersurface of space-time, and can thus be used to search for black holes in simulations without knowing the global properties of space-time and its future time evolution. It was shown [49, 50, 51] that the existence of an apparent horizon implies the existence of an outer or coinciding EH and a singularly contained within if cosmic censorship [8] is assumed to be true. On apparent horizons we can define *quasi-local* properties like mass and spin of an apparent horizon (and hence a black hole) and we can make use of this fact to measure properties of black holes during the course of our numerical simulations. In addition one can also introduce the concept of *isolated horizons* [52] and *dynamical horizons* (DH) [53]. Isolated horizons are horizons in equilibrium not undergoing any interaction with other parts of space-time. For most of the inspiral and also after ring-down we can regard the individual and later the common horizon in a binary black-hole merger simulation as isolated (to our numerical accuracy). However it is useful to generalize the concept of an isolated horizon to something called a DH. A DH is a non-expanding horizon but allows for the time-evolution of the horizon and

can also be used in the highly dynamical portions of a binary black-hole merger. In the following sections we will review the basic definitions and concepts regarding event, apparent, isolated and DHs as well as highlight some of their geometrical properties which will be become relevant in chapter 10. The notations in chapters 9 and 10 vary from the one presented here, as they are specifically adapted to the scenarios, that are considered in these chapters.

Figure 2.1: Event horizon evolution in a binary black-hole merger simulation. The two individual EHs merge and form a common EH as time proceeds from bottom to top of the figure. Figure by Peter Diener.

2.1 Event horizons

An EHs is defined as the past causal boundary of future null infinity [49]. All outgoing null geodesic on the EH form a set of closed geodesic curves. This automatically implies the EH itself being a null hypersurface in space-time. The EH forms a causal boundary between the interior and exterior space-time. No geodesic can escape from the interior space-time to the exterior. We call the region inside the EH a trapped region of space-time. Due to the non-locality of the definition of EHs, it is obvious that we have to know the complete future of the global space-time to determine whether an EH has formed or not. The main reason for that is the rate of exponential divergence of null geodesics as we approach the horizon from future null-infinity. The closer we get to the

horizon surface the slower this convergence goes. The global nature of their definition makes EHs of limited use in standard Numerical Relativity. In most applications we want to be able to determine the existence and properties of a black hole during the time evolution of a dynamical space-time. Using EHs we necessarily would first need to complete the whole evolution and then search 'backwards in time' for the EH. However, there exist implementations of EHs finders [54]. These EH finders typically work by integrating back in time null geodesics using the fact that the EH acts as an attractor of these null rays. For certain purposes, most importantly visualization of space-time geometry, EHs provide as useful tool to probe space-time properties 2.1. More details can be found in [55].

2.2 Apparent horizons

More practical for the use in numerical space-time simulations is the concept of an apparent horizon. An apparent horizon is defined as the outer boundary of a trapped region on a hypersurface of space-time. This definition already points out one of the key aspects of apparent horizons. We can determine whether an apparent horizon is present or not by evaluating data from only one spatial hypersurface, thus we are able to use apparent horizons as a probe of black-hole existence and properties during the course of a numerical simulation. Alternatively an apparent horizon can be defined as the outermost marginally outer trapped surface (MOTS) on a given hypersurface. A MOTS is defined as a closed 2-surface S with expansion of all future-directed outgoing null geodesics being zero. This definition makes use of the notion of the expansion of outgoing or in-going null geodesics, which is defined and illustrated next.

2.2.1 Expansion

In a hypersurface Σ consider a closed 2-surface S which is the boundary of a set Ω. We can define its unit space-like normal R^a and unit time-like normal T^a. We can now construct outgoing and in-going null normals to S as

$$\ell^a = \frac{1}{\sqrt{2}}(T^a + R^b), \tag{2.1}$$

and

$$n^a = \frac{1}{\sqrt{2}}(T^a - R^b), \tag{2.2}$$

where the normalization is given by the Cauchy slicing. Some of these quantities are illustrated in figure 2.2. The Cauchy slicing also induces a metric q_{ab} on S and the expansion along outgoing or in-going null geodesics is now defined as

$$\theta_{(l)} = q^{ab}\nabla_a l_b \tag{2.3}$$

and

$$\theta_{(n)} = q^{ab}\nabla_a n_b. \tag{2.4}$$

Using the expansion we can now characterize different surfaces S.

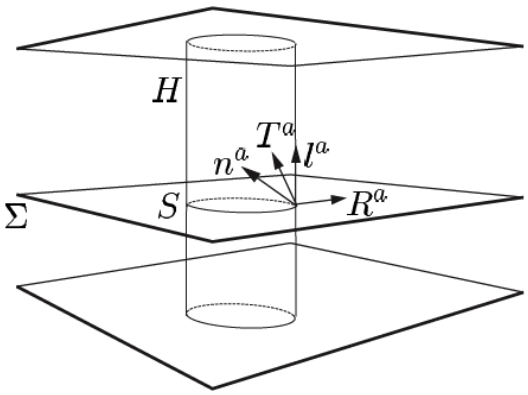

Figure 2.2: World-tube as traced out by an apparent horizon S. Shown is the embedding into the Cauchy hypersurface Σ with T^a being the unit time-like normal to Σ and R^a the outward pointing unit normal to S. l^a and n^a represent outgoing and in-going null vectors. Figure taken from [56].

2.2.2 Trapped surfaces

A closed 2-surface S is called *trapped*, if

$$\theta_{(l)} < 0, \qquad \theta_{(n)} < 0. \tag{2.5}$$

In this case both expansions are strictly negative and this leads to a substantially different behavior of the 2-surface S when compared to a 2-surface in flat space, which for comparison has

$$\theta_{(l)} > 0, \qquad \theta_{(n)} < 0. \tag{2.6}$$

The existence of a trapped surface implies the existence of a singularity [49, 50, 51] A closed 2-surface S is called *marginally trapped* if

$$\theta_{(l)} = 0, \qquad or \qquad \theta_{(n)} = 0, \tag{2.7}$$

and is called *marginally outer trapped* if

$$\theta_{(l)} = 0. \tag{2.8}$$

To recall, an apparent horizon is now defined as the outermost marginally trapped surface contained in a hypersurface Σ.

2.2.3 Properties of apparent horizons

The existence of an apparent horizon implies that a singularity is contained within future of the trapped region, as was shown in [49, 50, 51]. Assuming the cosmic censorship conjecture [8] to hold this also implies that an EH exists. Therefore apparent horizons provide a useful tool to probe space-time geometry in a numerical simulation.

We can determine whether an apparent horizon is present purely with data on one hypersurface and can therefore use it to track and measure black holes during the time evolution of our space-time. As a note of caution we should remark that apparent horizons depend on the Cauchy slicing in their shape. For that reason it is in some circumstances difficult to determine if we really found the outermost marginally trapped surface, since a multitude of those surfaces can appear at times during our simulation. These jumps are presented in chapter 10. The time-series of apparent horizon surfaces defines a world-tube, which can be null but does not have to be in general. In case it is stationary, it can be shown that it is null and that the apparent and EH coincide. This is for example the case for an (to our numerical precision) isolated single black hole with no matter or radiation crossing the horizon. Once we have found an apparent horizon we can use the isolated and DH definitions to determine it's properties like mass, area or spin.

2.3 Isolated and DHs

To measure properties of black holes like mass and spin, the formalism of isolated and DHs [52, 57, 58] has proven to be very useful. To introduce the basic ideas behind this formalism we first define a *non-expanding* horizon as a 3-hypersurface Δ of a space-time manifold $(\mathcal{M}, g_{ab})$ if the following conditions hold:

- Δ is $S^2 \times \mathbb{R}$ and null
- $\Theta_{(l)}$ vanishes on Δ where l is any null normal to N
- All equations of motion hold on Δ and if T_{ab} is non-zero, then $-T^a_b l^b$ is required to be future directed and causal for any future directed null normal l^b.

Condition 3 is satisfied by any matter fulfilling the null-energy condition and condition 2 implies that every cross-section of Δ is marginally trapped. An non-expanding horizon is for example modeled by a single black hole apparent horizon when it has settled down to a stationary state and its world-tube traces out a non-expanding horizon. A non-expanding horizon is invariant under choosing a different slicing of the space-time manifold and as we will show in the following also the notion of mass and spin are independent of the chosen slicing. In order to define the mass and angular momentum of an apparent horizon we require Δ to be not only a non-expanding horizon but also that its intrinsic geometry doesn't evolve. This is the definition of an *(weakly) isolated* horizon [59, 60]. However in the end it turns out that the expressions derived of mass and angular momentum are independent on requiring this extra structure on the surface so we skip the details about isolated horizons and proceed towards the result of the final expressions. Since we are often interested in measuring mass and spin of black holes not only for isolated horizons we first generalize the concept of an isolated horizons to a DH. As already implied in the definition itself, these surfaces can be used in dynamical situations which is what we are interested in in most cases. The concept of a DH generalizes a isolated horizon by not requiring the surface to be in equilibrium

and null, but allowing for a space-like surface. A DH is defined as follows: A smooth, three-dimensional sub-manifold Δ of a space-time manifold $(\mathcal{M}, g_{ab})$ is called a DH if there exists a foliation of closed 2-manifolds such that

- on each leaf S $\Theta_{(l)}$ of one null normal l^a vanishes
- $\Theta_{(n)}$ of the other null normal n^a is negative.

A DH is a world-tube foliated by marginally trapped surfaces and is a quasi-local quantity, since it does not require asymptotic flatness like the definition of the EH does. While DHs are an extremely useful concept they do not describe black holes in every situation since stationary space-times (i.e. an isolated Schwarzschild black hole) do not admit DHs to be identified. In addition on space-times that are dynamical many different DHs can be defined (all of them located within the EH of the black hole) so we need to take some care in determining the DH coinciding with the apparent horizon. Having determined the surface we can proceed and obtain expressions for mass and angular momentum of the DH.

2.3.1 Mass and angular momentum

We can define the mass and angular momentum of an apparent horizon using the isolated and DH frameworks, depending on if the apparent horizon is in equilibrium or not, as described in the previous subsections. The expressions for mass and spin yield the same result independent of if we use the isolated or DH framework. The angular momentum J_S on a cross-section S of an horizon Δ with a 3-hypersurface is [59]

$$J_S = \frac{1}{8\pi} \int_S (\phi^a R^b K_{ab}) d^2V, \tag{2.9}$$

and the integral is evaluated over S. S is required to be axi-symmetric to define angular momentum at all and R^b is the unit outward pointing normal to S, K_{ab} the extrinsic curvature on S and ϕ^a a tangent rotational Killing vector of the induced metric q_{ab} on S. The requirement on S to be axi-symmetric is necessary so that we are always able to find a Killing vector ϕ^a on S. For details on the different procedures to find these Killing vectors we refer to [56], but in most cases the Killing transport equation is solved. If we evaluate J_S at infinity it reduces to the ADM expression for the angular momentum. Additionally to the angular momentum we are often interested in the mass of a horizon which reads [59, 60]

$$M_S = \frac{1}{2R_S} \sqrt{R_S^4 + 4J_S}. \tag{2.10}$$

$R_S = (A_S/4\pi)^{1/2}$ here is the areal-radius, defined using the area of the horizon A, and J_S the angular momentum as defined before. This results is also found in Kerr space-times [61, 62] . Now we can also define the *irreducible mass* of a horizon as [61, 62]

$$M_{irr} = \frac{1}{2} R_S, \tag{2.11}$$

which is the mass M_S minus the rotational energy of the horizon.

3

Cauchy evolution systems

Einstein's equations describe the full 4-dimensional dynamics of space-time. Neither space nor time has a preferred meaning in the 4-dimensional space-time manifold. To make use of numerical techniques for the treatment of Einstein's equations it is however useful to cast the equations into a form parameterized by an explicit 'time' parameter. This allows us to numerically solve for the dynamics of space-times (i.e. like binary black-hole merger systems) that at present can not be solved analytically. We specify initial data on one hypersurface and then use a set of evolution equations to determine the future development of the system. A problem that can be formulated in this way is called an Cauchy initial value problem (CIVP). The solution on a future hypersurface is generally obtained from evaluating data on past hypersurfaces only. A CIVP is characterized by obtaining a solution to a hyperbolic partial differential equation (PDE) in a subset of or the full future development. This set of the future is parameterized by individual time-slices which are space-like [49, 63]. The solution is obtained in the course of the evolution on every one of these time-slices. We can call these surfaces *Cauchy surfaces*. A Cauchy hypersurface is defined as space-like and every time-like or null curve only intersects the hypersurface once. On an initial hypersurface Σ in a subset S the union of all causally connected events that are towards the future of S and can be uniquely determined from evaluating data only on S form the *Cauchy future development* or *domain of dependence* $D^+(S)$. Bounding the domain of dependence is the *future Cauchy horizon* $H^+(S)$. It determines which events in the future we can determine from a subset S on a initial hypersurface Σ. Figure 3.1 describes the concepts just introduced.

The Cauchy problem in GR forms a highly non-trivial system of equations due to the *non-linearity* of Einstein's equations. Furthermore a solution to Einstein's equations can only be determined up to gauge-invariance. That is solutions form a set of equivalence classes and to determine one member explicitly we have to fix the 4 degrees of gauge-freedom to a specific choice. It turns out that choosing an appropriate gauge for Einstein's equations is very difficult for numerical evolutions. More details on choosing a proper gauge will be given in section 3.4 One of the first attempts to cast Einstein's equations into an CIVP was worked out by Arnowitt, Deser and Misner [65]and is there-

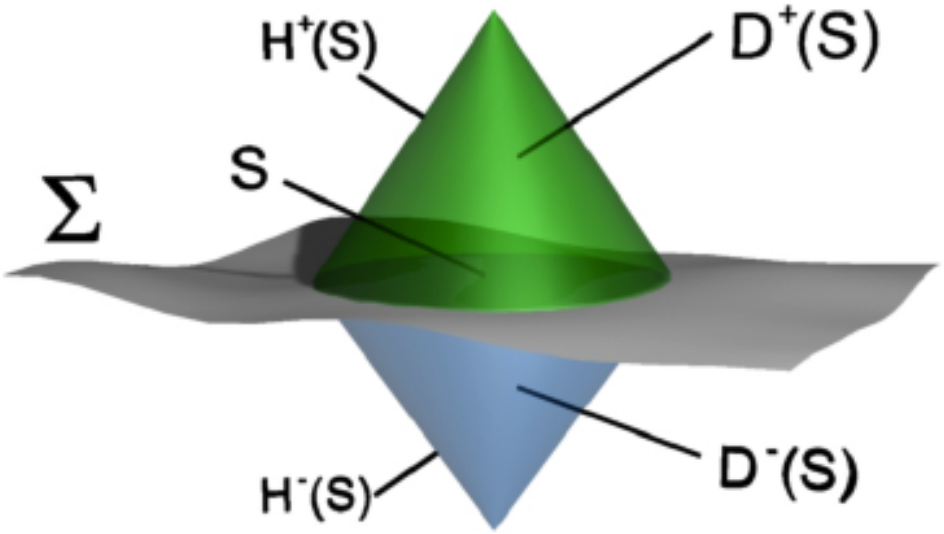

Figure 3.1: Initial data on a subset S of the initial hypersurface Σ determines the future domain of dependence $D^+(S)$. Also shown is the past domain of dependence $D^-(S)$ and the future and past Cauchy horizons $H^+(S)$ and $H^-(S)$. Figure taken from [64]

fore often called the ADM formulation of Einstein's equations. In their approach the 4-dimensional space-time manifold is foliated into 3-dimensional spatial hypersurface parameterized by a time-vector. This procedure is often referred to as a '3+1'-split of space-time. The ADM equations therefore are a reformulation of Einstein's equations into six evolution equations and four constraint equations. The constraint equations determine the solution on a given hypersurface of the foliation and the evolution equations govern the time evolution of the solution from one hypersurface to the next. Using the Bianchi identities one can show that once the four constraint equations are satisfied on the initial hypersurface, the evolution equations guarantee that the constraint equations will also be satisfied on any other hypersurface obtained during evolution for the continuum solution. Using the Bianchi identities one can actually show that the nine 3-metric components actually reduce to only six independent ones, and thus one only needs six of the nine equations to determine the system. These six equations can now conveniently chosen to be the six evolution equations. The remaining four constraint equations are then automatically satisfied. Numerical simulations based on the ADM system were first performed in [66, 67]. Although the system looks very appealing for numerical studies [68] it has the severe drawback of being only weakly hyperbolic and therefore not necessarily stable for numerical simulations. It permits exponentially growing modes that spoil any discretized evolution system based on the ADM equations. For obtaining stable discretized evolution systems it is necessary to

have a strongly hyperbolic continuum evolution system. For strongly hyperbolic evolution systems a well developed mathematical theory exists and can be used to discretized the continuum evolution system. In the following sections we will concentrate on two of the many strongly hyperbolic evolution systems for Einstein's equations, namely the BSSNOK and generalized harmonic systems. The BSSNOK system was first developed by Baumgarte, Shapiro, Nakamura, Shibata, Oohara, and Kujima [69, 70, 71]. In combination with choosing the right gauge, it represents a very robust discretized evolutions system that is used in many of today's applications of numerical evolutions. The other class of evolution system we will pay close attention to in this thesis is the generalized harmonic system [72]. Harmonic coordinates were already used in the first studies of GR (Einstein himself used harmonic coordinates to analyze aspects of his field equations) and reduce the principal part of the evolution equations to a set of wave-equations for the space-time metric. A generalized harmonic system has also been used for the first successful binary black-hole merger simulation [73, 74].

In the following sections we will first introduce the ADM decomposition of Einstein's equations and then continue to describe the BSSNOK and generalized harmonic classes of evolutions systems in detail.

3.1 The ADM formulation

The ADM formalism decomposes the 4-dimensional Einstein's equations and the space-time geometry they describe into a set of 3-dimensional spatial hypersurfaces and their embedding in the 4-dimensional space-time manifold. Space-time becomes foliated along a time-like vector field. Figure 12.1 illustrates a foliation and its embedding into the 4-dimensional space-time manifold. Many of the the calculations for the BSSNOK and generalized harmonic systems are based on basic ADM quantities and we therefore here first summarize the basic features of the ADM system. The text follows closely [75]

3.1.1 3+1 decomposition

Figure 12.1 two spatial hypersurfaces Σ_t and Σ_{t+dt} embedded into the 4-dimensional space-time geometry. The 4-dimensional geometry can be described by the following quantities: On a spatial hypersurface the geometry is described by the 3-metric γ_{ij} (indices i, j only range over 1,2,3). The time-like unit normal is defined as

$$n^\mu = -\alpha g^{\mu\nu} \nabla_\nu t. \tag{3.1}$$

Here $g^{\mu\nu}$ is the full 4-metric and t is a *universal time function*. The hypersurface Σ_i are level sets of the time function t and α can be identified as the *lapse function*, defined by

$$-\alpha^2 := -g^{\mu\nu} \nabla_\mu t \nabla_\nu t. \tag{3.2}$$

α is a gauge-function, it depends on the chosen foliation of time-slices. We can determine the lapse of proper time from one hypersurface Σ_t to a successive on Σ_{t+dt}

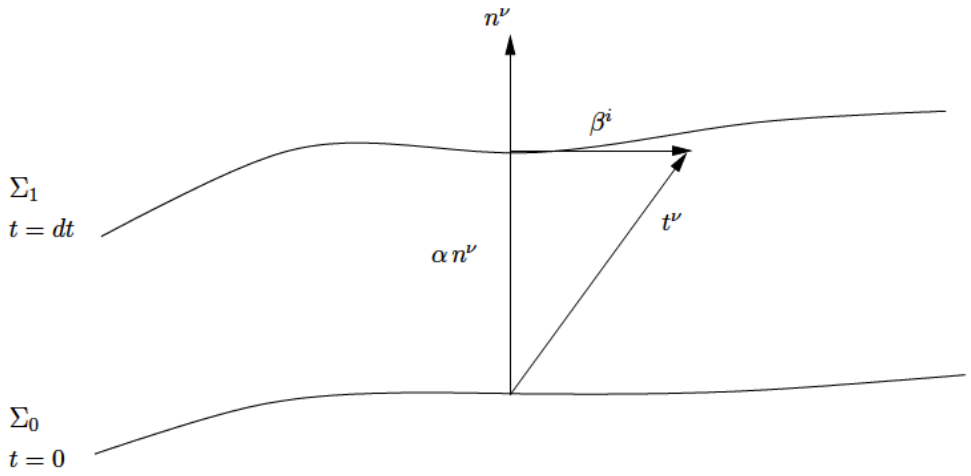

Figure 3.2: 3+1 decomposition of a space-time manifold into a series of spatial hypersurfaces Σ_i. Lapse function α and shift-vector-field β^i are schematically depicted as well as a time-like vector-field t^ν.

by

$$d\tau = \alpha(t, x^i)dt, \tag{3.3}$$

where x^i are the spatial coordinates on the hypersurface. In addition to the lapse we can define a time vector field

$$t^\mu = \alpha n^\mu + \beta^\mu. \tag{3.4}$$

Here β^μ is a purely spatial vector field $\beta^\mu = (0, \beta^i)$ which is commonly referred to as the *shift vector*. This vector yields the change in the coordinates x^i from one spatial hypersurface to the next, as it describes the lines of constant spatial coordinates on each slice,

$$x^i_{t+dt} = x^i_t - \beta^i(t, x^i)dt. \tag{3.5}$$

By choosing lapse and shift we can now fully determine our four degrees of gauge-freedom expressing the 4-metric line element using the ADM variables $\alpha, \beta^i, \gamma_{ij}$

$$ds^2 = -\alpha^2 dt^2 + \gamma_{ij}(dx^i + \beta^i dt)(dx^j + \beta^j dt). \tag{3.6}$$

The normal vector to the spatial hypersurface is given by

$$n_\mu = (-\alpha, 0, 0, 0) \qquad , \qquad n^\mu = \frac{1}{\alpha}(1, -\beta^i), \tag{3.7}$$

and using it we can express the 3-metric as

$$\gamma_{\mu\nu} = g_{\mu\nu} + n_\mu n_\nu. \tag{3.8}$$

With respect to the 3-metric we can now define a covariant derivate operating on the spatial hypersurface and using this derivative operator can express geometric quantities

intrinsic to the spatial hypersurface, most importantly the 3-Riemann tensor. However, in addition we need another quantity to fully determine the 4-geometry, the *extrinsic curvature* tensor.

3.1.2 Extrinsic curvature

The extrinsic curvature is defined as

$$K_{\mu\nu} = -\gamma^{\sigma}_{\mu}\gamma^{\rho}_{\nu}\nabla_{(\sigma}n_{\rho)}. \tag{3.9}$$

It describes the embedding of the spatial hypersurface Σ_t into the space-time manifold. $K_{\mu\nu}$ is symmetric and its only non-zero components are the spatial ones. We can also write it using the Lie-derivative along the normal-vector to the spatial hypersurface n_μ $\mathcal{L}_n$

$$K_{\mu\nu} = -\frac{1}{2}\mathcal{L}_n\gamma_{\mu\nu}. \tag{3.10}$$

The extrinsic curvature measures the rate of change in the 3-metric on a hypersurface Σ along the normal n_μ. It therefore yields the time evolution of the 3-metric γ_{ij}, given that n_μ can associated with the flow of time. $K_{\mu\nu}$ acts as a time-derivative of $\gamma_{\mu\nu}$.

3.1.3 The ADM equations

The ADM equations are a reformulation of Einstein's equations using the 3+1 quantities α, β^i, γ_{ij} and K_{ij}. The 3+1 decomposition of Einstein's equations can be achieved by using the *Gauss*, *Codazzi* and *Ricci* equations. As a result we get the ADM equations, which are a set of constraint equations, which determine the solution on a spatial hypersurface and a set of evolution equations which determine the evolution of the solution in time, i.e. from one hypersurface Σ_t to the next one Σ_{t+dt}. The evolution equations guaranty that if the constraints are fulfilled on the initial hypersurface, they will automatically be fulfilled also at any later time [1]. They constraint equations are

$$R + K^2 - K_{ij}K^{ij} = 16\pi\rho \quad \text{Hamiltonian constraint,} \tag{3.11}$$

$$D_jK^j_i - D_iK = 8\pi j_i \quad \text{momentum constraint,} \tag{3.12}$$

where D_i is the derivative operator in respect to the spatial 3-metric γ_{ij}, ρ is the total energy density as measured by an normal observer n^μ, defined as

$$\rho := n^\mu n^\nu T_{\mu\nu}, \tag{3.13}$$

and the momentum density j_μ is defined as

$$j_\mu = -\gamma^{\nu}_{\mu}n^\rho T_{\nu\rho}. \tag{3.14}$$

[1] This is true only for the continuum solution.

For vacuum space-times both the energy and momentum density are zero. The evolution equations are

$$\partial_t \gamma_{ij} = -2\alpha K_{ij} + D_i\beta_j + D_j\beta_i \tag{3.15}$$

$$\begin{aligned}\partial_t K_{ij} &= -D_j D_i \alpha_\alpha (R_{ij} - 2K_{ik}K^k_j + KK_{ij}) \\ &\quad -\alpha 8\pi(S_{ij} - \frac{1}{2}\gamma_{ij}(S-\rho)) \\ &\quad +\beta^k D)kK_{ij} + K_{ik}D_j\beta^k + K_{kj}D_i\beta^k.\end{aligned} \tag{3.16}$$

Lapse and shift can be freely chosen as they are not determined by the ADM equations. We can exploit the gauge-freedom to prescribe the lapse and shift. However it turns out be not straight-forward to find suitable lapse and shift functions in order to obtain stable numerical evolutions. For example singularities which are necessarily contained inside black-hole horizons should be avoided by a suitable choice of coordinates. The ADM formulation although used in the first attempts of numerical evolutions of black-hole space-times turned out to be numerically unstable for long-term 3D evolutions, so we will proceed to describe two other formulations of Einstein's equations which in practice turn out be more successful in obtaining stable numerical evolutions.

3.2 BSSNOK evolution

The ADM evolution equations, when discretized, lead to strong instabilities. This renders them of little use for numerical evolutions of black-hole space-times. The main reason for the instabilities are mixed second derivatives of the spatial metric that appear in the Ricci tensor (mixed here refers to derivatives both in time and space). It was shown that without these mixed terms the system would be hyperbolic since it could be written as a set of wave equations for the spatial metric [76]. Having a system that is hyperbolic is favorable because this guarantees the existence and uniqueness of solutions. In addition, stability theorems for the discretized system can be applied, making sure that the system yields stable numerical evolutions. Additionally one can use the fact that hyperbolic systems have characteristic lines of propagation for the solution, to construct proper boundary conditions which are another subtle and tricky part of numerical evolutions on compact domains. Nakamura, Oohara and Kojima first suggested to get rid of the mixed derivatives in the Ricci tensor [70] and later Shibata and Nakamura [71] and Baumgarte and Shapiro [69] extended this work. We therefore typically refer to systems based on their approach BSSNOK systems. In addition to their initial work a number of improvements and modifications have been introduced and we will describe the system here in its most up to date form [77, 78, 79]. The BBSNOK systems are shown to be strongly hyperbolic and therefore possess superior stability properties than the only weakly hyperbolic ADM system. While BSSNOK systems are widely used for state-of the art binary black-hole simulations and yield very robust discretized evolution systems, the reason as to why that is still being analyzed [80, 81, 82].

3.2.1 Conformal traceless 3+1 representation

To eliminate mixed derivatives in the Ricci tensor we can introduce auxiliary variables. First, we will conformally rescale the 3-metric by introducing a conformal factor $\Psi = e^{4\phi}$. As a result we obtain the conformal metric

$$\tilde{\gamma}_{ij} = e^{4\phi}\gamma_{ij}, \tag{3.17}$$

where the conformal factor is chosen as $\phi = (\ln(\gamma))/12$ with $\gamma = det(\gamma_{ij})$. This yields a truly conformal metric $\tilde{\gamma}_{ij}$ with unit determinant $\tilde{\gamma}$. In a similar fashion we can first split the extrinsic curvature into its trace and a trace-free part A_{ij} and then apply a conformal rescaling for the traceless part,

$$\tilde{A}_{ij} = e^{4\phi}(K_{ij} - \frac{1}{3}K). \tag{3.18}$$

Being a conformally rescaled quantity, indices of $\tilde{A}_{ij}$ are raised and lowered with the conformal metric $\tilde{\gamma}_{ij}$, so that we obtain the inverse $\tilde{A}^{ij} = e^{4\phi}A^{ij}$. By now taking the trace of the ADM evolution equation for the 3-metric (3.15) and using $\partial_t \ln\gamma = \gamma^{ij}\partial_t\gamma_{ij}$ we obtain

$$\partial_t \ln\gamma^{1/2} = -\alpha K + D_i\beta^i. \tag{3.19}$$

Taking the trace of the evolution equation of the extrinsic curvature (3.16) and using the Hamiltonian constraint (3.11) we get an evolution equation for the trace of the extrinsic curvature

$$\partial_t K = -D^2\alpha + \alpha(K_{ij}K^{ij} + 4\pi(\rho + S)) + \beta^i D_i K. \tag{3.20}$$

Further substituting for the extrinsic curvature, we get

$$\partial_t K = -\gamma^{ij}D_jD_i\alpha + \alpha(\tilde{A}_{ij}\tilde{A}^{ij} + \frac{1}{3}K^2) + 4\pi\alpha(\rho + S) + \beta^i\partial_i K. \tag{3.21}$$

The evolution equation for the conformal factor can now be obtained in an analogue way resulting in

$$\partial_t\phi = -\frac{1}{6}\alpha K + \beta^i\partial_i\phi + \frac{1}{6}\partial_i\beta^i. \tag{3.22}$$

The evolution equations for the trace-less quantities $\tilde{\gamma}_{ij}$ and $\tilde{A}_{ij}$ then yield

$$\partial_t\gamma_{ij} = -2\alpha\tilde{A}_{ij} + \beta^k\partial_k\tilde{\gamma}_{ij} + \tilde{\gamma}_{ik}\partial_j\beta^k + \tilde{\gamma}_{kj}\partial_i\beta^k - \frac{2}{3}\tilde{\gamma}_{ij}\partial_k\beta^k. \tag{3.23}$$

and

$$\begin{aligned}\partial_t\tilde{A}_{ij} = \quad & e^{4\phi}(-(D_iD_j\alpha)^{TF} + \alpha(R^{TF}_{ij} - 8\pi S^{TF}_{ij})) \\ & +\alpha(K\tilde{A}_{ij} - 2\tilde{A}_{il}\tilde{A}^l_j) \\ & +\beta^k\partial_k\tilde{A}_{ij} + \tilde{A}_{ik}\partial_j\beta^k + \tilde{A}_{kj}\partial_i\beta^k - \frac{2}{3}\tilde{A}_{ij}\partial_k\beta^k.\end{aligned} \tag{3.24}$$

The superscript ^{TF} in the last equation denotes the trace-free part of tensors, as defined already for the extrinsic curvature. The divergence terms of the shift vector field $\partial_i\beta^i$ arise due the conformal rescaling. The numeric factors in front of each of the last terms in equations (3.21)-(3.23) correspond to ϕ being a tensor density with weight $w = 1/6$, $\tilde{A}_{ij}$ and γ_{ij} being tensor densities with weight $w = -2/3$. We can continue and define the conformal connection symbols

$$\tilde{\Gamma}^i := \tilde{\gamma}^{jk}\tilde{\Gamma}^i_{jk} = -\tilde{\gamma}^{ij}_{,j}, \tag{3.25}$$

where $\tilde{\Gamma}^i_{jk}$ are the connection coefficients associated with the conformal metric $\tilde{\gamma}_{ij}$. We can no rewrite the Ricci tensor in the form

$$\begin{aligned}\tilde{R}_{ij} = \quad & -\frac{1}{2}\tilde{\gamma}^{lm}\tilde{\gamma}_{ij,lm} + \tilde{\gamma}_{k(i}\partial_{j)}\tilde{\Gamma}^k + \tilde{\Gamma}^k\tilde{\Gamma}_{(ij)k} + \\ & \tilde{\gamma}^{lm}\left(2\tilde{\Gamma}^k_{l(i}\tilde{\Gamma}_{j)km} + \tilde{\Gamma}^k_{im}\tilde{\Gamma}_{klj}\right).\end{aligned} \tag{3.26}$$

All the mixed second derivatives of $\tilde{\gamma}_{ij}$ besides the Laplace operator $\tilde{\gamma}^{lm}\tilde{\gamma}_{ij,lm}$ have now been absorbed into first derivatives of $\tilde{\Gamma}^i$. If we now treat the $\tilde{\Gamma}^i$ as independent functions we need to obtain an evolution equation for them, too. We get

$$\partial_t\tilde{\Gamma}^i = -\partial_j\left(2\alpha\tilde{A}^{ij} - 2\tilde{\gamma}^{m(j}\beta^{i)}_{,m} + \frac{2}{3}\tilde{\gamma}^{ij}\beta^l_{,l} + \beta^l\tilde{\gamma}^{ij}_{,l}\right). \tag{3.27}$$

and using the momentum constraint (3.12) we can further expand this to

$$\begin{aligned}\partial_t\tilde{\Gamma}^i = \quad & -2\tilde{A}^{ij}\partial_j\alpha + 2\alpha\left(\tilde{\Gamma}^i_{jk}\tilde{A}^{kj} - \frac{2}{3}\tilde{\gamma}^{ij}\partial_j K - 8\pi\tilde{\gamma}^{ij}S_j + 6\tilde{A}^{ij}\partial_j\phi\right) \\ & +\beta^j\partial_j\tilde{\Gamma}^i - \tilde{\Gamma}^j\partial_j\beta^i + \frac{2}{3}\tilde{\Gamma}^i\partial_j\beta^j + \frac{1}{3}\tilde{\gamma}^{li}\beta^j_{,jl} + \tilde{\gamma}^{lj}\beta^i_{,lj}.\end{aligned} \tag{3.28}$$

Equations (3.22), (3.23), (3.20), (3.24) and (3.28) form an equivalent evolution system and can be used instead of the ADM evolution equations. Because we have introduced the conformal connection coefficients $\tilde{\Gamma}^i$ as independent variables, we have also introduced their definition as one more constraint equation (3.25). The evolution variables of the BSSNOK formulation are

$$\phi, \qquad \tilde{\gamma}_{ab}, \qquad K, \qquad \tilde{A}_{ab} \qquad \text{and} \qquad \tilde{\Gamma}^a. \tag{3.29}$$

In [78, 79] it has been found that a different choice for the conformal factor improves the behavior of the numerical solution close to the singularity. We therefore here adept this choice, using

$$\hat{\phi}_k := (det\gamma_{ab})^{(-1/\kappa)}, \tag{3.30}$$

where $\kappa > 0$ is a parameter. It has been shown in [78] that the choice of $\chi := \hat{\phi}_3$ has the benefit of avoiding singularities in some evolution terms of Bowen-York initial data (see next section for details on initial data). In addition the choice of $W := \hat{\phi}_6$ provides the initial benefit of making sure that γ stays positive during the evolution [79].

This condition needs to enforced for χ, since it can create instabilities in the evolution system. Now the final set of evolution equations reads

$$\partial_t \hat{\phi}_\kappa = -\frac{2}{\kappa}\hat{\phi}_\kappa \alpha K + \beta^i \partial_i \hat{\phi}_\kappa - \frac{2}{\kappa}\hat{\phi}_\kappa \partial_i \beta^i. \tag{3.31}$$

$$\partial_t \tilde{\gamma}_{ij} = -2\alpha \tilde{A}_{ij} + \beta^k \partial_k \tilde{\gamma}_{ij} + \tilde{\gamma}_{ik}\partial_j \beta^k + \tilde{\gamma}_{kj}\partial_i \beta^k - \frac{2}{3}\tilde{\gamma}_{ij}\partial_k \beta^k. \tag{3.32}$$

$$\partial_t K = -\gamma^{ij} D_j D_i \alpha + \alpha(\tilde{A}_{ij}\tilde{A}^{ij} + \frac{1}{3}K^2) + 4\pi\alpha(\rho + S) + \beta^i \partial_i K. \tag{3.33}$$

$$\begin{aligned}\partial_t \tilde{A}_{ij} &= (\hat{\phi}_\kappa)^{\kappa/3}(-(D_i D_j \alpha)^{TF} + \alpha(R_{ij}^{TF} - 8\pi S_{ij}^{TF})) \\ &+\alpha(K\tilde{A}_{ij} - 2\tilde{A}_{il}\tilde{A}^l_j) \\ &+\beta^k \partial_k \tilde{A}_{ij} + \tilde{A}_{ik}\partial_j \beta^k + \tilde{A}_{kj}\partial_i \beta^k - \frac{2}{3}\tilde{A}_{ij}\partial_k \beta^k\end{aligned} \tag{3.34}$$

$$\begin{aligned}\partial_t \tilde{\Gamma}^i &= -2\tilde{A}^{ij}\partial_j \alpha + 2\alpha\left(\tilde{\Gamma}^i_{jk}\tilde{A}^{kj} - \frac{2}{3}\tilde{\gamma}^{ij}\partial_j K - 8\pi\tilde{\gamma}^{ij}S_j + 6\tilde{A}^{ij}\partial_j \phi\right) \\ &+\beta^j \partial_j \tilde{\Gamma}^i - \tilde{\Gamma}^j \partial_j \beta^i + \frac{2}{3}\tilde{\Gamma}^i \partial_j \beta^j + \frac{1}{3}\tilde{\gamma}^{li}\partial_l \partial_j \beta^j + \tilde{\gamma}^{lj}\partial_l \partial_j \beta^i\end{aligned} \tag{3.35}$$

A more detailed discussion on the BSSNOK systems can be found in [77, 78, 79]. The discretization of this system will be discussed in chapter 8

3.3 Generalized harmonic evolution

In this section we present the basic equations used for a generalized harmonic system formulated using the 3+1 variables. The formulation in generalized harmonic coordinates $x^\mu = (t, x^i)$ was first described by Friedrich and Rendall [293]. (We in the presentation here make minor alterations in the notation of [293] to conform to standard usage in numerical relativity.) This 3+1 foliation gives rise to the metric decomposition

$$g_{\mu\nu} = -n_\mu n_\nu + h_{\mu\nu} \tag{3.36}$$

where

$$n_\mu = -\alpha \partial_\mu t, \quad \alpha = \frac{1}{\sqrt{-g^{tt}}} \tag{3.37}$$

is the unit future directed time-like normal to the foliation. The evolution proceeds along the streamlines of the vector field $\partial_t = \alpha n^\mu \partial_\mu + \beta^\mu \partial_\mu$ determined by the lapse α and shift $\beta^\mu = (0, \beta^i)$.

In this formulation the constraints are

$$C^\mu := \Gamma^\mu - F^\mu \tag{3.38}$$

where Γ^μ is related to the Christoffel symbols by $\Gamma^\mu = g^{\rho\sigma}\Gamma^\mu_{\rho\sigma}$ and $F^\mu(g, x)$ are harmonic gauge source functions.

When the harmonic constraints are satisfied, i.e. $C^\mu = 0$, the Einstein equations reduce to a system of quasi-linear wave equations for the spatial metric h_{ij}, shift β^i and lapse α which take the form [293]

$$-g^{\mu\nu}\partial_\mu\partial_\nu h_{ij} = S_{ij} \tag{3.39}$$

$$\frac{1}{\alpha^2}\left(\partial_t - \beta^j\partial_j\right)^2\beta^i - h^{jk}\partial_j\partial_k\beta^i = S^i \tag{3.40}$$

$$\frac{1}{\alpha^2}\left(\partial_t - \beta^j\partial_j\right)^2\alpha - D_jD^j\alpha = S, \tag{3.41}$$

where D_i is the covariant derivative associated with h_{ij} and the right-hand-side S-terms do not enter the principle part. In detail, these terms are

$$\begin{aligned} S_{ij} = {} & \frac{2}{\alpha^2}K_{ij}\left(\partial_t\alpha - \mathcal{L}_\beta\alpha\right) + \frac{2}{\alpha^2}D_i\alpha D_j\alpha \\ & -2D_{(i}\left[h_{j)k}h^k_\nu F^\nu\right] + \frac{4}{\alpha^3}D_{(i}\alpha h_{j)k}\left(\partial_t\beta^k - \beta^\ell\partial_\ell\beta^k\right) \\ & +\frac{4}{\alpha^2}\left(\partial_{(j}\beta^k\right)\partial_t h_{i)k} + \frac{2}{\alpha^2}h_{\ell(i}\left(\partial_{j)}\beta^k\right)\left(\partial_k\beta^\ell\right) \\ & -\frac{2}{\alpha^2}\left(\partial_{(j}\beta^k\right)\mathcal{L}_\beta h_{i)k} - \frac{2}{\alpha^2}\left(\partial_{(j}\beta^k\right)\left(\partial_\ell h_{i)k}\right) \\ & +4K_{ik}K^k_j - 2K_{ij}K - 2\gamma^\ell_{ki}h_{n\ell}g^{km}\gamma^n_{mj} - 4\gamma^\ell_{km}h^{kn}h_{\ell(i}\gamma^m_{j)n} + B_{ij} \end{aligned} \tag{3.42}$$

$$\begin{aligned} S^i = {} & 4\left(K^{i\ell} - Kh^{i\ell}\right)D_\ell\alpha \\ & -2\alpha\left(K^{m\ell} - Kh^{m\ell}\right)\gamma^i_{\ell m} - \left(\partial_\ell\beta^i\right)\gamma^\ell \\ & +\left(\partial_\ell\beta^i\right)D^\ell\log\alpha \\ & +2\alpha n_\nu F^\nu\left[\gamma^i - D^i\log\alpha - h^i_\nu F^\nu\right] \\ & -2\alpha K h^i_\nu F^\nu - D^i\left(\alpha n_\nu F^\nu\right) - \left(\partial_t - \beta^k\partial_k\right)\left(h^i_\nu F^\nu\right) + B^i \end{aligned} \tag{3.43}$$

$$\begin{aligned} S = {} & -\alpha\left[K_{ij}K^{ij} - 4Kn_\nu F^\nu - 2\left(n_\nu F^\nu\right)^2 - 2K^2\right] \\ & +\left(\partial_t - \beta^k\partial_k\right)\left(n_\nu F^\nu\right) + B, \end{aligned} \tag{3.44}$$

where γ^k_{ij} are the Christoffel symbols associated with D_i, $\gamma^k = h^{ij}\gamma^k_{ij}$, $K_{ij} = (1/2\alpha)(\partial_t - \mathcal{L}_\beta)h_{ij}$ is the extrinsic curvature of the Cauchy foliation and the quantities B, B^i, B_{ij} are constraint modification terms defined in (3.56)-(3.58) which are used to stabilize the constraint propagation system. With the addition of constraint modification, (3.39)-(3.41) correspond to equations (2.33), (2.36) and (2.38). See [294] for further details.

Constraint preservation for the Cauchy problem follows from the system of homogeneous wave equations satisfied by the harmonic constraints (3.38). Constraint propagation can be extended to the initial-boundary value problem by implementing the hierarchy of Sommerfeld boundary conditions presented in [295, 296]. However, this

has not yet been incorporated in the version of the code being used for the results presented in this thesis. For the simulations presented in chapter 10 we maintain constraint preservation by causally isolating the region of interest from the outer boundary.

For the purpose of using the *Method of Lines* (MoL) to apply a *Runge-Kutta* (RK) time integrator, we re-write the system (3.39)-(3.41) as first differential order in time and second differential order in space by using the time-like vector

$$\tilde{n}^{\nu} = \frac{1}{\alpha}\left(\delta_0^{\nu} - w\beta^{\nu}\right) \tag{3.45}$$

to introduce the auxiliary variables

$$\tag{3.46}$$

$$\Pi := \mathcal{L}_{\tilde{\mathbf{n}}}\alpha = \tilde{n}^{\mu}\partial_{\mu}\alpha \tag{3.47}$$

$$\Pi^{i} := \mathcal{L}_{\tilde{\mathbf{n}}}\beta^{i} = \tilde{n}^{\mu}\partial_{\mu}\beta^{i} - \beta^{k}\partial_{k}\tilde{n}^{i} \tag{3.48}$$

$$\Pi_{ij} := \frac{1}{2}\mathcal{L}_{\tilde{\mathbf{n}}}g_{ij} = \frac{1}{2}\left[\tilde{n}^{\mu}\partial_{\mu}h_{ij} + g_{i\mu}\partial_{j}\tilde{n}^{\mu} + g_{j\mu}\partial_{i}\tilde{n}^{\mu}\right]. \tag{3.49}$$

Here the function w is chosen to be unity everywhere except near the boundary where it smoothly goes to zero. Inserting equation (3.45) into equations (3.47)-(3.49) gives the evolution equations for the lapse, shift and 3-metric,

$$\partial_t\alpha = \alpha\Pi + w\beta^{i}\partial_{i}\alpha \tag{3.50}$$

$$\partial_t\beta^{i} = \alpha\Pi^{i} + \frac{w}{\alpha}\beta^{i}\beta^{k}\partial_{k}\alpha - \beta^{i}\beta^{k}\partial_{k}w \tag{3.51}$$

$$\partial_t h_{ij} = 2\alpha\Pi_{ij} - \alpha\left[\tilde{n}^{k}\partial_{k}h_{ij} + g_{i\mu}\partial_{j}\tilde{n}^{\mu} + g_{\mu j}\partial_{i}\tilde{n}^{\mu}\right]. \tag{3.52}$$

The evolution equations for the auxiliary Π-variables then follow from the first time derivatives of (3.50)-(3.52), after using (3.50)-(3.52) and (3.39)-(3.41) to eliminate first and second time-derivatives of the metric variables.

3.3.1 Constraint damping

We modify the evolution system by terms vanishing when the constraints are fulfilled, based upon the results presented in [283]. For this purpose we set

$$A^{\mu\nu} = -\frac{a_1}{\sqrt{-g}}C^{\alpha}\partial_{\alpha}\left(\sqrt{-g}g^{\mu\nu}\right) + \frac{a_2 C^{\alpha}\nabla_{\alpha}t}{\varepsilon + e_{\rho\sigma}C^{\rho}C^{\sigma}}C^{\mu}C^{\nu} - \frac{a_3}{\sqrt{-g^{tt}}}C^{(\mu}\nabla^{\nu)}t \tag{3.53}$$

where ε is a small positive number, a_i are positive parameters and

$$e_{\rho\sigma} = n_{\mu}n_{\nu} + h_{\rho\sigma} \tag{3.54}$$

is a Euclidean 4-metric. In terms of

$$\tilde{A}_{\mu\nu} = g_{\mu\sigma}g_{\nu\rho}A^{\sigma\rho} - \frac{1}{2}g_{\mu\nu}g_{\rho\sigma}A^{\rho\sigma} \tag{3.55}$$

the B-terms added to (3.42)-(3.44) for constraint modification are

$$B = \frac{1}{\alpha}\left(-\beta^i\beta^j\tilde{A}_{ij} + 2g_{ij}\beta^j\beta^k g^{il}\tilde{A}_{kl} + 2g_{ij}\beta^j g^{ik}\tilde{A}_{tk}\right) \tag{3.56}$$

$$B^i = -2\left(\beta^j g^{ik}\tilde{A}_{kj} + g^{ij}\tilde{A}_{tj}\right) \tag{3.57}$$

$$B_{ij} = -2\tilde{A}_{ij}. \tag{3.58}$$

3.4 Gauge choices

GR is a gauge-invariant theory, that is no coordinate system is preferred over another one. Space-times that only differ up to a diffeomorphic transformation are equivalent. In order to perform a numerical evolution we however need to fix this gauge-freedom and explicitly choose a coordinate system since we need to represent the space-time variables on a computer. We already encountered the gauge-parameters α and β^i in the previous section in the 3+1 decomposition of Einstein's equations. They can be chosen freely, but proper care has to be taken in choosing appropriate functions as lapse and shift in order to obtain stable numerical evolutions. The choice of a proper gauge is crucial for the success of a numerical evolution, it has turned out. Choosing the most naive gauge (*geodesic slicing*) and starting a black-hole evolution we would find that our coordinates, after a short time, would fall into the singularity, making further evolution impossible. In order to find a proper gauge for black-hole evolution we desire a number of useful features:

- The gauge should adapt to the underlying symmetries of the space-time
- The formation of coordinate singularities should be avoided in any case. If in the space-time a physical singularity is present, the gauge should make sure to avoid this singularity.
- Gauge prescriptions should ideally be well behaved mathematically (in order to not introduce problematic features into the evolution system themselves)
- The gauge should be formulated in a coordinate-independent way. One way to ensure this is to apply covariance.

Practically formulating a gauge we can either prescribe conditions on the geometric variables of our evolution system themselves or relate them to the gauge functions by means of equations indirectly. This leads to gauge conditions ranging from simple algebraic equations to more complicated hyperbolic or elliptic PDEs and evolution equations and evolution equations. In this section we first review the basic gauge conditions used for the BSSNOK systems and then continue to describe typical gauge choices for the generalized harmonic system presented in the previous section.

3.4.1 Geodesic slicing

Geodesic slicing refers to the simplest gauge choice possible, i.e. $\alpha = 1$ and $\beta^i = 0$. Using this slicing condition one can show that a point initially located on the throat of a black will hit the singularity after proper time $\tau = t = \pi M$ [83]. Therefore a numerical evolution code would also crash after that time because the entire numerical grid would have fallen into the black hole. This makes geodesic slicing unusable for numerical evolutions of black-hole space-times. A slicing condition that doesn't have this limitation is *maximal slicing*.

3.4.2 Maximal slicing

Maximal slicing prevents the computational grid to fall into the black hole by choosing a lapse that approaches Minkoswki in the exterior of the black hole and approaches zero as it gets close to the singularity contained in the black-hole horizon. It 'freezes' time close to the black hole and allows time evolution in the exterior region. In combination with initial data where the singularity lies towards the future we can use maximal slicing to evolve black-hole space-times without hitting the singularity contained within [68, 84, 85, 86, 87, 88]. The name maximal slicing was chosen because the slices have maximal volume. They are characterized by

$$K := \gamma^{ij} K_{ij} = 0 = \frac{\partial K}{\partial t}. \tag{3.59}$$

By inserting this condition into the evolution equation for the trace of the extrinsic curvature K (3.20) we obtain a condition for the lapse

$$D^i D_i \alpha = \alpha R, \tag{3.60}$$

or using the Hamiltonian constraint

$$D^i D_i \alpha = \alpha K^{ij} K_{ij}. \tag{3.61}$$

The result is an elliptic equation that needs to be solved at every time-step during evolution to obtain the profile of the lapse and ensure maximal slicing. This is not only computational expensive but also it has turned out that maximal slicing leads to a phenomenon called *slice-stretching*, because it freezes time at the singularity. This stretches the slice to such an extent that the numerical evolution will crash eventually [87, 89]. This slice stretching can be avoided by providing suitable conditions for the shift vector-field β^i. Singularity avoiding slicing examples are depicted in figure 3.3

3.4.3 Hyperbolic slicing

Before continuing towards gauge conditions that do not have the drawback of being computationally very expensive we introduce a slightly modified condition on the extrinsic curvature, the *K-driver* condition. Considering again the maximal slicing condition with $K = 0$ we easily see that any perturbation in the lapse, i.e. as introduced by

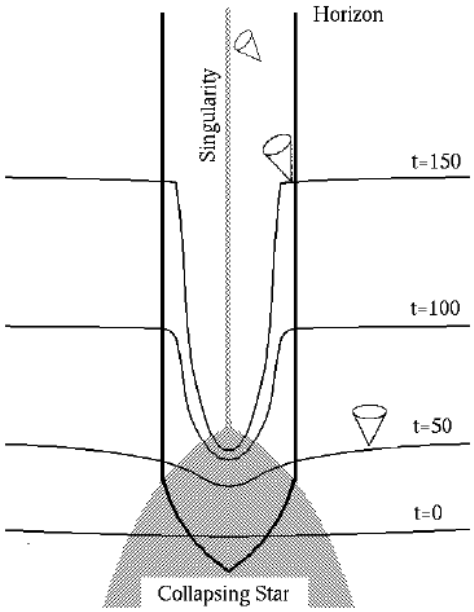

Figure 3.3: Singularity avoidance of a set of time-slices. The slices never hit the singularity but will suffer severe slice-stretching in the region close to the singularity. Figure taken from [90].

numerical error will yield K different from zero and the gauge condition in the way it is formulated has no possibility to reach $K = 0$ again. Therefore the K-driver condition has been introduced [91] which is of the form,

$$\frac{\partial K}{\partial t} + cK = 0, \tag{3.62}$$

with $c > 0$ being constant in time. This condition will exponentially drive k to zero and thus actively enforce $K = 0$ even if perturbations in the lapse are generated during the evolution. Using the Hamiltonian condition we can again write this as a condition for the lapse

$$D^i D_i \alpha = \beta^i \partial_i K + \alpha K^{ij} K_{ij}, \tag{3.63}$$

again a elliptic equation we can determine the lapse function from. Having to solve an elliptic equation every time-step is very computationally expensive and it is therefore desirable to find gauge prescriptions which yield parabolic or even better hyperbolic equations for relating the gauge functions to the geometric variables. If we generalize the idea of K-freezing and instead relate the first time derivative of the trace of the extrinsic curvature to the first or second time-derivative of the lapse-function we can achieve just that. We call the family of gauges the Bona-Masso-slicing conditions as they were first introduced by Bona and Masso [92]. One member of this family

of gauges, the so called 1 + log-slicing, in particular has proven to very robust and suitable for black-hole evolutions. In general for the Bona-Masso slicing family the lapse is determined by

$$\partial_t \alpha = -\alpha^2 f(\alpha) K, \tag{3.64}$$

which for $f > 0$ is a hyperbolic equation since it can reduced to a wave equation for the lapse with a propagation speed of $v_g = \alpha\sqrt{f\gamma^{ij}}$ along any spatial direction x^i. The particular choice of $f = 2/\alpha$ yields a solution of the form

$$\alpha = h(x^i) + \ln \gamma \tag{3.65}$$

with $h(x^i)$ being a positive time-independent function. This choice of slicing condition is referred to as the 1 + log slicing condition. It was shown to be singularity avoiding [84] and in general provides a very robust slicing condition for black-hole evolutions. Generalizing the 1 + log condition to the form

$$\partial_t \alpha - \beta^i \partial_i \alpha = -n\alpha(K - K_0), \tag{3.66}$$

with $K_0 = K(t = 0)$ being the initial value of the trace of the extrinsic curvature, n a constant usually chosen as $n = 2$ we obtain the form of slicing condition used in current numerical evolution codes based on the BSSNOK formulation of Einstein's equations. The additional advection term was introduced in [93] to remove unphysical gauge modes induced by the original form of the 1 + log-condition [94]. We have now obtained a singularity-avoiding, numerically efficient to solve and robust slicing condition yielding a prescription for the lapse-function α but still need to find a condition for the shift-vector to cure the effect of slice-stretching. This is realized by introducing the $\tilde{\Gamma} - driver$-condition for the shift which is described in the next section.

3.4.4 Hyperbolic $\tilde{\Gamma}^i$-driver condition

Both maximal and 1 + log-slicing conditions lead to the slice-stretching, that is the numerical grid near the singularity will be extremely stretched leading to a resolution loss around the black hole which ultimately will crash the numerical evolution scheme used. To avoid this we need to find a shift-condition which effectively counteracts this effect preventing slice-stretching to happen. We therefore need to find a outward-pointing shift, that just matches the velocity at which the coordinates are falling into the black-hole horizon. but since the evolution of black-hole space-times is very complex we cannot just prescribe the shift in an explicit form but need a dynamically adapting condition as we have found for the lapse in the previous section. This was achieved by introducing the hyperbolic $\tilde{\Gamma}$-driver condition [95, 96], which yields a hyperbolic equation for the shift vector. By setting $\partial_t \tilde{\Gamma} = 0$ and using the definition of the $\tilde{\Gamma}^i$ evolution variable of the BSSNOK system we can easily find an elliptic equation that we can solve for the shift. Setting $\partial_t \tilde{\Gamma} = 0$ is closely related to the well-known and studied *minimal distortion* condition, which is a very natural way time impose a nearly constant coordinate system. It minimizes the change in volume elements during the evolution

but also leads to an elliptic equation for β^i. It however possesses the properties we want to achieve and even further results in the TT-gauge in the weak-field limit [97] which will be a very useful property for the analysis of gravitational radiation. To circumvent having to solve an elliptic equation every time-step, we effectively only approximately solve it and use the fact that we do not have to find the exact solution due to our gauge-freedom [91]. To solve elliptic equations one usually introduces a fictitious time-coordinate and evolves the resulting parabolic equation until the solution reaches a stationary state and the solution of the original elliptic equation is therefore obtained. This problem can also be reformulated into an hyperbolic equation and we use this and only use the first relaxation step since we desire only to find an approximate solution. The hyperbolic driver condition can now be written as

$$\partial_t \beta^i - \beta^j \partial_j \beta^i = \frac{3}{4} \alpha B^i \tag{3.67}$$

$$\partial_t B^i - \beta^j \partial_j B^i = \partial_t \tilde{\Gamma}^i - \beta^j \partial_j \tilde{\Gamma}^i - \eta B^i, \tag{3.68}$$

with η being a damping factor which can be freely chosen. Recently it was shown that η may play a crucial role for the success of unequal-mass binary black-hole simulations [98, 99, 100]. However these modification were not used in the simulations performed for this thesis and thus we refer the reader to [98, 99, 100] for details. The advection terms on the left-hand side of equations (3.68) were not present in the original proposed form [95, 96] since in this work co-rotating coordinates were used. These terms are however required for using standard coordinates [93, 101] and one can show that the orbital motion of the punctures is actually completely induced by these terms. This can be understood by the fact that the choice of the $\tilde{\Gamma}$-driver gauge condition is designed to adapt to any dynamics induced in the geometry. This leads to the shift vector field not only adapting to the coordinates trying to fall into the black-hole horizons but also to the orbital motion of the binary black-hole system itself.

3.4.5 Generalized harmonic gauge choices

For the generalized harmonic system presented in section 3.3 gauge conditions in general cannot be imposed by choosing a lapse function and shift vector as is done for the BSSNOK system. The gauge variables α and β^i in this formulation have to be evolved according to (3.50) and (3.51) to keep the system in symmetric hyperbolic form (see chapter 6 for details on hyperbolicity and its connection to stability). However, we can specify the *gauge source* functions $F^\nu(x^\mu)$ and by their choice acquire a specific form for the lapse and shift. Different choices of gauge source functions have been used [73, 74, 102, 103]. For the results in this thesis the pure harmonic gauge source functions, *i.e.,* $F^\nu(x^\mu) = 0$ have been used and for simplicity we do not discuss the details of gauge choices for generalized harmonic systems here. For a detailed overview on state of the art gauge source functions for generalized harmonic formulations of Einstein's equations we refer to [102, 103].

3.5 Initial data

To start an evolution with the goal of solving an CIVP in GR we need to specify initial data. This initial data needs to satisfy the four elliptic constraint equations, the three momentum constraints and the Hamiltonian constraint. For binary black-hole merger initial data we are in general interested to construct initial data containing multiple black holes, which have initial spin and momenta such that they will follow in-spiraling orbits and finally merge. A key aspect in the generation of black-hole initial data is the treatment of the singularity contained within a black-hole horizon. For obtaining black-hole initial data we usually introduce a suitable topology. The first to introduce such a topology were Einstein and Rosen by creating what we call *Einstein-Rosen-bridges* [104]. Building on their initial idea additional topologies of these wormhole-like bridges were proposed [105, 106, 107, 108, 109]. The initial spatial slice of these bridges consist of multiple copies of $\mathbb{R}^3$ with some regions (typically spherical) removed. One then specifies boundary data on the inner and outer boundaries of the domain. In this data several asymptotically flat regions are connected via 'throats' or bridges with their interior removed by excising a region around the singularity. This way the other asymptotically flat-ends are removed, which is possible only because they are causally disconnected. One can use different topologies and strategies to solve the constraint equations. Misner type initial data [107] consists of two asymptotically flat spaces that are connected by as many throats as black holes are present, and are isometric copies of each other. To solve the equations outer and inner boundary conditions have to complete the data on the computational domain. For Misner type initial data this can be achieved by boundary conditions based on the isometry condition [106, 107]. *Conformal imaging* [110, 111, 112, 113, 114, 115] generalizes Misner initial data to construct time-symmetric initial data solving the momentum and Hamiltonian constraints but is unfortunately very complex. Since excision techniques induce additional boundaries and are usually difficult to handle in practice one ideally would want to construct initial data without the need of excising regions in the interior of the domain. A method to generate this type of initial data was first suggest by Brill and Lindquist [105], which compactified the internal asymptotically flat region and we can use one single domain of integration to solve the constraint equations [116, 117, 118]. This data is constructed on $\mathbb{R}^3$. The compactification of the asymptotically flat regions into a single point is called the *puncture* method with the singular points being identified as *punctures*. Besides the benefit of having only one domain of integration and only needing to specify outer boundary conditions punctures will turn out to be a suitable way to deal with singularities in our computational domain. Because of all these combined reasons puncture initial data is the method of choice in many of today's numerical relativity binary black-hole simulations. The two main strategies for constructing initial data are the *conformal transverse-traceless* decomposition of the metric on the initial slice [119, 120, 121] and using Bowen-York extrinsic curvature to solve the momentum constraints [111, 113]. An alternative route for constructing initial data provides the *thin-sandwich* decomposition [122], which describes initial data on two nearby hyper-

surfaces, which effectively determines the metric and its time derivative on the initial slice. While this method can control the dynamics of the space-time quantities, it can be shown that both methods are equivalent [123] and we choose to proceed with the easier approach of the conformal transverse-traceless decomposition [124]. In addition to the technical aspects of solving the constraint equations one needs to obtain the black-hole parameters mass, spin and momenta to generate initial data yielding the desired orbital configuration. This is typically done by first using a post-Newtownian (PN) evolution code to evolve both black holes until the separation we want to start the numerical evolution from is reached and then reading off the parameters as a result of the PN evolution. This method has been shown to be superior to simpler methods, i.e. effective potential based methods, in yielding low eccentricity orbits. All of the results presented in this thesis for binary black-hole mergers on in-spiraling orbits have been constructed using the method described in [125]. The details of the individual steps needed for constructing black-hole initial data are described in the following sections.

3.5.1 Conformal transverse-traceless decomposition

The conformal transverse-traceless decomposition was first introduced by Lichnerowicz, York and others [119, 120, 121] and consists of an Ansatz to prescribing initial data in terms of the conformal 3-metric and the extrinsic curvature to solve the Hamiltonian and momentum constraints. We again decompose the 3-metric γ_{ij} by using a conformal factor Ψ such that

$$\gamma_{ij} = \Psi^4 \tilde{\gamma}_{ij} \tag{3.69}$$

with $\tilde{\gamma}_{ij}$ being conformally flat, i.e. $\tilde{\gamma}_{ij} = \delta_{ij}$. We split the trace off the extrinsic curvature and construct

$$A^{ij} = K^{ij} - \frac{1}{3}\gamma^{ij} K, \tag{3.70}$$

and then conformally rescale $A^i j$ in the way

$$\tilde{A}^{ij} = \Psi^{10} A^{ij}. \tag{3.71}$$

Any symmetric traceless tensor can be split in the following way

$$S^{ij} = S^{ij}_* + (\mathbf{L}W)^{ij}, \tag{3.72}$$

with S^{ij}_* being a symmetric, traceless and *transverse* tensor ($D_j S^{ij}_* = 0$), W^i a vector and $\mathbf{L}$ an operator defined as

$$(\mathbf{L}W)^{ij} := D^i W^j + D^j W^i - \frac{2}{3}\gamma^{ij} D_k W^k. \tag{3.73}$$

$(\mathbf{L}W)^{ij}$ is the *conformal Killing form* associated with W^i and we call its contribution in (3.72) the *longitudinal part* of S^{ij}. If we now split $\tilde{A}^{ij}$ accordingly we obtain

$$\tilde{A}^{ij} = \tilde{A}^{ij}_* + (\tilde{\mathbf{L}}\tilde{W})^{ij}. \tag{3.74}$$

We now need to obtain $\tilde{A}^{ij}_*$ and we can construct it from any symmetric trace-free tensor $\tilde{M}^{ij}$, casting $\tilde{A}^{ij}$ into the form

$$\tilde{A}^{ij} = \tilde{M}^{ij} + (\tilde{\mathbf{L}}\tilde{V})^{ij}, \tag{3.75}$$

with V^i being a vector related to W^i. Details of this procedure can be found in [119, 126] . Using the splitted form of $\tilde{A}^{ij}$ we can cast the Hamiltonian and momentum constraints into the form

$$8\tilde{D}^2\Psi - \tilde{R}\Psi + \Psi^{-7}\tilde{A}_{ij}\tilde{A}^{ij} - \frac{2}{3}\Psi^5 K^2 + 16\pi\Psi^5\rho \quad = 0, \tag{3.76}$$

$$\tilde{\Delta}_{\tilde{\mathbf{L}}}\tilde{V}^i + \tilde{D}_j\tilde{M}^{ij} - \frac{2}{3}\Psi^6\tilde{D}^i K - 8\pi\Psi^1 0 j^i \quad = 0. \tag{3.77}$$

We now have to solve these four equations for Ψ and $\tilde{V}^i$, with data provided in the form of $\tilde{\gamma}_{ij}$, $\tilde{M}^{ij}$, K, and the energy and momentum densities ρ and j and reconstruct the physical quantities as

$$\gamma_{ij} \quad = \Psi^4\tilde{\gamma}_{ij}, \tag{3.78}$$

$$K^{ij} \quad = \Psi^{-10}\tilde{A}^{ij} + \frac{1}{3}\gamma^{ij}K. \tag{3.79}$$

The next step is now to describe in detail how to solve equations (3.11) and (3.12).

3.5.2 Bowen-York extrinsic curvature

A simple way of solving equation (3.12) is to impose the condition of time-symmetry ($K_{ij} = 0$). This however is in practice not very useful since we are generally interested in not stationary but dynamic situations, i.e. two merging black holes. A way to solve equation (3.12) without imposing time-symmetry was first suggested by Bowen and others [110, 111, 112, 113, 114, 115]. Of particular interest to us is the solution of the momentum constraint known as Bowen-York extrinsic curvature [111, 113]. Considering the momentum constraint (3.12) in vacuum ($\rho = j^i = 0$), choosing maximal slicing $K = 0$ and additionally choosing $\tilde{M}^{ij} = 0$, the momentum constraint reduces to

$$\tilde{\Delta}_{\tilde{\mathbf{L}}}\tilde{V}^i = \tilde{D}^2\tilde{V}^i + \frac{1}{3}\tilde{D}^i\tilde{D}_j\tilde{V}^j = 0. \tag{3.80}$$

This equation can be solved analytically and a solution can be obtained in the form

$$\tilde{V}^i = -\frac{1}{4r}[7P^i + n^i n_j P^j] + \frac{1}{r^2}\epsilon^{ijk}n_j S_k, \tag{3.81}$$

with P^i and S^i being constant vectors, n^i the outward pointing unit radial vector, and ϵ^{ijk} the antisymmetric Levi-Cevita symbol in three dimensions. From $\tilde{V}^i$ we can now construct the conformal trace-free extrinsic curvature

$$\begin{aligned}\tilde{A}_{ij} = (\tilde{\mathbf{L}}\tilde{V}) = \quad & \frac{3}{2r^2}[n_i P_j + n_j P_i n_k P^k (n_i n_j - \delta_{ij}] \\ & -\frac{3}{r^3}(\epsilon_{ilk}n_j + \epsilon_{jlk}n_i)n^l S^k,\end{aligned} \tag{3.82}$$

using $K_{ij} = \Psi^{-2}\tilde{A}_{ij}$. equation (3.82) is the definition of Bowen-York extrinsic curvature [111, 113]. The vectors P^i and S^i represent linear and angular momentum, which can be shown by using the $K_{ij} = \Psi^2\tilde{A}_{ij}$ in combination with the definitions of ADM linear and angular momentum

$$P^i = \frac{1}{8\pi}\lim_{r\to\infty}\int (K^i_l - \delta^i_l K)n^l dS \tag{3.83}$$

$$S^i = \frac{1}{16\pi}\lim_{r\to\infty}\int (\epsilon^{ijk}x_j K_{kl}n^l)dS. \tag{3.84}$$

Thus we can use P^i and S^i to prescribe the spin and linear momentum of a black hole and since the momentum constraint equations are linear we can superpose multiple solutions with different centers r_i to obtain multiple particle or black-hole initial data with clearly defined spin and angular momentum. One serious drawback of the Bowen-York initial data becomes evident when we look at single black holes. While a black hole with no linear and angular momentum reduces as expected to a Schwarzschild black hole, a single black hole with zero linear but non-zero angular momentum does not reduce to a Kerr black hole [127]. Bowen York black-hole initial data does not describe a stationary solution as the Kerr solution is. In addition to the stationary part an extra spurious gravitational radiation field is present. The same can be shown to be true for a boosted single black hole with no spin which does not reduce to a boosted single Schwarzschild black hole. The extra radiation present in this type of initial data limits the applicability to more extreme scenarios. For example with Bowen-York initial data it is not possible to construct maximally spinning (i.e. $|a| = 1$) black-hole initial data since this case can only be realized by the Kerr solution [9]. The spurious gravitational radiation field present in practice limits the spin to a value of about $|a| < 0.93$. Kerr-Schild initial data does not have this limitation and has been used to construct nearly maximally spinning black-hole initial data [128]. Since one in most cases is not interested in very extreme cases and in all others the spurious radiation does not interfere with the results of the simulation, Bowen-York initial data is widely used in numerical simulations. After having solved the momentum constraints we still need to find a effective way to solve the Hamiltonian constraint. The method which is state of the art, the puncture method, is described in the next section.

3.5.3 The puncture method

We will now proceed to solving the remaining Hamiltonian constraint. In contrast to the momentum constraint we cannot achieve this analytically anymore, since we have a non-trivial extrinsic curvature term, that forces us to employ numerical methods. One highly successful method was first introduced by Brandt and Bruegmann [118] and is known as the puncture method. It works without the use of inner boundaries to shield the singularity from the grid. This leads to the highly desirable feature of having one numerical domain and not having the technical difficulties that come with introducing inner boundary conditions like excision techniques do. We start by considering Brill-Lindquist type initial data as presented in section 3.5. Considering a topology of a

Schwarzschild space-time in quasi-isotropic coordinates, we can solve the constraint equations on $\mathbb{R}^3$ neglecting the point $r = 0$ by

$$\Psi = 1 + \frac{m}{2r}, \qquad K_{ij} = 0. \tag{3.85}$$

m here is the mass of the space-time and r the isotropic radius. We can use the isometry

$$r \to \frac{m^2}{4r} \tag{3.86}$$

which maps the entire region exterior to the sphere of radius $r = m/2$ into that sphere leaving the surface $r = m/2$ invariant. As a result of the isometry at $r = 0$ there must exist a second asymptotically flat region. It is furthermore possible to represent this solution by two copies of $\mathbb{R}^3$ with a sphere excised. If we want to generalize this solution to multiple black holes we can again by the linearity of the momentum constraint write the conformal factor as a superposition of the individual solutions

$$\Psi = 1 + \sum_{i=1}^{N} \frac{m_i}{2|\mathbf{r} - \mathbf{r_i}|}, \qquad K_{ij} = 0 \tag{3.87}$$

for time symmetric initial data. m_i denotes the mass of the ith black hole and $\mathbf{r_i}$ the location in the conformal flat 3-space. For $N = 2$ this results in a topology where the two throats connect to independent asymptotically flat regions. The solution is identical to the Brill-Lindquist solution [105]. For this initial data there is no isometry anymore between lower and upper sheet, due to the fact that there are two lower sheets and only one upper. Misner-type data however recovers the isometry between lower and upper sheet again by using an infinite series expansion. The Misner solution reduces to the wormhole solution also found by Misner [107] if the invariant spheres have the same radius. This Misner type initial data together with excision techniques were used for the first numerical simulations, but have mostly been replaced by Brill-Lindquist or puncture-type initial data in the last years. Figure 3.4 illustrates the different initial data topologies for some common scenarios.

For Brill-Lindquist initial data for every throat exactly one singular point $\mathbf{r_i}$ exists and we integrate the whole $\mathbb{R}^4$ due to the loss of an inner boundary caused by the absence of the isometry between lower and upper sheets. To deal with the singularity the basic idea driving the puncture approach is to explicitly separate the singular piece of the conformal factor

$$\Psi = \Psi_{BL} + u, \qquad \text{with} \qquad \Psi_{BL} = \sum_{i=1}^{N} \frac{m_i}{2|\mathbf{r} - \mathbf{r_i}|}. \tag{3.88}$$

Ψ_{BL} is the conformal factor of Brill-Lindquist initial data with the 1 absorbed into the function u and it has zero Laplacian on a 'punctured' $\mathbb{R}^3$,i.e. $\mathbb{R}^3$ with the points $\mathbf{r_i}$ removed. Using (3.88) the Hamiltonian constraint reduces to

$$D^2_{flat} u + \eta \left(1 + \frac{u}{\Psi_{BL}}\right) = 0, \tag{3.89}$$

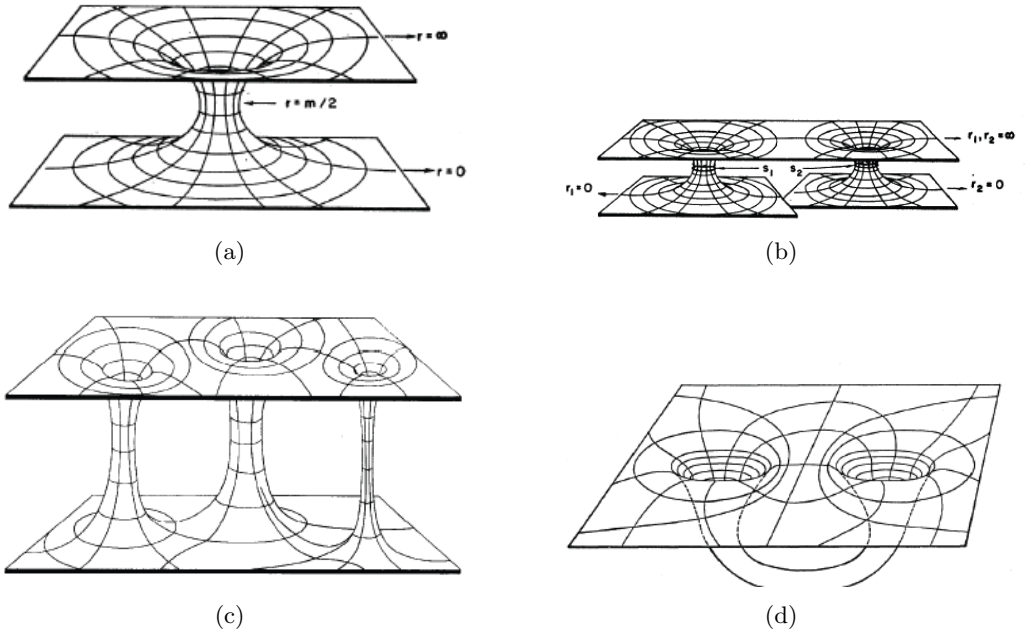

Figure 3.4: Four different black-hole initial data types.(a): Two dimensional Schwarzschild-Kruskal manifold when isometrically embedded into flat 3-space. The top and bottom sheets represent the asymptotically flat regions of the manifold and continue to infinity.(b):Brill-Lindquist [105] initial data where the two throats connect to a different asymptotically flat regions at the bottom.(c): Misner [107] type initial data where the three throats connect to the same asymptotically flat end at top and bottom.(d): Misner wormhole topology [106] when both spheres in the construction of Misner type data have the same radius. Figures from [105, 106, 107].

with D^2_{flat} being the Laplacian in respect to the flat 3-metric and

$$\eta = \frac{1}{8\Psi^7_{BL}} \tilde{A}_{ij}\tilde{A}^{ij}. \tag{3.90}$$

By using the maximal slicing condition and conformal flatness we have now obtained an equation we need to solve for u. To do so we impose boundary conditions, namely at infinity we require $u = 1 + k/r$ with k being a constant. For the boundary at the puncture it turns out that we do not need to impose a boundary condition since in the limit $\mathbf{r} \to \mathbf{r_i}$ η goes to zero and therefore the Hamiltonian constraint reduces to $D^2_{flat} = 0$. It can be shown that requiring these conditions a unique solution u that is C^2 exists to the Hamiltonian constraint equations on $\mathbb{R}^3$. In practice we can therefore neglect the puncture points when solving the Hamiltonian constraint by solving equation (3.89) for u. A solution for u can be obtained using a single-domain spectral solver [124]. Additionally we have to provide initial data for the gauge quantities lapse and shift. The shift we can simply choose as $\beta^i = 0$ and for the lapse we typically choose a

so-called pre-collapsed lapse [129]

$$\tilde{\alpha} = \frac{1 - (\frac{m_1}{2r_1} + \frac{m_2}{2r_2})}{1 + \frac{m_1}{2r_1} + \frac{m_2}{2r_2}}, \tag{3.91}$$

Now taking $\alpha = (1 + \tilde{\alpha})/2$ provides an initial lapse profile with values in the interval $[0, 1]$. Recently further work on puncture initial data and its evolution has shown that it introduces unnecessary gauge dynamics since the initial throat topology evolves and reaches a final state that is a trumpet-like topology [130]. It is therefore suggested to already construct trumpet initial data which would minimize gauge dynamics by already choosing the asymptotic topology for the initial data [131, 132]. The successful application of trumpet initial data for binary black-hole simulations has however still to be realized. The construction of our initial data has now been achieved by solving the momentum and Hamiltonian constraints. What is left to be done, is choosing proper parameter P^i and S^i for our space-time and the individual black holes in order to realize the astrophysical scenario of the final orbits of binary black-hole mergers. Strategies to obtain those parameters from PN evolution are presented in the next section.

3.5.4 Initial black-hole parameters from PN evolution

After having solved the constraint equations we now need to find parameters m_i, P^i, S^i and $\mathbf{r_i}$ that reflect a two black holes on in-spiraling orbits that are quasi-circular and represent a as realistic astrophysical scenario as possible. To do so we start by integrating the PN equations staring from a separation much larger than the one we finally need the initial parameters for our numerical simulation. This is typically of the order of $d = 10M$ and we choose to start the PN evolution from a separation of $d_{PN} = 40M$. We then solve the PN equations of motion until we reach the desired separation to read off the initial parameters for the individual black holes. This results typically in thousands or more orbits which guarantees that the radiation-reaction terms in the PN evolution equations successfully remove any left-over eccentricity still present before the PN evolution. The integration of the PN equations of motion is performed in the $ADM - TT$ gauge [133] which agrees to 2PN order with the puncture initial data as described in [134]. The conservative part of the Hamiltonian is given up to 3PN order [133, 135] The PN equations of motion are a system of coupled ordinary differential equations of the form (we here for simplicity report the form for the non-spinning case)

$$\frac{dx^i}{dt} = \frac{\partial H}{\partial p_i}, \tag{3.92}$$

$$\frac{dp^i}{dt} = -\frac{\partial H}{\partial x_i} + F_i, \tag{3.93}$$

with H being the conservative part of the full PN-Hamiltonian, x^i the separation vector and p_i the momentum of a particle in the center-of-mass rest frame. We note that the generalization to the spinning case is achieved by including additional evolution

equations for the spin vectors of both black holes. Finally F_i represents the radiation-reaction flux term, which can be calculated up to 3.5PN order [136, 137, 138]. By numerically integrating those equations we obtain our initial data parameters to construct the space-time for the numerical evolution from. The radiation reaction proves to be very efficient in yielding low-eccentricity initial data as was shown in [125]. Other ways of eccentricity reduction for binary black-hole initial data rely on iterative schemes where one first obtains a set of parameters, performs a short numerical simulation to measure the eccentricity and then iteratively corrects the initial parameters to counteract the measure eccentricity until one finds a small enough eccentricity [139, 140].

3.6 Dealing with space-time singularities

When evolving black-hole initial data as prescribed in the previous section on a computer we face the problem of how to treat the singularity contained within the black-hole horizon. since we cannot represent infinite numbers on the computer we need to find strategies to deal with singularities in our computer codes. One way that was first introduced by Seidel and Suen was to simply remove the region containing the singularity from the computational grid by a method described as *black-hole excision* [90]. Here one cuts out a spherical region containing the singularity (typically this region is chosen to be inside the black-hole apparent horizon). This is possible since the interior of the horizon is causally disconnected from the outer dynamics. This method is working successfully and straightforward in spherical symmetry but when going to three dimensions most current computational domains are constructed using Cartesian coordinates. This is cumbersome for construction of the excision surface since the topology of the apparent horizon is spherical and we need to find methods to approximate this on a Cartesian grid, i.e. *LEGO* excision. Now in addition we need to be able to move the excised regions around on the grid to track the orbital motion of the black holes and by doing so the technical treatment of black-hole excision becomes very complicated. Another method for treating space-time singularities in computer codes is the *puncture evolution* method. Here one conformally decomposes the 3-metric so that the singularity and its dynamics are absorbed in the conformal factor. This is analogue to what is done in the BSSNOK evolution system as discussed in section 3.2 and to the construction of puncture initial data as described in section 3.5. Keeping the singular part of the conformal factor static and in the form as prescribed by the initial data also during the evolution is referred to as *static* puncture evolution [89, 141]. While this method was used in the first attempts to evolve puncture initial data in [142, 143] it turned out to have severe limitations as it was difficult to achieve more than one orbit of inspiral motion. In a next step and by allowing the conformal factor to evolve as the other evolution variables several groups achieved a big break-through yielding multiple-orbit binary black-hole merger simulations [78, 101]. This method is called the *moving* puncture approach. Since this is the method in use in most of todays numerical evolution codes we describe it in more detail in the next section.

3.6.1 Puncture evolution

Puncture evolutions [78, 101] are todays methods of choice for treating space-time singularities in many computer codes. Combined with a BSSNOK evolution system they provide a powerful tool for representing black holes on a computational grid. In the static puncture evolution the irregular part of the metric is factored out analytically into the conformal factor Ψ_{BL}. This conformal factor is then kept fixed during the evolution which introduces artificial dynamics in the other space-time quantities. As the black holes inspiral and move closer and their punctures are kept fixed on their location severe stretching may occur on the spatial hypersurfaces. This can be overcome by introducing appropriate coordinates like co-rotating coordinate systems. However this may lead to other problems, like super-luminal coordinate speeds far away from the black holes and additionally complicate the outer boundary treatment of the computational domain. By allowing the punctures to move on the grid, i.e. keeping the full conformal factor and evolving it like all the other space-time variables, one allows for the punctures to move with the black holes and therefore does not have to address he issues presented in the previous paragraph. This is typically achieved by making sure the singular part is not located on a grid point to avoid numerical problems with treating infinities. Moving punctures are achieved by modifying the hyperbolic $\tilde{\Gamma}$-driver condition for the shift to the form

$$\partial_t \beta^i = \frac{3}{4}\alpha B^i, \qquad \partial_t B^i = \partial_t \tilde{\Gamma}^i + \beta^j \partial_j \tilde{\Gamma}^i - \eta B^i. \tag{3.94}$$

Here a term of Ψ_{BL}^{-2} that had been introduced to guarantee vanishing shift at the puncture locations has been now neglected to allow the punctures to move on the grid. In addition the term $\beta^j \partial_j \tilde{\Gamma}^i$ has been added to improve stability and accuracy of moving puncture evolutions by eliminating a zero speed mode. Using the modified $\tilde{\Gamma}$-driver condition [130] the singular part of the conformal factor quickly regularizes during the evolution of a single black hole. It obtains a stationary regular interior solution that results in a trumpet topology where the points close to the singularity are stretched into an infinitely long cylinder. Due to the lack of resolution, the slice then terminates close to but not at the singularity. The $\tilde{\Gamma}$-driver condition therefore acts as 'natural' excision algorithm [144]. It however has the advantage of not having to impose an inner boundary condition avoiding much of the complexity involved for that. Revisiting the idea of starting already from trumpet initial data it can be shown that in that case some of the physical parameters link directly to physical parameters, i.e. the puncture bare mass corresponds to the black-hole mass. The trumpet topology for a single Schwarzschild black hole as obtained by the puncture solution during evolution is shown in figure 3.5. To verify the validity of puncture evolutions comparisons against excision based binary black-hole simulations have been performed [145] and by comparing invariant curvature scalars it has been found that the resulting space-times in the two approaches are equivalent.

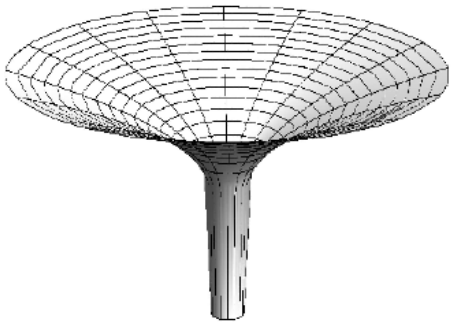

Figure 3.5: Trumpet topology for a single Schwarzschild black hole. The bottom asymptotically flat end becomes an infinitely long cylinder as the initial puncture solution evolves to the trumpet topology. Figure from [132]

4

Einstein-Maxwell evolution systems

So far we have focused on Einstein's equations in vacuum, i.e. with no external matter or radiation fields present. However in realistic scenarios one expects binary black-hole mergers to take place in an environment where either an accretion disk or low-density gas and magnetic fields are present. It is therefore highly interesting to model these scenarios numerically. In a first step towards a more realistic modeling we consider EM fields interacting with a binary black-hole merger space-time. The evolution of the EM fields is governed by Maxwell's equations in GR, i.e. on a curved space-time. Maxwell's equations can be formulated both in terms of the vector potential $\mathbf{A}$ or directly in terms of the electric and magnetic fields E^i and B^i. Since in the results presented in this thesis we have used a formulation using the electric and magnetic fields directly, we will concentrate our focus towards these equations. We will first present the evolution equations in a general form and then discuss different options for considering source-terms included in Maxwell's equations. Here we will focus on two choices. First, Maxwell's equations in *electro-vacuum*, i.e with no sources present. Second, the force-free approximation, which models a plasma with charges and currents present. Most of the presentation in the next sections follows closely [146]

4.1 Maxwell's equations in a GR

Maxwell's equation in general covariance take the form

$$\nabla_\nu F^{\mu\nu} = 4\pi I^\mu, \tag{4.1}$$

$$\nabla_\nu F^{\mu\nu} = 0 \tag{4.2}$$

with $F^{\mu\nu}$ being the Maxwell tensor of the EM field, $F^{\mu\nu}$ the Faraday tensor and I^μ the electric 4-current vector. Taking the divergence of equation (4.1) leads to the conservation law for the 4-current

$$\nabla_\mu I^\mu = 0. \tag{4.3}$$

In EV or a highly-ionized plasma, where both electric and magnetic susceptibility of the media vanish we can write the Faraday tensor simply as the dual of the Maxwell tensor

$$F^{\mu\nu} = \frac{1}{2}\epsilon^{\mu\nu\alpha\beta}F_{\alpha\beta}, \qquad F^{\mu\nu} = -\frac{1}{2}\epsilon_{\mu\nu\alpha\beta}F^{\alpha\beta}. \tag{4.4}$$

Here $\epsilon^{\mu\nu\alpha\beta}$ is the Levi-Cevita pseudo-tensor which can be written as

$$\epsilon^{\mu\nu\alpha\beta} = \frac{1}{\sqrt{\gamma}}\eta^{\mu\nu\alpha\beta}, \qquad \text{and} \qquad \epsilon_{\mu\nu\alpha\beta} = -\sqrt{\gamma}\eta_{\mu\nu\alpha\beta}, \tag{4.5}$$

where γ denotes the determinant of the 3-metric γ_{ij}. Assuming equation (4.4) to hold we can formulate the homogeneous equations (4.2) in terms of the Maxwell tensor

$$\nabla_\mu F_{\nu\alpha} + \nabla_\alpha F_{\mu\nu} + \nabla_\nu F_{\alpha\mu} = 0. \tag{4.6}$$

We will now go on to discuss how to represent Maxwell's equations as a set of evolution equations.

4.1.1 The potential vector

We can write the Maxwell tensor in terms of the 4-vector potential A_μ as

$$F_{\mu\nu} = \nabla_\mu A_\nu - \nabla_\nu A_\mu. \tag{4.7}$$

Now due to the Bianchi identities the inhomogeneous equation (4.1) holds trivially, and we obtain

$$\nabla_\nu F^{\mu\nu} = \nabla_\nu(\nabla^\mu A^\nu - \nabla^\nu A^\mu) = 4\pi I^\mu. \tag{4.8}$$

For the time component of (4.1) we can now write

$$\nabla_\nu F^{0\nu} = \nabla_i(\nabla^0 A^i - \nabla^i A^0) = 4\pi I^0, \tag{4.9}$$

which is a first time-integral of the full system and we can treat it as a constraint equation equivalently to the constraint equations obtained for Einstein's equations. The evolution of the potential A_μ is not fully determined since equation (4.9) introduces a gauge-freedom. We can change

$$A_\mu \to A_\mu + \partial_\mu \Lambda \tag{4.10}$$

with Λ being an arbitrary function. Specifically we can choose Λ such that the vector potential satisfies the *Lorentz gauge*

$$\nabla_\mu A^\mu = 0, \tag{4.11}$$

and in this gauge we get

$$\nabla^\nu \nabla_\nu A_\mu = 8\pi[T^\nu_\mu - \frac{T}{2}\delta^\nu_\mu]A_\nu - 4\pi I_\mu, \tag{4.12}$$

which is called the harmonic form of equation (4.9). This equation now is a symmetric hyperbolic evolution equation for the vector potential A_μ. It only couples in non-principal terms to Einstein's equations and acts as a wave equation. The Lorentz gauge is analogue to the harmonic gauge for Einstein's equations as discussed in chapter 3. The constraint we exploited by choosing the Lorentz gauge will be satisfied by our evolution equation at a continuum level but numerical error might develop in the discretized version. To minimize the error being injected into the system in this way by extending Maxwell's equations to the form

$$\nabla^\nu(F_{\mu\nu} + g_{\mu\nu}\Psi) = -4\pi I_\mu - \kappa n_\mu \Psi, \tag{4.13}$$

with $\Psi := \nabla^\mu A_\mu$ being a gauge-source function. We can get an evolution equation for Ψ by considering the time component of (4.13)

$$\nabla^\mu \nabla_\mu \Psi = -\kappa \nabla^\mu (n_\mu \Psi). \tag{4.14}$$

Now any gauge-constraint violation obtained during the evolution will propagate with the speed of light and be damped exponentially by the term involving κ and thus effectively minimized.

4.1.2 The electric and magnetic fields

It often is more intuitive to work with Maxwell's equation represented in terms of the standard electric and magnetic fields. We obtain the electric and magnetic field expressions by the decomposing the Faraday tensor as

$$F^{\mu\nu} = u^\mu E^\nu - u^\nu E^\mu + \epsilon^{\mu\nu\alpha\beta}\, B_\alpha\, u_\beta \tag{4.15}$$

$$^*F^{\mu\nu} = u^\mu B^\nu - u^\nu B^\mu - \epsilon^{\mu\nu\alpha\beta}\, E_\alpha\, u_\beta\,; \tag{4.16}$$

where u^μ is the unit time vector associated with a generic normal observer to the hypersurfaces. The vectors E^μ and B^μ are the purely spatial ($E^\mu t_\mu = 0 = B^\mu t_\mu$) electric and magnetic fields measured by such an observer. The expressions for the electric and magnetic field however are observer-dependent but it is desirable to construct observer-independent quantities. The simplest such scalars are

$$F_{\mu\nu}F^{\mu\nu} = 4E^\mu B_\mu, \qquad F_{\mu\nu}F^{\mu\nu} = 2(B^2 - E^2). \tag{4.17}$$

The electric current 4-vector can be decomposed into the 3+1 components

$$q := n_\nu I^\nu, \qquad J_i := I_i, \tag{4.18}$$

and we denote q and J_i as the charge density and the electric current as measured by a normal observer. We can now use these quantities to express the current conservation as

$$(\partial_t - \mathcal{L}_\beta)q + \nabla_i(\alpha J^i) = \alpha q K, \tag{4.19}$$

where the covariant derivatives are in respect to the spatial 3-metric γ_{ij}. We can write this in flux-conservative form

$$\partial_t[\sqrt{\gamma}q] + \partial_i[\sqrt{\gamma}(-\beta^i q + \alpha J^i)] = 0. \tag{4.20}$$

We note that to close the system we need to specify a relation for current J_i and E^i, B^i. This relation is commonly referred to as an Ohm's law. We will discuss the details of the different prescriptions for the current in the next section 4.2. To obtain evolution equations for the electric and magnetic field we now adopt again the extended version of Maxwell's equations with two extra scalar fields Ψ and Φ which lead to evolution equations for the EM constraints ($\nabla_i E^i = 0 = \nabla_i B^i$) described by damped wave equations analogue to what we have done for the vector potential in the previous section. In terms of E^μ and B^μ the $3+1$ version of (4.16)-(4.16) now reads

$$\mathcal{D}_t\, E^i - \epsilon^{ijk}\nabla_j(\,\alpha\, B_c\,) + \alpha\,\gamma^{ij}\nabla_j\,\Psi = \alpha\, K\, E^i \; - 4\pi\alpha J^i, \tag{4.21}$$

$$\mathcal{D}_t\, B^i + \epsilon^{ijk}\nabla_j(\,\alpha\, E_c\,) + \alpha\,\gamma^{ij}\nabla_j\,\Phi = \alpha\, K\, B^i\,, \tag{4.22}$$

$$\mathcal{D}_t\,\Psi + \alpha\,\nabla_i E^i = 4\pi\alpha q - \alpha\kappa\,\Psi\,, \tag{4.23}$$

$$\mathcal{D}_t\,\Phi + \alpha\,\nabla_i B^i = -\alpha\kappa\,\Phi\,. \tag{4.24}$$

where $\mathcal{D}_t \equiv (\partial_t - \mathcal{L}_\beta)$ and $\mathcal{L}_\beta$ is the Lie derivative along the shift vector $\boldsymbol{\beta}$. Exploiting that the covariant derivative in the second term of (4.22) - (4.24) reduces to a partial one

$$\epsilon^{ijk}\nabla_j B_k = \epsilon^{ijk}(\partial_j + \Gamma^c_{kj}B_k) = \epsilon^{ijk}\partial_j B_k, \tag{4.25}$$

and using a standard conformal decomposition of the spatial 3-metric as prescribed in chapter 3

$$\tilde{\gamma}_{ij} = e^{4\phi}\gamma_{ij} \;\;;\;\; \phi = \frac{1}{12}\ln\gamma \tag{4.26}$$

we obtain the final expressions

$$\begin{aligned}&\mathcal{D}_t\, E^i - \epsilon^{ijk}\, e^{4\phi}\,[\,(\partial_j\,\alpha\,)\,\tilde{\gamma}_{ck}\, B^c \,+\alpha\,(\,4\,\tilde{\gamma}_{ck}\;\partial_j\,\phi \,+\, \partial_j\,\tilde{\gamma}_{ck}\,)\,B^c\\ &+\alpha\,\tilde{\gamma}_{ck}\,\partial_j\, B^c\,] + \alpha\, e^{-4\phi}\,\tilde{\gamma}^{ij}\,\nabla_j\,\Psi = \alpha\, K\, E^i \; - 4\pi\alpha J^i,\end{aligned} \tag{4.27}$$

$$\begin{aligned}&\mathcal{D}_t\, B^i + \epsilon^{ijk}\, e^{4\phi}\,[\,(\partial_j\,\alpha\,)\,\tilde{\gamma}_{ck}\, E^c \,+\alpha\,(\,4\,\tilde{\gamma}_{ck}\;\partial_j\,\phi \,+\, \partial_j\,\tilde{\gamma}_{ck}\,)\,E^c\\ &+\alpha\,\tilde{\gamma}_{ck}\,\partial_j\, E^c\,] + \alpha\, e^{-4\phi}\,\tilde{\gamma}^{ij}\,\nabla_j\,\Phi = \alpha\, K\, B^i\,,\end{aligned} \tag{4.28}$$

$$\mathcal{D}_t\,\Psi + \alpha\,\nabla_i E^i = 4\pi\alpha q - \alpha\kappa\,\Psi\,, \tag{4.29}$$

$$\mathcal{D}_t\,\Phi + \alpha\,\nabla_i B^i = -\alpha\kappa\,\Phi\,. \tag{4.30}$$

Notice that the standard Maxwell equations in a curved background are recovered for $\Psi = \Phi = 0$. The Ψ and Φ scalars can then be considered as the normal-time integrals of the standard divergence constraints

$$\nabla_i E^i = 0\;,\;\; \nabla_i B^i = 0 \tag{4.31}$$

These constraints propagate with light speed and are damped during the evolution. By considering the extended Maxwell equations we also obtain a modified characteristic structure. Decomposing equations (4.16) and (4.16) along the direction of a normalized spatial vector $\mathbf{n}$ belonging to a tetrad $\{\mathbf{l}, \mathbf{m}, \mathbf{n}\}$ we obtain the eigenfield

- Constraint eigenfields:
$$\Psi \pm E_n, \qquad \Phi \pm B_n \tag{4.32}$$

- Light eigenfields: These represent physical EM waves, which are perpendicular to their direction of propagation $\mathbf{k}$.
$$E_l \pm B_m, \qquad E_m \mp B_l \tag{4.33}$$

The local characteristic speed for all cases is $-\beta^n \pm \alpha$.

4.1.3 The EM stress-energy tensor

The coupling between the Einstein and Maxwell equations is performed via the inclusion of the EM stress-energy tensor, which is given in terms of the Faraday tensor

$$T_{\mu\nu} = \frac{1}{4\pi}\left[F^{\lambda}_{\mu}F_{\nu\lambda} - \frac{1}{2}g_{\mu\nu}F^{\lambda\sigma}F_{\lambda\sigma}\right] \tag{4.34}$$

and we can decompose it into its 3+1 components

$$\tau = \frac{1}{8\pi}(E^2 + B^2) \quad , \quad S_i = \frac{1}{4\pi}\epsilon_{ijk}E^j B^k \quad , \tag{4.35}$$

$$S_{ij} = \frac{1}{4\pi}\left[-E_iE_j - B_iB_j + \frac{1}{2}\gamma_{ij}\left(E^2 + B^2\right)\right]. \tag{4.36}$$

where $E^2 \equiv E^k E_k$ and $B^2 \equiv B^k B_k$. The scalar component τ can be identified with the energy density of the EM field (i.e. $\rho_{\rm ADM}$ in [147]) and the energy flux S_i is the Poynting vector. The conservation of the stress-energy tensor leads to evolution equations for the Poynting vector S_i and the charge density q, which can also be obtained directly from Maxwell's equations. Note that however the conservation of the EM stress energy tensor leads to the conservation law

$$\nabla_\nu T^{\mu\nu} = -F^{\mu\nu}I_\nu, \tag{4.37}$$

which is only strictly conserved for the case of no EM sources are present (i.e. $I_\nu = 0$). If currents are present ($I_\nu \neq 0$) it is possible to transfer energy from the EM fields to the fluid and vice versa. In this scenario we need a generalized conservation law also taking into account the contribution from the fluid. This is realized by taking the divergence of the stress-energy tensor incorporating contribution from both the EM fields and the fluid itself.

4.2 Source prescriptions

Maxwell's equations (4.16)- (4.16) contain the source terms q and J^i. In order to describe the dynamics of the EM fields in black-hole space-times we need to find prescriptions for these source terms that are suitable for the astrophysical scenario we want to model. There are may choices for modeling these source terms, and they depend on highly different numerical techniques. We will describe in detail in the next sections two choices for the source terms, which are rather simple to implement numerically, but also well suited to the study binary black-hole mergers when the system is immersed in a uniform magnetic field or plasma. The first is EV, where no EM sources are present and the second is the *force-free approximation* which models a tenuous plasma and includes charges and currents as source for EM fields.

4.2.1 Electro-vacuum

The EV treatment does not include any EM source, i.e. it requires $q = 0$ and $J_i = 0$ and therefore purely allows for EM fields on a vacuum space-time.

4.2.2 The force-free approximation

When modeling matter and EM fields we need to consider contributions to the stress-energy tensor coming from both components, i.e.

$$T^{\mu\nu} = T^{\mu\nu}_{fluid} + T^{\mu\nu}_{EM} + ... \tag{4.38}$$

However turning our attention to the case where the magnetic field strength is large and the fluid density is low, the stress energy tensor is dominated by the EM part

$$T^{\mu\nu} \approx T^{\mu\nu}_{EM}. \tag{4.39}$$

Now taking the conservation law for $T^{\mu\nu}$ implies that the Lorentz force is negligible,

$$\nabla_\nu T^{\mu\nu} = -F^{\mu\nu} I_\nu = 0. \tag{4.40}$$

and this approximation is commonly referred to as the force-free approximation. The spatial projection of this last equation, in terms of Eulerian observers, can be written as

$$E^k J_k = 0 \tag{4.41}$$

$$qE^i + \epsilon^{ijk} J_j B_k = 0. \tag{4.42}$$

In the force-free approximation, the magnetic field evolution is performed by the standard Maxwell equations, however the electric field evolution equation now cannot be performed due to the presence of the current term on the right hand side, which still remains undetermined. One route is to evolve the Poynting vector (4.35) and the reconstruct the electric field from

$$E_i = -\frac{4\pi}{B^2} \epsilon_{ijk} S^j B^k. \tag{4.43}$$

Alternatively we can try to find a prescription for the current I_μ and then use the evolution equation of the electric field as obtained from the standard Maxwell 's equations. Computing the scalar and vectorial product of the equations (4.42) with the magnetic field B^i, we obtain

$$E^k B_k = 0 \tag{4.44}$$

$$J^i = q\frac{\epsilon^{ijk}E_j B_k}{B^2} + J_B\frac{B^i}{B^2}, \tag{4.45}$$

with J_B being the component of the current parallel to the magnetic field. Using the Maxwell equations to compute $\partial_t(E^i B_i) = 0$, we can derive a relation for J_B [148],

$$J_B = \frac{1}{\alpha}(B_i\epsilon^{ijk}\nabla_j(\alpha B_k) - E_i\epsilon^{ijk}\nabla_j(\alpha E_k)) \tag{4.46}$$

Using this prescription for the current we can use the evolution equation for the electric field. While this approach successfully imposes the force-free constraint equation (4.44) initially, it fails to succeed during later parts of the time evolution. To make sure that the evolution of the EM field remain in the regime covered by the force-free approximation we can enforce the force-free constraints during the evolution. Multiple approaches have been suggested and used. In [149] equation (4.45) was used for the current together with $J_B = 0$. However to ensure that the force-free approximation is still fulfilled the electric field needs to be modified after each time step, such that it satisfies equation (4.44),

$$E^i = E^i - (E^k B_k)\frac{B^i}{B^2} \tag{4.47}$$

and equation (4.45),

$$E^i = E^i((1-\Theta) + \frac{\sqrt{B^2}}{\sqrt{E^2}}\Theta), \tag{4.48}$$

Here, $\Theta = 1$ when $B^2 - E^2 < 0$, accounts for the role that the resistivity would play. An alternative approach to enforce the constraints (at a continuum level) during the evolution was introduced first in [148, 149, 150] and consists of using a suitable Ohm's law. In this approach the parallel component J_B can be computed from an Ohm's law of the type

$$J_B = \sigma_B E^k B_k, \tag{4.49}$$

where σ_B is the anisotropic conductivity along the magnetic field lines. This extra term in the current enforces the constraint equation (4.44) in a time scale $1/\sigma_B$, as

$$\partial_t(E^i B_i) = ... - \alpha\sigma_B(E^i B_i). \tag{4.50}$$

For σ_B sufficiently large, one can insure that the force-free constraint equation (4.44) is satisfied. While this approach is elegant in terms of not modifying the electric field by

enforcing extra conditions, but rather driving it to the right solution, it introduces a stiff term on the right hand side, that requires more complex computational methods (i.e. a implicit-explicit (IMEX) Runge-Kutta evolution scheme (see chapter 7 for details)). Enforcing the constraints for the current, the force-free approximation can still break down during the evolution in regions, where

$$E^2 - B^2 > 0. \tag{4.51}$$

We call these regions *current sheets*. The Alfven wave-speed becomes complex and the system of force-free electrodynamics is not longer hyperbolic [150]. A solution to this problem was introduced in [151], where the velocity of the drift current was modified such, that is always smaller than the speed of light,

$$J^i = q\frac{\epsilon^{ijk}E_jB_k}{B^2+E^2} + J_B\frac{B^i}{B^2}. \tag{4.52}$$

Additionally an alternative approach was presented in [152], which consists in adding another term to Ohm's law in order to account for the in-anomalous isotropic resistivity,

$$J^i = q\frac{\epsilon^{ijk}E_jB_k}{B^2} + \sigma_B(E^kB_k)\frac{B^i}{B^2} + \sigma_B(E^2-B^2)E^i\frac{E^2}{B^2}. \tag{4.53}$$

Here the added third term acts as a damping term in regions where $E^2 - B^2 > 0$ and acts in similar way as the second term. The approach realized by equation (4.53) is more elegant as it uses no ad-hoc assumptions to realize a suitable Ohm's law

5

The Weyl and EM complex scalars: Gravitational waves and EM radiation

The asymptotic properties of space-time are a crucial aspect of the analysis of the radiative properties of binary black-hole space-times. In order to properly define gravitational and EM radiation the idea of a conformal representation of space-time was introduced by Penrose [24, 25, 26]. The conformal representation of space-time makes it then possible to define the asymptotic properties of space-time and derive key results like the Peeling theorem which is essential for analyzing radiation in black-hole space-times. Ultimately, we can then also define quantities like total mass and angular momentum of asymptotically flat space-times. We will review these ideas and definitions in the next sections.

5.1 Space-time asymptotics

5.1.1 Conformal representation and structure

We can use a conformal rescaling of space-time to place infinity at a finite distance. We transform the physical metric $\tilde{g}$ to an unphysical metric g by introducing

$$\tilde{g}_{\mu\nu} \to g_{\mu\nu} = \Omega^2 \tilde{g}_{\mu\nu}. \tag{5.1}$$

with $\Omega \geq 0$ being a smooth function which is designed to approach zero towards spatial infinity. This transformation preserves angles and null vectors, which is important for the structure of our space-time metric. We now want to exploit the conformal transformation in such a way that all points at infinity in the physical metric get mapped to a finite distance in the unphysical metric. The three points I^+, I^- and I^0 are of special importance. All future directed time-like geodesics will terminate at future time-like infinity I^+, and respeticvely all past directed time-like geodesics

will terminate past time-like infinity I^-. All space-like geodesic will approach space-like infinity I^0. Additionally the two hypersurfaces $\mathcal{I}^+$ and $\mathcal{I}^-$ are future and past null infinity. $\mathcal{I}^+$ will be reached by all radially outgoing null geodesics and $\mathcal{I}^-$ is the origin of all radially in-going null geodesics. Especially $\mathcal{I}^+$ is of great importance when analyzing gravitational or EM radiation since both quantities are strictly only well defined at $\mathcal{I}^+$. The main aspects of these considerations can be captured in the definition of asymptotic simplicity.

5.1.2 Asymptotic simplicity

The behavior of asymptotically flat solutions to Einstein's equations at infinity can be characterized in terms of geometric quantities, as introduced by Penrose's definition of asymptotic simplicity [25, 26, 63, 153, 154]

Definition 5.1.1 *A smooth space-time $(\tilde{M}, \tilde{g})$ is asymptotically simple if there exists a smooth, oriented, time-oriented, causal space-time (M, g) and a smooth function Ω on M such that*

1. *M is a manifold with boundary $\mathcal{I} := \delta M$*
2. *$\Omega > 0$ on $M \cup \mathcal{I}$ and $\Omega = 0, d\Omega \neq 0$ on $\mathcal{I}$*
3. *an embedding Φ of $\tilde{M}$ onto $\Phi(\tilde{M}) = M$ $\mathcal{I}$ exists that is conformal such that $\Omega^2 \Phi^{-1*} \tilde{g} = g$*
4. *every null geodesic of $(\tilde{M}, \tilde{g})$has two distinct end points on $\mathcal{I}$.*

We call $(\tilde{M}, \tilde{g})$ the physical and (M, g) the unphysical space-time.

This definition determines the conformal structure of (M, g). The set $\mathcal{I} = \mathcal{I}^+ \cup \mathcal{I}^-$ is called the conformal boundary of $(\tilde{M}, \tilde{g})$ at null infinity. Definition (5.1.1) does not include black-hole space-times since they are not geodesically complete. To find a suitable definition that we can also use in black-hole space-times we require it to only hold in a neighborhood of $\Omega = 0$.

Definition 5.1.2 *$(\tilde{M}, \tilde{g})$ is weakly asymptotically simple if an asymptotically simple space-time $(\tilde{M}', \tilde{g}')$ and a neighborhood $\tilde{U}'$ of $\mathcal{I}'$ in $\tilde{M}'$ exist such that $\tilde{U}' \cap \tilde{M}'$ is isometric to an open subspace $\tilde{U}$ of $\tilde{M}$.*

Based on these definitions Penrose suggested

Proposal 5.1.1 *Penrose proposal: Far fields of isolated gravitating systems behave like that of (weakly) asymptotically simple space-times in the sense that they can be smoothly extended to null infinity after suitable conformal rescalings.*

To now make use of this proposal we will try to find solutions of Einstein's equations that fulfill the requirements of Definitions (5.1.1),(5.1.2).

5.1.3 Asymptotic mass and momentum

In many scenarios it is also useful to determine the asymptotic mass and angular momentum of a space-time. It is possible to express these quantities in terms of a 3+1 splitted space-time as presented in [65, 155]. To define the total mass and momentum of an isolated system we assume the metric far away from the source to be written in the form of $g_{\mu\nu} = \eta_{\mu\nu} + h_{\mu\nu}$ with $|h_{\mu\nu}| \ll 1$, i.e. a flat space-time plus a perturbation. We now define the total mass and angular momentum through the effects of the system on far-away test-masses. By evaluating the expression at spatial infinity I^0 we ensure that weak-field limit holds. The expressions for the total mass and momentum were first obtained by Arnowitt, Deser and Misner in [65] and are therefore called the ADM mass M_{ADM}, linear momentum P^i_{ADM} and angular momentum J^i_{ADM}. The expressions read

$$M_{ADM} = \frac{1}{16\pi} \lim_{r\to\infty} \oint_S (\delta^{ij}\partial_i h_{jk} - \partial_k h) dS^k, \tag{5.2}$$

$$P^i_{ADM} = \frac{1}{8\pi} \lim_{r\to\infty} \oint_S (K^i_j - \delta^i_j K) dS^j, \tag{5.3}$$

$$J^i_{ADM} = \frac{1}{8\pi} \lim_{r\to\infty} \oint_S (\epsilon^{ijk} x_j K_{kl}) dS^l, \tag{5.4}$$

with $dS^i = s^i dA$ and s^i being the outward-pointing normal vector to the surface S and dA the standard area element. These expression contain only quantities inherent to a spatial hypersurface of our space-time foliation and can therefore be evaluated locally in time. As these quantities represent global properties of the space-time the results obtained at different times must coincide. In the numerical evolution of space-times however we typically have to choose a finite domain of computation and can therefore not evaluate the expressions (5.4) at spatial infinity but instead have to use a finite distance away from the source. This introduces an intrinsic error into the calculation. In practice nevertheless the expression are widely used since the assumption of a Minkowski space-time plus a perturbation is shown to hold already at a finite distance of the source, such that the error by evaluating (5.4) at finite distances away from the source is minimal.

5.2 The Weyl tensor

The Weyl tensor plays a crucial role in the extraction of gravitational waves from (weakly) asymptotically simple space-times. We can identify the different components of the Weyl tensor with in- and outgoing gravitational radiation at $\mathcal{I}^+$ and the wave extraction methods presented in this section are based on this property (note that there are other ways to extract gravitational waves, like Cauchy characteristic extraction or the extraction via gauge-independent perturbations around a Schwarzschild black-hole space-time). In four dimensions the Riemann tensor contains more independent components that the Ricci tensor. Decomposing the Riemann tensor $R_{\mu\nu\lambda\sigma}$ into the

Ricci tensor $R_{\mu\nu}$ requires the introduction of an additional object, the Weyl tensor

$$C_{\mu\nu\lambda\sigma} := R_{\mu\nu\lambda\sigma} - [g_{\mu[\lambda}R_{\sigma]\nu} = g\nu[\lambda R_{\sigma]\mu}] + \frac{1}{3}g_{\mu[\lambda}g_{\sigma]\nu}R. \tag{5.5}$$

The Weyl tensor has vanishing trace

$$C^{\mu}_{\lambda\mu\sigma} = 0, \tag{5.6}$$

possesses the same symmetries as the Riemann tensor and has 10 independent components. In vacuum, it coincides with the Riemann tensor since the Ricci tensor vanishes. The Weyl tensor also is invariant under conformal transformations, i.e.

$$\tilde{C}^{\mu}_{\nu\lambda\sigma} = C^{\mu}_{\nu\lambda\sigma}, \tag{5.7}$$

which is an important property for the following steps. The Weyl tensor therefore is sometimes also called the conformal Weyl tensor. We can define the electric and magnetic components of the Weyl tensor as

$$E_{\mu\nu} := k^{\alpha}k^{\beta}C_{\alpha\mu\beta\nu} \tag{5.8}$$

$$B_{\mu\nu} := k^{\alpha}k^{\beta}C^{*}_{\alpha\mu\beta\nu}, \tag{5.9}$$

with k^{ν} being a time-like unit vector field and $C^{*}_{\alpha\mu\beta\nu}$ the dual of the Weyl tensor $C_{\alpha\mu\beta\nu}$ defined as

$$C^{*}_{\alpha\beta\mu\nu} := \frac{1}{2}C_{\alpha\beta\lambda\sigma}\epsilon^{\lambda\sigma}_{\mu\nu}. \tag{5.10}$$

with $\epsilon_{\lambda\sigma\mu\nu}$ being the completely anti-symmetric Levi-Cevita symbol. We can now express the Weyl tensor as

$$C_{\mu\nu\lambda\sigma} = 2\left[l_{\mu[\lambda}E_{\sigma]\nu} - l_{\nu[\lambda}E_{\sigma]\mu} - k_{[\lambda}B_{\sigma]\alpha}\epsilon^{\alpha}_{\mu\nu} - k_{[\mu}B_{\nu]\alpha}\epsilon^{\alpha}_{\lambda\sigma}\right], \tag{5.11}$$

with $l_{\mu\nu} := g_{\mu\nu} + 2k_{\mu}k_{\nu}$. This will become important in section 5.2.3, where we will calculate $B_{\mu\nu}$ and $E_{\mu\nu}$ on a given hypersurface from ADM quantities only and use these two components to construct the Weyl tensor.

5.2.1 The Newman-Penrose formalism

The analysis of asymptotic properties of space-times is commonly more easily achieved by working in a null frame. One can reduce the complexity of the equations involved by representing tensor quantities as spinors and spin-weighted scalars. This procedure is often referred as the *Newman-Penrose formalism* as it was first introduced by Newman and Penrose in [24]. By contracting tensor components with a suitable null tetrad we obtain a set of pseudo-scalars that then have specific transformation properties when we change the tetrad. We introduce a tetrad $(\mathbf{l}, \mathbf{n}, \mathbf{m}, \bar{\mathbf{m}})$ of null vectors

$$l^{\mu}l_{\mu} = n^{\mu}n_{\mu} = m^{\mu}m_{\mu} = \bar{m}^{\mu}\bar{m}_{\mu} = 0, \tag{5.12}$$

and we call the tetrad a *Newman-Penrose null tetrad* if the vectors satisfy

$$l_\mu n^\mu = -m^\mu \bar{m}_\mu = 1. \tag{5.13}$$

We can then construct the metric from the tetrad vectors

$$g_{\mu\nu} = 2l_{(\mu}n_{\nu)} - 2m_{(\mu}\bar{m}_{\nu)}, \qquad g^{\mu\nu} = 2l^{(\mu}n^{\nu)} - 2m^{(\mu}\bar{m}^{\nu)}, \tag{5.14}$$

and also use the tetrad to construct scalars from tensors by contracting all components with elements of the null tetrad

$$\eta = m^\mu ... m^\nu \bar{m}^\lambda ... \bar{m}^\sigma ... l^\alpha ... l^\beta n^\gamma ... n^\delta n_{\mu...\nu\lambda...\sigma\alpha...\beta\gamma...\delta}. \tag{5.15}$$

The 2-parameter subgroup of the Lorentz group preserving the two null directions l^μ and n^μ and the product $l_\mu n^\mu$ introduces a two-dimensional gauge-freedom. We can generate this group by applying a boost

$$l^\mu \to r l^\mu, \qquad n^\mu \to r^{-1} n^\mu, \tag{5.16}$$

and a spatial rotation of the form

$$m^\mu \to e^{i\theta} m^\mu. \tag{5.17}$$

Here r and θ are two real parameters. A transformation that can be a accomplished by applying a boost (5.16) and a rotation (5.16) form the class of *spin-boost transformations*. Defining $\lambda^2 = re^{i\theta}$ we can express any spin-boost transformation of η as

$$\eta \to \lambda^p \bar{\lambda}^q \eta. \tag{5.18}$$

Here the superscripts p and q denote simple powers and we call η a scalar with *spin-weight* $s = \frac{1}{2}(p-q)$ and boost-weight $b = \frac{1}{2}(p+q)$. Whenever we change the tetrad the scalar is transformed according to (5.18). We can also contract purely spin-weighted scalars by only contracting with m, $\bar{m}$. These scalars will be of special interest since by using m,$\bar{m}$ we can represent the intrinsic metric of a space-like 2-surface. We can now employ this formalism to represent the 10 independent components of the Weyl tensor by five complex spin and boost-weighted scalars, that are referred to as the *Weyl scalars*:

$$\Psi_0 := C_{\mu\nu\lambda\sigma} l^\mu m^\nu l^\lambda m^\sigma \tag{5.19}$$

$$\Psi_1 := C_{\mu\nu\lambda\sigma} l^\mu n^\nu l^\lambda m^\sigma \tag{5.20}$$

$$\Psi_2 := C_{\mu\nu\lambda\sigma} l^\mu m^\nu \bar{m}^\lambda n^\sigma \tag{5.21}$$

$$\Psi_3 := C_{\mu\nu\lambda\sigma} l^\mu n^\nu \bar{m}^\lambda n^\sigma \tag{5.22}$$

$$\Psi_4 := C_{\mu\nu\lambda\sigma} n^\mu \bar{m}^\nu n^\lambda \bar{m}^\sigma. \tag{5.23}$$

The Weyl scalars are tetrad-dependent as is obvious from there definition and transform according to (5.18). The two other classes of tetrad transformations that maintain orthonormality of the null tetrad are *null rotations of class I*

$$\begin{aligned} l^\mu \to l^\mu, \qquad m^\mu \to m^\mu + a l^\mu, \qquad \bar{m}^\mu \to \bar{m}^\mu + \bar{a} l^\mu, \\ n^\mu \to n^\mu + \bar{a} m^\mu + a \bar{m}^\mu + a\bar{a} l^\mu, \end{aligned} \tag{5.24}$$

and *null rotations of class II*

$$n^\mu \to n^\mu, \qquad m^\mu \to m^\mu + bn^\mu, \qquad \bar{m}^\mu \to \bar{m}^\mu + \bar{b}n^\mu,$$
$$l^\mu \to l^\mu + \bar{b}m^{mu} + b\bar{m}^\mu + b\bar{b}n^\mu. \tag{5.25}$$

The complex parameters a and b are the transformation parameters of the class I and class II transformation group. Together with the parameters r and θ of the class III null rotations (which for briefness we will not report in detail on) they form the 6 degrees of freedom contained in the tetrad, namely a rotation in space in combination with a Lorentz boost. In the next section we will see that the characterization of these transformation plays an important role in the interpreting the physical meaning of the Weyl scalars.

5.2.2 The Petrov classification and the Sachs-Peeling theorem

The Petrov classification [63, 126] provides a way of analyzing the algebraic structure of the Weyl tensor along null directions of a space-time. We have seen in the previous section that by defining the Weyl scalars we can completely determine the Weyl tensor components. By then applying null rotations of the form (5.25) we can analyze the behavior of the Weyl scalars under theses transformations. Applying a class II null rotation we find

$$\Psi_0 \quad \to \Psi_0 + 4b\Psi_1 + 6b^2\Psi_2 + 4b^3\Psi_3 + b^4\Psi_4, \tag{5.26}$$
$$\Psi_1 \quad \to \Psi_1 + 3b\Psi_1 + 3b^2\Psi_2 + b^3\Psi_3, \tag{5.27}$$
$$\Psi_2 \quad \to \Psi_2 + 2b\Psi_3 + b^2\Psi_4, \tag{5.28}$$
$$\Psi_3 \quad \to \Psi_3 + b\Psi_4, \tag{5.29}$$
$$\Psi_4 \quad \to \Psi_4. \tag{5.30}$$

By choosing b as the complex roots of

$$\Psi_0 + 4b\Psi_1 + 6b^2\Psi_2 + 4b^3\Psi_3 + b^4\Psi_4 = 0, \tag{5.31}$$

Ψ_0 vanishes and l^μ in turn becomes

$$l^\mu \to l^\mu + bm^\mu + b\bar{m}^\mu + b\bar{b}n^\mu. \tag{5.32}$$

The null vectors obtained by taking the roots of (5.31) are called the *principal null directions* of the Weyl tensor. The space-time is called algebraically special if we can find that some of these roots coincide. We can now classify space-times by analyzing the roots of (5.31), which is called the Petrov classification: *Petrov type I*: All four roots b_1, b_2, b_3, b_4 are distinct. In this case we can always find a null tetrad such that (Ψ_1, Ψ_2, Ψ_3) are non-vanishing. *Petrov type II*: Two roots coincide, $b_1 = b_2, b_3, b_4$, the others are distinct. In this case a null tetrad exists such that (Ψ_2, Ψ_3) are non-vanishing. *Petrov type III*: Three roots coincide, $b_1 = b_2 = b_3, b_4$. Only Ψ_3 does not vanish. *Petrov type N*: All four roots coincide, $b_1 = b_2 = b_3 = b_4$. Only Ψ_4 s non-zero. *Petrov type D*:

Two pairs of roots coincide, $b_1 = b_2, b_3 = b_4$. We can find a null tetrad, such that only Ψ_2 s non-zero. *Petrov type O*: The Weyl tensor vanishes, the space-time is conformally flat.

In the Petrov classification a space-time is characterized from the most general case of a Petrov type *I* space-time to more special cases of Petrov type *II* to Petrov type *O*. the classifications can also be expressed in terms of spinor calculus as presented in [63]. Another way of classifying the behavior of the Weyl scalars is given by the *Sachs-Peeling theorem*. It classifies the fall-off behavior with respect to large radii of the individual Weyl scalars [24, 26, 63, 154, 156, 157]. The fall-off depends on the spin and boost of the scalar and it is found to be

$$\Psi_n \approx \frac{1}{r^{5-n}}, \tag{5.33}$$

if we choose a null tetrad that corresponds to the choice of a *Bondi frame*. The Bondi frame represents the choice of one specific gauge at $\mathcal{I}$, but because we can choose the conformal factor freely we obtain a gauge-freedom at $\mathcal{I}$ since we can multiply by any positive real scalar field without changing the property of our conformal rescaling. We can therefore choose a frame, that is adapted to the topology of $\mathcal{I}$, which is $\mathbb{R} \times S^2$. The Sachs-Peeling theorem can also be expressed using the previously introduced Petrov classification

$$C_{\mu\nu\lambda\sigma} = \frac{[N]}{r} + \frac{[III]}{r^2} + \frac{[II]}{r^3} + \frac{[I]}{ri^4} + \mathcal{O}(r^{-5}). \tag{5.34}$$

(5.34) now implies that far away from an isolated system the asymptotic field in asymptotically simple space-times corresponds to type *N* Petrov space-time. Ψ_4 is therefore the only non-vanishing component and represents outgoing gravitational radiation. However, the Sachs-Peeling theorem is only applicable to weakly asymptotically simple space-times that extend smoothly to $\mathcal{I}$. It is not a priori clear that a binary black-hole space-time satisfies these requirements and the fall-off behavior of Einstein's equations in these space-times might be different in consequence. It is however evident by now that non-trivial solutions like black-hole space-times satisfy the properties of the Sachs-Peeling theorem [158, 159].

5.2.3 Extraction of gravitational waves using Ψ_4

Using the Weyl scalar Ψ_4 we can now obtain the outgoing gravitational radiation generated by an isolated source. To evaluate Ψ_4 in a numerical evolution it is convenient to first define an orthonormal basis $(\hat{\mathbf{r}}, \hat{\theta}, \hat{\phi})$ centered on the Cartesian grid center and oriented with poles along $\hat{\mathbf{z}}$. Using the normal to the 3 hypersurfaces to define a time-like vector $\hat{\mathbf{t}}$ we can construct a null frame

$$\mathbf{l} = \frac{1}{\sqrt{2}}(\hat{\mathbf{t}} - \hat{\mathbf{r}}), \qquad \mathbf{n} = \frac{1}{\sqrt{2}}(\hat{\mathbf{t}} + \hat{\mathbf{r}}), \qquad \mathbf{m} = \frac{1}{\sqrt{2}}(\hat{\theta} - \mathbf{i}\hat{\phi}). \tag{5.35}$$

We an now calculate Ψ_4 using a reformulation of (5.23) only using ADM quantities on a 3-hypersurface [160] using the decomposition into electric and magnetic part of the

Weyl tensor (5.5)

$$\Psi_4 = C_{ij}\bar{m}^i\bar{m}^j, \tag{5.36}$$

with

$$C_{ij} := E_{ij} = iB_{ij} = R_{ij} - KK_{ij} + K^k_i K_{kj} = i\epsilon^{kl}_i \nabla_l K_{jk}. \tag{5.37}$$

We can also compute the remaining four Weyl scalars in a similar way

$$\Psi_3 = \frac{1}{\sqrt{2}} C_{ij}\bar{m}^i e^j_r, \tag{5.38}$$

$$\Psi_2 = \frac{1}{2} C_{ij}\bar{e}^i_r e^j_r, \tag{5.39}$$

$$\Psi_1 = -\frac{1}{\sqrt{2}} C_{ij} m^i e^j_r, \tag{5.40}$$

$$\Psi_0 = C_{ij}\bar{m}^i m^j \tag{5.41}$$

with $\mathbf{e}^j_r := \hat{\mathbf{r}}$ being the unit radial vector.

5.3 EM complex scalars

In the Newman Penrose formalism we not only can define complex scalars representing the ten independent components of the Weyl tensor, but also define complex scalars as contractions of the Faraday tensor (as defined in chapter 4) [161]. The Faraday tensor contains the information about EM fields present in the space-time and we can by contracting it with a suitable null tetrad define the three spin- and boost-weighted complex scalars corresponding to the 6 independent components of the Faraday tensor

$$\Phi_0 := F_{\mu\nu} l^\mu m^\nu \tag{5.42}$$

$$\Phi_1 := \frac{1}{2} F_{\mu\nu}(l^\mu n^\nu + \bar{m}^\mu m^\nu) \tag{5.43}$$

$$\Phi_2 := F_{\mu\nu}\bar{m}^\mu n^\nu. \tag{5.44}$$

The fall-off behavior of the EM complex scalars is given by

$$\Phi_n \approx \frac{1}{r^{3-n}}, \tag{5.45}$$

obtained using the Sachs-Peeling theorem. We can now identify Φ_0 with in-going EM radiation and Φ_2 with outgoing EM radiation for $r \to \infty$.

5.4 The gravitational wave strain

Having obtained Ψ_4 as quantity representing outgoing gravitational radiation we are now interested in relating this to the actual gravitational wave strain, i.e the dimensionless displacement in space caused by a gravitational wave. The gravitational wave strain h is related to Ψ_4 by [34, 83, 161]

$$\frac{1}{2}\left(\ddot{h}_+ - \ddot{h}_\times\right) = \lim_{r\to\infty} \Psi_4. \tag{5.46}$$

"+" and "×" here denote the two polarizations of the gravitational wave strain and ¨ refers to a double time derivative. As this result is obtained from the linearized theory it is only valid far away from the source and in the TT-gauge we can find additionally a close relationship between the linearized Riemann tensor and the gravitational wave strain

$$R_{itjt} = -\frac{1}{2}\ddot{h}_{ij}^{TT}. \tag{5.47}$$

In practice it is often useful to compute the gravitational wave strain in terms of spin weighted spherical harmonic modes of Ψ_4,

$$h_+ - ih_\times = 2\lim_{r\to\infty}\sum_{l,m}\int_0^t dt' \int_0^{t'} dt'' \Psi_4^{lm}{}_{-2}Y_{lm}. \tag{5.48}$$

5.5 Radiated energy and momentum of gravitational waves

Binary black-hole systems radiate up to 10 percent of their mass in form of gravitational waves. For supermassive black-hole binaries this accounts to copious amounts of energies. Using the gravitational wave strain computed in the previous section we can also find expressions for radiated energy, radiated linear and radiated angular momentum. Once we have obtained the expression in terms of the strain h we can then easily express them in terms of Ψ_4. An expression for the radiated energy in terms of the gravitational wave strain was found in, derived by evaluating the Isaacson stress-energy tensor in the TT-gauge [35, 36]

$$T_{\mu\nu} = \frac{1}{32\pi}\langle \partial_\mu h_{ij}^{TT} \partial_\nu h_{ij}^{TT}\rangle. \tag{5.49}$$

By exploiting the expression for $h_{ij}^T T$ in terms of h_+ and $h_\times$ by introducing $H := h_+ - ih_\times$ we can write the Isaacson stress energy tensor as

$$T_{\mu\nu} = \frac{1}{16\pi}\mathrm{Re}\langle \partial_\mu H \partial_\nu H\rangle, \tag{5.50}$$

and using the asymptotic property $\partial_r h \approx -\partial_t h$ for outgoing waves we can integrate the components T^{0i} over a 2-surface located at infinity, we obtain

$$\frac{dE}{dt} = \lim_{r\to\infty}\frac{r^2}{16\pi}\int_{S^2}|\dot{H}|^2 d\Omega, \tag{5.51}$$

with $d\Omega = \sin\theta d\theta d\phi$ and S^2 being a 2-surface at infinity. We can now also write the radiated energy flux in terms of the Weyl scalar Ψ_4 [28, 161, 162]

$$\frac{dE}{dt} = \lim_{r\to\infty}\frac{r^2}{4\pi}\int_{S^2} d\Omega \left|\int_{-\infty}^t d\tilde{t}\Psi_4\right|^2. \tag{5.52}$$

The radiated linear momentum in binary black-hole mergers is of interest since a net linear momentum carried away by gravitational waves leads to a recoil effect of the

remnant black hole of merger 9. We will first derive an expression for the radiated linear momentum in terms of the strain h and then use this to find an direct expression for the linear momentum in terms of the extraction quantity Ψ_4. Taking into account the components T^{ir} of the Isaacson stress energy tensor and assuming $\partial_i H \approx (x_i/r)\partial_r H$ in a region far away from the source, we get [36, 163]

$$\frac{dP_i}{dt} = \lim_{r\to\infty} \frac{r^2}{16\pi} \int_\Omega l_i |\dot{H}|^2 d\Omega, \tag{5.53}$$

with l_i the radial unit vector in flat space. Writing the linear momentum in terms of Ψ_4 we find [162]

$$\frac{dP_i}{dt} = \lim_{r\to\infty} \frac{r^2}{16\pi} \int_{S^2} d\Omega l_i \left| \int_{-\infty}^{t} d\tilde{t} \Psi_4 \right|^2 d. \tag{5.54}$$

Additionally we can also evaluate the radiated angular momentum by relating it to the strain h and Ψ_4. In the case of angular momentum special care has to be taken when using the short-wave-length approximation to obtain the Isaacson stress-energy tensor, because by averaging over a number of wavelength and also neglecting angular derivatives we will ignore the main contributions to the angular momentum carried by gravitational waves. An expression for the angular momentum flux was first introduced by DeWitt in 1971 and later presented in [37]. The expression reads

$$\frac{\partial J_i}{\partial t} = -\lim_{r\to\infty} \frac{r^2}{16\pi} \mathrm{Re} \int_{S^2} \hat{J}_i H \partial_t \bar{H} d\Omega, \tag{5.55}$$

using the angular momentum operators $\hat{J}_i$ given by

$$\hat{J}_x = \frac{1}{2}\left(\hat{J}_+ + \hat{J}_-\right), \tag{5.56}$$

$$\hat{J}_y = -\frac{i}{2}\left(\hat{J}_+ - \hat{J}_-\right), \tag{5.57}$$

$$\hat{J}_z = \partial_\phi, \tag{5.58}$$

where J_+ and J_i are the usual angular momentum ladder operators. Writing now the angular momentum in terms of Ψ_4 we obtain [162]

$$\frac{dJ_i}{dt} = -\lim_{r\to\infty} \frac{r^2}{16\pi} Re\{ \int_{S^2} \left(\int_{-\infty}^{t} \bar{\Psi}_4 dt' \right) \times \hat{J}_i \left(\int_{-\infty}^{t} \int_{-\infty}^{t'} \Psi_4 dt'' dt' \right) d\Omega \}. \tag{5.59}$$

5.6 Radiated energy and momentum of EM waves

Similarly to the expressions for the gravitational wave energy and momentum flux we can obtain expressions for the energy flux for EM waves in terms of the complex scalars Φ_2 and Φ_0. This is of great interested when comparing the power emitted by a binary black-hole merger system in gravitational waves and EM radiation as presented

in detail in chapter 11. The flux of energy carried by EM waves in general is given by the pointing flux S_i defined as

$$S_i = \sqrt{\gamma}\epsilon_{ijk}E^j B^k, \tag{5.60}$$

with the ϵ^{ijk} being the completely anti-symmetric Levi-Cevita symbol and E^i and B^i the electric and magnetic fields. Since E^i and B^i are gauge-dependent it is desirable to express the Poynting flux in terms of the gauge-independent (but however tetrad-dependent) quantities Φ_2 and Φ_0. In general we can write [161]

$$\frac{dE}{dt} = \lim_{r\to\infty} \int r^2 \left(|\Phi_2|^2 - |\Phi_0|^2\right) d\Omega. \tag{5.61}$$

Now we have found an expression of the radiated energy by EM waves in terms of the net flux of outgoing EM radiation Φ_2 and in-going radiation Φ_0. We note that in scenarios that model a compact source the in-going term can be neglected. However, since for some of the results obtained in this thesis 11 this assumption does not hold we present here the general expression.

5. THE WEYL AND EM COMPLEX SCALARS: GRAVITATIONAL WAVES AND EM RADIATION

Part II

Numerics and Implementation

6

Discretization of PDEs

To put us in place to perform numerical simulations of Einstein's equations we need to formulate the equations for the evolution systems as presented in chapter 3 in a discretized form. While this is often a simple task for ordinary differential equations, the non-linearity of Einstein's equations poses a major problem. The analytical analysis of discretized non-linear PDEs is very difficult and practical only for simple systems. Therefore a detailed analysis of the stability properties of the different formulations of Einstein's equations in a discretized form poses a major problem. One of the key aspects in this analysis is the *hyperbolicity* of the equations. For certain classes of hyperbolic equations mathematical theorems can be obtained that guarantee the stability of the equations even in a discretized form. In the case of Einstein's equations, for example, it can be shown that the generalized harmonic formulation are symmetric hyperbolic and yield stable evolution in the discretized scheme. In addition also the BSSNOK formulation of Einstein's equations yield stable numerical evolutions. In general not all combinations of equations with different discretization schemes lead to stable discretized equations. A crucial tool for the analysis of discretized systems is the von Neumann stability analysis. The MoL is used to split the discretization of space and time components of the equations, making the stability analysis considerably easier and allowing for a greater flexibility in choosing a suitable discretization scheme for the two different components. *Convergence* is crucial for any numerical approximative solution to be meaningful. It guarantees the numerical error of the solution to be bounded and the solution in the limit of infinite resolution of the discretized scheme to converge to the continuum one. In the next sections we will briefly review these concepts.

6.1 Finite differences

The main aspect of formulating a set of discretized equations as an approximation to the continuum case is the treatment of derivatives,

$$f'(x) := \lim_{h \to 0} \frac{f(x+h) - f(x)}{h}, \tag{6.1}$$

as we have to find a way to approximate the limit $h \to 0$ in this equation. The easiest and most straightforward choice is just to replace $h \to 0$ with a certain choice of h. This approximation is called *finite differences*. For the evaluation of the finite difference expression we now only need the function values $f_i := f(x_i)$ at a set of discrete points x_i and then taking derivatives reduces to additions and subtractions. The set of points x_i represents our numerical domain. In the case of finite differences they are usually uniformly spaced in their sampling of the numerical domain. In the case of binary black-hole merger simulations such a uniform sampling (with the addition of adaptive mesh-refinement which we will introduce in section 7.2) is suitable but in the case of more complicated topologies different schemes are more appropriate. Other methods, for example *finite volumes* or *discontinuous Galerkin* [164] are used instead since they allow for non-uniformly and even unstructured grids that can be very well adapted to any physical topology. In addition to the structure of the numerical grid finite difference methods assume the solutions to be continuous functions of a certain class of differentiability C^q. This is necessary for any derivative to be well-defined, but is not applicable in situations where discontinuous solutions, such as shock-fronts in hydrodynamical simulations, may arise. In those scenarios one therefore transforms the PDEs into a integral equations by the help of test-functions and again can use finite volume or discontinuous Galerkin methods to solve these equations. Luckily, in the case of binary black-hole space-times, the vacuum Einstein equations can be easily discretized using finite differences. However, there is also an effort in using *spectral methods* to achieve more accurate solutions. This effort is mostly carried out by the Caltech-Cornell group, which have developed a spectral-method base code and provide highly accurate numerical simulations of binary black-hole mergers [45, 103]. We will now proceed and provide a quick overview of the finite-difference scheme used to produce the results in the thesis.

6.1.1 Finite difference operators

Finite difference operators are used to approximate partial derivatives. The simplest choice of such an operator is

$$f'(x) := \frac{f(x+h) - f(x)}{h} + \mathcal{O}(h^2). \tag{6.2}$$

This operator is first-order accurate, so the error will decrease linearly with increase in resolution (decreasing h). We can obtain a more accurate operator by using a Taylor expansion around x to obtain

$$f'(x) := \frac{f(x+h) - f(x-h)}{2h} + \mathcal{O}(h^3) \tag{6.3}$$

with

$$f(x+h) = f(x) + f'(x)(x+h) + \frac{1}{2}f''(x)(x+h)^2 + \mathcal{O}(f^3), \tag{6.4}$$

$$f(x-h) = f(x) + f'(x)(x-h) + \frac{1}{2}f''(x)(x-h)^2 + \mathcal{O}(f^3). \tag{6.5}$$

This operator now is second-order accurate, we have taken terms up to second order in the Taylor expansion of $f(x)$. Another crucial difference between the first order operator (6.2) and the second order one, is that the first one is one-sided, while the second one is centered in respect to the point of evaluation x. In numerical evolutions it turns out that the use of one-sided or centered finite difference operators has a strong impact on the stability of the discretization scheme. In practice we use fourth- or eight-order accurate finite difference operators as they can be extended to arbitrary high-order q [165] as long as the functions are C^q. The use of higher-order schemes provides a higher accuracy and less high-frequency noise at a given resolution and the solution converges faster to the continuum solution. Any extra high-frequency noise present in our solution can be cured by applying artificial dissipation operators which we will discuss in the next section.

6.1.2 Dissipation operators

Any finite difference operator introduces spurious high-frequency noise due to its inability to resolve higher-frequency components of the solution. This additional error introduced in the computational domain can cause simulations to crash since it influences the numerical scheme in an non-linear manner. To weaken the impact of high-frequency noise finite-difference operators are usually bundled in application with artificial dissipation operators which are designed to damp high-frequency oscillations in the numerical grid. A typical choice of these dissipation operators is the *Kreiss-Oliger dissipation* as introduced in [166]. For a finite difference scheme of order q and of the form

$$u_m^{n+1} = n_m^n + \Delta t S(u_m^n), \tag{6.6}$$

where n is the time-level at which the solution u is represented, m the grid-point where it is evaluated, and $S(u_m^n)$ a spatial finite-difference operator, we extend this to the form

$$u_m^{n+1} = n_m^n + \Delta t S(u_m^n) - \epsilon \frac{\Delta t}{\Delta x}(-1)^N \Delta_x^{2N}(u_m^n). \tag{6.7}$$

Here $\epsilon > 0$ and $N \geq 1$ is an integer and $\Delta_x^{2N}(u_m^n)$ is a difference operator of order $2N$. It now can be shown [126] that the extra term damps effectively frequencies of the same length-scale as the grid spacing Δx, while leaving longer wavelengths unaffected. In the continuum limit equation (6.7) reads

$$\partial_t u = S(u) - \epsilon(-1)^N (\Delta x)^{2N-1} \partial_x^{2N} u, \tag{6.8}$$

and the extra term introduced and acting in a dissipative way vanishes in the limit $\Delta x \to 0$. To preserve the overall order of accuracy of our finite difference scheme the dissipation operator needs to fulfill $2N - 1 \geq q$, *i.e.,* it has to be one order higher than the finite difference operator itself to yield the same accuracy.

6.2 MoL

By using MoL [167] we can use independent discretization schemes for the spatial and time components of our PDEs. It allows us to disentangle the discretization scheme in time from the spatial one. This allows us to study the stability of the time discretization for a given spatial discretization and vice versa. After having chosen a discretization scheme in space S we typically proceed by splitting the time derivatives of our PDEs into a first-order form. Now the MoL performs an averaging in space that reduces u to only be a function of the form $u(t)$. This procedure allows to use standard ordinary differential equation (ODE) integrators, for example a RK scheme, to perform the time integration. To highlight the discretization in time performed by using the MoL we assume to have a continuum differential operator S and can write an evolution equation for our solution u in the form

$$\partial_t u = S(u). \tag{6.9}$$

We now discretize in time by introducing a sampling t_n and denote the solution at a given time-level as $u^n = u(t_n)$. For illustrative purposes we now choose a very simple scheme, the Euler step scheme, which is first-order in accurate to obtain

$$u^{n+1} = u^n + \Delta t S(t_n, u^n), \tag{6.10}$$

which enables us to obtain the time evolution of our solution u. However it turns out that this very simple approximation does not lead to stable evolution [167] in time and a better approximation for the time discretization is given by the RK scheme, which we describe next. The standard scheme used in binary black-hole simulations is the fourth-order accurate RK scheme, which consists of evaluation of successive sub-steps to obtain the solution at next time-level. We can write it as

$$\mathbf{k}_1 = S(t_n, \mathbf{u}^{n-1}), \tag{6.11}$$

$$\mathbf{k}_2 = S\left(t_{n-1} + \frac{\Delta t}{2}, \mathbf{u}^{n-1} + \frac{\Delta t}{2}\mathbf{k}_1\right), \tag{6.12}$$

$$\mathbf{k}_3 = S\left(t_{n-1} + \frac{\Delta t}{2}, \mathbf{u}^{n-1} + \frac{\Delta t}{2}\mathbf{k}_2\right), \tag{6.13}$$

$$\mathbf{k}_4 = S\left(t_{n-1} + \Delta t, \mathbf{u}^{n-1} + \Delta t \mathbf{k}_3\right), \tag{6.14}$$

$$\mathbf{u}^n = \mathbf{u}^{n-1} + \frac{\Delta t}{6}\left(\mathbf{k}_1 + 2\mathbf{k}_2 + 2\mathbf{k}_3 + \mathbf{k}_4\right) + \mathcal{O}\left(\Delta t^5\right). \tag{6.15}$$

The evaluation at a number of intermediate sub-steps ensures a higher accuracy of this scheme. The discretization order in time should be of the same order of accuracy as the discretization in space so as to not limit the overall accuracy of the numerical implementation. However in practice it turns out that the error introduced by a lower order time discretization scheme (*i.e.,* a fourth-order RK method in combination with a 8th-order spatial differencing scheme) is sub-dominant in binary black-hole merger simulations, thus making the choice of a fourth-order RK method the standard one used in our simulations. We note that some time-discretization schemes do not lead

to stable evolutions. In practice we can analyze the Fourier modes of the discretized PDE [167] to determine the stability properties of the time discretization scheme. In the next section we will give a brief overview over the stability and well-posedness of solutions to PDEs.

6.3 Stability and well-posedness

Well-posedness and *Stability* are two properties of major importance when analyzing PDEs. While well-posedness ensures that a PDE problem at the continuum level is posed in mathematically consistent way, while stability requires the discretized form of the equation to behave in an analogue way. A well-posed continuum problem does not necessarily lead to a stable discretized problem as this depends on the choice of discretization. We refer to a stable numerical scheme, if the continuum problem is well-posed and the discretization scheme prevents late-time exponential growth of the numerical solution. The von Neumann analysis [167, 168, 169] provides a useful tool to analyze the stability properties of a discretized PDE by transforming the analysis into the Fourier domain. In addition to these key aspects we will also review the *Courant-Friedrichs-Levy* (CFL) condition [170] which determines the maximum time-step depending on the grid-spacing used in the spatial part of the domain. We will briefly state these concepts in the next sections.

6.3.1 Well-posedness

Well-posedness requires a problem to be formulated in a way, that it has a solution u, that this solution is unique, and that it depends continuously on the initial data of the problem. For a system of PDEs, we can pose a initial value boundary problem on the domain $x \in [0, 1]$ by

$$\mathbf{u}_t = P\left(x, t, \frac{\partial}{\partial x}, \frac{\partial}{\partial x^2}, ...\right)\mathbf{u} + \mathbf{F}, \qquad t \geq t_0, \tag{6.16}$$

$$\mathbf{u}(\mathbf{x}, t) = \mathbf{f}(\mathbf{x}), \tag{6.17}$$

$$\mathbf{L}_0\left(t, \frac{\partial}{\partial x}, \frac{\partial}{\partial x^2}, ...\right)\mathbf{u}(0, t) = g_0, \tag{6.18}$$

$$\mathbf{L}_1\left(t, \frac{\partial}{\partial x}, \frac{\partial}{\partial x^2}, ...\right)\mathbf{u}(1, t) = g_1, \tag{6.19}$$

with L_0 and L_1 being differential operators and $\mathbf{F}$ a forcing function. We can now define well-posedness for a homogeneous boundary conditions ($\mathbf{F} = g_0 = g_1 = 0$) [167].

Definition 6.3.1 *The problem* (6.19) *with* $F = g_0 = g_1 = 0$ *is well-posed if, for every* $\mathbf{f} \in C^\infty$ *that vanishes in a neighborhood of* $x = 0, 1$*, it has a unique solution that satisfies*

$$||\mathbf{u}(\cdot, t)|| \leq \mathbf{K}e^{\alpha(t-t_0)}||\mathbf{u}(\cdot, t_0)||, \tag{6.20}$$

with $\mathbf{K}$ *and* α *not depending on* $\mathbf{f}$ *and* t_0.

For inhomogeneous boundary data we extend (6.3.1)

Definition 6.3.2 *The problem* (6.2) *is strongly well-posed if it is well-posed and the solution that satisfies*

$$||\mathbf{u}(\cdot,t)|| \leq \mathbf{K}(t,t_0)\left(||\mathbf{u}(\cdot,t)|| + \int_{t_0}^{t}(||\mathbf{F}(\cdot,\tau)||^2 + |g_0(\tau)|^2 + |g_1(\tau)|^2)d\tau\right), \tag{6.21}$$

with $\mathbf{K}(t,t_0)$ *is a bounded function in every finite interval, i.e.,* $\infty > ||\mathbf{K}(t,t_0)||_\infty$ *and does not depend on the data.*

6.3.2 Stability

Stability is the discrete analogue of well-posedness and determines the ability of a discretized set of PDEs to allow for long term evolutions. In the case where the discretized system is unstable exponentially growing modes can develop and cause the error to grow without bounds. We can write a general finite difference approximation of a linear system of PDEs as [167]

$$Q_{-1}\mathbf{u}^{n+1} = \sum_{\sigma=0}^{q} Q_\sigma \mathbf{u}^{n-\sigma}, \qquad n = q, q+1, ... \tag{6.22}$$

$$\mathbf{u}^\sigma = \mathbf{f}^{(\sigma)}, \qquad \sigma = 0, 1, ..., q. \tag{6.23}$$

where the Q_σ are finite difference operators and q denotes the number of time-levels evaluated. If we in addition now assume that Q_{-1} is uniformly bounded and its inverse Q_{-1}^{-1} is too in the limit of grid and time step $h,\ k \to 0$, we can evolve the solution step by step in time. For simplicity, we restrict ourselves in this section to the case of $q = 0$, thus we only evaluate the current and next time level. The general expressions can be found in [167]. By reformulating (6.23)

$$\mathbf{u}^{n+1} = Q(t_n)\mathbf{u}^n, \qquad n = 0, 1, ... \tag{6.24}$$

$$\mathbf{u}^0 = \mathbf{f} \tag{6.25}$$

with $Q(t_n) = Q_{-1}^{-1}Q_0$ and $\mathbf{f}$ defining the data on the initial time-level t_0, we can write the discrete solution as

$$\mathbf{u}^n = S_h(t_n, t_\nu)\mathbf{u}^\nu. \tag{6.26}$$

We can now obtain

Definition 6.3.3 *Given the constraints* α_S, C *and* K_S, *the difference approximation is said to be stable for* $h \leq h_0$, *if for all* h *the discrete operator in its norm satisfies*

$$||Q_{-1}^{-1}||_h \leq C, \qquad ||S_h(t_n, t_\nu)||_h \leq K_S e^{\alpha_S(t_n - t_\nu)}. \tag{6.27}$$

From Definition (6.3.3) we can now get an estimate on the growth on the norm of the solution $\mathbf{u}^n$ as

$$||\mathbf{u}^n||_h \leq K(t_n)||\mathbf{f}||_h, \qquad K(t_n) = K_S e^{\alpha_S t_n}. \tag{6.28}$$

This estimate states that the norm of the solution vector at later times is bounded by the initial data. Solutions that are exponential in nature are accounted by including the exponential factor into this estimate. In specialized cases where no exponentially growing modes are present in the continuum problem, more restrictive forms of (6.3.3) might be used, for example neglecting the exponential factor. In practice we often use a slightly different definition of stability, which reads

Definition 6.3.4 *Suppose the continuous solution operator $S(t, t_0)$ is bounded in the form*

$$||S(t, t_0)||_{op} \leq K e^{\alpha(t-t_0)}. \tag{6.29}$$

We then call a finite difference approximation strictly stable if in addition to (6.3.3) *it satisfies*

$$||S_h(t_n, t_0)||_h \leq K_S e^{\alpha_S(t_n-t_0)}, \tag{6.30}$$

with $\alpha_S \leq \alpha + \mathcal{O}(k)$.

6.3.3 von Neumann analysis

A particularly useful analysis technique for discretized PDEs is the von Neumann stability analysis which is using a *Fourier mode analysis* technique. By exploiting the MoL it first transforms the semi-discretized PDE in space to Fourier space, *i.e.,* the spatial finite difference operators are applied to Fourier modes $\hat{u}_j = \Psi e^{i\omega h x_j}$ with Ψ being the amplitude, ω the wave number, h the grid spacing and j the index of the grid point. This yields for a centered finite difference operator D approximating ∂_x

$$\hat{D}_0 \hat{h}_j = \Psi e^{i\omega h x_j} i \frac{\sin(\omega h)}{h}. \tag{6.31}$$

We can now solve the Fourier-transformed PDE

$$\partial_t \hat{u} = \hat{Q}\hat{u} \tag{6.32}$$

to obtain solutions of the form

$$\hat{u} = e^{\lambda t}, \qquad Re(\lambda) = 0, \tag{6.33}$$

with λ denoting the eigenvalues of $\hat{Q}$. A necessary condition for stability now can be found in the expression

$$|\lambda| \leq e^{\alpha_S \mathbf{k}}, \tag{6.34}$$

which is the von Neumann condition. An ODE method now is stable if the λk lie within the methods region of stability. To determine this regions of stability is beyond what we can present in this section but we refer to [167, 168] for details. Besides the von Neumann stability analysis there exist other methods for analyzing the stability properties of PDEs. One example is the *energy method* [167], which operates in physical space and uses a suitable norm such that the growth of the solution in every sub-step is bounded by an exponential factor.

6.3.4 The CFL condition

The CFL condition [170] states that the numerical domain of dependence of a solution should always incorporate the mathematical domain of dependence. It is another necessary condition for the stability of numerical evolution schemes. The basic idea is depicted in figure 6.1. It can be derived as a consequence of the von Neumann stability analysis for **explicit** time evolution schemes. Formulated in a different way it states, that the largest characteristic speed v_{max} along every direction n_i cannot exceed the corresponding numerical speed

$$v_{max} < n_i v^i_{num}, \qquad v^i_{num} = \frac{s\Delta x^i}{\Delta t}. \tag{6.35}$$

Here s denotes the stencil width of the difference operator. Effectively the CFL condition sets a limit on the maximal time-step we can choose and that still yields stable evolutions

$$\Delta t \leq C\Delta x, \tag{6.36}$$

with $C = \frac{s}{v_{num}}$. To overcome this limit one can use implicit schemes for the time

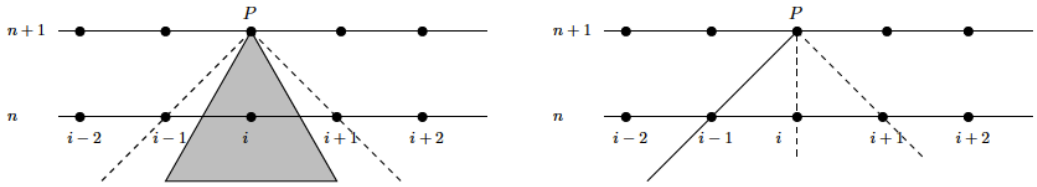

(a) Suppose a problem like the wave equation. In a correct discretization, the theoretical (gray triangle) is enclosed by the numerical domain of dependence (dashed triangle). Here, the difference scheme approximates the value at P with a spatial stencil that spans over the grid points $i-1, i, i+1$.

(b) Incorrect discretization, *e.g.* for an advection equation. The theoretical domain of dependence (straight line) does not coincide with the numerical one (dashed triangle). A correct discretization would involve $i-1, i$ (upwind scheme) instead of $i, i+1$ (downwind scheme).

Figure 6.1: Two example representations of theoretical and numerical domains of dependence. In the left panel, the numerical domain of dependence includes the theoretical one while in the right the opposite is true. Figure from [64].

discretization, which do not have the limitation of the CFL condition.

6.4 Hyperbolicity

In this section we will briefly review the concept of hyperbolicity, since it is of crucial importance when trying to find a formulation of Einstein's equations that yields stable numerical evolutions for black-hole space-times. Hyperbolicity reflects a condition on the coefficients of a system of PDEs, which ensures that given suitable initial data on an initial hypersurface, a unique solution can be obtained in neighborhood of the hypersurface and that the solution depends on the initial data in a continuous way [171]. In addition finite propagation velocities follow as a consequence of hyperbolicity. To

state the concept of hyperbolicity in a more formal and precise way we investigate a first order system of evolution equations

$$\partial_t u + M^i \partial_i u = 0, \tag{6.37}$$

with the M^i being $n \times n$ *characteristic matrices* of the PDE and the index i denotes an index in spatial dimensions only. Using a contraction with a unit vector n_i we can construct the *principal symbol*

$$P(n_i) := M^i n_i. \tag{6.38}$$

which we can now use to classify PDEs in terms of their hyperbolic properties. We call a system of PDEs *strongly hyperbolic* if P has real eigenvalues and a complete set of eigenvectors for all n_i. A system of PDEs for which P has real eigenvalues, but for which a complete set of eigenvectors for all n_i cannot be obtained is called *weakly hyperbolic*. If a system of PDEs is strongly hyperbolic and in addition all M^i are symmetric matrices, we call it *symmetric hyperbolic*. Last a *strictly hyperbolic* system has only real eigenvalues of its principal symbol P and all of these eigenvalues are distinct for all n_i. In case the P has only imaginary eigenvalues the system is called *elliptic* and in the case of both real and imaginary eigenvalues the set of equations is said to be *parabolic*. For symmetric and strongly hyperbolic systems we can always find a positive definite Hermitian matrix $H(n_i)$ that satisfies

$$HP - P^T H^T = HP - P^T H = 0, \tag{6.39}$$

with ^{T} denoting the transpose of any matrix. H is called the symmetrizer and we can use it to construct an inner product and a norm on the space of solutions of a given PDE. For two solutions of a given system of PDEs u, v we define

$$\langle u, v \rangle \quad := u^\dagger H v, \tag{6.40}$$

$$||u||^2 \quad := \langle u, u \rangle, \tag{6.41}$$

where $u^\dagger$ denotes the adjunct of u. The norm introduced in (6.41) is usually called an energy norm and the symmetrizer H acts as a metric tensor on the space of solutions to the system of PDEs. We can now exploit the energy norm to obtain the growth over time of the a solution u. We first transform u into Fourier space

$$u(x,t) = \tilde{u}(t) e^{ik\mathbf{xn}}, \tag{6.42}$$

and now use equation (6.42) in combination to obtain the time-derivative of the energy norm

$$\begin{aligned} \partial_t ||u||^2 \quad &= \partial_t (u^\dagger H u) = \partial_t (u^\dagger) H u + u^\dagger H \partial_t (u) \\ &= ik\tilde{u}^T \left(P^T H - HP \right) \tilde{u} = 0. \end{aligned} \tag{6.43}$$

Now Eq. (6.43) demonstrates that for symmetric and strongly hyperbolic systems the energy norm does not grow in time, which ensures well-posedness of the system of

PDEs. The generalized harmonic formulation of Einstein's equations is a symmetric hyperbolic system of equations and therefore an ideal candidate for a stable numerical evolution system. In addition it can be shown that the BSSNOK formulation is strongly hyperbolic while the ADM system of equations is only weakly hyperbolic, making it unsuitable for long stable numerical evolutions. A detailed account on various hyperbolic properties of different formulations of Einstein's equations can be found in [126].

6.5 Consistency and Convergence

A numerically obtained solution to a PDEs is meaningless without estimates for the errors in the approximation. Without error estimates we cannot determine if we are approaching the continuum solution (which the numerical solution is an approximation to) or still far away. Consequently we need to find tools to estimate the error of a numerical solution. Starting from a differential equation in the form

$$\mathcal{L}u = 0, \tag{6.44}$$

where $\mathcal{L}$ is a differential operator and u a function, we write its discretized form as

$$\mathcal{L}_\Delta u_\Delta = 0. \tag{6.45}$$

Here Δ is used to represent the step-size of the discretization scheme. To obtain an error estimate for the solution to the discretized system u_Δ we need to relate it to the continuum one, u. A useful quantity in this context is the *truncation error* of our finite difference approximation defined as

$$\tau_\Delta := \mathcal{L}_\Delta u, \tag{6.46}$$

which is a measure for the residual of applying $\mathcal{L}$ to the continuum solution u. The truncation error should vanish in the limit of infinite resolution, *i.e.,*

$$\lim_{\Delta\to 0} \tau_\Delta = 0. \tag{6.47}$$

If the discretized version at every grid-point approaches the continuum PDE, we call our finite difference approximation *consistent*. Consistency is a fundamental property of any finite difference approximation. Otherwise we will be unable to obtain the correct solution of the continuum problem in the limit of infinite resolution. For a consistent finite difference approximation the truncation error will approach zero as a function which is a power of the discretization parameter Δ. The order n of the finite difference approximation is then defined from

$$\lim_{\Delta\to\infty} \tau_\Delta \approx \Delta^n. \tag{6.48}$$

Consistency is a local property as it determines whether the finite difference approximation locally reduces to the PDE in the continuum limit. In order to classify the

global property of an numerical approximation we need to introduce another concept, *convergence*. We first introduce the *solution error*

$$\epsilon_\Delta := u - u_\Delta, \tag{6.49}$$

where again the subscript Δ denotes the quantities obtained from finite difference approximation to the continuum problem. The solution error measures the difference between the continuum solution and the numerical solution of the discretized version of the PDE. An approximation is said to be convergent if the solution error ϵ_Δ vanishes in the limit of infinite resolution. A consistent approximation can still fail to converge and even diverge. The *Lax equivalence theorem* relates the properties of consistency and convergence.

Theorem: Given an initial value problem that is mathematically well-posed and a finite difference approximation that is consistent, then stability is a necessary and sufficient condition such that the approximative solution converges to the continuum one.

Stated differently, if we can show that our numerical scheme is stable, then our solution to the discretized problem will converge to the continuum solution. For further details on the convergence and consistency of the numerical implementation of Einstein's equations we refer to [172].

6.5.1 Convergence testing

To test simulations for their convergence in practice we have to perform the same simulation for at least two resolutions to put us in position to make any statement about its error properties. A solution obtained from the discretized system behaves like the solution to the continuum problem plus error terms if the numerical scheme is stable

$$u_\Delta(t,x) = u(t,x) + \Delta e_1(t,x) + \Delta^2 e_2(t,x) + ..., \tag{6.50}$$

where the $e_i(t,x)$ denote the error functions to order i. Depending on the accuracy order of the numerical scheme used we expect some of these error functions to vanish, *i.e.,* for a second order scheme the first and second order error functions should be present, but the higher order terms should vanish. For determining the convergence properties of a discretized problem where a continuum solution is known (actually that is not the case for binary black-hole mergers) we can now with a set of two simulations at different resolutions Δ_1 and Δ_2 construct the convergence factor as

$$c := \frac{||e_{\Delta_1}||}{||e_{\Delta_2}||}, \tag{6.51}$$

where e_{Δ_1} and e_{Δ_2} refer to the solution errors for the two different resolution refer to the solution errors for the two different resolutions. Using expression (6.51) we can now extrapolate and find

$$\lim_{\Delta\to 0} c = \left(\frac{\Delta_1}{\Delta_2}\right)^n := r^n. \tag{6.52}$$

In a scenario where a continuum solution is not known, we need to perform a certain simulation at least at three resolutions to determine whether the approximate solution is convergent. For three resolutions $\Delta_1 > \Delta_2 > \Delta_3$ we can define the convergence factor as

$$c := \frac{||u_{\Delta_1} - u_{\Delta_2}||}{||u_{\Delta_2} - u_{\Delta_3}||}. \tag{6.53}$$

In the continuum limit this results to

$$\lim_{\Delta \to 0} = \frac{\Delta_1^n - \Delta_2^n}{\Delta_2^n - \Delta_3^n}. \tag{6.54}$$

In addition to considering the norms in Eq. (6.53) we can also determine the convergence factor for every grid point. The remaining solution error can now be evaluated using two resolutions and the Richardson expansion (6.54)

$$\begin{aligned} u_{\Delta_1} - u_{\Delta_2} \quad &= e_n \left(\Delta_1^n - \Delta_2^n\right) + \mathcal{O}(\Delta^{n+1}) \\ &= e_n \Delta_2^n (r^n - 1) + \mathcal{O}(\Delta^{n+1}) \\ &\approx \epsilon_{\Delta_2} (r^n - 1), \end{aligned} \tag{6.55}$$

with ϵ_{Δ_2} is the solution error estimation for the highest resolution. By writing (6.55) as

$$\epsilon_{\Delta_2} \approx \frac{1}{r^n - 1} \left(u_{\Delta_1} - u_{\Delta_2}\right), \tag{6.56}$$

we can now estimate the error in the numerical solution.

7

Computational infrastructure

Performing numerical simulations requires state-of-the-art computational infrastructure to handle the complexity involved in performing parallel computations on modern supercomputers. To name a view of the aspects that are key components handled by the computational infrastructure we mention I/O, parallelization, and memory management. Representing the numerical grid structure of a typical binary black-hole merger simulation alone is a highly complicated task as it involves nesting multiple grids with different resolutions, splitting the domain over many processors, handling boundary and overlapping zones and organizing the communication between the different processors. This is commonly done via the concepts of *adaptive-mesh refinement* (AMR) or *fixed-mesh refinement* (FMR). The tools used to perform these tasks on computer systems are of crucial importance to the success and efficiency of modern numerical relativity codes. The *Cactus* computational toolkit [173, 174, 175] is at the heart of most of today's finite difference based evolution codes for binary black-hole space-times. It handles input/output, memory management, provides tools for managing the flow in a computation and greatly simplifies the task of implementing a Einstein equations based evolution code. It is designed to be used as a general toolkit for solving PDEs. Another key component of the codes used to produce the results in this thesis is the *Carpet* [176, 177] AMR driver. It handles the nesting of grids with different resolutions, takes care of the resulting refinement-level boundaries and generally allows us to treat different regions of our computational domain (*i.e.,* the regions containing the black holes) with different resolutions. It is the AMR that makes modern long binary black-hole simulations feasible. We will in this chapter briefly review the main aspects of these core components of the computer codes we use. Finally, we mention that while recent additions like *multi-block schemes* improve the computational infrastructure used for binary black-hole mergers in terms of improving the accuracy of long simulations they were not used for the results in this thesis and we therefore will not describe them in detail here.

7.1 The Cactus computational toolkit

The Cactus computational toolkit [173, 174, 175] is an application framework for the development of computer code for solving PDEs on large-scale supercomputers. It introduces an abstraction layer that provides functions that perform common tasks such that the application programmer does not have to deal with the detailed implementation of these functions. This becomes more and more important as current computer codes become more complex and the hardware infrastructure develops at a rapid pace. The main goal of a application framework like Cactus now is to provide the technical implementation for the interaction with different hardware platforms as well as software platforms and making sure that it stays up to date and adepts to changes in the platforms. In this way the application programmer can solely focus on the task of implementing for example a PDE solver for Einstein's equations, while a computer science oriented programmer can purely focus on the abstracted functionality of the toolkit itself. In the next section we will briefly describe the main components of the Cactus computational toolkit. For further details on Cactus we refer to [173, 174, 175].

7.1.1 Structural design

The core components of Cactus are the 'flesh' and 'thorns'. The flesh is the backbone of the toolkit and executes the main program, controls the overall flow, hands over control to thorns for specific tasks and reads parameters to the program. Thorns are the part of Cactus where any actual calculation is done and user-functionality is implemented. Thorns form the basic (independent) modules of Cactus. Different thorns can communicate with each other via the flesh application programming interface (API), which handles the connection and communication of individual thorns to the flesh. A program based on Cactus in the end consists of a thorn-list defining which thorns to be included in the program. At execution the program then reads a parameter file that determines options handed over to the program altering its flow in a specific way. Cactus is therefore a very flexible toolkit for application development as we can easily change the components included into an application. The main program flow of a typical Cactus based application is depicted in figures 7.1 and 7.2.

7.1.2 Modularity

The thorns of Cactus come with their own namespace and any variables or parameters of a thorn are defined in its namespace. The user can decide which variables or functions of a thorn should be available to others. Two quantities that are at the heart of most thorn implementations are *grid variables* and *implementations*. Grid variables are variables defined on the whole computational grid and are *i.e.,* commonly used for the evolution variables of a formulation of Einstein's equations. The grid variables are accessible by all thorns, can be modified and updated. Grid variables can be of the type of scalar, grid function and grid array. A grid scalar is a scalar quantity defined at every point of the computational grid, a grid function an array with a fixed size, and a grid array

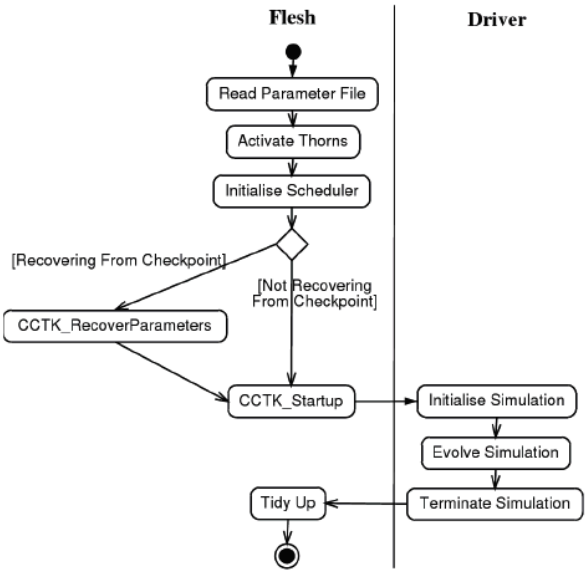

Figure 7.1: Main work flow schematics for the Cactus flesh. Figure taken from [175].

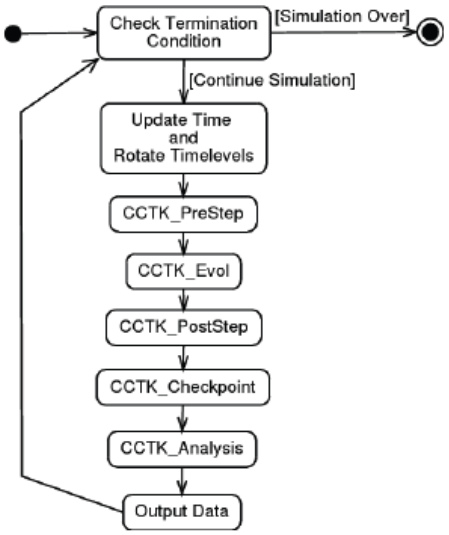

Figure 7.2: Evolution action item as processed in the Cactus scheduler. Figure taken from [175].

an array with an adaptable size. The visibility of variables to other thorns is controlled via its *scope*, which can be *private*, *protected* or *public*. A functionality provided by a

specific thorn in turn is denoted as an implementation. A thorn provides a functionality to the other thorns through the flesh API. Thorn parameters are handled similar to grid variables. The execution of a specific functionality or routine from a thorn is controlled by the Cactus scheduler, which controls the basic work-flow of the program.

7.1.3 Scheduling

Calling routines that are provided by thorns is handled by the Cactus scheduler. The scheduler is a component of the flesh and controls when and how a routine is called. It uses the concept of *time-bins* to call routines in a desired order. The scheduler typically loops over a finite number of time-bins and routines can therefore be called in the right order. *i.e.,* in a typical evolution step of an Einstein evolution code the update of the evolution variables is performed in a time-bin called $CCTK\_Evol$, while any analysis quantities like the constraint are calculated at $CCTK\_Analysis$. Inside one time-bin the order of a number of routines to be called can be controlled by conditional statements. By using the concept of *control inversion* the Cactus scheduler then determines the order in which routines should be executed. In this way the independence of the individual components is ensured.

7.1.4 Memory management and message passing

On current large-scale supercomputer evolution codes are run on a large number of processors in parallel. By running the program in parallel we can ideally split the computational domain into n subsets that are each handled by one of the n processors cores assigned to perform the computation. This leads, at least in principle, to a speed-up of the computation of a factor of n. However since most large-scale computer systems do not provide shared memory between all processor cores (typically only the cores contained within one node (≈ 16) have access to the same memory) we need to split the computational domain in memory. However, since the typical finite difference schemes involve high stencil widths every processor not only needs to know data on its sub-domain, but also on part of the domains of neighboring processors. To obtain this, a copy operation from one processor to the other is necessary and this complicates the computation. The regions which hold copies of the domain assigned to different processors are called interprocessor boundary zones and their updating introduces a substantial amount of communication among processors. Performing this communication in an efficient way is crucial to the performance of numerical evolutions and are handled by an abstraction layer. The most commonly used one is the message passing interface (MPI) standard [178]. It defines standard routines for copying, updating and many other common communication tasks while running one MPI processes on each processor core. When using higher-order accurate finite difference approximations the amount of data in the interprocessor boundary zones can be enormous. To circumvent this bottleneck OpenMP [179] can be used which makes use of the shared memory within a processor by running multiple *threads* on each of the cores of a processor. In this way there is one MPI process per processor and then multiple threads running on

every core. The amount in memory saved by the fact that no interprocessor boundary zones have to be setup between the threads on different processor cores can be substantial. Together with additionally reducing the communication between the threads this leads to a advantage both in memory allocation and results in a speed-up of the program execution. The main parts of Cactus support OpenMP parallelization. This functionality in Cactus is handled by the concept of drivers. A driver handles for example memory allocation, parallelization and other low-level tasks. One such driver, the *Carpet* mesh refinement driver is described in the next section.

7.2 AMR

In black-hole simulations large gradients are present in a small region close to the singularity. On the other hand the solution in most of the rest of the computational grid does not show heavy variations or dynamics in time, but we need to allow for a large computational domain to perform analysis task like gravitational wave extraction which is only meaningful far away from the source. It is therefore desirable to have different resolutions in different regions of the numerical grid. This provides the benefit of saving computational costs while obtaining a high resolution in the regions that require it. The savings in cost compared to a uniformly space grid throughout the whole computational domain can be drastic. The practical implementation of this *non-uniform* computational domain is achieved by using a method called *mesh refinement*. Mesh-refinement can be achieved in two different flavors. In FMR the location of the nested grids in respect to the overall computational domain is fixed in the time evolution. In the approach of AMR [180] we allow the nested grids with higher resolution to move around. In this way we can enable them to track the physical dynamics in our system. In practice, for binary black-hole simulations we enable the nested grids to track the orbital dynamics of the black holes as the high spatial resolution is required in the vicinity of them. A example of the grid structure for a basic binary black-hole simulation at a fixed time is presented in figure 7.3. Adaptive mesh refinement was used since a long time for fluid dynamics [181, 182] simulations and in 3D numerical relativity FMR was introduced in [177], and later expanded to moving FMR. In the next section we will describe the essential aspects of the implementation of a mesh-refinement infrastructure.

7.2.1 The Carpet mesh refinement driver

Carpet [176] is a mesh-refinement driver for Cactus that has been developed by Schnetter and collaborators [177]. Due to the scheduler design and specifically the property of control-inversion it is straightforward to use Carpet within Cactus instead of another grid driver. Any application level functionality like user thorns only have to adjusted in minor ways to account for the more complicated grid topology. *i.e.,* the update of the evolution variables now has to be performed on each refined grid, while other calculations, for example interpolation operations need not be changed. To enable these

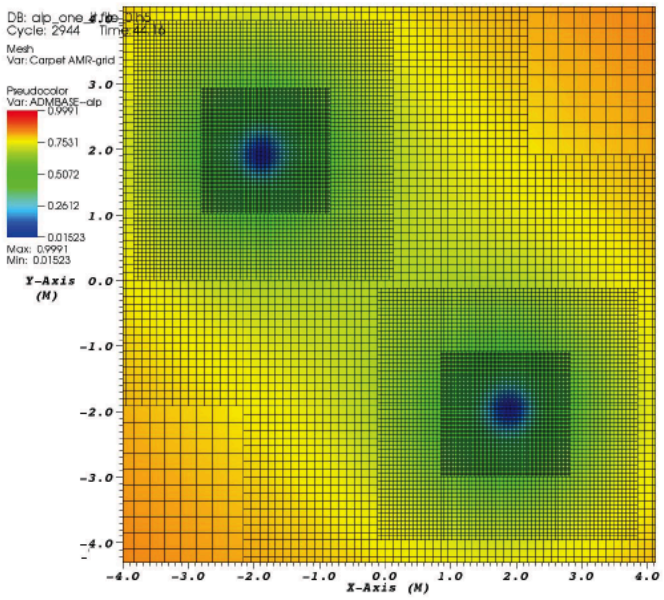

Figure 7.3: AMR. Shown is the lapse function α on a 2D-slice of our computational domain. The black meshes illustrate the nested grid structure centered around the two black holes. Figure taken from [64].

distinction Carpet uses the techniques describe in the next sections.

7.2.2 Mesh refinement method

Carpet employs Berger-Oliger mesh refinement [180], specifically minimal Berger-Oliger mesh refinement [180]. The computational domain and all sub-domains are rectangular Cartesian grids, and the boundaries of the coarsest grid are aligned with the grid lines. The boundaries of the refined regions are not required to be on a grid point and an example of the resulting grid topology is depicted in figure 7.4. The computational grid is grouped into a set of *refinement levels* L^k. Each refinement level contains a number of grids G_j^k with grid spacings Δx^k (for simplicity we restrict ourselves here to the one-dimensional case). The grid spacings of the different grids are now related by

$$\Delta x^k = \Delta x^{k-1}/N_{refine}, \tag{7.1}$$

with N_{refine} being the *integer refinement factor*. For all our simulation we always have $N_{integer} = 2$. L^0 is called the coarse level and covers the entire computational domain while the L^k with $k \neq 0$ represented the refined regions. They have to be properly nested, any G_j^k must be contained within the set of grids of the next coarser refinement levels L^{k-1}. The extent and location of the refined regions within the computational domain has to be specified by the user or a user application. We in practice track the evolution of the either the black-hole apparent horizon or the puncture and adjust the nested grids according to that information.

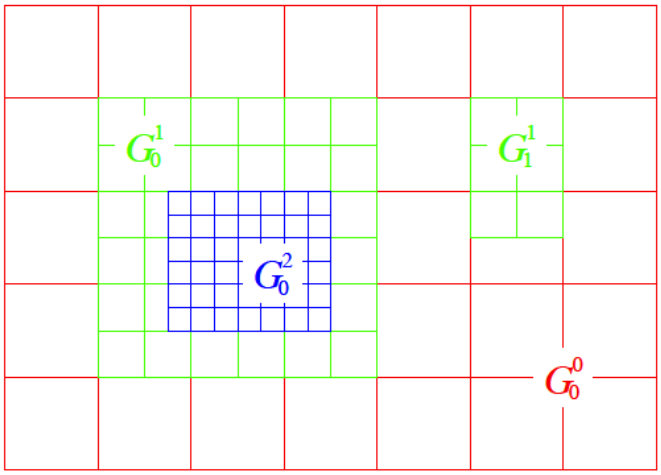

Figure 7.4: Grid alignment in an AMR/FMR nested grid structure. Figure taken from [177].

7.2.3 Time evolution

The time evolution in our mesh-refinement framework is performed according to the Berger-Oliger AMR scheme [180]. First, the coarse grid data is evolved in time, then any refined grids are updated and evolved in time. This guarantees that we can use the coarse grid evolved in time data as boundary data for the refined regions. In practice this is achieved by *prolongation*, *i.e.,* polynomial interpolation in time and space to acquire the data at the position and time needed for the refined region. In case both refinement levels exist at the time, the data can simply be copied from one refinement level to the other. In general, for hyperbolic systems the time-step needs to be adjusted on a refined grid to match the CFL condition given the higher spatial resolution. The time-step needs to be reduced by the same refinement factor N_{refine} as the resolution. We therefore need to perform N_{refine} time-steps on a level k to match one time-step on the next coarser level $k+1$. In the case of many refinement levels this procedure is carried out from coarsest to finest in a recursive manner until all refinement levels have been advanced in time. This scenario is illustrated in figure 7.5.

Since most of the higher-order accurate time integration schemes like Runge-Kutta, consist of multiple sub-steps in time, the prolongation and restriction operations have to be performed multiple times for updating one time-step. Providing boundary conditions on refined grids can be done in different ways. In [177] no boundary condition was specified but instead the boundary zones enlarged such that boundary points could be calculated like regular interior grid points. This of course was only applied to prolongation of the refinement region boundaries, the outer boundaries of the computational domain were handled by providing boundary conditions. The use of these so called buffer zones may be computationally more expensive depending on the cost of the alternatively to be applied boundary condition.

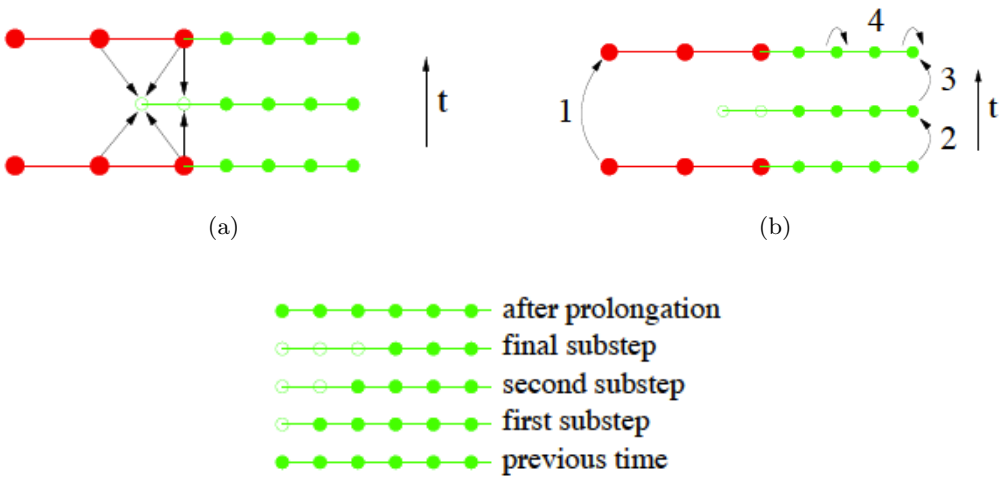

(a) (b)

(c)

Figure 7.5: AMR logic for updating points from buffer zones.(a) describes the prolongation operation in 1+1 dimensions for a two-level grid. Red circles represent data on the coarse grid, while green circles (filled) refer to points on the fine grid. Arrows indicate interpolation operations to obtain boundary data for the fine grid.(b) shows a time evolution scheme in 1+1 dimensions. Again, red circles refer to the coarse grid data points while green ones refer to the fine level data. The numbers indicate the steps in the algorithm: 1) coarse grid evolution step 2) and 3) fine grid evolution steps 4) restriction from fine to coarse grid. (c) illustrates the "buffer" zones used during time integration. The empty green circles represent data near the boundary where no boundary condition is provided. Since these points are left out in the time integration sub-steps data is provided after an prolongation operation. Figure taken from [177].

8

Cauchy evolution systems: Implementation details

After having described the computational infrastructure that is used in our evolution codes in the previous chapter we now continue by presenting the details of how the evolution systems for Einstein's equations are discretized and solved. We will focus on the two formulations of Einstein's equations that were used to obtain the results in this thesis, namely the BSSNOK and generalized harmonic evolution systems. In addition we will also describe the implementation of some key components of our evolution codes such as the generation of puncture initial data, puncture tracking and horizon finding. Puncture initial data is obtained using a single-domain spectral method [124]. Puncture tracking is a technique to determine the location of punctures in our numerical grid. It enables us to move the refined regions according to the motion of the black holes which can be approximated by the motion of the punctures. Searching and finding apparent horizons in black-hole simulations in turn serves mainly two purposes. First, we can use it to track the motion of the black holes independent of the punctures (*i.e.,* this is important in cases where the punctures are excised from the grid). Second, the apparent horizon surface is a excellent tool for the analysis of quasi-local properties related to the black holes itself. We use it to determine the mass and spin of black holes as well as to analyze the geometric properties of a binary black-hole space-time which is one of the key results in this thesis and is presented section 10. We will in the next sections briefly discuss all these aspects in the following sections.

8.1 Discretization of the Cauchy evolution systems

The two evolution codes used in this thesis are based on two different formulations of Einstein's equation as already detailed in chapter 3. Nevertheless they are build using the same computational infrastructure and share many analysis tools. The CTGamma code is based on a BSSNOK formulation of Einstein's equations and is a 3D Cartesian AMR code. It can use up to 8th order finite differencing operators. The HADM code is based on a 3+1 generalized harmonic formulation of Einstein's equations. It uses the

standard spatial 3-metric as an evolution variable and is a 3D Cartesian evolution code that can use up 4th order accurate finite difference operators. We will now first describe the common aspects of the two evolution systems and then continue to describe each of them in detail in the next sections.

8.1.1 The Numerical grid structure

The underlying structure of the numerical grid in both formulations is the same. We use a 3D Cartesian computational domain employing AMR. The grid is indexed by i,j, and k and in the case of the simplest scenario, where we only have one uniform grid, the coordinates x^μ are labeled as

$$x_i^l = x_0^l + (i-1)h, \qquad with \qquad i = 1...N_l. \tag{8.1}$$

x_0^l denotes the lower boundary of the domain in coordinate direction l, and N_l the number of grid points. We can now label a grid function u as

$$u_{ijk} := u(x^\mu_{ijk}) := u(x_i, y_j, z_k). \tag{8.2}$$

If we however have multiple nested grids, this labeling is far from simple, and needs to be done with proper care. In Cactus this is realized in the Carper AMR driver, as discussed in chapter 7 and the user application only has to deal with one uniform grid. This is realized in Cactus by splitting the AMR grid into a number of uniform sub-grids that are then handled locally, *i.e.,* any calculation routine is scheduled locally on all sub-grids, and the whole grid is later reassembled by Carpet.

8.1.2 Discretization of the evolution equations

Using the MoL allows us to treat the discretization of space and time separately. We therefore proceed and discretize the evolution equations first. The right hand sides (RHS) of the equations are fully expanded in terms of the evolution variables, which are available as grid functions in the Cactus framework. Any additional temporary variables are calculated locally, *i.e.,* at every grid point. Examples are the derivatives of a evolution variable or any intermediate variable needed in a calculation. Next the RHSs of the evolution equations need to be evaluated at every grip point. This is performed by a simple loop over all grid points, and the resulting expressions are then passed to the time integrator. The time integrator now evolves the evolution variables to the next time-level using the previously obtained RHS expressions. As an example we give the evolution equation for the conformal factor ϕ in the BSSNOK system in its discretized form and note that all other equations are discretized in the same way.

$$(\hat{\phi}_{RHS})^n_{ijk} = \frac{2}{\kappa}(\hat{\phi}_\kappa)^n_{ijk}\alpha^n_{ijk}K^n_{ijk} + \left[(\beta^h)^n_{ijk}D_h\right](\hat{\phi}_\kappa)^n_{ijk} = \frac{2}{\kappa}(\hat{\phi}_\kappa)^n_{ijk}\left(D_h(\beta^h)^n_{ijk}\right) \tag{8.3}$$

Here n specifies the current time-level, ijk the position in the grid index and D_i is a finite difference operator in the three spatial directions $i = x, y, z$. Depending on the

position index ijk these operators may either be using a centered or off-centered stencil to obtain the finite difference expressions. Dissipation will be added as an extra term in an additional step after the RHS is obtained to ensure that high-frequency noise is kept at a minimum. The dissipation coefficients determining the amount of dissipation can be varied both depending on the refinement level and on the position in the grid index ijk. As an example in the HADM code we typically apply a higher amount of dissipation in the vicinity of the apparent horizon, while we try to minimize the amount of dissipation in the rest of the computational domain. After the time-integrator has completed all sub-steps to obtain the evolution variable at the next time-level, the evolution variables are transformed back to the ADM variables to perform extra analysis steps as the calculation of the constraints or any other quantities of interest. These steps constitute the main stages of one evolution step and the procedure is repeated until the designated end-time of the simulation is reached.

8.1.3 The CTGamma code

CTGamma is a BSSNOK evolution system based 3D Cartesian AMR code. It supports different choices for the conformal variable as presented in section 3.2. Additionally it can use different finite difference accuracy orders and provides the option of including a multi-block domain. The accuracy of the evolution is monitored by evaluating the Hamiltonian and momentum constraints. The gauge condition for lapse and shift are specified in the form of specific condition, *i.e.,* the hyperbolic $\tilde{\Gamma}$-driver condition for the shift in combination with the 1+log slicing for the lapse.

8.1.4 The HADM code

HADM is a generalized harmonic formulation based code. It is formulated using the standard 3+1 variables α, β^i and g_{ij} as evolution variables. This minimizes the effort spent on transforming back to ADM variables after each evolution step. As CTGamma, HADM is also a 3D Cartesian AMR code and shares most of the infrastructure. It allows for the use of up to fourth-order accurate finite difference operators. The accuracy of the evolution is monitored by using the generalized harmonic constraints. Gauge conditions are chosen by evolving the gauge quantities lapse and shift according to their evolution equations in the generalized harmonic evolution scheme. Specific gauges can be indirectly chosen by providing suitable gauge source functions $F^\mu(x^\nu)$ as presented in section 3.3.

8.2 Generation of puncture initial data

In this section we will focus on the detailed implementation of the calculation of puncture initial data as it is most commonly used to obtain black-hole initial data for our evolution codes. The method used was introduced in [124] and is implemented in a Cactus thorn *TwoPunctures*. To obtain black-hole initial data with angular and

linear momentum one has to solve the Hamiltonian and momentum constraint equations (3.11), (3.12). A procedure for solving these equations is a conformal decomposition of the space-time and then solve the reduced Hamiltonian constraint for the conformal factor only. The momentum constraint can be solved by using the Bowen-York extrinsic curvature (3.82). Using puncture initial data it is possible to solve the Hamiltonian constraint equation without the need to specify inner boundary conditions at the singularity. These equations are elliptic in nature and are commonly solved using pseudo-spectral methods with collocation points for the derivatives and a preconditioned biconjugate gradient stabilized Krylov subspace based method for the linear system of equations. By introducing a special set of coordinates mapping $\mathbb{R}^3$ including the puncture points and spatial infinity into a single rectangular domain it is possible to obtain C^∞ at the punctures allowing us to fully exploit the exponential convergence property of spectral methods. However we need to note that Bowen-York extrinsic curvature is only C^4 [183] in the limit $r \to \infty$ and thus limits the overall accuracy of the spectral scheme to sixth-order in the continuum limit. We need to solve an elliptic equation of the form

$$f(u) := \Delta u + \sigma(u) = 0. \tag{8.4}$$

Δ denotes the Laplace operator and $\sigma(u)$ is a source-term that may depend on u. We can solve this equation numerically for u on a set of grid points (A_i, B_j, ϕ_k) where the coordinates (A, B, ϕ_k) are specified in their range by

$$A \in [0, 1], \qquad B \in [-1, 1], \qquad \phi_k \in [0, 2\pi). \tag{8.5}$$

We now introduce $U = u/(A-1)$ and can represent this on the gridpoints of the numerical domain as

$$U_{ijk} = U(A_i, B_j, \phi_k), \tag{8.6}$$

where the indices i, j, k are specified as

$$0 \leq i < n_A, \qquad 0 \leq j < n_b, \qquad 0 \leq k < n_\phi. \tag{8.7}$$

We next have to represent the function U by the discrete values at every gridpoint by using a pseudo-spectral collocation method. Using an infinite series expansion of the U_{ijk} we obtain

$$U = \sum_{ijk} U_{ijk} T_i T_j F_k, \tag{8.8}$$

where we have used Chebyshev polynomial expansions $T_{n_A}(1-2x)$ and $T_{n_B}(-x)$ as the basis functions for A and B and a Fourier expansion $F = \sin(n_\phi \phi)$ as the basis function for ϕ. The gridpoint locations are then chosen such that

$$A_i = \sin^2\left[\frac{\pi}{2n_A}\left(i + \frac{1}{2}\right)\right] \tag{8.9}$$

$$B_i = -\cos\left[\frac{\pi}{n_B}\left(j + \frac{1}{2}\right)\right] \tag{8.10}$$

$$\phi_k = 2\pi \frac{k}{n_\phi}. \tag{8.11}$$

We can now calculate derivatives by differentiating the basis functions. Since the infinite series expansion in practice has to be stopped at a finite number of included terms, it limits the accuracy of the method. By substituting the vector

$$\vec{U} = (U_{000}, ..., U_{(n_A-1)(n_B-1)(n_\phi-1)})^T \tag{8.12}$$

with

$$\vec{f}(\vec{U}) = (f_{000}, ..., f_{(n_A-1)(n_B-1)(n_\phi-1)})^T, \tag{8.13}$$

where the $f(u)$ are evaluated at the grid points (A_i, B_j, ϕ_k), we have now transformed the elliptic equation into a set of non-linear algebraic equations of the type

$$\vec{f}(\vec{U}) = 0. \tag{8.14}$$

The U_{ijk} can be decomposed by using a Newton-Raphson iteration scheme as

$$\vec{U} = \lim_{N\to\infty} \vec{U}_N, \tag{8.15}$$

$$\vec{U}_{N+1} = \vec{U}_N - \vec{V}_N \tag{8.16}$$

with $\vec{V}_N$ satisfying the linear equation

$$J_N \vec{V}_N = \vec{b}_N, \tag{8.17}$$

using

$$J_N = \frac{\partial \vec{f}}{\partial \vec{U}}(\vec{U}_N), \qquad \vec{b}_N = \vec{f}(\vec{U}_N). \tag{8.18}$$

The linear set of equations is now solved using a biconjugate gradient stabilized (BICGSTAB) method, where the preconditioning scheme chosen is crucial to maintain the overall accuracy of the solution. The preconditioned used in this case is based on solving (8.14) in linearized form applying finite difference techniques on a uniform grid. After having provided a strategy of solving the system of equations we need to specify the coordinate mapping for A, B, n_ϕ. The choice of coordinates covers the whole domain including spatial infinity and the puncture point itself. Regularity of u at the punctures is guaranteed by using analytic functions for the distance r to the punctures which enables us to obtain puncture initial data that is C^∞ [183]. For creating initial data containing two punctures we use the mapping (details on the coordinate transformation can be found in [124])

$$\begin{aligned}(A, B, \phi) \quad &\to (\xi, \eta, \phi) \to (X, R, \phi) \to (x, \rho, \phi) \\ &\to (x, y, z).\end{aligned} \tag{8.19}$$

The choice of this transformation is motivated by achieving: 1) regularity of r (function of the distance to the puncture) at both punctures 2) mapping the entire (x, y, z)

coordinate space into a rectangular domain in $\mathbb{R}^{\not\vdash}$. The final transformation reads

$$x = b\frac{A^2+1}{A^2-1}\frac{2B}{1+B^2} \tag{8.20}$$

$$y = b\frac{2A}{1-A^2}\frac{1-B^2}{1+B^2}\cos\phi \tag{8.21}$$

$$z = b\frac{2A}{1-A^2}\frac{1-B^2}{1+B^2}\sin\phi. \tag{8.22}$$

As a last step we have to also provide boundary conditions at infinity ($r \to \infty$) to equation (8.4) as

$$\lim_{r\to\infty} u = 0. \tag{8.23}$$

We ultimately need to obtain the solution on the Cartesian coordinates of the evolution code. This is possible, since the representation of the solution in terms of Chebyshev polynomials is close to a polynomial of best approximation for a continuous function, and we can therefore, knowing the coefficients U_{ijk} of the Chebyshev polynomial, obtain the function everywhere in the domain.

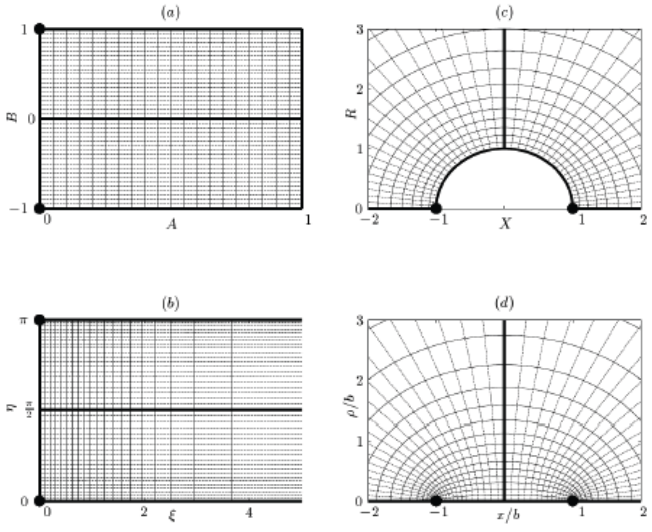

Figure 8.1: Coordinate patches for two-puncture initial data. (a) shows equidistant coordinate lines in the coordinates (A, B), (b) shows the same in the coordinates (ξ, η). (c) depicts the coordinate lines in coordinates (X, R) and (d) in the coordinates (x, ρ). The punctures are indicated by the filled black circles. The black lines indicate sections of the x-axis, the $x = 0$-plane and spatial infinity ($A = 1$). Figure taken from [124].

8.3 Puncture tracking

We track the punctures during the course of our BSSNOK evolutions to adjust the refinement regions to the motion of the black holes. The location of the punctures in the grid can be determined by solving the coordinate equations of motion

$$\partial_t x^i = -\beta^i. \tag{8.24}$$

The RHS is given by the shift vector, which completely determines the motion of the punctures in the grids by the choice of the hyperbolic $\tilde{\Gamma}$-driver gauge condition. The discretization of equation (8.24) reads

$$x^i_n = x^i_{n-1} - \Delta t \beta^i_n(x^i_{n-1}), \tag{8.25}$$

where again n denotes the current time-level, Δt the time-step and $\beta^i_n(x^i_{n-1})$ is the shift vector evaluated at the puncture location of the previous $n-1$ time-level. We can use this equations and the initial data where we know the puncture locations to track their motion during our evolution. Since it is not guaranteed that the puncture locations coincide with grid points in general we need to interpolate the value of the shift vector in order to evaluate expression (8.25).

8.4 Apparent horizon finding

Finding an apparent horizon and determining its shape in a numerical simulation represents a highly useful analysis tool for the space-time geometry. On the S^2 shape of the apparent horizon we can use the isolated horizon framework to calculate various quasi-local properties such as the mass or the spin of the black hole. In addition we can construct a number of useful curvature measure, *i.e.,* the mean curvature or the signature of the determinant of the induced 2-metric. These quantities will become important in chapters 9, 10. where we will use them and other quantities to draw conclusions about the space-time geometry in the head-on black-hole merger space-times. Furthermore, apparent horizon can also be used to move the refinement regions along with the motion of the black holes when puncture locations are unknown or cannot be tracked. We recall that an apparent horizon is defined as the outermost marginally trapped surface, and we can use the expansion, which has to be zero to find the apparent horizon in a numerical simulation. We can write the expansion in terms of the ADM variables and use the fact that it has to vanish for an apparent horizon to obtain

$$\theta_{(l)} := \nabla_i n^i + K_{ij} n^i n^j - K = 0. \tag{8.26}$$

Here n^i is the outward pointing unit normal to the 2-surface S and K_{ij} the extrinsic curvature. We can now use equation (8.26) to find MOTS in a space-time obtained by numerical simulation and then select the outermost one as the apparent horizon. In practice we follow the procedure of first providing an initial guess for a point inside the apparent horizon [184]. Initially this is easy to obtain as it is known from initial

data and in the consequent evolution steps we can take the data from the previous time-level as a guess. We next construct the radius $r := [\sum_i (x - x_i)^2]^{1/2}$ as a function of the angular coordinates ρ, σ as $r = h(\rho, \sigma)$. With the assumption of the apparent horizon being a star-shaped region we can rewrite Eq. (8.26) in terms of the horizon shape function $h(\rho, \sigma)$

$$\theta_{(l)}(h, \partial_u h, \partial_{uv} h, g_{ij}, \partial_k g_{ij}, K_{ij}) = 0, \tag{8.27}$$

with ∂_u and ∂_{uv} denoting first and second derivatives along angular coordinates. This equation is an elliptic PDE for h on S^2. We can now discretize S^2 (we use an inflated cube six-patch coordinate system) and approximating the partial derivative with finite differences obtain a set of N_{ang} algebraic equations for h which we can solve using a Newton-Raphson method. The exact strategy is presented in [184] which we refer the interested reader to.

Part III

Black-hole simulations

9

Dynamics of MOTS: Explaining the anti-kick in binary black-hole mergers

Understanding the dynamics of colliding black holes is of major importance. Not only is this process one of the main sources of gravitational waves, but it is also responsible for the final recoil velocity (*i.e., "kick"*) of the merged object, which could play an important role in the growth of supermassive black holes via mergers of galaxies and on the number of galaxies containing black holes. The recoil of black holes due to anisotropic emission of gravitational wave has been known for decades [185, 186] and first estimates for the velocity have been made using approximated and semi-analytical methods such as a particle approximation [163, 187, 188], post-Newtonian methods [189, 190, 191, 192] and the close-limit approximation [193, 194]. However, it is only thanks to the recent progress in numerical relativity that accurate values for the recoil velocity have been computed [195, 196, 197, 198, 199, 200, 201, 202].

Indeed, simulations of black holes inspiraling on quasi-circular orbits have shown, for instance, that asymmetries in the mass can lead to kick velocities $v_{\rm k} \lesssim 175\,{\rm km/s}$ [195, 197], while asymmetries in the spins can lead respectively to $v_{\rm k} \lesssim 450\,{\rm km/s}$ or $v_{\rm k} \lesssim 4000\,{\rm km/s}$ if the spins are aligned [199, 200, 202] or perpendicular to the orbital angular momentum [196, 203, 204] (see [205, 206] for recent reviews).

In addition to a net recoil, many of the simulations show an *"antikick"*, namely, one (or more) decelerations experienced by the recoiling black hole at late times. In the case of merging black holes, such antikicks seems to take place after a single apparent horizon has been found [207] (see figure 8 of [202] for some examples). An active literature has been developed over the last few years in the attempt to provide useful interpretations to this process [207, 208, 209, 210, 211]. Interestingly, some of these works do not even require the merger of the black holes. As pointed out in [212] when studying the scattering of black holes, in fact, the presence of the common apparent horizon is not a necessary condition for the antikick to occur. Furthermore, as highlighted in [213], it is also possible to describe this process without ever discussing black holes and just

using the mathematically properties of the evolution of a damped oscillating signal[1].

Although the presence of a common apparent horizon is not a necessary condition for the appearance of an antikick (which could indeed be produced also by the scattering of a system involving one or two neutron stars), when a common apparent horizon *is present* through the merger of black-hole binary, we can use information on the latter to gain insight in the physical mechanisms behind the antikick[2]. We believe that constructing an intuitive picture of the dynamics of general relativity in a region of very strong field is not only interesting but also useful to explain this process. In [214], in fact, a new conjecture was suggested in which the antikick produced in the head-on collision of two black holes with unequal masses was understood in terms of the dissipation of the apparent horizon intrinsic deformation. As shown in the schematic cartoon in figure 9.1, the kick and antikick can be easily interpreted in terms of simple dynamical concepts. Initially the smaller black hole moves faster and linear momentum is radiated mostly downwards, thus leading to an upwards recoil of the system [stage (1)]. When a single apparent horizon is formed at the merger, the curvature is higher in the upper hemisphere of the distorted black hole and linear momentum is radiated mostly upwards leading to the antikick [stage (2)]. The black hole decelerates till a uniform curvature is restored on the apparent horizon [stage (3)]. The qualitative picture showed in the cartoon, was then investigated by exploiting the analogy between this process and the evolution of Robinson-Trautman space-times [215, 216] and by showing that a one-to-one correlation could be found between the properties of the apparent horizon perturbation and the size of the recoil velocity [214].

In this chapter we provide further support to the conjecture proposed in [214] by extending our considerations to more generic initial data, but also by investigating in detail how the analysis made in [214] is validated in numerical space-times describing the head-on collision of two black holes with unequal masses. To do this we introduce a *cross-correlation* picture in which the dynamics of the space-time can be read-off from two "screens" represented at least ideally by the black-hole event horizon and by future null infinity $\mathcal{I}^+$. In practice, using the standard $3+1$ approach in numerical relativity, we replace these screens with effective ones represented respectively by a dynamical horizon $\mathcal{H}^+$ and by a time-like tube $\mathcal{B}$ at large spatial distances. We then define a phenomenological curvature vector $\tilde{K}_i^{\rm eff}(t)$ in terms of the mass multipoles of the Ricci scalar curvature ${}^2R$ at $\mathcal{H}^+$ and show that this is closely correlated with a *geometric quantity* $(dP_i^{\mathcal{B}}/dt)(t)$, representing the variation of the Bondi linear momentum in time on $\mathcal{I}^+$. This construction, which is free of fitting coefficients and valid beyond the axisymmetric scenario considered here, correlates quantities on the apparent horizon with quantities at large distance, thus providing us with two important tools. Firstly, it allows us to confirm the conjecture that the antikick can be associated with the dissipation of anisotropic distribution of curvature on the apparent horizon. Secondly,

[1] Of course, if an exponentially-damped oscillating signal is present, this is indeed a signature of the presence of a black hole ringing down.

[2] We will actually show in this chapter show that even when an horizon is not present, the considerations made here can be extended on a suitably defined 2-surface.

it opens a new route to the analysis of strong-field effects in terms of purely local quantities evaluated either on the apparent horizon or on other suitable surfaces.

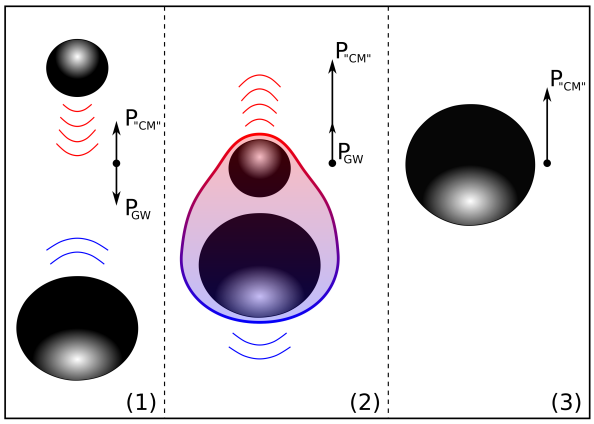

Figure 9.1: Generation of the antikick in the head-on collision of two unequal-mass Schwarzschild black holes as described in [214]. Initially the smaller black hole moves faster and linear momentum is radiated mostly downwards, thus leading to an upwards recoil of the system [stage (1)]. At the merger the curvature is higher in the upper hemisphere of the distorted black hole (*cf.* red-blue shading) and linear momentum is radiated mostly upwards leading to the antikick [stage (2)]. The black hole decelerates till a uniform curvature is restored on the apparent horizon [stage (3)].

The first part of this chapter is organized as follows. section 9.1 introduces an executive summary, where the main concepts are summarized for those not wishing to enter into the mathematical details. section 9.2 is then used to apply the concepts and the diagnostics to black-hole space-times representing the head-on collision of unequal-mass black holes. In this section we also develop the mathematical tools necessary to measure the relevant quantities on the two screens and we show how they closely correlate. Finally, the conclusions are discussed in section 9.11.

In the second part of this chapter we present a more detailed discussion of the mathematical aspects of our framework. In particular, we revisit there the evolution of relevant geometric objects on the apparent horizon and introduce preferred null normals on a dynamical horizon. In our discussion of a news-like function on the dynamical horizon and its relation to the problem of quasi-local linear momentum, we also stress the importance of the inner horizon when evaluating fluxes across the horizon. The presentation in this chapter follows very closely the one in [217, 218].

9.1 The cross-correlation approach: an executive summary

This section is meant to provide a general summary of the results and methodology presented in this chapter, focusing mostly on the conceptual aspects and leaving aside

the mathematical details, which can instead be found in the corresponding main texts.

We start by recalling that [214] suggested an approach to study the near-horizon nonlinear dynamics of the gravitational fields based on the systematic analysis of the deformations in the black-hole horizon geometry. In particular, it was shown how the gravitational dynamics responsible for the antikick after a binary merger can be understood in terms of the anisotropies in the intrinsic curvature of the apparent horizon of the resulting merged black hole. Considering a Robinson-Trautman space-time, the kick velocity constructed from the Bondi momentum (a geometric quantity at null infinity) was put in a one-to-one correspondence with a quasi-local geometric quantity constructed on the horizon, namely, with the effective *curvature parameter* $K_{\rm eff}$. This geometric parameter $K_{\rm eff}$ encodes the part of the apparent horizon geometry whose *dissipation* through gravitational radiation can be related to the final value of the kick. Stated differently, very different binary systems, e.g with very different mass ratio, give rise to the same final kick velocity as long as they share the same value of the $K_{\rm eff}$ parameter.

The following criteria were employed in [214] for the construction of the *curvature parameter* $K_{\rm eff}$: i) $K_{\rm eff}$ should not depend on how the apparent horizon is embedded in the space-time; ii) $K_{\rm eff}$ should change sign (*i.e.,* it should be an odd function) under reflection with respect to a plane normal to a given axis. From the first requirement, $K_{\rm eff}$ was constructed in terms of the intrinsic geometry of the apparent horizon, namely as a functional on the Ricci scalar ${}^2R$ associated with the induced metric on the apparent horizon. The Ansatz for $K_{\rm eff}$ in [214], compatible with requirement ii) above and within axisymmetry, had the following structure

$$K_{\rm eff} = f_{\rm even}\left(M_{2\ell}\right) \times f_{\rm odd}\left(M_{2\ell+1}\right) \,, \tag{9.1}$$

where M_ℓ's are the so-called *isolated-horizon mass multipoles* associated with a spherical harmonic decomposition of ${}^2R$ in the axisymmetric case [219, 220]. The odd part $f_{\rm odd}$ accounts for the directionality of the kick, whereas the even part $f_{\rm even}$ controls its intensity.

While the focus in [214] was on expressing the difference between the *final* kick velocity v_∞ and the instantaneous kick velocity $v_{\rm k}(u)$ at an (initial) given time u, in terms of the geometry of the common apparent horizon at that time u, we here focus on geometric quantities that are evaluated at a given time during the evolution. More specifically, we will consider the variation of the Bondi linear momentum vector in time $(dP_i^{\rm B}/du)(u)$ as the relevant geometric quantity to monitor at null infinity $\mathcal{I}^+$. To this scope, we need first to construct a vector $\tilde{K}^i_{\rm eff}(v)$ (function of an advanced time v) as a counterpart on the black-hole horizon $\mathcal{H}^+$. Then, we need to determine how $\tilde{K}^i_{\rm eff}(v)$ on $\mathcal{H}^+$ correlates to $(dP_i^{\rm B}/du)(u)$ at $\mathcal{I}^+$.

In the Robinson-Trautman case, the causal relation between the white-hole horizon $\mathcal{H}^-$ and null infinity $\mathcal{I}^+$ made possible to establish an explicit functional relation between $dv_{\rm k}/du$ and $K'_{\rm eff}(u)$. In the case of generic black-hole horizon, however, such a direct causal relation between the inner horizon and $\mathcal{I}^+$ is lost (see figures. 9.2 and 9.3). However, since their respective causal pasts partially coincide, non-trivial *correlations*

are still possible and expected. This can be measured through the cross-correlations of geometric quantities $h_{\rm inn}(v)$ at $\mathcal{H}^+$ and $h_{\rm out}(u)$ at $\mathcal{I}^+$, both considered here as two timeseries[1]. In particular, we will take $\tilde{K}^i_{\rm eff}(v)$ as $h_{\rm inn}(v)$ and $(dP^{\rm B}_i/du)(u)$ as $h_{\rm out}(u)$.

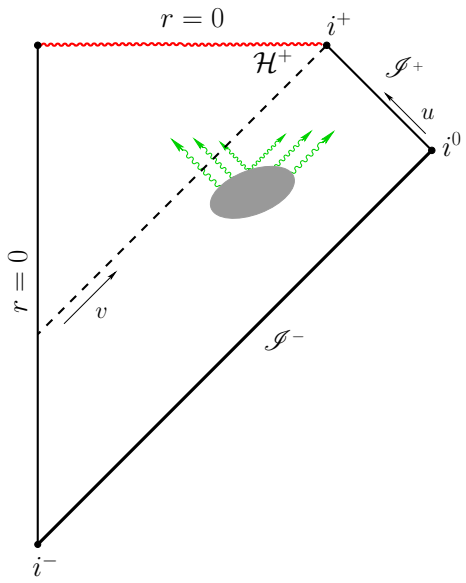

Figure 9.2: Carter-Penrose diagram illustrating the *scattering* approach to near-horizon gravitational dynamics in a generic spherically symmetric collapse. The event horizon $\mathcal{H}^+$ and null infinity $\mathcal{I}^+$ provide spacetime canonical screens on which *geometric quantities*, respectively accounting for horizon deformations and wave emission, are defined. Their cross-correlation encodes non-trivially information about the bulk spacetime dynamics.

This approach to the exploration of near-horizon gravitational dynamics resembles therefore the methodology adopted in *scattering* experiments. Gravitational dynamics in a given spacetime region affects the geometry of appropriately chosen *outer* and *inner* hypersurfaces of the black-hole spacetime. These hypersurfaces are then understood as *test screens* on which suitable *geometric quantities* must be constructed. The correlations between the two encodes geometric information about the dynamics in the bulk, providing information useful for an *inverse-scattering* approach to the near-horizon dynamics. As a result, in asymptotically flat black-hole spacetimes, null infinity $\mathcal{I}^+$ and the (event) black-hole horizon $\mathcal{H}^+$ provide preferred choices for the outer and inner screens. This is nicely summarized in the Carter-Penrose diagram in figure 9.2, which illustrates the cross-correlation approach to near-horizon gravitational dynamics. The event horizon $\mathcal{H}^+$ and null infinity $\mathcal{I}^+$ provide spacetime screens on which geometric

[1]Note that the meaningful definition of timeseries cross-correlations requires the introduction of a (gauge-dependent) relation between advanced and retarded time coordinates v and u. In an initial value problem this is naturally provided by the $3+1$ spacetime slicing by time t.

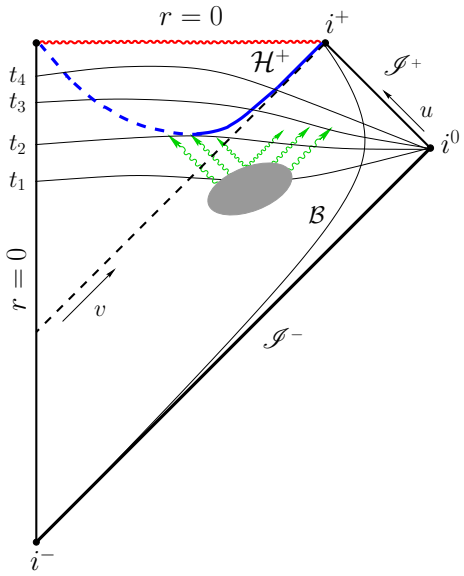

Figure 9.3: Carter-Penrose diagram for the *scattering* picture in a Cauchy initial value approach. The dynamical horizon $\mathcal{H}^+$ and a large-distance time-like hypersurface $\mathcal{B}$ provide inner and outer screens. Note that a the dynamical horizon is split in two portions: outer and inner (solid and dashed blue lines, respectively) and that the $3+1$ slicing sets a common time t for cross-correlations.

quantities, respectively accounting for horizon deformations and wave emission, are defined. Their cross-correlation encodes information about the bulk spacetime dynamics.

Although the picture offered by figure 9.2 is quite simple and convincing, it is not well adapted to the 3+1 approach usually adopted in numerical studies of dynamical spacetimes. Indeed, neither the black-hole event horizon nor null infinity are in general available during the evolution[1]. However, we can adopt as inner and outer screens a dynamical horizon $\mathcal{H}^+$ (future outer trapping horizon [221, 222, 223]) and a time-like tube $\mathcal{B}$ at large spatial distances, respectively. In this case, the time function t associated with the $3+1$ spacetime slicing provides a (gauge) mapping between the retarded and advanced times u and v, so that cross-correlations between geometric quantities at $\mathcal{H}^+$ and $\mathcal{B}$ can be calculated as standard timeseries $h_{\rm inn}(t)$ and $h_{\rm out}(t)$. This is summarized in the Carter-Penrose diagram in figure 9.3, which is the same as in figure 9.2, but where the $3+1$ slicing sets an in-built common time t for cross-correlations between the dynamical horizon $\mathcal{H}^+$ (*i.e.,* the inner screen) and a large-distance time-like hypersurface $\mathcal{B}$ (*i.e.,* the outer screen).

Within this conceptual framework it is then possible to define a phenomenological curvature vector $\tilde{K}_i^{\rm eff}(t)$ in terms of the mass multipoles of the Ricci scalar curvature ${}^2R$

[1]The latter would properly require either characteristic or a hyperboloidal evolution approach.

at $\mathcal{H}^+$ and show that this is closely correlated with a geometric quantities $(dP_i^{\mathcal{B}}/dt)(t)$, representing the variation of the Bondi linear momentum time on $\mathcal{I}^+$. How to do this in practice for a black-hole spacetime is the subject of the following sections.

9.2 Black-Hole spacetimes: Head-on collisions

9.2.1 Mass multipoles

Given a closed 2-surface $\mathcal{S}$, the invariant content of its intrinsic geometry is encoded in the Ricci scalar curvature ${}^2R$ associated with the induced metric q_{ab} on $\mathcal{S}$. Moreover, if $\mathcal{S}$ is an axisymmetric surface, with ϕ^a as the axial Killing vector, a preferred coordinate system $(\tilde{\theta}, \tilde{\varphi})$ can be constructed such that q_{ab} has the form [219, 220]

$$q_{ab}dx^a dx^b = R_{\rm H}^2 \left(f^{-1}\sin^2\tilde{\theta}\, d\tilde{\theta}^2 + f\, d\tilde{\varphi}^2 \right) , \tag{9.2}$$

where $f(\tilde{\theta}) = q_{ab}\phi^a\phi^b/R_{\rm H}^2$, with $R_{\rm H}$ the areal radius ($A = \int_{\mathcal{S}} dA = 4\pi R_{\rm H}^2$). The coordinate $\tilde{\theta}$ is determined by

$$D_a\tilde{\zeta} = \frac{1}{R_{\rm H}^2}\,{}^2\epsilon_{ba}\phi^b, \tag{9.3}$$

where the coordinate $\tilde{\zeta}$ is defined by $\tilde{\zeta} \equiv \cos\tilde{\theta}$ and ${}^2\epsilon_{ba}$ is the alternating symbol. In addition, the normalization condition $\oint_{\mathcal{H}} \tilde{\zeta} dA = 0$ must be imposed. We note that the Ricci scalar ${}^2R$ on $\mathcal{S}$ can be written as [219]

$${}^2R = -\frac{1}{R_{\rm H}^2}\frac{d^2 f}{d\tilde{\zeta}^2}(\tilde{\zeta}) , \tag{9.4}$$

and that regularity conditions on the metric impose

$$\lim_{\tilde{\zeta}\to\pm 1} f(\tilde{\zeta}) = 0 , \quad \lim_{\tilde{\zeta}\to\pm 1} \frac{df}{d\tilde{\zeta}}(\tilde{\zeta}) = \pm 2 . \tag{9.5}$$

A crucial feature of this coordinate system is that the associated expression for the area element is proportional to that of the *"round sphere"* metric $dA = R_{\rm H}^2 \sin\tilde{\theta}\, d\tilde{\theta} d\tilde{\varphi}$. This provides the appropriate *measure* on $\mathcal{S}$ to define the standard spherical harmonics $Y_{\ell,m=0}(\tilde{\theta})$ with the standard orthonormal relations

$$\oint_{\mathcal{S}} Y_{\ell,0}(\tilde{\theta}) Y_{\ell',0}(\tilde{\theta}) dA = R_{\rm H}^2 \delta_{\ell\ell'} , \tag{9.6}$$

so that the dimensionless geometric multipoles I_ℓ can be introduced as the spherical harmonics components of the Ricci scalar curvature ${}^2R$ [219]

$$I_\ell \equiv \frac{1}{4}\oint_{\mathcal{S}} {}^2R\, Y_{\ell,0}(\tilde{\theta})\, dA , \;\; {}^2R = \frac{4}{R_{\rm H}^2}\sum_{n=0}^{\infty} I_\ell Y_{\ell,0}(\tilde{\theta}) . \tag{9.7}$$

The mass multipoles M_ℓ's are then defined as an appropriate dimensionful rescaling of the geometric I_ℓ's

$$M_\ell \equiv \sqrt{\frac{4\pi}{2n+1}} \frac{M_{\rm H}(R_{\rm H})^\ell}{2\pi} I_\ell \,, \tag{9.8}$$

where $M_{\rm H}$ denotes an appropriate quasi-local mass for the surface $\mathcal{S}$. Because we will consider here initial data with with zero angular momentum, $M_{\rm H}$ will denote the irreducible mass $M_{\rm irr} = \sqrt{A/(16\pi)} = R_{\rm H}/2$. For later convenience, we introduce the rescaled geometric multipoles $\tilde{I}_\ell$

$$\tilde{I}_\ell \equiv \frac{1}{M_{\rm irr}^2} I_\ell = \frac{4}{(R_{\rm H})^2} I_\ell, \tag{9.9}$$

with dimensions $[\tilde{I}_\ell] = [\text{length}]^{-2}$. The Ricci scalar curvature can then be written as

$$^2R = \sum_{\ell=0}^{\infty} \tilde{I}_\ell Y_{\ell 0} \ . \tag{9.10}$$

A crucial remark for the discussion in section 9.2.3 is the vanishing of the $\ell = 1$ mode, *i.e.,* $\tilde{I}_1 = 0$, which can be interpreted as a choice of *center of mass frame* of the apparent horizon in [219]. This follows by first inserting expression (9.4) into the definition of $\tilde{I}_1$, so that $\tilde{I}_1 \propto \int_{-1}^{1} f''(\tilde{\zeta})\tilde{\zeta} d\tilde{\zeta}$, and then by making use of regularity conditions (9.5) after integrating by parts.

9.2.2 Numerical Setup and Results

The numerical solution of the Einstein equations has been performed using a three-dimensional finite-differencing code solving a conformal-traceless "3 + 1" BSSNOK formulation of the Einstein equations (see [224] for the full expressions) using the `Einstein Toolkit` [225], the `Carpet` [226] adaptive mesh-refinement driver, `AHFinderDirect` [227] to track the apparent horizons, and `QuasiLocalMeasures` [228] to evaluate the mass multipoles associated with them. Recent developments, such as the use of 8th-order finite-difference operators or the adoption of a multiblock structure to extend the size of the wave zone have been recently presented in [159, 224]. Here, however, to limit the computational costs and because a very high accuracy in the waveforms is not needed, the multiblock structure was not used. Also, for compactness we will not report here the details of the formulation of the Einstein equations solved for the form of the gauge conditions adopted. All of these aspects are discussed in detail in [224], to which we refer the interested reader.

Our initial data consists of head-on (*i.e.,* zero angular momentum) Brill-Lindquist initial data with a mass-ratio of $q = 1/2$. The initial separation of both black holes is $10M$ and they are initially located at $(0, 0, 6.6666)$ and $(0, 0, -3.3333)$ to reflect their center-of-mass offset. Both black holes have no angular nor linear momentum initially. We use a 3D Cartesian numerical grid with 7 levels of mesh-refinement for the higher mass and 8 levels of mesh-refinement for the lower mass black hole. The resolution of our

finest grid is $h = M/64$, while the angular grid used to find the apparent horizons and evaluate any property on these 2-surfaces has a resolution of 65 points in φ-direction and 128 points in θ-direction. The extraction of gravitational waves is performed calculating Ψ_4 at finite-radius detection spheres with radii of $r_1 = 60\,M$, $r_2 = 85\,M$ and $r_3 = 145\,M$ and then extrapolating to infinity.

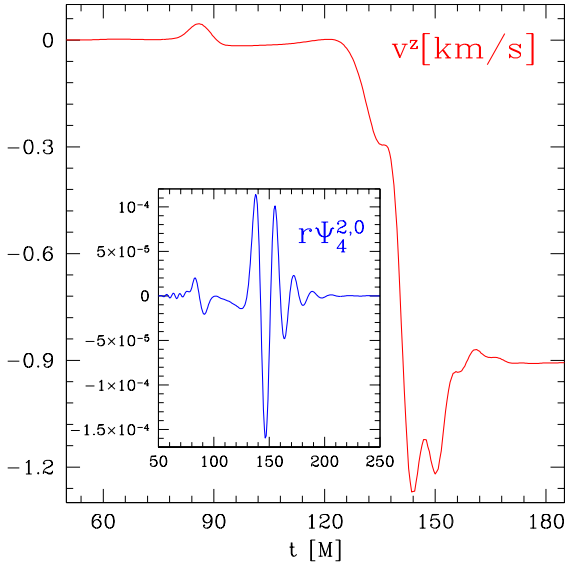

Figure 9.4: Evolution of the velocity (red curve) measured with the flux of momentum carried out by the gravitational waves. Note the antikick at about $t/M \approx 145$ that decelerates the system before the final kick velocity is reached. The gravitational wave signal is instead shown in the inset, namely the dominant $\Psi_4^{2,0}$ multipole (blue curve).

Some of the most salient results of the numerical simulations are summarized in figure 9.4, which reports the evolution of the recoil velocity (red curve) measured with the flux of momentum carried out by the gravitational waves. Note the development of the antikick at about $t/M \approx 145$ (followed by several smaller oscillations) that decelerates the black hole before the final kick velocity is reached. Also shown in the inset is gravitational wave signal in its larger multipolar component $\Psi_4^{2,0}$ (blue curve). Similarly, figure 9.5 provides a realization of the cartoon in figure 9.1 with numerical data from a simulation of head-on collision with mass ratio $q = 1/2$. Shown with a color code is the mean curvature on the apparent horizons, which shares the same qualitative properties, and in particular the anisotropic behaviour, of the intrinsic curvature. As intuitively described in figure9.1, once the common horizon is formed, the curvature is stronger in the region of the smaller black hole and is dissipated as the evolution proceeds. Note that the curvature distribution is anisotropic already at the beginning, as the black holes are tidally distorting each other.

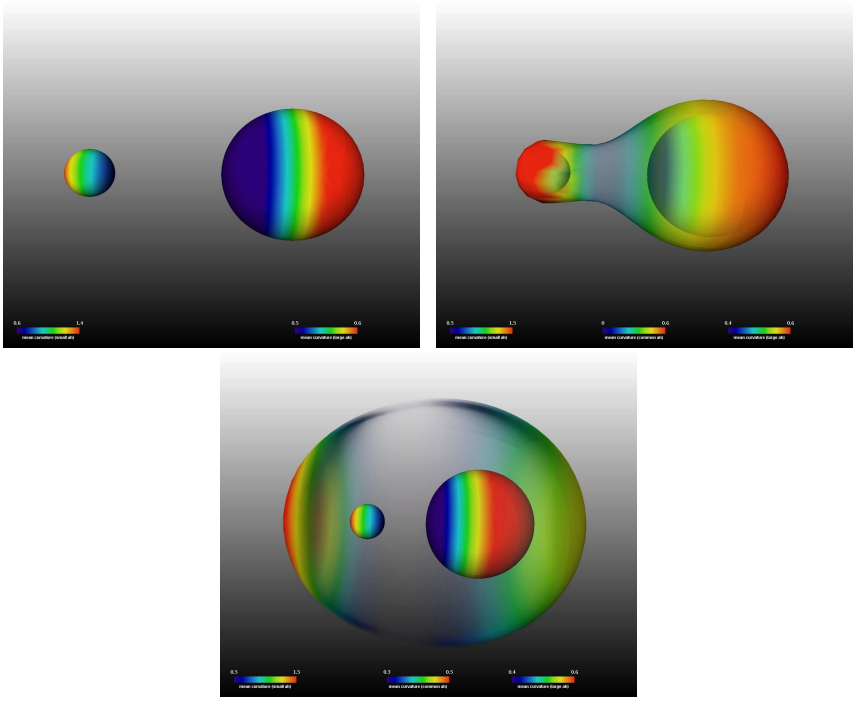

Figure 9.5: Realization of the cartoon in figure 9.1 with numerical data from a simulation of head-on collision with mass ratio $q = 1/2$. The color code shows the mean curvature on the apparent horizons, which has the same anisotropic behaviour of the intrinsic curvature. As described in figure9.1, once the common horizon is formed, the curvature is stronger in the region of the smaller black hole and is dissipated during the evolution.

9.2.3 Geometric quantities at the black-hole horizon: $\tilde{K}_i^{\rm eff}(t)$

When considering standard $3+1$ numerical solutions of black-hole spacetimes, we study the near-horizon dynamics responsible for the black-hole recoil in terms of the time cross-correlations between a vector $(dP_i^{\mathcal{B}}/dt)(t)$ at a large-radius hypersurface $\mathcal{B}$ and an effective curvature vector $\tilde{K}_i^{\rm eff}(t)$ constructed from the intrinsic geometry on the dynamical black-hole horizon $\mathcal{H}^+$. The vector $(dP_i^{\mathcal{B}}/dt)(t)$ on $\mathcal{B}$ approximates the Bondi linear momentum flux $(dP_i^{\rm B}/dt)(t)$ at $\mathcal{I}^+$. From now on we will systematically refer to $(dP_i^{\rm B}/dt)(t)$ (and to $\mathcal{I}^+$ instead of $\mathcal{B}$), understanding that we are actually using an approximation.

The construction of $\tilde{K}_i^{\rm eff}(t)$ at $\mathcal{H}^+$ is based on the following two guiding lines: a) $\tilde{K}_i^{\rm eff}(t)$ is built out of the intrinsic geometry Ricci scalar curvature ${}^2R$ on $\mathcal{H}^+$ sections; b) the functional form of $(dP_i^{\rm B}/dt)(t)$ in terms of the geometry at $\mathcal{I}^+$ guides the choice of the functional dependence of $\tilde{K}_i^{\rm eff}(t)$ on ${}^2R$. The first requirement is motivated by the success in the Robinson-Trautman case, whereas the second one aims at preserving those basic structural features of the specific function to be cross-correlated.

Following these guidelines, we start by expressing the flux of Bondi linear momen-

tum at null infinity. In terms of a retarded time u parameterizing $\mathcal{I}^+$, its Cartesian components can be written as

$$\frac{dP_i^{\rm B}}{du}(u) = \lim_{(u,r\to\infty)} \frac{r^2}{8\pi} \oint_{\mathcal{S}_{u,r}} s_i \, |\mathcal{N}(u,\Omega)|^2 d\Omega \,, \tag{9.11}$$

where r parameterizes the large radius spheres $\mathcal{S}_{u,r}$ along a $u =$ const. hypersurface, $r^2 d\Omega$ is the area element on $\mathcal{S}_{u,r}$, s^i is its normal unit vector with Cartesian components $s^i = (\sin(\theta)\cos(\varphi), \sin(\theta)\sin(\varphi), \cos(\theta))$, and the *news functions* $\mathcal{N}(u)$ can be expressed in terms of the Weyl scalar Ψ_4 as

$$\mathcal{N}(u,\Omega) = \int_{-\infty}^{u} \Psi_4(u',\Omega) du' \,. \tag{9.12}$$

In our $3+1$ setting with an outer boundary at a finite spatial distance we need to express the flux with respect to the time function t parameterizing the spatial slices Σ_t, so that we replace $\mathcal{S}_{u,r}$ with $\mathcal{S}_{t,r}$

$$\frac{dP_i^{\rm B}}{dt}(t) = \lim_{r\to\infty} \frac{r^2}{16\pi} \oint_{\mathcal{S}_{t,r}} s_i \left| \int_{-\infty}^{t} \Psi_4(t',\Omega) dt' \right|^2 d\Omega \,, \tag{9.13}$$

and where we can think of t (related to u by $u = t - r$ near $\mathcal{I}^+$) as parameterizing the cuts of $\mathcal{I}^+$ by hyperboloidal slices or, alternatively, the cuts of the time-like hypersurface $\mathcal{B}$ approximating $\mathcal{I}^+$ at large r. We can now rewrite expression (9.13) in terms of a generic vector ξ^i transverse to $\mathcal{S}_{u,r}$ (*i.e.,* with a generically non-vanishing component along the normal to $\mathcal{S}_{u,r}$), so that the component of the flux of Bondi linear momentum along ξ^i is

$$\frac{dP^{\rm B}[\xi]}{dt}(t) = \lim_{r\to\infty} \frac{r^2}{16\pi} \oint_{\mathcal{S}_{t,r}} (\xi^i s_i) \left| \int_{-\infty}^{t} \Psi_4(t',\Omega) dt' \right|^2 d\Omega \,. \tag{9.14}$$

We take this expression as the starting point for the construction of $\tilde{K}_i^{\rm eff}$. It provides the functional form of the Bondi linear momentum flux in terms of the relevant component of the Riemann tensor at $\mathcal{I}^+$, namely Ψ_4. Then, the two above-mentioned guidelines for the construction of $\tilde{K}_i^{\rm eff}$ can be met by considering a heuristic substitution of Ψ_4 by ${}^2R$ in expression (9.14).

It is important to note that in the same way in which the outgoing null coordinate u parameterizes naturally $\mathcal{I}^+$, the ingoing null coordinate v, which runs along $\mathcal{I}^-$, is a natural label to parameterize the horizon $\mathcal{H}^+$. However, within our $3+1$ setting, we use equation (9.14) as the Ansatz leading to the following proposal for the component $\tilde{K}_{\rm eff}[\xi](t)$ of $\tilde{K}_i^{\rm eff}(t)$ along a vector ξ^i (tangent to the slice Σ_t) transverse to the section $\mathcal{S}_t$ of $\mathcal{H}^+$

$$\tilde{K}^{\rm eff}[\xi](t) \equiv -\frac{1}{16\pi} \oint_{\mathcal{S}_t} (\xi^i s_i) \left| \tilde{\mathcal{N}}(t,\Omega) \right|^2 dA \,, \tag{9.15}$$

with

$$\tilde{\mathcal{N}}(t,\Omega) \equiv \int_{t_c}^{t} {}^2R(t',\Omega)dt' + \tilde{\mathcal{N}}^{t_c}(\Omega)\,. \tag{9.16}$$

In the equations above, dA is the area element of $\mathcal{S}_t$, the global negative sign accounts for the relative change of the orientation of outgoing vector normal to inner and outer boundary spheres, s^i are the components of the unit normal vector to $\mathcal{S}_t$ tangent to Σ_t, and $\tilde{\mathcal{N}}^{t_c}(\Omega)$ is a generic function on the surface to be fixed.

Some remarks are in order concerning expressions (9.15) and (9.16). First, there is a clear asymmetry between expressions (9.14) and (9.15) when substituting the complex quantity Ψ_4 at $\mathcal{I}^+$ (encoding two independent modes corresponding to the gravitational wave polarizations) by the real quantity ${}^2R$ on the inner horizon (a single dynamical mode). Inspection of equation (9.14) immediately suggests an alternative to ${}^2R$ by the natural inner boundary analogue of Ψ_4, *i.e.,* Ψ_0. However, this strategy must face the issue of identifying an appropriate null tetrad at $\mathcal{H}^+$ for the very construction of Ψ_0. Second, the lower limit in the time integration, $t \to -\infty$, appearing in equation (9.14) must be replaced by the time t_c of first appearance of the common horizon, when quantities as ${}^2R(t,\Omega)$ start to be well defined. However, there is still a deeper difference between $\mathcal{N}(t,\Omega)$ and $\tilde{\mathcal{N}}(t,\Omega)$. Even though one can construct the former as in equation (9.12), *i.e.,* as the time integral of Ψ_4, the definition of the news function is local in time depending only on quantities on $\mathcal{S}_t$ and not requiring the knowledge of the past history of $\mathcal{H}^+$. The latter though is here defined as the time integral of ${}^2R$ and there is no reason to expect the same local-in-time behavior, specially as $t \to \infty$. Therefore, we fix the function $\tilde{\mathcal{N}}^{t_c}(\Omega)$ by imposing $\lim_{t\to\infty} \tilde{\mathcal{N}}(t,\Omega) = 0$.

All the points raised above are addressed in detail in the second part of this chapter and we adopt here a purely effective approach to $\tilde{K}^i_{\rm eff}(t)$, since ${}^2R$ represents an unambiguous geometric object that captures the (possibly many, if matter is included) relevant dynamical degrees of freedom in a single effective mode. Ultimately, this heuristic proposal for the effective curvature is acceptable only as long as it can be correlated with $dP^{\rm B}_i/dt$, and this is what we will show in the following.

9.2.3.1 Axisymmetric black-hole spacetimes

As a first application of the Ansatz (9.15), we consider the axisymmetric case of the head-on collision of two black holes with unequal masses. We adopt therefore a coordinate system (r,θ,φ) adapted to the horizon $\mathcal{H}^+$ so that $r =$ const. characterizes sections $\mathcal{S}_t$ and we can write $s_i = MD_ir$, with $M^{-2} = D_irD^ir$ (*i.e.,* $M^{-2} = \gamma^{rr}$). Then, taking advantage of the axisymmetry, we adopt on $\mathcal{S}_t$ the preferred coordinated system $(\tilde{\theta},\tilde{\varphi})$ discussed in section 9.2.1 and consider the Cartesian-like coordinates constructed from $(r,\tilde{\theta},\tilde{\varphi})$ by standard spherical coordinates relations: $x = r\sin\tilde{\theta}\cos\tilde{\varphi}, y = r\sin\tilde{\theta}\sin\tilde{\varphi}, z = r\cos\tilde{\theta}$. In these coordinates we have $s_i = M(\sin\tilde{\theta}\cos\tilde{\varphi}, \sin\tilde{\theta}\sin\tilde{\varphi}, \cos\tilde{\theta})$. Assuming the z-axis to be adapted to the axisymmetry, we choose ξ^i in equation (9.15) as $(\xi_z)^i = M^{-1}(\partial_z)^i$, so that $(\xi_z)^i s_i = \cos\tilde{\theta}$. Inserting expression (9.10) in equa-

tions (9.15) and (9.16) we obtain

$$\begin{aligned}\tilde{K}_z^{\rm eff}(t) &\equiv \tilde{K}^{\rm eff}[\xi_z](t) = \\ &= -\frac{1}{16\pi}\oint_{\mathcal{S}_t}(\cos\tilde{\theta})\left(\sum_{\ell=0}^{\infty}\tilde{\mathcal{N}}_\ell(t')Y_{\ell,0}(\tilde{\theta})dt'\right)^2 dA,\end{aligned} \tag{9.17}$$

with

$$\tilde{\mathcal{N}}_\ell(t) \equiv \int_{t_c}^{t} dt' \tilde{I}_\ell(t') + \tilde{\mathcal{N}}_\ell^{t_c}\ , \tag{9.18}$$

being the coefficients of a multipolar expansion of equation (9.16). Inserting the form $dA = R_{\rm H}^2 \sin\tilde{\theta} d\tilde{\theta} d\tilde{\varphi}$ of the area element on $\mathcal{S}_t$ and performing the angular integration we finally find

$$\tilde{K}_z^{\rm eff}(t) \equiv -\frac{R_{\rm H}^2}{16\pi}\sum_{\ell=2}\tilde{\mathcal{N}}_\ell\left(D^{(0)}_{\ell,0}\tilde{\mathcal{N}}_{\ell-1} + D^{(0)}_{\ell+1,0}\tilde{\mathcal{N}}_{\ell+1}\right)\ , \tag{9.19}$$

with

$$D^{(0)}_{\ell,0} \equiv \frac{\ell}{\sqrt{(2\ell+1)(2\ell-1)}}\,. \tag{9.20}$$

As for the definition of $K_{\rm eff}$ in the Robinson-Trautman case, equation (9.19) is quadratic in the (geometric) mass multipoles, *i.e.,* the spherical harmonic components of the intrinsic curvature Ricci scalar curvature ${}^2R$, although it involves a time integration. Also, it is an odd function under reflection with respect to $z =$ const. planes and it involves only products of odd and even multipoles, precisely one of the criteria for the construction of $K_{\rm eff}$ leading to the Ansatz in equation (9.1)[1]. In essence, expression (9.19) for $\tilde{K}_z^{\rm eff}$ fulfills the two basic requirements for the curvature parameter $K_{\rm eff}$ with the added value that it is fully general and no phenomenological parameters need to be fitted. An additional and crucial feature is that terms involving $\ell = 0, 1$ are absent, due to the vanishing[2] of $\tilde{I}_1$ as discussed after equation (9.10).

The quantity $\tilde{K}_z^{\rm eff}$ at the horizon $\mathcal{H}^+$ is to be correlated with the component $(dP_z^{\rm B}/dt)(t)$ of the flux of Bondi linear momentum at $\mathcal{I}^+$, which is useful to express in its multipolar expansion. First, we decompose Ψ_4 in its multipoles

$$\Psi_4 = \sum_{\ell\geq 2, m\leq|\ell|}\Psi_4^{\ell,m}\,{}_{-2}Y^{\ell,m}(\theta,\varphi)\,, \tag{9.21}$$

where ${}_{-2}Y^{\ell,m}(\theta,\varphi)$ are the spin-weighted $s=-2$ spherical harmonics. The explicit expression for the component of $(dP_i^{\rm B}/dt)(t)$ along the z-axis (*e.g.,* Ref. [229]) then becomes

$$\frac{dP_{\rm B}^z}{dt}(t) = \lim_{r\to\infty}\frac{r^2}{16\pi}\sum_{\ell\geq 2, m\leq|\ell|}\mathcal{N}^{\ell,m}\times\left(C^{(-2)}_{\ell,m}\bar{\mathcal{N}}^{\ell,m} + D^{(-2)}_{\ell,m}\bar{\mathcal{N}}^{\ell-1,m} + D^{(-2)}_{\ell+1,m}\bar{\mathcal{N}}^{\ell+1,m}\right), \tag{9.22}$$

[1] Note that expression (9.19) cannot be factorized as a product of even and odd functions, as proposed in (9.1).

[2] Neither the function $\tilde{\mathcal{N}}^{t_c}(\Omega)$ in equation (9.16) introduces $\ell = 1$ modes.

with

$$\mathcal{N}^{\ell,m} \equiv \int_{-\infty}^{t} dt' \Psi_4^{\ell,m} \tag{9.23}$$

being the corresponding multipolar components of the news functions introduced in (9.12), with the coefficients $C_{\ell,m}^{(-2)}$ and $D_{\ell,m}^{(-2)}$ given by

$$C_{\ell,m}^{(-2)} \equiv \frac{2m}{\ell(\ell+1)}\,, \tag{9.24}$$

$$D_{\ell,m}^{(-2)} \equiv \frac{1}{\ell}\sqrt{\frac{(\ell-2)(\ell+2)(\ell-m)(\ell+m)}{(2\ell-1)(2\ell+1)}}\,. \tag{9.25}$$

The axisymmetric reduction of expression (9.22) is obtained by setting $m = 0$ in the expressions above. Note that Ψ_4 is purely real in this case[1]. The resulting coefficients are therefore

$$C_{\ell,0}^{(-2)} = 0\,, \tag{9.26}$$

$$D_{\ell,0}^{(-2)} = \sqrt{\frac{(\ell-2)(\ell+2)}{(2\ell-1)(2\ell+1)}}\,, \tag{9.27}$$

and we can write equation (9.22) as

$$\frac{dP_z^{\rm B}}{dt}(t) = \lim_{r\to\infty}\frac{r^2}{16\pi}\sum_{\ell\geq 2}\int_{-\infty}^{t} dt' \Psi_4^{\ell,0}\int_{-\infty}^{t} dt''\left(D_{\ell,0}^{(-2)}\Psi_4^{\ell-1,0} + D_{\ell+1,0}^{(-2)}\Psi_4^{\ell+1,0}\right). \tag{9.28}$$

Expression (9.28) has obvious similarities with equation (9.19) for $\tilde{K}_z^{\rm eff}(t)$. First, the (real) modes $\Psi_4^{\ell,0}$ play a role analogous to those of the mass multipoles $\tilde{I}_\ell$. The common geometric nature of the underlying quantities Ψ_4 and ${}^2R$ as curvatures, in particular their dimensions as second derivatives of the metric, is indeed at the heart of the definition of the geometric multipoles $\tilde{I}_\ell$'s by equations (9.9) and (9.10) as the correct analogues of $\Psi_4^{\ell,0}$. Second, modes $\ell = 0, 1$ are absent in both expressions. This is nontrivial since the reasons underlying each case are different: the $s = 2$ spin-weight of Ψ_4 in equation (9.28) and the vanishing of $\tilde{I}_1$ in (9.19), respectively. This is a crucial feature for its directly impacts the determination of the mode dominating the dynamical behavior and, therefore, singles out the Ricci scalar ${}^2R$ as a preferred quantity to be monitored instead of any other (spin-weighted $s \neq 2$) function that could measure in some way the deformations of the horizon (for instance, the mean curvature). Besides the similarities, there are also differences between expressions (9.28) and (9.19). First, the coefficients $D_{\ell,0}^{(s)}$ in (9.20) and (9.26) differ due to the different spin-weight of ${}^2R$ and Ψ_4. Therefore, the correlation between $(dP_z^{\rm B}/dt)(t)$ and $\tilde{K}_i^{\rm eff}$ encodes information

[1]For instance, the gravitational wave cross polarization $h_\times$ vanishes: $\Psi_4 = -\ddot{h}_+ + i\ddot{h}_\times$.

about the relative weight of the different couplings. Second, the lower time-integration bound ($t \to -\infty$) is well-defined for $(dP_z^{\rm B}/dt)(t)$, whereas $\tilde{K}_z^{\rm eff}(t)$ can be measured only after the formation of the common horizon. Finally, due to the absence in the general case of a preferred coordinate system on $\mathcal{S}_t$ and their associated spherical harmonics, there is no natural multipolar expression for $\tilde{K}_i^{\rm eff}$ in the non-axisymmetric case and one must resort to the full expression (9.15).

9.2.4 Correlation between the screens

The effective curvature vector $\tilde{K}_i^{\rm eff}$ introduced in previous Section can now to be used as a probe of the degree of correlation between the geometry at the horizon and the geometry far from the black hole. More specifically, we aim at assessing the correlation between $h_{\rm inn}(t) = \tilde{K}_z^{\rm eff}(t)$ at the horizon and $h_{\rm out}(t) = (dP_z^{\mathcal{B}}/dt)(t)$ at large distances, considering these two quantities as timeseries. As discussed in section 9.1, the use of a common time variable t for functions $h_{\rm inn}$ and $h_{\rm out}$ assumes a (gauge) mapping (*cf.* footnote 2 in section 9.1) between the advanced v and retarded u times, parameterizing $\mathcal{H}^+$ and $\mathcal{I}^+$, respectively. The $3+1$ slicing by hypersurfaces $\{\Sigma_t\}$ provides such a mapping, though an intrinsic time-stretching ambiguity between the signals at the two screens is present, due to the gauge nature of the slicing. This will be discussed in more detail later in this section.

To quantify the similarities in the timeseries we employ the correlation function between timeseries $h_1(t)$ and $h_2(t)$, $\mathcal{C}(h_1, h_2; \tau)$, defined as

$$\mathcal{C}(h_1, h_2; \tau) = \int_{-\infty}^{\infty} h_1(t+\tau) h_2(t) dt \,. \tag{9.29}$$

The structure of $\mathcal{C}(h_1, h_2; \tau)$ encodes a quantitative comparison between the two timeseries as a function of the time-shift τ (referred to as "lag") between them. This correlation function encodes the frequency components held in common between h_1 and h_2 and provides crucial information about their relative phases. Because the timeseries are intrinsically different by a time lag, we measure the correlation between h_1 and h_2 as

$$\mathcal{M}(h_1, h_2) = \max_{\tau} \left(\frac{\mathcal{C}(h_1, h_2; \tau)}{[\mathcal{C}(h_1, h_1; 0)\, \mathcal{C}(h_2, h_2; 0)]^{\frac{1}{2}}} \right) \,. \tag{9.30}$$

This number is confined between 0 and 1 (where 1 indicates perfect correlation, and 0 no correlation at all) and provides the maximum matching between the timeseries h_1 and h_2 obtained by shifting one with respect to the other in time, and then normalized in frequency space. Besides providing a measure of the correlation, expression equation (9.30) also gives a quantitative estimate of the coordinate time delay $\tau_{\rm max}$ between the two signals.

Note that one should not expect a perfect match between $(dP_z^{\mathcal{B}}/dt)(t)$ at $\mathcal{I}^+$ and $\tilde{K}_z^{\rm eff}(t)$ at $\mathcal{H}^+$, even if the latter results to be a good estimator of the former. Indeed, (nonlinear) gravitational dynamics in the bulk spacetime affect and distort the possible

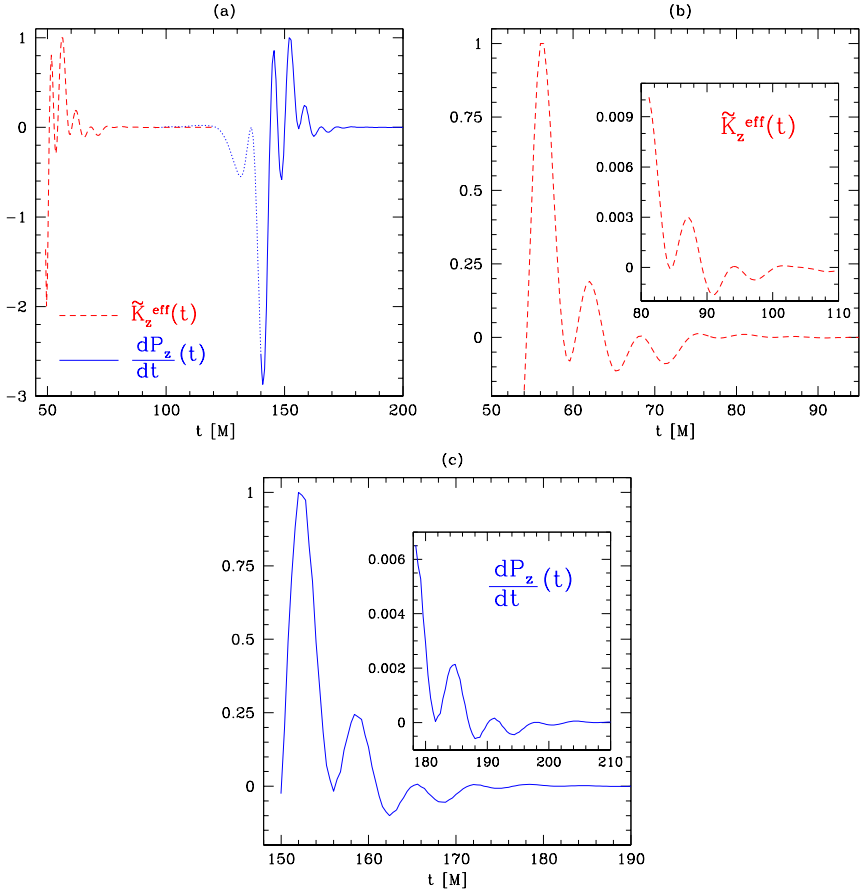

Figure 9.6: Effective curvature $\tilde{K}_z^{\rm eff}$ defined at the horizon via equation (9.15) (red dashed curve) and flux of momentum $(dP_z^{\mathcal{B}}/dt)$ evaluated at an approximation of $\mathcal{I}^+$ with equation (9.11) (blue dotted and solid curves). These quantities encode respectively the information of the common horizon deformation and the flux of momentum carried away by gravitational waves in the head-on collision of black holes with mass ratio 1/2. Note, at panel (a), the qualitative agreement between those curves, which allows us to distinguish the momentum radiated before (blue dotted curve) and after (blue solid curve) the merge. Panel (b) and (c) compares the same quantities for latter times, where one can still see the good agreement.

relation between both quantities. Furthermore, given the related but different nature of ${}^2R$ and Ψ_4 it is not obvious that a correlation should be found at all.

In order to assess the validity of the approach, we construct $\tilde{K}_z^{\rm eff}(t)$ and $(dP_z^{\mathcal{B}}/dt)(t)$ from the numerical simulations described in section 9.2.2. Note that because $\tilde{I}_1$ vanishes identically, the contributions $\tilde{\mathcal{N}}_0\tilde{\mathcal{N}}_1$ and $\tilde{\mathcal{N}}_1\tilde{\mathcal{N}}_2$ are absent in the expression for $\tilde{K}_z^{\rm eff}(t)$. Furthermore, since higher-order multipoles $\tilde{I}_\ell$ become increasingly difficult to calculate, we truncate expression (9.19) at $\ell = 6$; in our case, this has little influence on the overall

results as we will show that the lowest (*i.e.,* $\ell = 2, 3$) modes are by large the dominant ones.

The values for $(dP_z^{\mathcal{B}}/dt)$ and $\tilde{K}_z^{\rm eff}$ as functions of the time t, and corresponding to the numerical simulations described in the previous section 9.2.2, are presented in figure 9.6. The signals have been normalized with respect to their maximum value (a global rescaling does not affect the cross-correlations properties of two functions $h_1(t)$ and $h_2(t)$). In figure 9.6 (a), the quantity $\tilde{K}_z^{\rm eff}$ is shown from the time $t_c \approx 49.2M$ of first appearance of the common horizon (red dashed line). After time $t_{\rm max} \approx 120M$ the error in the calculation of the $\tilde{I}_\ell$ multipoles becomes comparable with the value of the multipoles, spoiling the evaluation of the integrals in (9.18). Hence, we set $\tilde{K}_z^{\rm eff}$ to zero for $t > t_{\rm max}$. Similarly, the flux of Bondi linear momentum $(dP_z^{\mathcal{B}}/dt)$ as computed by an observer at $100\,M$ from the origin, is split in a part before the appearance of the common apparent horizon (blue dotted line) and in one which is to be compared with $\tilde{K}_z^{\rm eff}$ (blue dashed line). In panels (b) and (c) of figure 9.6 we show instead $\tilde{K}_z^{\rm eff}$ and $(dP_z^{\mathcal{B}}/dt)$ separately and in different time intervals for a better emphasis of the similarities.

Some interesting remarks on figure 9.6 can be made already at a qualitative level. In particular, it is clear that $\tilde{K}_z^{\rm eff}$ succeeds in tracking key features of $(dP_z^{\mathcal{B}}/dt)$. This is apparent in the relative magnitude of the three first positive peaks in the two signals and the qualitative agreement is maintained in time. As expected, some specific features of $(dP_z^{\mathcal{B}}/dt)$ are not faithfully captured in $\tilde{K}_z^{\rm eff}$, such as the magnitude of the negative peak around $t \approx 148M$ relative to the neighbouring peaks. However given the heuristic character of $\tilde{K}_z^{\rm eff}$ and the fact that its geometric definition does not leave room for any tuning, the overall qualitative agreement with $(dP_z^{\mathcal{B}}/dt)$ at $\mathcal{I}^+$ already represents a remarkable result, shedding light on the near-horizon dynamics. This agreement between $(dP_z^{\mathcal{B}}/dt)$ and $\tilde{K}_z^{\rm eff}$ is indeed the main result of this section and the ultimate justification for the introduction of $\tilde{K}_z^{\rm eff}$. It is also worth stressing that attempts employing other quantities (*e.g.,* a blind application of the methods used for Robinson-Trautman spacetimes) would not lead to such a clear matching.

From a quantitative point of view, the correlation analysis for the time intervals shown in figure 9.6 (b) and (c) indicates that the two signals yield a typical correlation $\mathcal{M} \approx 0.93$ and a time lag $\tau = 97M$ (we recall that the observer is at $100\,M$ and that the common apparent horizon has the size of a couple of M). However, as one tries to extend the analysis to the very first time of the formation of the apparent horizon, the correlation drops significantly. The reason for this drop is related to the stretching of the time coordinate between the two screens. In addition to the obvious time delay between the $(dP_z^{\mathcal{B}}/dt)(t)$ and $\tilde{K}_z^{\rm eff}(t)$ due to the finite (coordinate) speed of light, in fact, the dependence of the two signals in coordinate time t is not the same and is stretched between the two screens. This effect is the result of the in-built gauge mapping between sections of $\mathcal{I}^+$ and the horizon $\mathcal{H}^+$ defined by the spacetime slicing, but also of the physical blueshift (redshift) of signals at the inner (outer) boundaries in the black-hole spacetime.

Although approaches to disentangle the physical and gauge contributions can be

derived, for instance by introducing proper-times of suitably-defined observers, this goes beyond what we choose o present. Rather, we opt here for a more straightforward approach in which only comparisons based on sequences of (absolute values and signs of the) maxima and minima in the signals $h_{\rm inn}(t)$ and $h_{\rm out}(t)$ are considered significant, since the relative shape of $h_{\rm inn}(t)$ and $h_{\rm out}(t)$ can be subject to a time reparametrization. This association is possible when the quantities which are compared are scalars, so that the values of maxima and minima are well defined and independent of coordinates. This is possible in the case of axisymmetry as it gives a privileged direction along which to contract the effective curvature vector $\tilde{K}_i^{\rm eff}$. In a more generic configuration one would need to build an appropriate frame to produce scalars by contraction with tensorial quantities. Once the correspondence between maxima and minima in the two signals $h_{\rm inn}(t)$ and $h_{\rm out}(t)$ is established, a mapping $t_{\rm out} = t_{\rm out}(t_{\rm inn})$ can be easily constructed. With this matching, the calculation of the correlation parameter gives typically values $\mathcal{M} \geqslant 0.9$ for any chosen time interval [1].

It is worth stressing that while the very high matching numbers found between the two quantities (*i.e.,* $\mathcal{M} \geqslant 0.9$) are already a strong indication of the correlation between the two screens, no tuning is possible to increase such a correlation. In fact, if the sequences of maxima and minima in the two signals do not correspond to each other "naturally", it is virtually impossible to obtain a good matching. At the same time, however, it is also true that the nature of the signals is such that the first couple of maxima and minima play a dominant role in the estimate, possibly shadowing the role of the smaller peaks appearing at later times. To address this point and weight equally all parts of the signals, we model them as exponentially decaying periodic functions, *i.e.,* $h^\kappa_{\rm inn}(t) \equiv e^{\kappa_{\rm inn} t} h_{\rm inn}(t)$ and $h^\kappa_{\rm out}(t) \equiv e^{\kappa_{\rm out} t} h_{\rm out}(t)$, finding

$$\kappa_{\rm inn} = 0.179 \pm 0.005\,, \qquad \kappa_{\rm out} = 0.181 \pm 0.006\,, \tag{9.31}$$

through a least-square fitting. The resulting functions $h^\kappa_{\rm inn}(t)$ and $h^\kappa_{\rm out}(t)$ after the exponential decay has been subtracted are shown in figure 9.7. Once again it is apparent that the two timeseries are very similar and indeed the matching computed even without introducing any time mapping is $\mathcal{M}(h^\kappa_{\rm inn}, h^\kappa_{\rm out}) = 0.87$ and thus remarkably high.

The main reason behind the good correlation also of the undamped signals is that the next-to-leading-order term, *i.e.,* term $\tilde{\mathcal{N}}_3\tilde{\mathcal{N}}_4$ and the corresponding $\ell = 3$ and $\ell = 4$ coupling in equation (9.28), are much smaller than the leading-order term $\mathcal{N}_2\mathcal{N}_3$. Indeed, we have found that it is possible to express to a very good approximation $\tilde{K}_z^{\rm eff} \approx \tilde{\mathcal{N}}_2\tilde{\mathcal{N}}_3$ and $(dP_z^{\mathcal{B}}/dt) \approx \mathcal{N}_2\mathcal{N}_3$. This is confirmed by the corresponding power spectra, which are shown in figure 9.8 and are dominated in both cases by two frequencies: $\Omega_1^{\rm inn} = 0.22 \pm 0.04$, $\Omega_2^{\rm inn} = 0.98 \pm 0.05$ for the signal $h_{\rm inn}(t)$, and $\Omega_1^{\rm out} = 0.22 \pm 0.04$, $\Omega_2^{\rm out} = 0.97 \pm 0.04$ for the signal $h_{\rm out}(t)$.

[1] Interesting information can also be gained by studying in more detail the properties of the mapping $t_{\rm out} = t_{\rm out}(t_{\rm inn})$. More specifically, we have found that the derivative $dt_{\rm out}/dt_{\rm inn}$ is not constant and starts as being larger than unity (indicating that initially the coordinate time at $\mathcal{I}^+$ runs faster than the time at $\mathcal{H}^+$), but then oscillates around unity at late times. This is consistent with the fact that as stationarity is approached, the evolution vector t^a adapts to the time-like Killing vector.

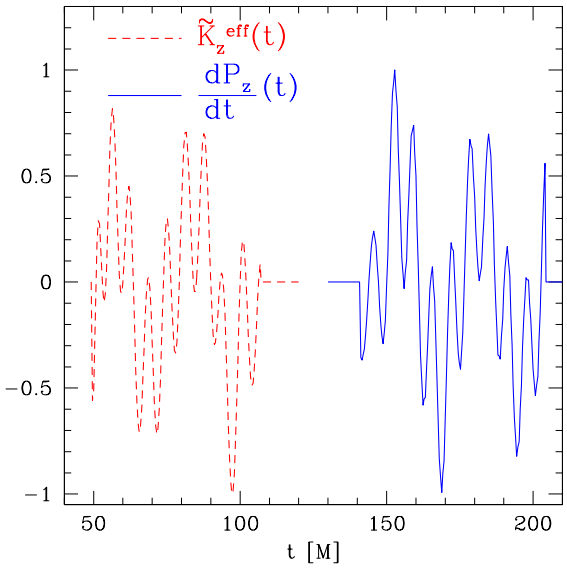

Figure 9.7: Quantities on $\mathcal{H}^+$ (red dashed line) and $\mathcal{I}^+$ (blue solid line) as shown in figure 9.6 but without an overall exponential decay in time. The close similarity in the signals is confirmed by the very large correlation which is $\mathcal{M} = 0.87$, obtained without a time mapping.

These frequencies are closely related to the quasi-normal modes of the merged black hole, interfering to lead to a beating signal. To see this, we model each function $\tilde{\mathcal{N}}_\ell$ and $\mathcal{N}_\ell$ as an exponentially damped sinusoid, *i.e.*, $\tilde{\mathcal{N}}_\ell \sim e^{-\kappa_\ell^{\tilde{\mathcal{N}}} t}\sin(\Omega_\ell^{\tilde{\mathcal{N}}} t + \varphi^{\tilde{\mathcal{N}}})$ and $\mathcal{N}_\ell \sim e^{-\kappa_\ell^{\mathcal{N}} t}\sin(\Omega_\ell^{\mathcal{N}} t + \varphi^{\mathcal{N}})$. Then, under the approximation $\tilde{K}_z^{\rm eff} \approx \tilde{\mathcal{N}}_2\tilde{\mathcal{N}}_3$ and $(dP_z^{\mathcal{B}}/dt) \approx \mathcal{N}_2\mathcal{N}_3$ it follows

$$\Omega_{\ell=2}^{\tilde{\mathcal{N}}} = \frac{\Omega_2^{\rm inn} - \Omega_1^{\rm inn}}{2}\,, \quad \Omega_{\ell=3}^{\tilde{\mathcal{N}}} = \frac{\Omega_2^{\rm inn} + \Omega_1^{\rm inn}}{2}\,, \tag{9.32}$$

at $\mathcal{H}^+$, whereas

$$\Omega_{\ell=2}^{\mathcal{N}} = \frac{\Omega_2^{\rm out} - \Omega_1^{\rm out}}{2}\,, \quad \Omega_{\ell=3}^{\mathcal{N}} = \frac{\Omega_2^{\rm out} + \Omega_1^{\rm out}}{2}\,, \tag{9.33}$$

at $\mathcal{I}^+$, consistent with the "beating" behaviour shown by the power spectra in figure 9.8. Similarly, the decay timescales are then given by

$$\kappa_{\rm inn} = \kappa_{\ell=2}^{\tilde{\mathcal{N}}} + \kappa_{\ell=3}^{\tilde{\mathcal{N}}} \quad , \quad \kappa_{\rm out} = \kappa_{\ell=2}^{\mathcal{N}} + \kappa_{\ell=3}^{\mathcal{N}}. \tag{9.34}$$

These frequencies and timescales match very well the real ($\omega_\ell^{\rm R}$) and imaginary ($\omega_\ell^{\rm I}$) parts of the fundamental ($n = 0$) quasi-normal-modes (QNM) eigenfrequencies of a Schwarzschild black hole [230]. A detailed comparison is presented in Table 9.1, whose first six columns report the properties of the signals $h_{\rm inn}(t)$ and $h_{\rm out}(t)$ in their constituent frequencies $\Omega_{\ell=2,3}^{\mathcal{N}}$ defined in equations (9.32)–(9.33), and compare them with

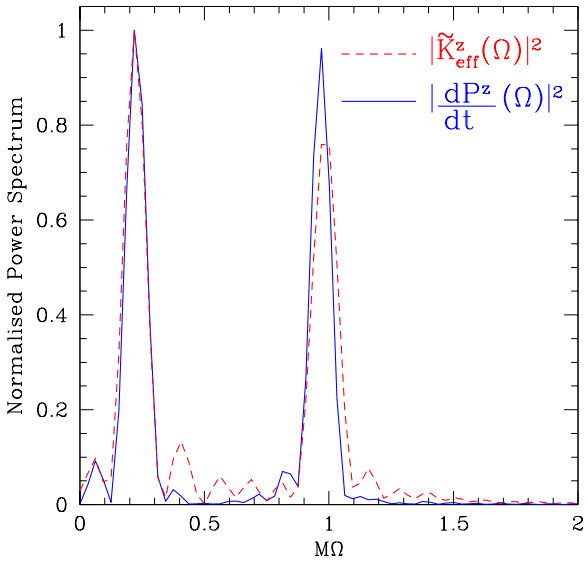

Figure 9.8: Normalized power spectrum for $K_z^{\rm eff}(\Omega)$ (red dashed line) and $(dP_z/dt)(\Omega)$ (blue solid line) as measured at $\mathcal{H}^+$ and $\mathcal{I}^+$, respectively (*cf.* figure 9.7). Both spectra are dominated by two frequencies: $\Omega_1^{\rm inn} = 0.22 \pm 0.04$ and $\Omega_2^{\rm inn} = 0.98 \pm 0.05$ (red dashed line) and $\Omega_1^{\rm out} = 0.22 \pm 0.04$ and $\Omega_2^{\rm out} = 0.97 \pm 0.04$ (blue solid line) which are linear combinations of the quasi-normal ringing modes of the merged black hole (*cf.* Table 9.1).

the corresponding real parts of the eigenfrequencies of a Schwarzschild black hole, $\omega^{\rm R}_{\ell=2,3}$. The close match in the oscillatory part is accompanied also by a very good correspondence in the decaying part of the signal. Defining, in fact, the overall decay time in terms of the imaginary parts of the QNM eigenfrequencies, *i.e.*, as $\kappa_{\rm decay} \equiv \omega_{\rm I}^{\ell=2} + \omega_{\rm I}^{\ell=3}$, it is easy to realize from the last three columns in Table 9.1, that this decay time is indeed very close to the one associated to the signal at the two screens, *i.e.*, equation (9.34).

This role of QNMs is not entirely surprising for a measure at $\mathcal{I}^+$, but it is far less obvious to see it imprinted also for a quantity measured at $\mathcal{H}^+$. This indicates that the bulk spacetime dynamics responsible for the recoil physics is a relatively mild one, so that a QNM ringdown behaviour dominates the dynamics of the deformed single apparent horizon and imprints the properties of the radiated linear momentum. It is interesting that a purely (quasi-)local study of the apparent horizon geometric properties permits to read the behaviour of quantities which are intrinsically defined at infinity, thus confirming the main thesis in [214].

As a concluding remark for this section, we make use of our results, and in particular on the spectral and decaying properties of our measures on the screens, to make contact with the analysis carried out in [213]. More specifically, we can define a characteristic decay time $\tau \equiv (2\pi)/\kappa^{\rm inn/out}$ and an oscillation characteristic time $T \equiv 2\pi/\Omega_1^{\rm inn/out}$,

Table 9.1: The first six columns offer a comparison between the properties of the signals $h_{\rm inn}(t)$ and $h_{\rm out}(t)$ in their constituent frequencies $\Omega^{\rm N}_{\ell=2,3}$ defined in equations (9.32)–(9.33), with the corresponding real parts of the eigenfrequencies of a Schwarzschild black hole, $\omega^{\rm R}_{\ell=2,3}$. The last three columns show instead a comparison between the damping times $\kappa_{\rm inn,out}$ defined in equation (9.34), with the corresponding decay time $\kappa_{\rm decay}$ computed from the imaginary parts of the eigenfrequencies. In all cases, the close match is remarkable and not at all obvious for quantities measured at $\mathcal{H}^+$.

$M\Omega^{\rm N}_{\ell=2}$	$M\Omega^{\hat{\rm N}}_{\ell=2}$	$M\omega^{\rm R}_{\ell=2}$	$M\Omega^{\rm N}_{\ell=3}$	$M\Omega^{\hat{\rm N}}_{\ell=3}$	$M\omega^{\rm R}_{\ell=3}$	$M\kappa_{\rm inn}$	$M\kappa_{\rm out}$	$M\kappa_{\rm decay}$
0.38 ± 0.04	0.37 ± 0.04	0.37367	0.60 ± 0.04	0.59 ± 0.04	0.59944	0.181 ± 0.006	0.179 ± 0.005	0.18166

from which to build our equivalent of the *"slowness parameter"* $P \equiv T/\tau$ introduced in [213]. The specific case discussed above then yields $\tau \simeq 34.9M$, $T \simeq 28.6M$ and thus $P \simeq 0.82$. As detailed in [213], small antikicks should happen when the two timescales are comparable, *i.e.,* for $P \lesssim 1$, thus corresponding to an oscillation which is over-damped. This expectation is indeed confirmed by the recoil velocity shown in figure 9.4, where the relative antikick is only $\sim 30\%$ and thus compatible with the slowness parameter that we have associated to our process. This qualitative agreement with the phenomenological approach discussed in [213] is very natural. While we here concentrate on modeling the local curvature properties at the horizon, [213] concentrates on the spectral features of the signal at large distances. Since we have demonstrated that the two are highly correlated, it does not come to a surprise that the two phenomenological approaches are compatible. Looking at the local horizon's properties has however the added value that it provides a precise framework in which to predict not only the strength of the antikick, but also its directionality. Furthermore, such an approach permits an interpretation of black-hole dynamics in terms of viscous hydrodynamics, as we will discuss in detail in section 9.4 . In particular, we shall show there that the horizon viscous analogy naturally leads to a geometric prescription for an (instantaneous) slowness parameter P, in terms of timescales τ and T respectively related to bulk and shear viscosities.

The logic developed above for the calculation of the slowness parameter can be brought a step further by assuming that the final black hole produced by the merger of a binary system in quasi-circular orbit can be described at the lowest order by an oscillation and decay times

$$\tau \equiv \frac{2\pi}{\omega^{\rm I}_{\ell=2} + \omega^{\rm I}_{\ell=3}}\,, \qquad T \equiv \frac{2\pi}{\omega^{\rm R}_{\ell=3} - \omega^{\rm R}_{\ell=2}}\,, \tag{9.35}$$

to which corresponds a slowness parameter defined as

$$P \equiv \frac{T}{\tau} = \frac{\omega^{\rm I}_{\ell=2} + \omega^{\rm I}_{\ell=3}}{\omega^{\rm R}_{\ell=3} - \omega^{\rm R}_{\ell=2}}\,. \tag{9.36}$$

Using the semi-analytic expressions derived for estimating the spin of the final black hole, *e.g.,* [231, 232, 233], it is possible to predict the values of τ and T for any binary whose initial spins and masses are known, and thus predict qualitatively through P the strength of the antikick which will be produced in any of these configurations. We have tested this idea by considering the data presented in Ref. [202] both for the kick/antikick velocities and for the final spin of the merged black hole. This conjecture about the predictability of the antikick in terms of the slowness parameter is indeed supported by the example data collected in figure 9.9. More specifically, the left panel in figure 9.9 shows the correlation between the slowness parameter $P = T/\tau$ as computed in equation (9.36) and the dimensionless spin of a black hole $a_{\rm fin}$ produced, for example, in the merger of a binary system (expressions to estimate the QNM eigenfrequencies for rotating black holes can be found in a number of works which are collected in the review [230]). The mid panel shows instead the good correlation between the relative antikick velocity $\Delta v/v_{\rm fin} \equiv (v_{\rm max} - v_{\rm fin})/v_{\rm fin} = v_{\rm k}/v_{\rm fin}$ and the dimensionless final spin as computed from the data taken from [202] (indicated with error bars are the estimated numerical errors). Finally, the right panel combines the first two and shows the correlation between the antikick velocity and the slowness parameter. All in all, this figure confirms also for the case of binaries in quasi-circular orbits the suggestion [213] that the smaller the slowness parameter P gets, the larger is the expected value of the antikick. Large antikicks should then be expected for $P \ll 1$ [213]. Furthermore, it highlights that it is indeed possible to predict qualitatively the antikick merely on the basis of the initial properties of the black holes when the binary is still widely separated.

9.3 Conclusions

We have demonstrated that qualitative aspects of the post-merger recoil dynamics at infinity can be understood in terms of the evolution of the geometry of the common horizon of the resulting black hole. This extends to binary black-hole spacetimes the conclusions presented in [214] based on Robinson-Trautman spacetimes. More importantly, we have shown that suitably-built quantities defined on inner and outer world-tubes (represented either by dynamical horizons or by time-like boundaries) can act as test screens responding to the spacetime geometry in the bulk, thus opening the way to a cross-correlation approach to probe the dynamics of spacetime.

The extension presented here is however nontrivial and it involves the construction of a phenomenological vector $\tilde{K}_i^{\rm eff}(t)$ from the Ricci curvature scalar ${}^2R$ on the dynamical horizon sections, which then captures the global properties of the flux of Bondi linear momentum $(dP_i^{\rm B}/dt)(t)$ at infinity, namely (proportional to) the acceleration of the black hole. At the same time, the proposed approach involves the development of a cross-correlation methodology which is able to compensate for the in-built gauge character of the time evolution on the two surfaces. A proper mapping between the times on the two surfaces is needed and its gauge nature highlights that the physical information encoded in the surface quantities is not in its *local* (arbitrary) time dependence, but rather in the *global* structure of successive maxima and minima.

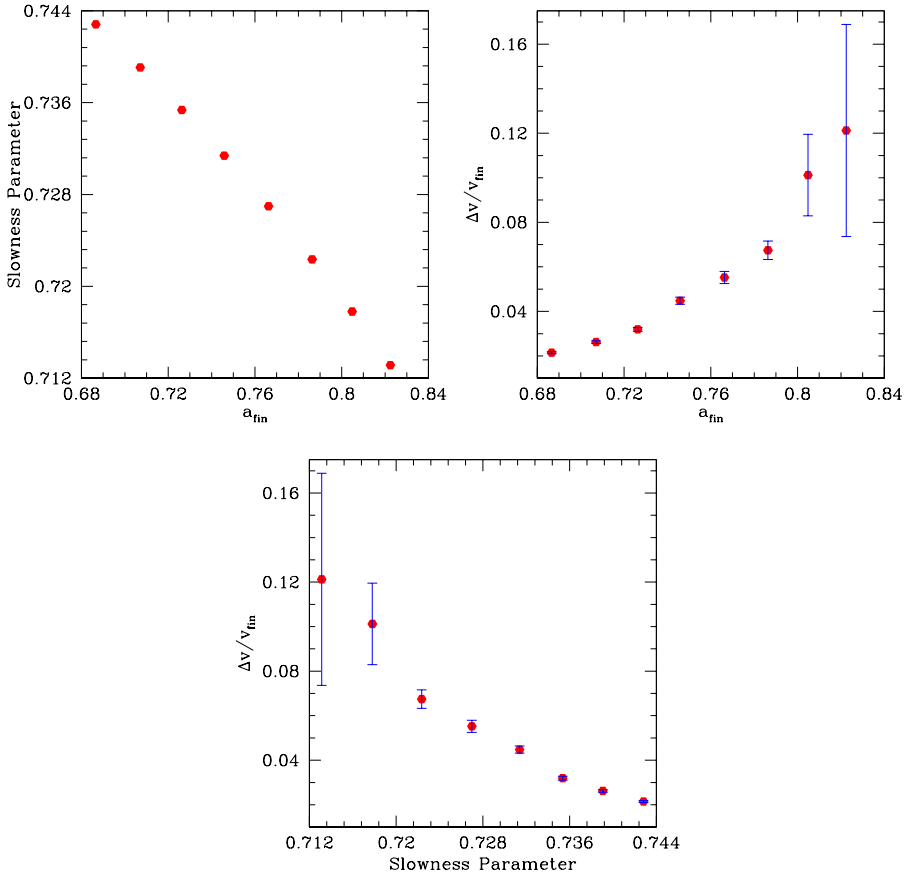

Figure 9.9: Predictability of the antikick in terms of the slowness parameter and the antikick. The left panel shows the correlation between the slowness parameter $P = T/\tau$ as computed in equation (9.36) and the dimensionless spin of a black hole $a_{\rm fin}$. The mid panel shows instead the good correlation between the relative antikick velocity $\Delta v/v_{\rm fin} = v_{\rm k}/v_{\rm fin}$ and the dimensionless final spin, using the data taken from [202] (indicated with error bars are the estimated numerical errors). Finally, the right panel combines the first two and shows the correlation between the antikick velocity and the slowness parameter.

By analyzing Robinson-Trautman spacetimes, [214] proposed that when a single horizon is formed during the merger of two black holes, the observed decelerations/accelerations of the newly formed black hole can be understood in terms of the dissipation of an anisotropic distribution of the Ricci scalar curvature on the horizon. The results presented here confirm this picture, although through quantities which are suited to black-hole spacetimes. Being computed on the horizon, these quantities reflect the properties of the black hole and in particular its exponentially damped ringing. The timescales associated with this process, which are inevitably imprinted in our geometric variables, provide also a natural connection with the approach discussed in Ref. [213],

where the antikick is explained in terms of the spectral features of the signal at large distances. Because we have shown that the latter is closely correlated with the signal at the horizon, we can adopt the same slowness parameter introduced in Ref. [213] to predict qualitatively the magnitude of the antikick from the merger of black-hole binaries with spin aligned to the orbital angular momentum, finding a very good agreement with the numerical data.

As a final remark we note that looking at the horizon's properties has the added value that it provides a precise framework in which to predict not only the strength of the antikick, but also its directionality. Furthermore, our geometric (cross-correlation) framework presents a number of close connections with (and potential implications on) the literature developing around the use of horizons to study the dynamics of black holes, as well as with the interpretations of such dynamics in terms of a viscous hydrodynamics analogy. Much of the machinery developed using dynamical trapping horizons as inner screens can be extended also when a common horizon is not formed (as in the calculations reported in Ref. [212]). While in such cases the identification of an appropriate hypersurface for the inner screen can be considerably more difficult, once this is found its geometrical properties can be used along the lines of the cross-correlation approach discussed here for dynamical horizons.

9.4 Geometry

In the previous sections a *cross-correlation* methodology for studying near-horizon strong-field physics was outlined. Spacetime dynamics was probed through the cross-correlation of timeseries $h_{\rm inn}$ and $h_{\rm out}$ defined as geometric quantities on *inner* and *outer* hypersurfaces, respectively. The latter are understood as *test screens* whose geometries respond to the bulk dynamics, so that the (global) functional structure of the constructed cross-correlations encodes some of the features of the bulk geometry. This is in the spirit of reconstructing spacetime dynamics in an *inverse-scattering* picture. In the context of asymptotically flat black hole (black-hole) spacetimes, the black-hole event horizon $\mathcal{E}$ and future null infinity $\mathcal{I}^+$ provide natural test hypersurfaces from a global perspective. However, when a $3+1$ approach is adopted for the numerical construction of the spacetime, dynamical trapping horizons $\mathcal{H}$ provide more appropriate hypersurfaces to act as inner test screens. In the application of this correlation strategy to the study of black-hole post-merger recoil dynamics, an effective curvature vector $\tilde{K}_i^{\rm eff}(v)$ was constructed [234] on $\mathcal{H}$ as the quantity $h_{\rm inn}$ to be cross-correlated with $h_{\rm out}$, where the latter is the flux of Bondi linear momentum $(dP_i^{\rm B}/du)(u)$ at $\mathcal{I}^+$ (here, u and v denote, respectively, advanced and retarded times[1]). We now explore some geometric structures underlying and extending the heuristic construction in [234] of this effective local probe into black-hole recoil dynamics.

The adaptation of geometric structures and tools from $\mathcal{I}^+$ to black hole horizons is at the basis of important geometric developments in black-hole studies, notably the

[1]Cross-correlation of quantities at $\mathcal{H}$ and $\mathcal{I}^+$ requires the choice of a gauge mapping between the advanced and retarded times u and v.

quasi-local frameworks of isolated and dynamical trapping horizons [221, 222, 223] (see also [235, 236]). In this spirit, the construction of $\tilde{K}_i^{\rm eff}(v)$ on the horizon $\mathcal{H}$ partially mimics the functional structure of the flux of Bondi linear momentum at $\mathcal{I}^+$. In particular, $(dP_i^{\rm B}/du)(u)$ can be expressed in terms of (the dipolar part of) the square of the news function $\mathcal{N}$ on sections of $\mathcal{I}^+$, whereas the definition of $\tilde{K}_i^{\rm eff}(v)$ involves the (dipolar part of the) square of a function $\tilde{\mathcal{N}}$ constructed from the Ricci scalar ${}^2R$ on sections of $\mathcal{H}$. However, the functions $\mathcal{N}$ and $\tilde{\mathcal{N}}$ differ in their spin-weight and, more importantly, they show a different behaviour in time: whereas $\mathcal{N}(u)$ is an object well defined in terms of geometric quantities on time sections $\mathcal{S}_u \subset \mathcal{I}^+$, nothing guarantees this *local-in-time* character of $\tilde{\mathcal{N}}(v)$ [see equation (9.40) below]. The latter is a crucial characteristic of the news function, so that $\tilde{\mathcal{N}}(v)$ cannot be considered as a valid *news-like* function on $\mathcal{H}$.

These structural differences suggest that, in spite of the success of $\tilde{K}_i^{\rm eff}$ in capturing effectively (at the horizon) some qualitative aspects of the flux of Bondi linear momentum (at null infinity), a deeper geometric insight into the dynamics of $\mathcal{H}$ can provide hints for a *refined* correlation treatment. In this context, the specific goals in the following sections: i) to justify the role of $\tilde{K}_i^{\rm eff}$ as an *effective* quantity to be correlated to $(dP_i^{\rm B}/du)$, suggesting candidates offering a refined version; ii) to explore the introduction of a valid news-like function on $\mathcal{H}$, only depending on the geometry of sections $\mathcal{S}_v \subset \mathcal{H}$; iii) to establish a link between the cross-correlation approach in [234] and other approaches to the study of the black-hole recoils based on quasi-local momentum.

This part of this chapter is organized as follows. section 9.5 introduces the basic elements on the inner screen $\mathcal{H}$ geometry and revisits the effective curvature vector developed in the previous sections. Aiming at understanding the dynamics of the latter, a geometric system governing the evolution of the intrinsic curvature along the horizon $\mathcal{H}$ is discussed, making apparent the key driving role of the Weyl tensor. In section 9.6 some fundamental results on dynamical horizons are discussed, in particular a *rigidity structure* enabling a preferred choice of null tetrad on $\mathcal{H}$. Proper contractions of the latter with the Weyl tensor leads in section 9.7 to news-like functions and associated *Bondi-like fluxes* on $\mathcal{H}$ providing refined quantities on the horizon to be correlated with Bondi fluxes at $\mathcal{I}^+$, as well as making contact with quasi-local approaches to black-hole linear momentum. In section 9.9 we emphasize the physical relevance of *internal horizons* when computing fluxes along $\mathcal{H}$ and in section 9.10 our geometric discussion is related to the viscous-fluid analogy of black-hole horizons, providing in particular a geometric prescription for the *slowness parameter* P in [213]. Conclusions are presented in section 9.11. We use a spacetime signature $(-,+,+,+)$, with abstract index notation (first letters, a, b, c..., in Latin alphabet) and Latin mid-alphabet indices, i, j, k..., from space-like vectors. We also employ the standard convention for the summation over repeated indices. All the quantities are expressed in a system of units in which $c = G = 1$.

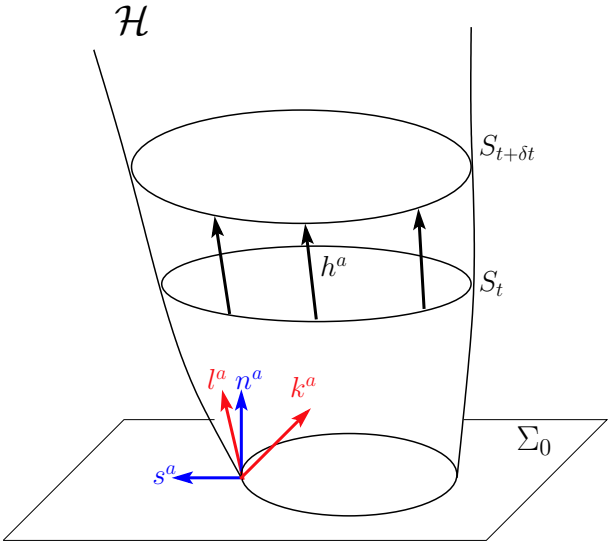

Figure 9.10: Worldtube $\mathcal{H}$ foliated by closed space-like surfaces $\{\mathcal{S}_t\}$ as the result of a $3+1$ space-like foliation $\{\Sigma_t\}$. The evolution vector h^a (tangent to $\mathcal{H}$ and normal to $\{\mathcal{S}_t\}$) transports the slice $\mathcal{S}_t$ to $\mathcal{S}_{t+\delta t}$. The normal plane at each point of $\mathcal{S}_t$ can be spanned by the outgoing and ingoing null normal vectors ℓ^a and k^a or by n^a, the unit time-like normal to Σ_t, and s^a, the space-like outgoing normal to S_t and tangent to Σ_t.

9.5 Geometric evolution system on the horizon: the role of the Weyl tensor

9.5.1 The inner screen $\mathcal{H}$

Let us consider a black-hole spacetime $(\mathcal{M}, g_{ab})$, with associated Levi-Civita connection ∇_a, endowed with a 3+1 space-like foliation $\{\Sigma_t\}$. Let us consider an *inner* hypersurface $\mathcal{H}$, to be later identified with the black-hole horizon, such that the intersection of the slices Σ_t with the worldtube $\mathcal{H}$ defines the foliation of $\mathcal{H}$ by closed space-like surfaces $\{\mathcal{S}_t\}$. We consider an evolution vector h^a along $\mathcal{H}$, characterized as that vector tangent to $\mathcal{H}$ and normal to the slices $\{\mathcal{S}_t\}$ that transports the slice $\mathcal{S}_t$ onto the slice $\mathcal{S}_{t+\delta t}$. The normal plane at each point of $\mathcal{S}_t$ can be spanned in terms of the *outgoing* null vector ℓ^a and the *ingoing* vector k^a, chosen to satisfy $\ell^a k_a = -1$. Directions of ℓ^a and k^a are fixed, though a rescaling freedom remains (see figure9.10). In particular, and without loss of generality in our context, we can write [237]

$$h^a = \ell^a - Ck^a, \tag{9.37}$$

so that $h^a h_a = 2C$. Therefore: h^a is, respectively, space-like if $C > 0$, null if $C = 0$, and time-like if $C < 0$.

Regarding the intrinsic geometry on $\mathcal{S}_t$, the induced metric is denoted by q_{ab}, its Levi-Civita connection by ${}^2D_a$ and the corresponding Ricci curvature scalar by ${}^2R$. The area form is ${}^2\epsilon = \sqrt{q}dx^1 \wedge dx^2$ and we will denote the area measure as $dA = \sqrt{q}d^2x$.

The infinitesimal evolution of the intrinsic geometry along $\mathcal{H}$, *i.e.,* the evolution of the induced geometry q_{ab} along h^a, defines the *deformation tensor* $\Theta^{(h)}_{ab}$

$$\Theta^{(h)}_{ab} \equiv \frac{1}{2}\delta_h q_{ab} = \sigma^{(h)}_{ab} + \frac{1}{2}\theta^{(h)} q_{ab}\,, \tag{9.38}$$

where the trace $\theta^{(h)} = \Theta^{(h)}_{ab} q^{ab}$, referred to as the *expansion* along h^a, measures the infinitesimal evolution of the $\mathcal{S}_t$ element of area along $\mathcal{H}$, whereas the traceless *shear* $\sigma^{(h)}_{ab}$ controls the deformations of the induced metric . Here δ_h can be identified with the projection on $\mathcal{H}$ of the Lie derivative $\mathcal{L}_h$. Before reviewing the effective curvature vector $\tilde{K}^{\rm eff}_i$, let us discuss the time parameterization of $\mathcal{H}$.

We recall that jumps of apparent horizons are generic in $3+1$ evolutions of black-hole spacetimes. The dynamical trapping horizon framework offers a spacetime insight into this behaviour by understanding the jumps as corresponding to marginally trapped sections of a (single) hypersurface bending in spacetime, but multiply foliated by spatial hypersurfaces in the $3+1$ foliation $\{\Sigma_t\}$ [220, 238, 239, 240, 241]. In the particular case of binary black-hole mergers this picture predicts, after the moment of its first appearance, the splitting of the common apparent horizon into two horizons: a growing *external* common horizon and an shrinking *internal* common horizon [220, 240]. It is standard to track the evolution of the external common horizon, the proper apparent horizon, but to the internal common horizon as physically irrelevant.

In figure 9.11 we illustrate this picture in a simplified (spherically symmetric) collapse scenario that retains the relevant features of the discussion. On one side, the relevant outer screen boundary (namely, null infinity $\mathcal{I}^+$) is parameterized by the retarded time u, something explicitly employed in the expression of the flux of Bondi momentum in equations ((33) and (34)). On the other side, from the $3+1$ perspective, the moment t_c of first appearance of the (common) horizon corresponds to the coordinate time t at which the $3+1$ foliation $\{\Sigma_t\}$ firstly intersects the dynamical horizon $\mathcal{H}$. For $t > t_c$, Σ_t slices intersect twice (multiply, in the generic case) the hypersurface $\mathcal{H}$ giving rise to the external and internal common horizons (*cf.* $\mathcal{H}$ in figure 9.11). Therefore, the time function t is not a good parameter for the whole dynamical horizon $\mathcal{H}$. An appropriate parameterization of this hypersurface $\mathcal{H}$ is given in terms of an advanced time, such as v, parameterizing past null infinity $\mathcal{I}^-$. More precisely, (for a space-like worldtube portion of $\mathcal{H}$) we can label sections of $\mathcal{H}$ by an advanced time v starting from an initial value v_0 corresponding to the first $v =$ const null hypersurface hitting the spacetime singularity, *i.e.,* $\mathcal{H} = \bigcup_{v\geq v_0} \mathcal{S}_v$.

9.5.2 Effective curvature vector $\tilde{K}^{\rm eff}_i$

In the previous sections the effective curvature vector $\tilde{K}^{\rm eff}_i$ was introduced using the parameterization of $\mathcal{H}$ by the time function t associated with the spacetime $3+1$ slicing. In particular, $\tilde{K}^{\rm eff}_i(t)$ was defined only on the external part of the horizon $\mathcal{H}$, for $t \geq t_c$. We can now extend the definition of $\tilde{K}^{\rm eff}_i$ to the whole horizon $\mathcal{H}$ (more precisely, to a space-like worldtube portion of it) by making use of its parameterization

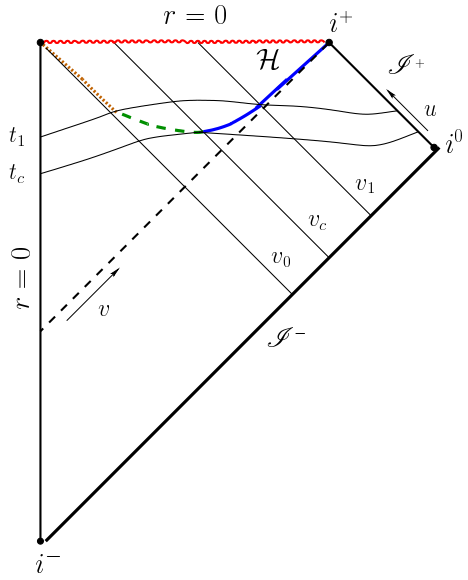

Figure 9.11: Carter-Penrose diagram (corresponding, for simplicity, to a generic spherically symmetric collapse) illustrating the time parameterization of the outer and inner screens. The outer boundary given by $\mathcal{I}^+$ is properly parameterized by the retarded time u, whereas an advanced time v runs along inner boundaries, in particular the dynamical horizon $\mathcal{H}$. Given a $3+1$ foliation $\{\Sigma_t\}$, t_c denotes the time t at which the horizon first appears. For $t > t_c$, Σ_t slices intersect multiply the hypersurface $\mathcal{H}$, giving rise to internal and external horizons. On the contrary, the advanced coordinate v provides a good parameterization of $\mathcal{H}$ from an initial $v > v_0$.

by the advanced time v adapted to the $3+1$ slicing of $\mathcal{H}$. Given a section $\mathcal{S}_v \subset \mathcal{H}$, we consider a vector ξ^i transverse to it (*i.e.,* generically not tangent to $\mathcal{S}_v$) and tangent to the 3-slice Σ_t that intersects $\mathcal{H}$ at $\mathcal{S}_v$ (*i.e.,* $\mathcal{S}_v = \mathcal{H} \cap \Sigma_t$). Then, the component $\tilde{K}^{\rm eff}[\xi](v)$ is expressed as[1]

$$\tilde{K}^{\rm eff}[\xi](v) \propto -\oint_{\mathcal{S}_v} (\xi^i s_i) \left(\tilde{\mathcal{N}}(v)\right)^2 dA\,, \tag{9.39}$$

where s_i is the space-like normal to $\mathcal{S}_v$ and tangent to Σ_t, and

$$\tilde{\mathcal{N}}(v) \equiv \int_{v_0}^{v} {}^2R(v')dv' + \tilde{\mathcal{N}}_{v_0}\,, \tag{9.40}$$

where ${}^2R$ is the Ricci curvature scalar on $(\mathcal{S}_v, q_{ab})$ and $\tilde{\mathcal{N}}_{v_0}$ is an initial function to be fixed. As commented above, in spite of the formal similarity with the news function

[1]For avoiding the introduction of lapse functions related to different parameterizations of $\mathcal{H}$, we postpone the fixing of the coefficient to section 9.7. We note that a global constant factor is irrelevant for cross-correlations.

$\mathcal{N}(u)$ at $\mathcal{I}^+$ (*cf.* equation (34)), definition (9.40) does not guarantee the local-in-time character of $\tilde{\mathcal{N}}(v)$ since it is expressed in terms of a time-integral on the past history.

In order to study the dynamics of $\tilde{K}_i^{\rm eff}$, we consider the evolution of the Ricci scalar curvature ${}^2R$ along the worldtube $\mathcal{H}$. In terms of the elements introduced above, the evolution of the Ricci scalar curvature ${}^2R$ along h^a has the form

$$\delta_h {}^2R = -\theta^{(h)}\, {}^2R + 2\, {}^2D^a {}^2D^b \sigma^{(h)}_{ab} - {}^2\Delta\theta^{(h)} \ , \tag{9.41}$$

where ${}^2\Delta = q^{ab}{}^2D_a {}^2D_b$ denotes the Laplacian on $\mathcal{S}_t$. Expression (9.41) is a fundamental one in our work and it applies to *any* hypersurface $\mathcal{H}$ foliated by closed surfaces $\mathcal{S}_t$. Contact with black holes is made when $\mathcal{H}$ is taken as the spacetime event horizon or as the dynamical horizon associated with the foliation $\{\Sigma_t\}$.

9.5.3 Geometry evolution on black-hole horizons

We briefly recall the notions of black-hole horizon relevant here. First, the event horizon (EH) $\mathcal{E}$ is the boundary of the spacetime region from which no signal can be sent to $\mathcal{I}^+$, *i.e.,* the region in $\mathcal{M}$ not contained in the causal past $J^-(\mathcal{I}^+)$ of $\mathcal{I}^+$. The EH is a null hypersurface, characterized as $\mathcal{E} = \partial J^-(\mathcal{I}^+) \cap \mathcal{M}$. Second, a dynamical horizon (DH) or (dynamical) *future outer trapping horizon* (FOTH) $\mathcal{H}$ is a quasi-local model for the black-hole horizon based on the notion of a world-tube of apparent horizons. More specifically, a FOTH $\mathcal{H}$ is a hypersurface that can be foliated by marginally (outer) trapped surfaces $\mathcal{S}_t$, *i.e.,* $\mathcal{H} = \bigcup_{t\in\mathbb{R}} \mathcal{S}_t$ with outgoing expansion $\theta^{(\ell)} = 0$ on $\mathcal{S}_t$, satisfying: i) a *future* condition $\theta^{(k)} < 0$, and ii) an *outer condition* $\delta_k\theta^{(\ell)} < 0$. In the dynamical regime, *i.e.,* when matter and/or radiation cross the horizon (namely when $\delta_\ell\theta^{(\ell)} \neq 0$), the outer condition is equivalent to the condition that $\mathcal{H}$ is space-like [242][1]. Therefore, for dynamical trapping horizons we have $C > 0$ in equation (9.37).

For both EHs and DHs, an important area theorem holds: $\delta_h A = \oint_{\mathcal{S}_t} \theta^{(h)} dA > 0$. In the case of an EH, Hawking's area theorem [244, 245] guarantees the growth of the area, whereas in the case of a DH, the positivity of $\delta_h A = -\oint_{\mathcal{S}_t} C\theta^{(k)} dA$ is guaranteed by its space-like character ($C > 0$) together with the future condition $\theta^{(k)} < 0$.

We make now contact with equation (9.41) and interpret the elements that determine the dynamics of ${}^2R$. The growth of the area of a black-hole horizon guarantees the (average) positivity of $\theta^{(h)}$. This offers a qualitative understanding of the dynamical decay of ${}^2R$: the first term in the right hand side drives an exponential-like decay of the Ricci scalar curvature. More precisely, non-equilibrium deformations of the Ricci scalar curvature ${}^2R$ in black-hole horizons decay exponentially as long as the horizon grows in area. Regarding the elliptic operators acting on the shear and the expansion [second and third terms in the right hand side of equation (9.41)] they provide dissipative terms smoothing the evolution of ${}^2R$. Indeed, in section 9.10 we will review a viscosity interpretation of $\theta^{(h)}$ and $\sigma^{(h)}_{ab}$, in particular associating with them respective decay and oscillation timescales of the horizon geometry.

[1] This property actually substitutes the outer condition in the DH characterization [221, 243] of quasi-local horizons.

9.5.3.1 Complete evolution system driving ${}^2R$

A further understanding of equation (9.41) requires a control of the dynamics of the shear $\sigma^{(h)}_{ab}$, of the expansion $\theta^{(h)}$ and of the induced metric q_{ab}, the latter controlling the elliptic operators ${}^2D^a{}^2D^b$ and ${}^2\Delta$. Therefore, we need evolution equations determining $\delta_h q_{ab}$, $\delta_h\theta^{(h)}$ and $\delta_h\sigma^{(h)}_{ab}$:

i) $\delta_h q_{ab}$: *definition of the deformation tensor.* The evolution of q_{ab} is dictated by $\sigma^{(h)}_{ab}$ and $\theta^{(h)}$ [*cf.* equation (9.38)].

ii) $\delta_h\theta^{(h)}$: *focusing or Raychadhuri-like equation.* The evolution of $\theta^{(h)}$ involves the Ricci tensor R_{ab}, *i.e.,* the "trace part" of the spacetime Riemann tensor $R^a{}_{bcd}$, thus introducing the stress-energy tensor T_{ab} through Einstein equations.

iii) $\delta_h\sigma^{(h)}_{ab}$: *tidal equation.* The evolution of $\sigma^{(h)}_{ab}$ is driven by the Weyl tensor $C^a{}_{bcd}$, *i.e.,* the traceless part of the spacetime Riemann tensor, thus involving dynamical gravitational degrees of freedom but not directly the Einstein equations.

The structural feature that we want to underline about these equations is shared by evolution systems on EHs and DHs, although the explicit form of the equations differ in both cases. More specifically, whereas for EHs the evolution equations for ${}^2R$, q_{ab}, $\theta^{(h)}$ and $\sigma^{(h)}_{ab}$ form a "closed" evolution system, in the DH case additional geometric objects (requiring further evolution equations) are brought about through the evolution equations $\delta_h q_{ab}$, $\delta_h\theta^{(h)}$ and $\delta_h\sigma^{(h)}_{ab}$. Moreover, an explicit dependence on the function C, related to the choice of $3+1$ slicing as discussed later [*cf.* equation (9.49)], is involved in the DH case. For these reasons, and for simplicity, in the rest of this subsection we restrict our discussion to the case of an EH, indicating that the main qualitative conclusion also holds for DHs, whose details will be addressed elsewhere.

The EH $\mathcal{E}$ is a null hypersurface generated by the evolution vector h^a, a null vector in this case: $h^a = \ell^a$. The null generator ℓ^a satisfies a pregeodesic equation $\ell^c\nabla_c\ell^a = \kappa^{(\ell)}\ell^a$. Choosing an affine reparametrization such that ℓ^a is geodesic, *i.e.,* $\kappa^{(\ell)} = 0$, the evolution equations for ${}^2R$, q_{ab}, $\sigma^{(h)}_{ab}$ and $\theta^{(h)}$ close the evolution system

$$\delta_\ell{}^2R = -\theta^{(\ell)}\,{}^2R + 2\,{}^2D^a{}^2D^b\sigma^{(\ell)}_{ab} - {}^2\Delta\theta^{(\ell)}\,, \tag{9.42}$$

$$\delta_\ell q_{ab} = 2\sigma^{(\ell)}_{ab} + \theta^{(\ell)}q_{ab}\,, \tag{9.43}$$

$$\delta_\ell\theta^{(\ell)} = -\frac{1}{2}(\theta^{(\ell)})^2 - \sigma^{(\ell)}_{ab}\sigma^{(\ell)\,ab} - 8\pi T_{ab}\ell^a\ell^b\,, \tag{9.44}$$

$$\delta_\ell\sigma^{(\ell)}_{ab} = \sigma^{(\ell)}_{cd}\sigma^{(\ell)\,cd}q_{ab} - q^c{}_a q^d{}_b C_{lcfd}\ell^l\ell^f\,. \tag{9.45}$$

Once initial conditions are prescribed, the only remaining information needed to close the system are the matter term $T_{ab}\ell^a\ell^b$ in the focusing equation and $q^c{}_a q^d{}_b C_{lcfd}\ell^l\ell^f$ in the tidal equation. Using a null tetrad $(\ell^a, k^a, m^a, \overline{m}^a)$ they can be expressed in terms of Ricci and Weyl scalars: $8\pi T_{ab}\ell^a\ell^b = R_{ab}\ell^a\ell^b = 2\Phi_{00}$ and $q^c{}_a q^d{}_b C_{lcfd}\ell^l\ell^f = \Psi_0\overline{m}_a\overline{m}_b + \overline{\Psi}_0 m_a m_b$. The complex Weyl scalar Ψ_0 and the Ricci scalar Φ_{00} drive the evolution of the geometric system (9.42)–(9.45) on the horizon. Being determined in terms of the bulk dynamics (Ψ_0 relates to the near-horizon dynamical tidal fields and

incoming gravitational radiation, whereas Φ_{00} accounts for the matter fields), fields Ψ_0 and Φ_{00} act as *external forces* providing (modulo initial conditions) all the relevant dynamical information for system (9.42)–(9.45) on $\mathcal{E}$.

In the DH case, although the evolution system is more complex, the qualitative conclusions reached here remains unchanged. More specifically, the differential system on $\mathcal{H}$ governing the evolution of ${}^2R$ is also driven by external forces given by particular combination of Weyl and Ricci scalars[1].

In the present cross-correlation approach, these dynamical considerations strongly support Ψ_0 as a natural building block in the construction[2] of the quantity $h_{\rm inn}(v)$ at $\mathcal{H}$, to be correlated in vacuum to $dP_i^{\rm B}/du$ at $\mathcal{I}^+$. This is hardly surprising, given the dual nature of Ψ_0 and Ψ_4 on inner and outer boundaries, respectively.

Particularly relevant are the following remarks. First, in the presence of matter, the scalar Φ_{00} plays a role formally analogous to that of Ψ_0. Therefore, in the general case, it makes sense to consider Φ_{00} on an equal footing as Ψ_0 in the construction of $h_{\rm inn}(v)$. Second, equation (9.42) is completely driven by the rest of the system, without back-reacting on it. For this reason, although Ψ_0 (and Φ_{00}) encodes the information determining the dynamics on the horizon, at the same time the evolution of ${}^2R$ is sensitive to all relevant dynamical degrees of freedom, providing an *averaged* response. This justifies the crucial role of ${}^2R$ in the construction of the effective $\tilde{K}_i^{\rm eff}$

A serious drawback for the use of Ψ_0 and Φ_{00} in the construction of a quantity $h_{\rm inn}(v)$ at $\mathcal{H}$ is their dependence on the rescaling freedom of the null normal ℓ^a by an arbitrary function on $\mathcal{S}$. We address this point in the following section.

9.6 Fundamental results on Dynamical Horizons

The introduction of a preferred null tetrad on the horizon requires some kind of rigid structure. We argue here that DHs provide such a structure. We point out that the presentation in this section has a certain overlap with the one found in section 10.1, which states some of the concepts introduced here in a slightly different and more detailed context. We first review two fundamental geometric results about DHs

a) *Result 1 (DH foliation uniqueness)* [246]: Given a DH $\mathcal{H}$, the foliation $\{\mathcal{S}_t\}$ by marginally trapped surfaces is unique.

b) *Result 2 (DH existence)* [247, 248]: Given an *outer stable* marginally trapped surface $\mathcal{S}_0$ in a Cauchy hypersurface Σ_0, for each $3+1$ spacetime foliation $\{\Sigma_t\}$ containing Σ_0 there exists a unique DH $\mathcal{H}$ containing $\mathcal{S}_0$ and sliced by marginally trapped surfaces $\{\mathcal{S}_t\}$ such that $\mathcal{S}_t \subset \Sigma_t$.

These results have the following important implications:

i) *The evolution vector h^a is completely fixed on a DH* (up to a time reparametrization). By Result 1 any other evolution vector h'^a does not transport marginally trapped

[1] In a DH, the leading term in the external driving force is indeed given by Ψ_0, but corrections proportional to C also appear.

[2] Constructed as in equations (9.39) and (9.40) but substituting ${}^2R$ by Ψ_0.

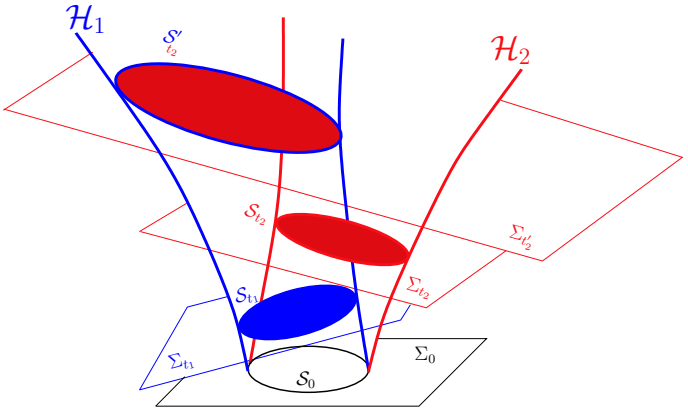

Figure 9.12: Worldtubes $\mathcal{H}_1$ (blue) and $\mathcal{H}_2$ (red) respectively associated with two different $3+1$ slicing $\{\Sigma_{t_1}\}$ and $\{\Sigma_{t_2}\}$ and providing evolutions from a given marginally trapped surface $\mathcal{S}_0$ in an initial Cauchy hypersurface Σ_0. They illustrate the non-unique evolution of apparent horizons into DHs. The foliation $\{\mathcal{S}_{t_1}\}$ (resp. $\{\mathcal{S}_{t_2}\}$) by marginally trapped surfaces is defined by the intersections of $\mathcal{H}_1$ with $\{\Sigma_{t_1}\}$ (resp. $\mathcal{H}_2$ and $\{\Sigma_{t_2}\}$). Note that, from the DH foliation uniqueness Result 1 [246], surfaces $\mathcal{S}'_{t_2} = \mathcal{H}_1 \cap \Sigma_{t_2}$ are not (in general) marginally trapped surfaces.

surfaces into marginally trapped surfaces.

ii) *The evolution of an apparent horizon into a DH is non-unique.* Let us consider an initial apparent horizon $\mathcal{S}_0 \subset \Sigma_0$ and two different $3+1$ slicings $\{\Sigma_{t_1}\}$ and $\{\Sigma_{t_2}\}$, compatible with Σ_0. From Result 2 there exist DHs $\mathcal{H}_1 = \bigcup_{t_1} \mathcal{S}_{t_1}$ and $\mathcal{H}_2 = \bigcup_{t_2} \mathcal{S}_{t_2}$, with $\mathcal{S}_{t_1} = \mathcal{H}_1 \cap \Sigma_{t_1}$ and $\mathcal{S}_{t_2} = \mathcal{H}_2 \cap \Sigma_{t_2}$ marginally trapped surfaces. Let us consider now the sections of $\mathcal{H}_1$ by $\{\Sigma_{t_2}\}$, *i.e.*, $\mathcal{S}'_{t_2} = \mathcal{H}_1 \cap \Sigma_{t_2}$, so that $\mathcal{H}_1 = \bigcup_{t_2} \mathcal{S}'_{t_2}$. In the generic case, slicings $\{\mathcal{S}'_{t_2}\}$ and $\{\mathcal{S}_{t_1}\}$ of $\mathcal{H}_1$ are different (deform $\{\Sigma_{t_2}\}$ if needed). Therefore, from Result 1, $\mathcal{S}'_{t_2}$ cannot be marginally trapped surfaces. Reasoning by contradiction, we then conclude that $\mathcal{H}_1$ and $\mathcal{H}_2$ are different hypersurfaces in $\mathcal{M}$, as illustrated in figure9.12.

The two results above establish a fundamental link between DHs and the $3+1$ approach here adopted. We denote the unit time-like normal to slices Σ_t by n^a and the space-like (outgoing) normal to $\mathcal{S}_t$ and tangent to Σ_t by s^a (see figure9.10). We denote by N the lapse associated to the spacetime slicing function t, *i.e.*, $n_a = -N\nabla t$. Given a marginal trapped surface $\mathcal{S}_0$ in an initial slice Σ_0, and given a lapse function N, let us consider the (only) DH $\mathcal{H}$ given by Result 2. Then the unique evolution vector h^a on $\mathcal{H}$ associated with Result 1 can be written up to a time-dependent rescaling[1] as

$$h^a = Nn^a + bs^a \ , \tag{9.46}$$

where b is a function on $\mathcal{S}_t$ to be determined in terms of N and C [see equation (9.49) below]. Certainly such a decomposition of an evolution vector compatible with a given

[1]This applies, strictly, to the external part of the horizon discussed in section 9.5.1. For the internal part one must reverse the evolution with respect to that defined by the $3+1$ foliation: $h^a = -Nn^a + bs^a$. The following discussion goes then through.

$3+1$ slicing $\{\Sigma_t\}$, in the sense $h^a\nabla_a t = 1$, is valid for any hypersurface but, in the case of a DH and due to Result 1, the evolution vector h^a determined by equation (9.46) has an intrinsic meaning (up to time reparametrization, which is irrelevant in a cross-correlation approach) as an object on $\mathcal{H}$ not requiring a $3+1$ foliation. On the other hand, equation (9.37) provides the expression of vector h^a in terms of the null normals. More specifically, equation (9.37) links the scaling of ℓ^a and k^a to that of h^a by imposing $h^a \to \ell^a$ as the DH is driven to stationarity ($C \to 0 \Leftrightarrow \delta_\ell\theta^{(\ell)} \to 0$). Writing the null normals at $\mathcal{H}$ as $\ell^a = (f/2)(n^a + s^a)$ and $k^a = (n^a - s^a)/f$, for some function f, expressions (9.37) and (9.46) for h^a lead to

$$\ell^a_N = \frac{N+b}{2}\,(n^a + s^a)\ ,\ k^a_N = \frac{1}{N+b}\,(n^a - s^a)\ , \tag{9.47}$$

where the subindex N denotes the explicit link of $\mathcal{H}$ to a $3+1$ slicing. In order to determine b, we evaluate the norm of h^a and note that the function C in equation (9.37) is expressed in terms of N and b as

$$C = \frac{1}{2}\left(b^2 - N^2\right)\ . \tag{9.48}$$

On the other hand, for a given lapse N, the trapping horizon $\delta_h\theta^{(\ell)} = 0$ condition translates into an elliptic equation for C

$$\begin{aligned} &-{}^2\Delta C + 2\Omega^{(\ell)}_c{}^2D^cC - C\left[-{}^2D^c\Omega^{(\ell)}_c + \Omega^{(\ell)}_c\Omega^{(\ell)c} - \frac{1}{2}{}^2R\right] \\ &= \sigma^{(\ell)}_{ab}\sigma^{(\ell)ab} + 8\pi T_{ab}\tau^a\ell^b\,. \end{aligned} \tag{9.49}$$

Therefore, for a given DH $\mathcal{H}$ associated with a 3+1 slicing with lapse N, equations (9.49) and (9.48) fix the value of b. Prescription (9.47) provides preferred null normals on a DH $\mathcal{H}$ compatible with the foliation defined by N. Completed with the complex null vector m^a on $\mathcal{S}_t$, we propose

$$(\ell^a_N, k^a_N, m^a, \overline{m}^a)\ , \tag{9.50}$$

as a preferred null tetrad (up to time reparametrization) on a DH. To keep the notation compact, hereafter we will denote the preferred ℓ^a_N and k^a_N simply as ℓ^a and k^a and omit the symbol N from all quantities evaluated in this tetrad. The tetrad (9.50) then leads to a notion of preferred Weyl (and Ricci) scalars on the horizon $\mathcal{H}$. In particular,

$$\Psi_0 \;=\; C^a{}_{bcd}\,\ell_a m^b\ell^c m^d\,, \tag{9.51}$$

$$\Phi_{00} \;=\; \frac{1}{2}R_{ab}\,\ell^a\ell^b\,. \tag{9.52}$$

In summary: we have introduced preferred null normals on a DH $\mathcal{H}$ by: i) linking the normalization of ℓ^a to that of h^a by requiring $h^a \to \ell^a$ in stationarity; and ii) fixing the normalization of h^a (up to a time-dependent function) by the foliation uniqueness result on DHs (Result 1). The latter is the *rigid structure* needed to fix a preferred null tetrad on $\mathcal{H}$. In the particular case of constructing $\mathcal{H}$ in an Initial Value Problem approach (Result 2 on DHs), the free time-dependent function is fixed by the lapse N of the given global foliation $\{\Sigma_t\}$.

9.7 News-like functions and Bondi-like fluxes on a dynamical horizon

9.7.1 News-like functions: vacuum case

In section 9.5 we have identified the Weyl scalar Ψ_0 as the object that encodes (in vacuum and for $C = 0$) the relevant geometric information on the black-hole horizon understood as an inner screen. Then in section 9.6 we have introduced a preferred scaling for Ψ_0 on DHs. With these elements we can now introduce the following vectorial quantity on $\mathcal{H}$

$$\tilde{K}[\xi](v) \equiv -\frac{1}{8\pi} \oint_{\mathcal{S}_v} (\xi^i s_i) \left| \tilde{\mathcal{N}}^{(\ell)}_{\Psi}(v) \right|^2 dA \,, \tag{9.53}$$

where

$$\tilde{\mathcal{N}}^{(\ell)}_{\Psi}(v) \equiv \int_{v_0}^{v} \Psi_0(v') dv' \,, \tag{9.54}$$

where we make use of an advanced time v parameterizing $\mathcal{H}$ (*cf.* section 9.5.1 and figure 9.11) and adapted to the $3+1$ slicing at $\mathcal{H}$ (namely, we choose $h^a \nabla_a v = 2$).

The quantity $\tilde{K}_i$ could be used as a refined version of $\tilde{K}^{\rm eff}_i$ for the correlation with $dP^{\rm B}_i/du$ at $\mathcal{I}^+$. However, whereas $\tilde{K}^{\rm eff}_i$ is explicitly understood as an *effective* quantity and, consequently, one can relax the requirement on the $\tilde{\mathcal{N}}$ constructed out of ${}^2R$ in (9.40) to be mathematically equivalent to a news function, the situation is different for $\tilde{K}_i$ in (9.53): the geometric dual nature of Ψ_4 and Ψ_0 would call for a news-like function character for $\tilde{\mathcal{N}}^{(\ell)}_{\Psi}$ in (9.54).

Whereas expressions for the flux of Bondi momentum and the news function at $\mathcal{I}^+$ (*cf.* equations (33) and (34)) are valid under the (strong) conditions enforced by asymptotic simplicity at null infinity and in a given Bondi frame, no geometric structure supports the "a priori" introduction of quantities $\tilde{K}_i$ and $\tilde{\mathcal{N}}^{(\ell)}_{\Psi}$ on $\mathcal{H}$. In particular, the news function $\mathcal{N}(u)$ is an object well defined in terms of geometric quantities on sections $\mathcal{S}_u \subset \mathcal{I}^+$, that can be expressed as a time integral [*cf.* equation (34)] due to the key relation $\partial_u \mathcal{N} = \Psi_4$ holding for Bondi coordinate systems at $\mathcal{I}^+$. On the contrary, the quantity $\tilde{\mathcal{N}}^{(\ell)}_{\Psi}$ defined by time-integration of Ψ_0 is not an object defined in terms of the geometry of a section $\mathcal{S}_v$ (justifying the use of a "tilde"). Such a local-in-time behaviour is a crucial property to be satisfied by any valid news function. Therefore, one would expect additional terms to Ψ_0 (with vanishing counterparts at $\mathcal{I}^+$), contributing in $\tilde{\mathcal{N}}^{(\ell)}_{\Psi}$ to build an appropriate news-like function on $\mathcal{H}$.

In the absence of a sound geometric news formalism on $\mathcal{H}$, we proceed heuristically by modifying $\tilde{\mathcal{N}}^{(\ell)}_{\Psi}$ so that it acquires a local-in-time character. Such a property would be guaranteed if the integrand in definition (9.54) could be expressed as a total derivative in time of some quantity defined on sections $\mathcal{S}_v$. The scalar Ψ_0 in equation (9.54) does not satisfy this property. However, with this guideline, inspection of (9.45) suggests some of the terms to be added to Ψ_0 [system (9.42)–(9.45) applies to the EH case] so

that they integrate in time to a quantity on $\mathcal{S}_v$, namely the shear. Considering first, as an intermediate step, the EH case and using a tensorial rather a complex notation[1], let us introduce a news-like tensor[2] $(\mathcal{N}^{(\ell)}_{\Psi})_{ab}$ whose time variation is

$$(\dot{\mathcal{N}}^{(\ell)}_{\Psi})_{ab} = \frac{1}{\sqrt{2}}\left(q^c{}_a q^d{}_b C_{lcfd}\ell^l\ell^f - \sigma^{(\ell)}_{cd}\sigma^{(\ell)\,cd}q_{ab}\right), \tag{9.55}$$

that is, such that $(\dot{\mathcal{N}}^{(\ell)}_{\Psi})_{ab} = -1/\sqrt{2}\delta_\ell\sigma^{(\ell)}_{ab}$ (the global factor $1/\sqrt{2}$ is required for the correct coefficient in the leading-order contribution). Upon time integration (9.54) and setting vanishing initial values at early times, this choice leads to

$$(\mathcal{N}^{(\ell)}_{\Psi})_{ab} = -\frac{1}{\sqrt{2}}\sigma^{(\ell)}_{ab} \quad . \tag{9.56}$$

If we write

$$(\mathcal{N}^{(\ell)}_{\Psi})_{ab} = \frac{1}{\sqrt{2}}\int_{v_0}^{v}\left(q^c{}_a q^d{}_b C_{lcfd}\ell^l\ell^f - 2\mathcal{N}^{(\ell)}_{cd}\mathcal{N}^{(\ell)\,cd}q_{ab}\right)dv', \tag{9.57}$$

and substitute $(\mathcal{N}^{(\ell)}_{\Psi})_{ab}$ iteratively in the right hand side, we can express the news-like function $(\mathcal{N}^{(\ell)}_{\Psi})_{ab}$ in terms of Ψ_0 so that the lowest-order term is indeed given by expression (9.54).

This identification, in the EH case, of a plausible news-like tensor as the shear along the evolution vector suggests the following specific proposal for the news-like tensor for DHs

$$\mathcal{N}^{(\mathcal{H})}_{ab} \equiv -\frac{1}{\sqrt{2}}\sigma^{(h)}_{ab}\,. \tag{9.58}$$

This proposal has a tentative character. Once identified the basics, we postpone a systematic study to a forthcoming work.

9.8 News-like functions: matter fields

As discussed in section 9.5, in system (9.42)–(9.45) the Ricci scalar Φ_{00} plays a role analogous to that of Ψ_0. From this perspective, in the matter case, it is reasonable to define as in (9.54)

$$\tilde{\mathcal{N}}^{(\ell)}_{\Phi}(v) \equiv \frac{\alpha_{\rm m}}{2}\int_{v_0}^{v}\Phi_{00}(v')\,dv', \tag{9.59}$$

such that $\tilde{K}_i$ in (9.53) is rewritten

$$\tilde{K}[\xi](v) \equiv -\frac{1}{8\pi}\oint_{\mathcal{S}_v}(\xi^i s_i)\left[\left|\tilde{\mathcal{N}}^{(\ell)}_{\Psi}(v)\right|^2 + \left(\tilde{\mathcal{N}}^{(\ell)}_{\Phi}(v)\right)^2\right]dA\,. \tag{9.60}$$

[1] We write complex numbers as 2×2 traceless matrices.

[2] Note that we remove now the "tilded" notation to emphasize its news-like local-in-time character,

The parameter $\alpha_{\rm m}$ is introduced to account for possible different relative contributions of Ψ_0 and Φ_{00} (distinct choices for $\alpha_{\rm m}$ are possible, depending on the particular quantity to be correlated at $\mathcal{I}^+$). However, also the function $\tilde{\mathcal{N}}^{(\ell)}_{\Phi}$ is affected by the same issues discussed above for $\tilde{\mathcal{N}}^{(\ell)}_{\Psi}$, namely it lacks a local-in-time behavior. As in the vacuum case, we proceed first by looking at EHs. We then complete Φ_{00} with the terms in equation (9.44), so that $\dot{\mathcal{N}}^{(\ell)}_{\Phi}(v) = -(\alpha_{\rm m}/2)\delta_\ell\theta^{(\ell)}$. That is

$$\dot{\mathcal{N}}^{(\ell)}_{\Phi}(v) = \frac{\alpha_{\rm m}}{2}\left(8\pi T_{cd}\ell^c\ell^d + \frac{1}{2}(\theta^{(\ell)})^2 + \sigma^{(\ell)}_{cd}\sigma^{(\ell)\,cd}\right) ,$$

so that $\mathcal{N}^{(\ell)}_{\Phi} = -(\alpha_{\rm m}/2)\theta^{(\ell)}$. This *matter news-like* function can be equivalently expressed in tensorial form as follows

$$(\mathcal{N}^{(\ell)}_{\Phi})_{ab} = -\frac{\alpha_{\rm m}}{2\sqrt{2}}\theta^{(\ell)}q_{ab} \ . \tag{9.61}$$

As in vacuum, the passage from EHs to DHs is accomplished by using the natural evolution vector h^a along $\mathcal{H}$ for the expansion. Then, combining the tensorial form (9.61) with (9.58), we can write a single news-like tensor as

$$\mathcal{N}^{(\mathcal{H})}_{ab} = -\frac{1}{\sqrt{2}}\left(\sigma^{(h)}_{ab} + \frac{\alpha_{\rm m}}{2}\theta^{(h)}q_{ab}\right) \ . \tag{9.62}$$

Interestingly, if $\alpha_{\rm m} = 1$ the complete news tensor acquires a clear geometric meaning as the deformation tensor along h^a, *i.e.,* as the the time variation of the induced metric

$$\mathcal{N}^{(\mathcal{H})}_{ab} = -\frac{1}{\sqrt{2}}\Theta^{(h)}_{ab} = -\frac{1}{2\sqrt{2}}\dot{q}_{ab}\,. \tag{9.63}$$

9.8.1 Bondi-like fluxes on $\mathcal{H}$

The motivation for introducing $\tilde{K}^{\rm eff}_i$ and $\tilde{K}_i$ in equation (9.53) [or, more generally, $\tilde{K}_i$ in equation (9.60)] is the construction of quantities on $\mathcal{H}$ to be correlated to quantities at $\mathcal{I}^+$, namely the flux of Bondi linear momentum. We have been careful not to refer to them as to "fluxes", since they do not have an instantaneous meaning. However, once the news-like tensor $\mathcal{N}^{(\mathcal{H})}_{ab}$ has been introduced in (9.62), formal fluxes can be constructed by integration of the squared of these news. More specifically, we can introduce the formal fluxes on $\mathcal{H}$

$$\frac{dE^{(\mathcal{H})}}{dv}(v) = \frac{1}{8\pi}\oint_{\mathcal{S}_v}\mathcal{N}^{(\mathcal{H})}_{ab}\mathcal{N}^{(\mathcal{H})ab}dA\,, \tag{9.64}$$

$$\frac{dP^{(\mathcal{H})}[\xi]}{dv}(v) = -\frac{1}{8\pi}\oint_{\mathcal{S}_v}(\xi^i s_i)\left(\mathcal{N}^{(\mathcal{H})}_{ab}\mathcal{N}^{(\mathcal{H})ab}\right)dA\,, \tag{9.65}$$

where their formal notation as total time derivatives is meant to make explicit its local-in-time nature. The purpose of quantities $dE^{(\mathcal{H})}/dv$ and $(dP^{(\mathcal{H})}[\xi]/dv)$ is to provide improved quantities at $\mathcal{H}$ for the cross-correlation approach. In particular, $(dP^{(\mathcal{H})}[\xi]/dv)$

provides a refined version of the effective $\tilde{K}_i^{\rm eff}$, to be correlated with $(dP_i^{\rm B}/du)(u)$ at $\mathcal{I}^+$. In this context, $\tilde{K}_i$ in equation (9.53) has played the role of an intermediate stage in our line of arguments.

Of course, we can introduce formal quantities $E^{(\mathcal{H})}$ and $P_i^{(\mathcal{H})}$ on $\mathcal{H}$, by integrating expressions in (9.64) along $\mathcal{H}$. However, in the absence of a physical conservation argument or a geometric motivation, referring to them as (Bondi-like) energies and momentum would be just a matter of definition[1]. Thus, we rather interpret them simply as well-defined instantaneous quantities leading ultimately to a timeseries $h_{\rm inn}(v)$.

It is illustrative to expand the squared of the news in (9.64) as

$$\mathcal{N}^{(\mathcal{H})}_{ab}\mathcal{N}^{(\mathcal{H})ab} = \frac{1}{2}\left[\sigma^{(h)}_{ab}\sigma^{(h)ab} + \frac{\alpha_{\rm m}}{2}(\theta^{(h)})^2\right], \tag{9.66}$$

to be inserted in the expression for $dE^{(\mathcal{H})}/dv$ and $(dP^{(\mathcal{H})}/dv)[\xi]$. The relative weight of the different terms as we depart from equilibrium can be made explicit by expressing the evolution vector as $h^a = \ell^a - Ck^a$ [*cf.* equation (9.37)], with associated $\sigma^{(h)}_{ab} = \sigma^{(\ell)}_{ab} - C\sigma^{(k)}_{ab}$ and $\theta^{(h)} = -C\theta^{(k)}$. We can then write

$$\begin{aligned}\mathcal{N}^{(\mathcal{H})}_{ab}\mathcal{N}^{(\mathcal{H})ab} &= \frac{1}{2}\Big[\sigma^{(\ell)}_{ab}\sigma^{(\ell)ab} - 2C\sigma^{(\ell)}_{ab}\sigma^{(k)ab} \\ &\quad + C^2\left(\sigma^{(k)}_{ab}\sigma^{(k)ab} + \frac{\alpha_{\rm m}}{2}(\theta^{(k)})^2\right)\Big].\end{aligned} \tag{9.67}$$

On a DH, terms proportional to $\alpha_{\rm m}$ only enter at a quadratic order in C. Two values of $\alpha_{\rm m}$ are of particular interest. First, the case $\alpha_{\rm m} = 0$, corresponding to an analysis of pure gravitational dynamics. Second, the case $\alpha_{\rm m} = 1$ where [*cf.* (9.63)]

$$\begin{aligned}\frac{dE^{(\mathcal{H})}}{dv}(v) &= \frac{1}{8\pi}\oint_{\mathcal{S}}\mathcal{N}^{(\mathcal{H})}_{ab}\mathcal{N}^{(\mathcal{H})ab}dA = \frac{1}{16\pi}\oint_{\mathcal{S}}\Theta^{(h)}_{ab}\Theta^{(h)ab}dA \\ &= \frac{1}{32\pi}\oint_{\mathcal{S}}\frac{1}{2}(\dot{q}_{ab})^2 dA\,,\end{aligned} \tag{9.68}$$

that admits a suggestive interpretation as a Newtonian *kinetic energy* term of the intrinsic horizon geometry.

9.8.2 Relation to quasi-local approaches to horizon momentum and application to recoil dynamics

As emphasized in the previous section, the essential purpose of $dE^{(\mathcal{H})}/dv$ and $(dP^{(\mathcal{H})}[\xi]/dv)$ in (9.64) is to provide geometrically sound proposals for $h_{\rm inn}(v)$ at $\mathcal{H}$. Having said this, it is worthwhile to compare the resulting expressions, for specific values of $\alpha_{\rm m}$, with DH physical fluxes derived in the literature. This provides an internal consistency test

[1] For instance, the leading-order contribution from matter to the black-hole energy and momentum should come from the integration of the appropriate component of the stress-energy tensor T_{ab}, an element absent in (9.64) where matter contributions only enter through terms quadratic in T_{ab}.

of the line of thought followed from $\tilde{K}_i^{\rm eff}$ to equations (9.64). In particular, for $\alpha_{\rm m}=0$ we obtain

$$\frac{dE^{(\mathcal{H})}}{dv}(v)=\frac{1}{8\pi}\oint_{\mathcal{S}}\mathcal{N}^{(\mathcal{H})}_{ab}\mathcal{N}^{(\mathcal{H})ab}dA=\frac{1}{16\pi}\oint_{\mathcal{S}}\sigma^{(h)}_{ab}\sigma^{(h)ab}dA=\frac{1}{16\pi}\oint_{\mathcal{S}}\left[\sigma^{(\ell)}_{ab}\sigma^{(\ell)ab}-2C\sigma^{(\ell)}_{ab}\sigma^{(k)ab}+C^2\sigma^{(k)}_{ab}\sigma^{(k)ab}\right]dA \tag{9.69}$$

Expression (9.69) allows us to draw analogies with the energy flux proposed in the DH geometric analysis of [221, 249]. In particular, the leading term in the integrand of this expression, $\sigma^{(\ell)}_{ab}\sigma^{(\ell)ab}$, is directly linked (*cf.* equation (3.27) in [221]) to the term identified in [250, 251] as the flux of *transverse* gravitational propagating degrees of freedom[1]. The DH energy flux also includes a *longitudinal* part depending on $\Omega^{(\ell)}_a\Omega^{(\ell)a}$, absent in quantities in equation (9.64). In this sense, dE^N/dv provides a quantity $h_{\rm inn}(v)$ accounting only for the transverse part of gravitational degrees of freedom [251, 253, 254] at $\mathcal{H}$ and therefore particularly suited for cross-correlation with $(dP^{\rm B}_i/du)(u)$, which corresponds to (purely transverse) gravitational radiation at $\mathcal{I}^+$.

Motivated now by the resemblance of (9.69) with the flux of a physical quantity, we can consider a heuristic notion of *Bondi-like* 4-momentum flux through $\mathcal{H}$. Considering the (time-like) unit normal $\hat{\tau}^a$ to $\mathcal{H}$

$$\hat{\tau}^a=\frac{\tau^a}{\sqrt{|\tau^b\tau_b|}}=\frac{1}{\sqrt{2C}}(\ell^a+Ck^a)=\frac{1}{\sqrt{2C}}(bn^a+Ns^a)\ , \tag{9.70}$$

we can introduce the component of a 4-momentum flux (dP^τ_i/dv) along a generic 4-vector η^a, as

$$\begin{aligned}\frac{dP^\tau[\eta]}{dv}&\equiv-\frac{1}{8\pi}\oint_{\mathcal{S}_v}(\eta^c\hat{\tau}_c)\left(\mathcal{N}^{(\mathcal{H})}_{ab}\mathcal{N}^{(\mathcal{H})ab}\right)dA\\&=-\frac{1}{16\pi}\oint_{\mathcal{S}_v}(\eta^c\hat{\tau}_c)\left(\sigma^{(h)}_{ab}\sigma^{(h)ab}\right)dA\ ,\end{aligned} \tag{9.71}$$

that has formally the expression of the flux of a *Bondi-like* 4-momentum. The corresponding flux of *energy* associated with an Eulerian observer n^a is

$$\frac{dE^\tau}{dv}(v)\equiv\frac{dP^\tau[n^a]}{dv}=\frac{1}{16\pi}\oint_{\mathcal{S}}\frac{b}{\sqrt{2C}}\left(\sigma^{(h)}_{ab}\sigma^{(h)ab}\right)dA\ , \tag{9.72}$$

where $\frac{b}{\sqrt{2C}}=\sqrt{1+N^2/2C}$. Analogously, the flux of linear momentum for ξ^a tangent to Σ_t would be

$$\frac{dP^\tau[\xi]}{dv}=-\frac{1}{16\pi}\oint_{\mathcal{S}_v}\frac{N}{\sqrt{2C}}(\xi^i s_i)\left(\sigma^{(h)}_{ab}\sigma^{(h)ab}\right)dA. \tag{9.73}$$

[1]We note that $\oint_{\mathcal{S}}\sigma^{(\ell)}_{ab}\sigma^{(\ell)ab}dA$ was used in [252] as a practical dimensionless parameter to monitor horizons approaching stationarity. Here they would correspond to a vanishing flow of transverse radiation.

Near equilibrium, *i.e.,* for $C \to 0$, we have $\sigma^{(h)}_{ab}\sigma^{(h)\,ab} \sim C$ on DHs so that the integrands in expressions (9.72) and (9.73) are $O(\sqrt{C})$, therefore regular and vanishing in this limit. Considering $(dP^\tau[\xi]/dv)$ as an estimate of the flux of gravitational linear momentum[1] through $\mathcal{H}$, the quantity P^τ_i would provide a *heuristic* prescription for a quasi-local DH linear momentum, a sort of *Bondi*-like counterpart of the heuristic *ADM*-like linear momentum introduced for DHs in Ref. [255], by applying the ADM expression for the linear momentum at spatial infinity i^o to the DH section $\mathcal{S}_t$

$$P[\xi^a] = \frac{1}{8\pi}\int_{\mathcal{S}_t} (K_{ab} - K\gamma_{ab})\,\xi^a s^b\, dA \ . \tag{9.74}$$

In this sense, the cross-correlation methodology we propose here and in paper I, can be formally compared with the quasi-local momentum approaches in [255, 256] to the study of the recoil velocity in binary black-holes mergers, showing the complementarity among these lines of research.

However, attempting to derive in our context a rigorous notion of quasi-local momentum on $\mathcal{H}$ would require the development of a systematic news-functions *framework* on DHs, in particular considering the possibility of longitudinal gravitational terms as in the DH energy flux (*cf.* [257, 258, 259, 260] for important insights in this topic). Such a discussion is beyond our present heuristic treatment, and we stick to our approach of considering the constructed local fluxes on $\mathcal{H}$ as quantities encoding information about (transverse) propagating gravitational degrees of freedom to be cross-correlated to the flux of Bondi momentum at $\mathcal{I}^+$.

9.9 Relevance of the 3+1 inner common horizon

In this section we emphasize the role of the inner horizon present in 3+1 slicings of black-hole spacetimes, and discussed in section 9.5.1, when considering the time integration of fluxes along the DH history. This is of specific relevance to the discussion made in the previous subsection, but it also applies to more general contexts.

Given the flux $F(v)$ through $\mathcal{H}$ of a physical quantity $Q(v)$, we can write

$$Q(v) = Q(v_0) + \mathrm{sign}(C)\int_{v_0}^{v} F(v')dv' \ , \tag{9.75}$$

and this requires a good parameterization of $\mathcal{H}$ by the (advanced) coordinate[2] v, as well as an initial value $Q(v_0)$. Finding such an initial value is in general non-trivial and this is precisely the motivation to consider in this section the evaluation of the fluxes along the whole spacetime history of $\mathcal{H}$, though from a $3+1$ perspective.

Given the $3+1$ slicing $\{\Sigma_t\}$, we can split the integration along the DH into an external and an internal horizon parts, as discussed in section 9.5.1. Denoting by v_c

[1] A related alternative prescription for a DH linear momentum flux would be given by angular integration of the appropriate components in the effective gravitational-radiation energy-tensor in [251].

[2] The coefficient $\mathrm{sign}(C)$, $+1$ for space-like and -1 for time-like sections of $\mathcal{H}$, corrects the possibility of integrating twice (null) fluxes through $\mathcal{H}$, when time-like sections of the trapping horizon $\mathcal{H}$ occur.

the advanced time associated with the moment t_c of first 3+1 appearance of the horizon, $\mathcal{H}$ is separated into the inner horizon $\mathcal{H}_{\rm int}$ labeled by $v_0 \leq v \leq v_c$ and the outer horizon $\mathcal{H}_{\rm out}$ labeled by $v_c \leq v \leq \infty$: $\mathcal{H} = \mathcal{H}_{\rm int} \cup \mathcal{H}_{\rm ext} = \left(\bigcup_{v_0 \leq v \leq v_c} \mathcal{S}_v\right) \cup \left(\bigcup_{v_c \leq v \leq \infty} \mathcal{S}_v\right)$. We can then rewrite equation (9.75) as

$$Q(v) = Q(v_0) + \mathrm{sign}(C) \int_{v_0}^{v} F(v')dv' = Q(v_0) + \mathrm{sign}(C) \int_{v_0}^{v_c} F^{\rm int}(v')dv' + \mathrm{sign}(C) \int_{v_c}^{v} F^{\rm ext}(v')dv' \quad (9.76)$$

$$= Q(v_0) + \mathrm{sign}(C) \int_{v_c}^{2v_c - v_0} F^{\rm int}(2v_c - v'')dv'' + \mathrm{sign}(C) \int_{v_c}^{v} F^{\rm ext}(v')dv' \,, \quad (9.77)$$

where $F^{\rm int}$ and $F^{\rm ext}$ denote, respectively, the flux of Q along the internal and external horizons. Note that in the second term in (9.77) we have inverted the integration limits in order to have an expression which is ready to be translated for an integration in t.

The coordinate v is not usually adopted in standard 3+1 numerical constructions of spacetimes. Because of this, we employ the time t defining the slicing $\{\Sigma_t\}$. Although the t function is not a good parameter on the whole $\mathcal{H}$, it correctly parameterizes the evolution of both the inner $\mathcal{H}_{\rm int}$ and outer $\mathcal{H}_{\rm ext}$ horizons separately: $\mathcal{H} = \mathcal{H}_{\rm int} \cup \mathcal{H}_{\rm ext} = \left(\bigcup_{t \geq t_c} \mathcal{S}_t^{\rm ext}\right) \cup \left(\bigcup_{t \geq t_c} \mathcal{S}_t^{\rm int}\right)$. Considering the splitting in equation (9.76), the use of t in the flux integration is perfectly valid as long as the t-integration includes both the standard external horizon part *and* an internal horizon part.

From equation (9.77) we write

$$Q(t) = Q_0 + \mathrm{sign}(C) \int_{t_c}^{\infty} F^{\rm int}(t')dt' + \mathrm{sign}(C) \int_{t_c}^{t} F^{\rm ext}(t')dt'$$

$$= Q_0 + \mathrm{sign}(C) \int_{t_c}^{t} F^{\rm int}(t')dt' + \mathrm{sign}(C) \int_{t_c}^{t} F^{\rm ext}(t')dt' + \mathrm{Res}(t) \,, \quad (9.78)$$

where Q_0 is a constant and the error $\mathrm{Res}(t)$

$$\mathrm{Res}(t) = \int_{t}^{\infty} F^{\rm int}(t')dt', \quad (9.79)$$

must be taken into account, since we cannot integrate up to $t \to \infty$ during the $3+1$ evolution. This error satisfies $\mathrm{Res}(t) \to 0$ as $t \to \infty$, so that the evaluation of $Q(t)$ by ignoring $\mathrm{Res}(t)$ in equation (9.78) improves as we advance in time t (*cf.* figure 9.11). Of course, this approach requires a good numerical tracking of the inner horizon, something potentially challenging from a numerical point of view (see [261] for a related discussion).

9.10 Link to the Horizon viscous-fluid picture

The basic idea proposed in [214] is that certain qualitative aspects of the late-time black-hole recoil dynamics, and in particular the anti-kick, can be understood in terms of the dissipation of the anisotropic distribution of curvature on the horizon. This picture in which the black-hole recoils as a result of the emission of anisotropic gravitational radiation in response to an anisotropic curvature distribution suggests that

the interaction of the moving black hole with its environment induces a *viscous* dissipation of the gravitational dynamics. In particular, one can consider a fluid analogy in which the distorted common apparent horizon can be replaced by a distorted and flexible membrane immersed in an ambient fluid. If the spherical shape represents that of equilibrium for the membrane, it will attain it after dissipating part of the energy in the deformation in the form of sound waves emitted in the ambient fluid. These sound waves will carry linear momentum and, for the conservation of the total linear momentum, the distribution of the deformations on the membrane will dictate the direction in which it will recoil.

In the black hole case, radiation is of course not emitted from horizon surface, which is causally disconnected from distant observers. However, the geometry of the horizon indeed reacts to the dynamics of the environment, so that horizon anisotropies can be used effectively to monitor the gravitational dynamics in the near-horizon region, in particular those aspects responsible of the recoil. With this picture in mind of the horizon as a test screen subject to viscous dynamics we have developed, a systematic framework based on a cross-correlation approach to probe near horizon dynamics in the spirit of an inverse-scattering problem. Starting from an effective quantity constructed on the intrinsic geometry of horizon sections, namely the Ricci scalar ${}^2R$, our analysis has led us in section 9.7 to the identification of the shear $\sigma^{(h)}_{ab}$ and of the expansion $\theta^{(h)}$ as the underlying relevant geometric objects, in particular interpreted in terms of news-like functions at $\mathcal{H}$. This identification permits to cast naturally the viscous-fluid picture into a gravitational framework, exploiting the fact that $\theta^{(h)}$ and $\sigma^{(h)}_{ab}$ have indeed an interpretation in terms of a bulk and shear viscosities. Stated differently, the cross-correlation approach offers a realization of the idea proposed in [214], expressing it in terms of more sound geometrical quantities. This result can already be appreciated explicitly in equation (9.41), but acquires a sound basis in the context of the membrane paradigm that we review below.

9.10.1 The black-hole horizon viscous-fluid analogy

Hawking and Hartle [262, 263, 264] introduced the notion of *black-hole viscosity* when studying the response of the event horizon to external perturbations. This leads to a viscous-fluid analogy for the treatment of the physics of the EH, fully developed by Damour [265, 266] and by Thorne, Price and Macdonald [267, 268], in the so-called *membrane paradigm* (see also [269, 270]). In this approach, the physical properties of the black hole are discussed in terms of mechanical and electromagnetic properties of a 2-dimensional viscous fluid. A quasi-local version of some of its aspects, applying for dynamical trapping horizons, has been developed in [271, 272, 273, 274].

In the fluid analogy of the membrane paradigm, dissipation in black hole dynamics is accounted for in terms of the shear and bulk viscosities of the fluid. The viscosity coefficients are obtained in the dissipative terms appearing in the momentum and energy balance equations for the 2-dimensional fluid. These equations are identified from the projection of the appropriate components of the Einstein equations on the horizon's

worldtube, namely evolution equations for $\theta^{(\ell)}$ and $\Omega_a^{(\ell)}$. For an EH these equations are [272]

$$\begin{aligned}\delta_\ell\theta^{(\ell)} - \kappa^{(\ell)}\theta^{(\ell)} &= -\frac{1}{2}\theta^{(\ell)2} - \sigma^{(\ell)}_{ab}\sigma^{(\ell)ab} - 8\pi T_{ab}\ell^a\ell^b \ , \\ \delta_\ell\Omega^{(\ell)}_c + \theta^{(\ell)}\,\Omega^{(\ell)}_a &= {}^2D_a\left(\kappa^{(\ell)} + \frac{\theta^{(\ell)}}{2}\right) - {}^2D_c\sigma^{(\ell)c}{}_a \\ &\quad +8\pi T_{cd}\,\ell^c q^d{}_a \, . \end{aligned} \tag{9.80}$$

The first one (*i.e.,* the Raychaudhuri equation (9.44) not assuming a affine geodesic parameterization, so that $\kappa^{(\ell)} \neq 0$) is interpreted as an energy dissipation equation. In particular, a *surface energy density* is identified as $\varepsilon \equiv -\theta^{(\ell)}/8\pi$. The second evolution equation for the normal form $\Omega_a^{(\ell)}$ provides a momentum conservation equation for the fluid, a Navier-Stokes-like equation (referred to as Damour-Navier-Stokes equation), once a momentum π_a for the 2-dimensional fluid is identified as $\pi_a \equiv -\Omega_a^{(\ell)}/(8\pi)$ [note that $\Omega_a^{(\ell)}$ is associated with a density of angular momentum. Dividing equations (9.80) by -8π and applying these identifications we obtain

$$\delta_\ell\varepsilon + \theta^{(\ell)}\varepsilon = -\frac{\kappa}{8\pi}\varepsilon - \frac{1}{16\pi}(\theta^{(\ell)})^2 + \frac{1}{8\pi}\sigma^{(\ell)}_{cd}\sigma^{(\ell)cd} + T_{ab}\ell^a\ell^b \ , \tag{9.81}$$

$$\delta_\ell\pi_a + \theta^{(\ell)}\pi_a = -{}^2D_a(\frac{\kappa}{8\pi}) + \frac{1}{8\pi}{}^2D^c\sigma^{(\ell)}_{ca} - \frac{1}{16\pi}{}^2D_a\theta^{(\ell)} - q^c{}_a T_{cd}\ell^d \ . \tag{9.82}$$

Writing the null evolution vector as $\ell^a = \partial_t + V^a$, for some (velocity) vector V^a tangent to $\mathcal{S}_t$, one can write: $\theta^{(\ell)} = D_aV^a + \partial_t \ln\sqrt{q}$ and $2\sigma^{(\ell)}_{ab} = \left({}^2D_aV_b + {}^2D_bV_a\right) - \theta^{(\ell)}q_{ab} + \frac{1}{2}\partial_t q_{ab}$. Then one can identify a fluid pressure $P \equiv \kappa/(8\pi)$, a (negative) bulk viscosity coefficient $\zeta = -1/(16\pi)$, a shear viscosity coefficient $\mu = 1/(16\pi)$, an external energy production rate $T_{ab}\ell^a\ell^b$ and external force density $f_a \equiv -q^c{}_aT_{cd}$. See also [275] for a criticism of this interpretation.

The analogue equations in the dynamical trapping horizons are obtained from the equations $\delta_h\theta^h$ and $\Omega_a^{(\ell)}$. These can be written as [271, 273, 274]

$$\left(\delta_h + \theta^{(h)}\right)\theta^{(h)} = -\kappa^{(h)}\theta^{(h)} + \sigma^{(h)}_{ab}\sigma^{(\tau)ab} + \frac{(\theta^{(h)})^2}{2} - 2{}^2D^aQ_a + 8\pi T_{ab}\tau^a h^b - \frac{\theta^{(k)}}{8\pi}\delta_h C \tag{9.83}$$

$$\left(\delta_h + \theta^{(h)}\right)\Omega^{(\ell)}_a = {}^2D_a\kappa^{(h)} - {}^2D^c\sigma^{(\tau)}_{ac} - {}^2D_a\theta^{(h)} + 8\pi q^b{}_a T_{bc}\tau^c - \theta^{(k)}{}^2D_aC \tag{9.84}$$

with $Q_a = \frac{1}{4\pi}\left[C\Omega^{(\ell)}_a - \frac{1}{2}{}^2D_aC\right]$ and $\kappa^{(h)} = -k_ah^b\nabla_b\ell^a$. Then, by introducing a *DH surface energy density* $\bar{\varepsilon} \equiv -\theta^{(\tau)}/(8\pi) = \theta^{(h)}/(8\pi)$ and keeping the definition for π_a, we can write for DHs (see [273, 274] for a complete interpretation of these equations)

$$\begin{aligned}\delta_h\bar{\varepsilon} + \theta^{(h)}\varepsilon &= -\frac{\kappa}{8\pi}\theta^{(h)} + \frac{1}{8\pi}\sigma^{(h)}_{ab}\sigma^{(\tau)ab} + \frac{(\theta^{(h)})^2}{16\pi} - {}^2D^aQ_a + T_{ab}\tau^a h^b - \frac{\theta^{(k)}}{8\pi}\delta_h C \ , \\ \delta_h\pi_a + \theta^{(h)}\pi_a &= -{}^2D_a\left(\frac{\kappa}{8\pi}\right) + {}^2D^c\left(\frac{\sigma^{(\tau)}_{ac}}{8\pi}\right) + \frac{{}^2D_a\theta^{(h)}}{16\pi} - q^b{}_aT_{bc}\tau^c + \frac{\theta^{(k)}}{8\pi}{}^2D_aC \ . \end{aligned} \tag{9.85}$$

We can now justify the viscosity interpretation of $\theta^{(h)}$ and $\sigma^{(h)}_{ab}$ by remarking that from the equations above, $\theta^{(h)}$ represents the expansion of the fluid appearing in the bulk viscosity term [with positive bulk viscosity coefficient $\zeta = 1/(16\pi)$]. Similarly, $\sigma^{(h)}_{ab}$ corresponds to the shear strain tensor and $\sigma^{(\tau)}_{ab}/(8\pi)$ to the shear stress tensor. Note that $\sigma^{(\tau)}_{ab}/(8\pi)$ and $\sigma^{(h)}_{ab}$ are not proportional in the strict dynamical case, $C \neq 0$, and therefore one cannot define a shear viscosity coefficient μ (In other words, a DH is not a Newtonian fluid).

Finally let us consider the observer given by the (properly normalized) time-like normal to $\mathcal{H}$ and let us define the 4-momentum current density associated with this observer: $p_a \equiv -T_{ab}\tau^b$. Then we note that the components of p_a are fixed by equations (9.85) together with the trapping horizon defining constraint equation (9.49). Indeed, $p_a h^a = -T_{ab}\tau^b h^a$ corresponds to the energy $\bar{\varepsilon}$ balance equation, while $p_b q^b{}_a = -T_{bc}\tau^c q^b{}_a$ gives the momentum π_a conservation equation, and $p_a\tau^a = -T_{ab}\tau^b\tau^a$ is a linear combination, using $\tau^a = 2\ell^a - h^a$, of the energy dissipation equation and the trapping horizon condition ($\delta_h\theta^{(\ell)} = 0$) depending on $T_{ab}\tau^a\ell^b$. Given the fundamental role of the latter in the geometric properties of the DH, in particular in the derivation of an area law under the future condition $\theta^{(k)} < 0$, this suggests the possibility of using the component $p_a\tau^a$ to define a balance equation for an appropriate entropy density. This point echoes the discussion of a hydrodynamic entropy current discussed in the context of a fluid-gravity duality [276, 277, 278, 279].

9.10.2 A viscous "slowness parameter"

The viscosity interpretation outlined in the previous subsection allows us now to make contact with the *slowness parameter* P introduced in [213]. We recall that the parameter P is constructed in terms of two dynamical timescales: a decay timescale τ and a oscillation timescale T

$$P = \frac{T}{\tau}. \tag{9.86}$$

In our fluid analogy, the bulk viscosity term $\theta^{(h)}$ controls the dynamical decay, whereas the shear viscosity term $\sigma^{(h)}_{ab}$ is responsible for the (shape) oscillations of the geometry. Given their physical dimensions $[\theta^{(h)}] = [\sigma^{(h)}_{ab}] = [\text{Length}]^{-1}$, averaging over horizon sections we can build instantaneous timescales[1] at any coordinate time t as

$$\frac{1}{\tau(t)} \equiv \frac{1}{A}\oint_{\mathcal{S}_t}(\xi^i_t s_i)\theta^{(h)}dA\ , \tag{9.87}$$

$$\frac{1}{T(t)^2} \equiv \frac{1}{A}\oint_{\mathcal{S}_t}(\xi^i_t s_i)\left(\sigma^{(h)}_{ab}\sigma^{(h)\,ab}\right)dA\ , \tag{9.88}$$

where ξ^i_t is the unit vector in the instantaneous direction of motion of the black hole. The term $(\xi^i_t s_i)$ in the definitions (9.87) - (9.88) is needed for giving a timescale associated with a change in linear momentum [if not, we would be dealing with a timescale

[1] These are not the only possibility to define τ and T, and therefore P, from viscosity scales. All variants should though give the same qualitative estimates.

for a change in energy, *cf.* (9.64)]. In other words, it is needed to account for the dissipation and oscillation of anisotropies in the geometry and not for spherically symmetric growths. This is consistent with the beating-frequency behaviour found in the timeseries developed for the head-on collision of two black holes. Note that equations (9.87)-(9.88) provide geometric prescriptions for the instantaneous timescales at the merger of a binary, a problem pointed out in [213]. Combining equations (9.86) and (9.87)-(9.88), and denoting $|\sigma^{(h)}|^2 = \sigma^{(h)}_{ab}\sigma^{(h)\,ab}$, we get

$$P(t) = \frac{\oint_{\mathcal{S}_t}(\xi^i_t s_i)\theta^{(h)}dA}{\left[A\oint_{\mathcal{S}_t}(\xi^i_t s_i)|\sigma^{(h)}|^2 dA\right]^{\frac{1}{2}}} \ . \tag{9.89}$$

As a consistency check we can verify for DHs that in situations close to stationarity (*i.e.,* $C \to 0$), the following scaling holds $\theta^{(h)} \sim C$ and $|\sigma^{(h)}|^2 \sim C$, so that $P \sim 1$, as suggested in the analysis of [213].

9.11 Conclusions

The analysis of spacetime dynamics is a very hard task in the absence of some rigid structure, such as symmetries or a preferred background geometry. However, this is the generic situation in the strong-field regime described by general relativity. In this context, (complementary) *effective* approaches providing insight into the qualitative aspects of the solutions and suggesting avenues for their quantitative modeling are of much value. In this spirit, we have discussed a cross-correlation approach to near-horizon dynamics. Other schemes, such as the curvature-visualization tools suggested in [280], share some aspects of this methodological approach.

In particular, we have argued that, in the setting of a $3+1$ approach to the black-hole spacetime construction, the foliation uniqueness of dynamical horizons provides a rigid structure that confers a preferred character to these hypersurfaces as probes of the black-hole geometry. Employed as inner screens in the *cross-correlation* approach, this DH foliation uniqueness permits to introduce the preferred normalization (9.47) of the null normals to apparent horizon sections and, consequently, a preferred angular scaling in the Weyl scalars on these horizons. The remaining time reparametrization freedom (time-stretch issue) does not affect the adopted cross-correlation scheme, where only the structure of the respective sequence maxima and minima is of relevance in the correlation of quantities defined in outer and inner screens.

Although this natural scaling of the Weyl tensors on DHs has an interest of its own, we have employed it here as an intermediate stage, linking the effective curvature vector $\tilde{K}^{\rm eff}_i(t)$ to the identification of the shear $\sigma^{(h)}_{ab}$, associated with the DH evolution vector h^a, as being proportional to a geometric DH news-like function $\mathcal{N}^{(\mathcal{H})}_{ab}$ in equation (9.58) [see also the role of $\theta^{(h)}$, in the more general $\mathcal{N}^{(\mathcal{H})}_{ab}$ in equation (9.62)]. On the one hand, this identification provides a (refined) geometric flux quantity $(dP^{(\mathcal{H})}/dv)_i(v)$ on DH sections to be correlated to the flux of Bondi linear momentum $(dP^{\rm B}/du)_i$ at $\mathcal{I}^+$

(these DH fluxes also share elements with quasi-local linear momentum treatments in the literature). On the other hand, given the role of $\sigma^{(h)}_{ab}$ and $\theta^{(h)}$ in driving the Ricci scalar ${}^2R$ along $\mathcal{H}$, equation (9.41) and system (9.42)-(9.45), this analysis justifies the use of $\tilde{K}^{\rm eff}_i(t)$ as an effective local estimator at $\mathcal{H}$ of dynamical aspects at $\mathcal{I}^+$.

The cross-correlation analysis has also produced two important by-products. First, we advocate the physical relevance of tracking the internal horizon in $3+1$ black-hole evolutions. This follows from the consideration of the time integration of fluxes along the horizon and its splitting (9.78) into internal horizon and external horizon integrals. Such expression is fixed up to an early-times integration constant, controlled by dynamics previous to the formation of the (common) DH (and possibly vanishing in many situations of interest). Second and most importantly, from the perspective of a viscous-horizon analogy we have identified a dynamical decay timescale τ associated with bulk viscosity and an oscillation timescale T associated with the shear viscosity. This is particularly relevant in the context of black-hole recoil dynamics, where the analysis in [213] shows that the qualitative features of the late time recoil can be explained in terms of a generic behaviour controlled by the relative values of a decay and an oscillation timescales. The viscous picture meets the rationale in [214] and offers an understanding of the relevant dynamical timescales from the (trace and traceless parts in the) evolution of the horizon intrinsic geometry, in particular providing *instantaneous* dynamical timescales at the merger and a geometric prescription for the slowness parameter $P = T/\tau$ introduced in [213].

As a final remark we note that while the material presented here places the arguments made in [214] on a much more robust geometrical basis, much of our treatment is still heuristic and based on intuition. More work is needed for the development of a fully systematic framework and this will be the subject of our future research.

9. DYNAMICS OF MOTS: EXPLAINING THE ANTI-KICK IN BINARY BLACK-HOLE MERGERS

10

Dynamics of MOTS: The pre-merger and merger phase

An unexpected feature has been observed in the simulation of binary black holes following their inspiral and merger [281]. After formation of a common apparent horizon, as the two MOTS, corresponding to the individual black holes continued to approach, they eventually touched and then penetrated each other. This con-penetration was surprising because it had not been expected from analytical discussions and had not been observed in prior simulations of binary black hole mergers. In retrospect, it is tempting to speculate in some heuristic sense that should a small black hole enter a very large black hole, the latter would hardly notice its presence. In fact, it has been been conjectured on the basis of the equivalence principle that a very small black hole should, in some appropriate sense, fall into the large one along a geodesic. However, such a perturbative picture is unreliable in the interior of the event horizon surrounding the two black holes, where the MOTS exist. Here we use an independent evolution code to first confirm that the individual MOTS do con-penetrate following a binary black hole merger and we analyze some of the highly interesting features revealed by the simulations. The presentation follows closely [4]

The simulations which first demonstrated the con-penetration of the individual MOTS were carried out with a code which was based upon Fock's treatment [282] of the harmonic formulation in terms of the densitized metric $\sqrt{-g}g^{\mu\nu}$ and which had been developed for the purpose of studying outer boundary conditions [283, 284]. By incorporating adaptive mesh refinement and a horizon tracker available in the CACTUS toolkit [285], the code was further developed to simulate a binary black hole inspiral using excision to deal with the internal singularities. The simulations presented in the present section are based upon an independent harmonic code based upon standard 3+1 variables and treating the singularities via punctures [286] rather than excision [287]. The evolution system is describe in section 3.3.

The work of Hayward [288] and Ashtekar and Krishnan [289] has led to a very rich mathematical theory of the dynamical horizons traced out by the evolution of MOTS, as reviewed in [290]. This theory has provided insight into both the classical and quantum

properties of black holes. In particular, the subject has strong bearing on numerical relativity because a MOTS can be identified quasi-locally by the vanishing expansion of its outward directed null rays, whereas the identification of an event horizon requires global information which is not available at the early stages of a simulation. Thus MOTS play a central role in the preparation of initial data sets for black holes and in tracking their subsequent evolution. A numerical study of MOTS has been carried out [291, 292], which confirmed the main features expected from the theory regarding the early stages of a binary inspiral. Recently, there has been substantial new theoretical development centered around the uniqueness and stability of MOTS [302, 303, 304, 307]. This recent theory has important bearing on how MOTS approach each other and penetrate. We review the main mathematical results and their relevance to the binary black hole problem in section 10.1.

The simulations presented in this chapter confirm the results observed in [281] and significantly extend the degree of con-penetration of the MOTS. There are five distinct stages as the MOTS approach and penetrate.

- The large separation of the individual MOTS. The properties of this stage are mainly determined by the choice of binary black hole initial data.
- Formation of a common apparent horizon as the MOTS approach.
- The initial osculation of the two MOTS.
- The con-penetration of the two MOTS.
- The ultimate fate of the individual MOTS.

The original simulation showing the con-penetration of two MOTS [281] and the numerical study of MOTS in the early stages of a binary black hole [292] were confined to the case of equal mass black holes. Here we consider the unequal mass case, with the goal of shedding light on what happens in the extreme mass ratio regime. Because of the computational cost in resolving different length scales, we limit ourselves to the case of a mass ratio $m_{small}/m_{large} = 1/4$. In order to better understand the geometry of the merger, we also restrict ourselves to the simplest case of a head-on collision. Already in this case, there are quite complicated geometrical effects.

Our simulations are based on time symmetric initial data for the two black holes. The time symmetry introduces some non-intuitive features of the initial MOTS, particularly when they are close together, which emphasize the importance of looking at their invariant geometrical properties rather than their coordinate description. We repeat, for the unequal mass case, the simulation of the head-on collision carried out by Krishnan and Schnetter [292] for equal mass black holes. They simulated this equal mass case with a code based upon a $3+1$ formulation of Einstein's equations (a BSSNOK formulation close to th one present in section 3.2), which is quite different than the harmonic formulation used here. As a check on our code, we find qualitative agreement with the results of [292] for the early stages before the individual MOTS touch. We then

continue the simulation of the head-on collision to the later stage where the individual MOTS penetrate, which could not be treated in [292] because of loss of accuracy. The original simulations of the con-penetration in [281] were limited by the excision region inside the individual MOTS. The simulations presented in this chapter are performed with a code that is able to track the con-penetration to a much further stage, essentially until the small MOTS has penetrated halfway into the large MOTS. At that stage its interior puncture is close to the large MOTS and the horizon tracker breaks down.

We demonstrate by numerical simulation that before the individual MOTS make contact a common outer apparent horizon forms, in accord with the theory described in section 2.2. When the two MOTS first touch, the expectation is that their mean surface curvatures agree at the point of osculation. Consistent with this expectation, our simulations show that the small MOTS produces a very strong tidal effect that causes the mean curvature of the large MOTS to rapidly grow, i.e. its curvature radius rapidly shrinks. On the other hand, as might be expected, the large MOTS has only a small tidal effect on the small one. We track this growth of mean curvature of the large MOTS as the con-penetration proceeds further. If the small black hole were to con-penetrate the large one completely a dramatic consequence of the underlying uniqueness theorems for MOTS would ensue. At the time where the back of the small MOTS enters the front of the large one, the theorems imply that the two MOTS must identically merge, either through shrinkage of the large MOTS or expansion of the small MOTS. Although our simulations cannot proceed to this stage, they provide some glimpse of how it might proceed.

10.1 Uniqueness and stability of MOTS

In this section we review some analytical results obtained for the uniqueness and stability of MOTS and time evolution. We will first present analytical results for the stability and uniqueness of the outermost MOTS in a given space-time. In a next step we will introduce the maximum principle as useful tool to probe the behavior and properties of MOTS. Last, we will cover some results obtained for the time evolution of MOTS and properties of MOTTs. Again consider a 3+1 foliation $x^\alpha = (t, x^i)$ with metric decomposition

$$g_{\mu\nu} = -n_\mu n_\nu + h_{\mu\nu} \tag{10.1}$$

where n_μ is the unit future directed time-like normal to the foliation. In a slice $\mathcal{M}_\tau = \{t = \tau\}$ consider a 2-surface $\mathcal{S}$ which is the boundary of a set Ω. We define its outward unit space-like normal N_i to point out of Ω. If $\mathcal{S}$ is defined as the level set of a function s, then

$$N_i = \frac{1}{\sqrt{D}} \partial_i s \tag{10.2}$$

with

$$D = h^{kl}(\partial_k s)(\partial_l s). \tag{10.3}$$

Setting $N_\mu = h^i_\mu N_i$ (so that $N^\mu \nabla_\mu t = 0$), this leads to the further decomposition

$$h_{\mu\nu} = N_\mu N_\nu + s_{\mu\nu}. \tag{10.4}$$

The outgoing null direction normal to $\mathcal{S}$ is

$$\ell^\mu = n^\mu + N^\mu, \tag{10.5}$$

where the normalization is determined by the Cauchy slicing. Its expansion is

$$\theta_+ = P + H \tag{10.6}$$

where

$$H = s^{\mu\nu}\nabla_\mu N_\nu \tag{10.7}$$

is the mean curvature of $\mathcal{S}$ in the Cauchy slicing,

$$P = s^{\mu\nu}\nabla_\mu n_\nu \tag{10.8}$$

is the 2-trace of the extrinsic curvature of the Cauchy slicing and ∇ is the covariant derivative with respect to g.

$\mathcal{S}$ is a MOTS if $\theta_+ = 0$, i.e. $P + H = 0$. Similarly,

$$\theta_- = P - H \tag{10.9}$$

is the expansion of the in-going null direction

$$k^\mu = n^\mu - N^\mu \tag{10.10}$$

normal to $\mathcal{S}$. The MOTS $\mathcal{S}$ is marginally trapped if $\theta_- < 0$. Since $\theta_- = \theta_+ - 2H = -2H$ for a MOTS, the trapping condition is equivalent to $H > 0$.

10.1.1 Stable and outermost MOTS

For a given slice $\mathcal{M}_\tau$ and a MOTS $\mathcal{S} \subset \mathcal{M}_\tau$ one can consider the normal graphs $\mathcal{S}_u$ of a function $u \in C^\infty(\mathcal{S})$, i.e. the surface parameterized by

$$F_u : \mathcal{S} \to \mathcal{M}_\tau : p \mapsto \exp(uN^i) \tag{10.11}$$

where exp denotes the exponential map of $\mathcal{M}_\tau$. The operator $\Theta_+ : C^\infty(\mathcal{S}) \to C^\infty(\mathcal{S})$ that maps a function u to the pull-back of the value of θ_+ on $\mathcal{S}_u$ to $\mathcal{S}$ has linearization given by

$$Lf = -\Delta f - 2s^{AB}S_A\partial_B f + f(\tfrac{1}{2}R_{\mathcal{S}} - S_A S^A + D^A S_A - \tfrac{1}{2}\chi^{AB}\chi_{AB} - G_{\mu\nu}\ell^\mu k^\nu) \tag{10.12}$$

with Δ the surface Laplacian of $\mathcal{S}$, $S_\mu = \nabla_\mu n_\nu N^\nu$, $R_{\mathcal{S}}$ denotes the scalar curvature of $\mathcal{S}$, $\chi_{\mu\nu} = \nabla_\mu \ell_\nu$, $G_{\mu\nu}$ denotes the Einstein tensor of the space-time and capital letters

refer to intrinsic coordinates x^A for $\mathcal{S}$. In particular s^{AB} denotes the inverse of the tangential projection of $s_{\mu\nu}$ to $\mathcal{S}$.

Although L is not self-adjoint, there exists a real eigenvalue $\lambda(\mathcal{S}) \in \sigma(L)$, which is the unique minimizer for the real part in the spectrum $\sigma(L)$ of L. This eigenvalue is simple, and the corresponding eigenfunction ϕ can be chosen with a definite sign. If $\lambda(\mathcal{S}) \geq 0$ we say that $\mathcal{S}$ is *stable*, if $\lambda(\mathcal{S}) > 0$ it is called *strictly stable*. We refer to [303, 304] for further details.

For the following, we require the surfaces $\mathcal{S}$ in question to be either bounding, $\mathcal{S} = \partial\Omega$, or bounding with respect to an interior boundary $\partial\mathcal{M}$, that is $\mathcal{S} = \partial\Omega \setminus \partial\mathcal{M}$. In both cases, we write $\mathcal{S} = \partial^+\Omega$ or refer to $\mathcal{S}$ being an outer boundary in this situation. In the scenario considered here, the inner boundary exists and is formed by trapped surfaces enclosing the punctures.

A MOTS $\mathcal{S} = \partial^+\Omega$ is called *outermost* if for all other MOTS $\mathcal{S}' = \partial^+\Omega'$ with $\Omega' \supset \Omega$ it follows that $\Omega' = \Omega$. In other words, there are no MOTS on the outside of $\mathcal{S}$.

In [306] it was shown that if $\mathcal{M}_\tau$ contains bounding outer trapped surfaces, as is the case if $\mathcal{M}_\tau$ is asymptotically flat, then there exists an outermost MOTS $\mathcal{S}^{\text{out}}$ that bounds the trapped region in $\mathcal{M}_\tau$. This means, that it is the enclosure of the region that contains outer trapped surfaces. Note that $\mathcal{S}^{\text{out}}$ is not necessarily connected. All components of $\mathcal{S}^{\text{out}}$ are stable, and $\mathcal{S}^{\text{out}}$ has area bounded uniformly from above by a constant depending only on the geometry of the slice $\mathcal{M}_\tau$. Furthermore, it has the property that there exists a positive $\delta > 0$, again depending only on the geometry of the slice $\mathcal{M}_\tau$, such that any geodesic starting on $\mathcal{S}^{\text{out}}$ in direction of its outward normal N^i does not intersect $\mathcal{S}^{\text{out}}$ within distance δ. In particular, two distinct components of $\mathcal{S}^{\text{out}}$ have distance at least δ. The constants mentioned depend in particular on an intrinsic curvature bound and on bounds for the second fundamental form $\nabla_\mu n_\nu$ and its derivatives. For the details of these estimates and all the dependencies of the constants we refer to [306]. Similar results have also been derived in [308, 309]. In the situation considered here, Galloway [310] established that $\mathcal{S}^{\text{out}}$ is a union of topological spheres. In [305] it has been furthermore established that the second fundamental form $\nabla_i N_j$ of a stable MOTS $\mathcal{S}$ is bounded in the supremum norm, provided the geometry of the slice is bounded.

10.1.2 The maximum principle for MOTS

A useful tool in the analysis of MOTS is the strong maximum principle. To state it, assume that $\mathcal{S}_\alpha$ for $\alpha = 1, 2$ are two connected C^2-surfaces with outer normals N^i_α. Assume further that there is a point p such that $\mathcal{S}_1$ and $\mathcal{S}_2$ touch at p. If the outer normals agree, $N^i_1 = N^i_2$, at p and $\mathcal{S}_2$ lies to the outside of $\mathcal{S}_1$, that is in direction of N^i_1, and furthermore

$$\sup_{\mathcal{S}_1} \theta_+[\mathcal{S}_1] \leq \inf_{\mathcal{S}_2} \theta_+[\mathcal{S}_2] \tag{10.13}$$

then $\mathcal{S}_1 = \mathcal{S}_2$. This version can be found in [306, Proposition 2.4] or in [307]. It implies in particular that two distinct MOTS $\mathcal{S}_1$ and $\mathcal{S}_2$ can not touch in such a way that their normals point in the same direction and one is enclosing the other.

The strong maximum principle provides an interpretation of strict stability. Assume that $\mathcal{S}$ is a strictly stable MOTS with outward normal N^i. Let ϕ be the principal eigenfunction of L. Deforming $\mathcal{S}$ in direction of the vector field ϕN^i then yields a foliation of a tubular neighborhood U of $\mathcal{S}$ with the following properties. First $U \setminus \mathcal{S} = U^- \cup U^+$ where N^i points into U^+. Moreover, U^+ is foliated by surfaces with $\theta_+ > 0$ and U^- is foliated by surfaces with $\theta_+ < 0$. The maximum principle then implies that there are no surfaces $\mathcal{S}' \subset U^+$ which bound relative to $\mathcal{S}$ and have $\theta_+[\mathcal{S}'] \leq 0$. Furthermore, there is no MOTS in U with outward normal aligned with that of $\mathcal{S}$.

10.1.3 Evolution of MOTS to MOTTs

Regarding the evolution of MOTS there are different approaches. In [303] it was shown that a strictly stable MOTS $\mathcal{S}$ can locally be continued to a smooth space-time track of MOTS, i.e. a marginally outer trapped tube (MOTT). More precisely, for a given $\bar{\tau}$ such that $\mathcal{M}_{\bar{\tau}}$ contains a strictly stable MOTS $\mathcal{S}_{\bar{\tau}}$ there exists $\varepsilon > 0$ such that for all $\tau \in (\bar{\tau} - \varepsilon, \bar{\tau} + \varepsilon)$ there is a stable MOTS $\mathcal{S}_\tau$ in $\mathcal{M}_\tau$ such that the $\mathcal{S}_\tau$ form a smooth space-like manifold. To emphasize the role of the stability operator in this picture, we recall the argument from [303]. Assume that $\mathcal{S}_\tau$ is a smooth family of MOTS passing through $\mathcal{S}_{\bar{\tau}}$. Then we can parameterize this tube by a map

$$F^\mu : (\bar{\tau} - \varepsilon, \bar{\tau} + \varepsilon) \times \mathcal{S}_{\bar{\tau}} \to \bigcup_{\tau \in (\bar{\tau} - \varepsilon, \bar{\tau} + \varepsilon)} \mathcal{M}_\tau \tag{10.14}$$

such that $\frac{\partial F^\mu}{\partial \tau} = V^\mu$, where V^μ is perpendicular to $\mathcal{S}_\tau$ at each point along the tube. Note that V^μ can be decomposed

$$V^\mu = \alpha n^\mu + \gamma N^\mu = \alpha(n^\mu + N^\mu) + (\gamma - \alpha)N^\mu = \alpha \ell^\mu + f N^\mu \tag{10.15}$$

where as before α denotes the lapse function of the slicing. Calculating the change of θ_+ under the deformation by V^μ at time $\bar{\tau}$, we thus obtain

$$\delta_{V^\mu} \theta_+[\mathcal{S}_{\bar{\tau}}] = \delta_{\alpha \ell^\mu} \theta_+[\mathcal{S}_{\bar{\tau}}] + \delta_{f N^\mu} \theta_+[\mathcal{S}_{\bar{\tau}}] = -\alpha W + Lf \tag{10.16}$$

where the first contribution is calculated via the Raychaudhuri equation with

$$W = \chi^{AB} \chi_{AB} + G_{\mu\nu} \ell^\mu \ell^\nu, \tag{10.17}$$

and the second part is just the definition of the stability operator. Since V^μ is tangent to a MOTT we have $\delta_{V^\mu} \theta_+[\mathcal{S}_{\bar{\tau}}] = 0$ and thus

$$Lf = \alpha W. \tag{10.18}$$

The operator L and the function W are given by the geometry of $\mathcal{S}_{\bar{\tau}}$ and the space-time geometry of $\mathcal{M}_{\bar{\tau}}$, whereas f is a function determined by equation (10.16). If $\mathcal{S}_{\bar{\tau}}$ is strictly stable then L is invertible. Thus the previous calculation can be turned around to conclude the existence of the desired MOTT. The causal structure of the tube follows

by the observation that the null energy condition implies $W \geq 0$. From stability one then obtains $f \geq 0$ via equation (10.18) as in [303, Lemma 3].

A similar argument was used in [302] to construct a MOTT through $\mathcal{S}_{\bar{\tau}}$ in the case it is stable but not strictly stable assuming $W \geq 0$ and $W \not\equiv 0$. A different approach is to take the outermost MOTS $\mathcal{S}_\tau^{\text{out}}$ of all slices $\mathcal{M}_\tau$ and define the apparent horizon of the slicing as $\mathcal{H} = \bigcup_\tau \mathcal{S}_\tau^{\text{out}}$. In generic space-times $\mathcal{H}$ is smooth up to a discrete set of outward jumps. See [302] for the details and the particular notion of generecity used therein. The same reference also provides the causal character of $\mathcal{H}$, namely that $\mathcal{H}$ is achronal. Moreover, if Ω_τ denotes the interior of $\mathcal{S}_\tau^{\text{out}}$, then $J^+(\Omega_\tau) \cap \mathcal{M}_\sigma \subset \Omega_\sigma$ for all $\tau < \sigma$. Here $J^+(\Omega_\tau)$ denotes the causal future of Ω_τ. In particular, if there is a MOTS at an initial time $\bar{\tau}$, then it will persist for all times.

10.1.4 Approaching MOTS

Assume that the space-time and the slicing are completely regular. Then the constant δ, the bound for the area, and the length of the second fundamental form of $\mathcal{S}^{\text{out}}$ remains uniformly controlled. If in this situation two components of a MOTS are closer than δ, none of these two components can be part of $\mathcal{S}^{\text{out}}$. In particular, the evolution of $\mathcal{S}^{\text{out}}$ will be discontinuous at some stage of the evolution. By the causality of $\mathcal{H}$, the jump is outward, and a new outermost MOTS has formed outside the tubes of the two original ones. Generically, after the jump time the jump target will split into two branches of MOTTs, a stable branch traveling outward and an unstable branch traveling inward. For a complete discussion of this jump in the outermost MOTS, we refer to [302]. An important fact to point out is that if two MOTS are close to each other then there is no reason to expect that they be stable, in contrast to the stability of $\mathcal{S}^{\text{out}}$.

Note that it is not known whether the area is of $\mathcal{S}^{\text{out}}$ is monotonic across the jumps. For jumps of MOTS other than $\mathcal{S}^{\text{out}}$, it is not even clear whether monotonicity of area should be expected along smooth pieces.

10.1.5 Exterior osculation of MOTS

The following considerations pertain to the collision between the MOTS of a large and small black hole as they first touch. Note that this situation is not prevented by the strong maximum principle. However, at the time of first contact, a common horizon already has formed according to the previous section 10.4.

In (10.6), the contribution to θ_+ from P is common to both MOTS, so that at a common point of osculation we must have

$$H_{(small)} = H_{(large)}. \tag{10.19}$$

Here the two mean curvatures are defined with respect to the respective outer normals, which in this case have opposite orientations. Thus the two MOTS do not share the same outgoing null direction ℓ. As a result of (10.19), the mean extrinsic curvature radius of the large and small MOTSs must match at the point of osculation. This can

be deceiving in terms of a coordinate picture of the MOTS since the connection of the Cauchy slice enters into the mean curvature. We have

$$H = s^{ij}\partial_i N_j - s^{ij}\Gamma^k_{ij}N_k. \tag{10.20}$$

At the point of osculation $N_{i(small)} = -N_{i(large)}$ so that the second term has the same magnitude but opposite sign for the small and large MOTS. Hence (10.19) implies

$$s^{ij}\partial_i N_{j(small)} = s^{ij}\partial_i N_{j(large)} - 2s^{ij}\Gamma^k_{ij}N_{k(large)} \tag{10.21}$$

or

$$D^{-1/2}_{(small)}s^{ij}\partial_i\partial_j s_{(small)} = D^{-1/2}_{(large)}s^{ij}\partial_i\partial_j s_{(large)} - 2s^{ij}\Gamma^k_{ij}N_{k(large)}. \tag{10.22}$$

This relates the coordinate curvatures $\partial_i\partial_j s$ of the functions describing the MOTS, as provided graphically by the code output. More geometrically meaningful output are plots of H during the evolution of the large and small MOTS, plots of the time dependence of their surface area, at a sequence of times elapsed during the evolution. An important property is whether $H > 0$ so that the MOTS are trapped.

In Thornburgh's apparent horizon finder [300, 301], $s = r - h(y^A)$, where r is a standard radial coordinate measuring Euclidean distance from some point x^i_0 and y^A are spherical coordinates arising from a six-patch treatment of the unit sphere. Then

$$\partial_i s = \frac{x^i}{r} - \partial_i h. \tag{10.23}$$

In the axisymmetric case corresponding to the head-on collision of black holes, we must have $\partial_i h = 0$ on the symmetry axis and therefore also at the points where an osculation can occur. Thus, at an an osculation point, we have $\partial_i s = (x^i - x^i_0)r^{-1}$ and $D = h_{ij}(x^i - x^i_0)(x^j - x^j_0)r^{-2} = h_{zz}$, where we align the symmetry about the z-axis. Thus $D_{small} = D_{large}$ at the point of osculation and (10.22) reduces to

$$s^{ij}\partial_i\partial_j s_{(small)} = s^{ij}\partial_i\partial_j s_{(large)} - 2s^{ij}\Gamma^k_{ij}\partial_k s_{(large)}, \tag{10.24}$$

where $\partial_k s_{(large)} = -\partial_k s_{(small)}$.

10.1.6 Interior Osculation

If the MOTS of the small black hole were to remain intact and continue to completely penetrate the large one then there would again be a point of osculation between them just as the small one completely passes inside. At this second contact point p, the two outer null directions have the same orientation. Thus $\theta_+(p) = 0$ for the common outgoing null direction $\ell(p)$. The strong maximum principle implies in the present case that the two MOTS coincide globally. Thus the mean curvatures of the large and small MOTS must adjust dramatically to match each other unless full con-penetration is prevented by a singularity or some other feature.

According to section 10.1.2, it is impossible in this case that either of the two osculating MOTS is strictly stable up to the time of coincidence. In fact, the normal

separation of one MOTS above the other, yields after linearization at the time where they coincide a function in the kernel of the stability operator. If the approach is fast enough, this function is non-zero and changes sign. This implies instability of the two individual MOTS shortly before and at the time of coincidence.

If the two individual inner MOTS do coalesce to a single one, this raises the possibility of a scenario in which the two MOTTs traced out by the individual MOTS merge and then connect via the unstable branch of the forming common horizon to the MOTT traced out by the apparent horizon, as described in section 10.4 and depicted in figure 10.1. Although this figure looks highly suggestive, there is no reason to believe that it is actually valid. What currently is known is that there always exists an outermost MOTS, that it can jump, and that at the time of the jump there are two branches emanating from the jump target. The current state of the analytic theory is not such that it is able to determine how long the unstable MOTS continue to exist. See [302] for a related discussion.

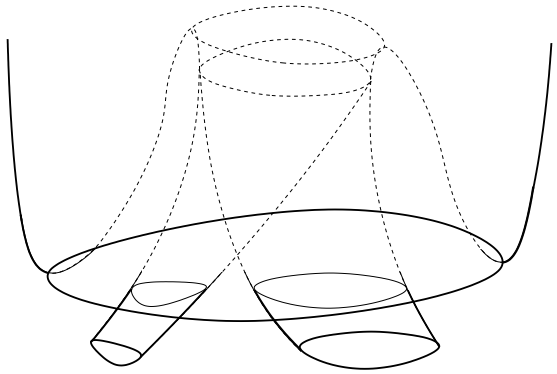

Figure 10.1: A possible scenario for the evolution of the trapped tubes. The outermost MOTS are drawn in bold. The common outermost MOTS develops before the first time of contact. After the separate MOTTs penetrate, the diagram illustrates the speculative scenario that they merge and join with the unstable branch from the jump. This speculative part of the figure is indicated by the dashed part .

10.2 Simulation results

We present the results of the simulation of the head-on collision of two black holes with initial masses M and $M/4$. Besides outputting the coordinate shapes of the MOTS detected by the horizon finder, in order to analyze their intrinsic geometrical structure we also output the time dependence of their total area, surface plots of their mean curvature H and surface plots of the determinant Q of the intrinsic 2-metric q_{ab} of the MOTT which they trace out. As the theory implies that a stable MOTS traces out a space-like 3-surface, this requires that $Q > 0$ uniformly on the surface, i.e. the MOTT must have positive signature. Thus Q provides a useful numerical tool for monitoring

when a MOTS has become unstable [292].

10.3 Initial configuration of the MOTS

We use the same time symmetric Brill-Lindquist data to initiate an axisymmetric head-on-collision as in [292] with the exception that the black holes now have the unequal masses M and $M/4$. The conformal flatness of the initial 3-metric provides a natural choice of Euclidean coordinates (x, y, z). We choose the z-axis to be the axis of symmetry. The punctures corresponding to the two black holes are initially located at $z_1 = 0.8M$ and $z_2 = -0.2M$, with a displacement of a half grid-step off the axis of symmetry in order to avoid numerical problems. This configuration reduces the initial tidal distortion of the black holes.

As the initial data sets are time-symmetric, the MOTS condition reduces to $H = 0$, i.e. from (10.20)

$$s^{ij}\partial_i\partial_j s = s^{ij}\Gamma^k_{ij}\partial_k s. \tag{10.25}$$

Then for a sequence of initial data for which the two black holes approach each other, (10.22) implies

$$s^{ij}\partial_i\partial_j s_{(small)} \to -s^{ij}\partial_i\partial_j s_{(large)} \tag{10.26}$$

at the point of closest approach. Thus if one MOTS appears convex at the point of closest approach then the other must appear concave with the exact same magnitude of curvature.

Another feature of the sequence of time symmetric data sets is that the MOTS do not touch as their initial separation is made smaller. This is also a consequence of the uniqueness theorem for MOTS. In the time symmetric case both MOTS satisfy $\theta_+ = \theta_- = 0$. If they were to touch, at the common point the outer null normal to one MOTS would be the same as the inner null normal to the other. But since both null directions have vanishing expansion, this would violate the uniqueness theorem. Note that in the time symmetric case, a MOTS is also a minimal surface so that this result also follows from the uniqueness theorem for minimal surfaces. For a more detailed study of a sequence of initial data sets we refer the interested reader to [240].

10.4 Approaching MOTS

As the individual MOTS approach, a common outer horizon (apparent horizon) forms before they touch at $t = 0.384M$, in accord with the theory described in section 10.4. Figure 10.2 shows the MOTS before and just after the appearance of the common horizon at time $t = 0.384M$ and $T = 1.452M$.

Surface plots, on the 6-patch system of the horizon finder, of the mean curvature H of the individual MOTS at times $0.384M$ and $1.452M$ are shown in figure 10.3. Initially, these mean curvatures are zero, as a result of the time symmetry. At $t = 0.384M$, they are fairly uniform on the scale shown (if we were to choose a refined scale we would see that indeed already at this stage small anisotropies are present) and have roughly

the 4 to 1 ratio of the initial masses. At $t = 1.452M$, the larger MOTS has significant tidal distortion due to the the smaller one.

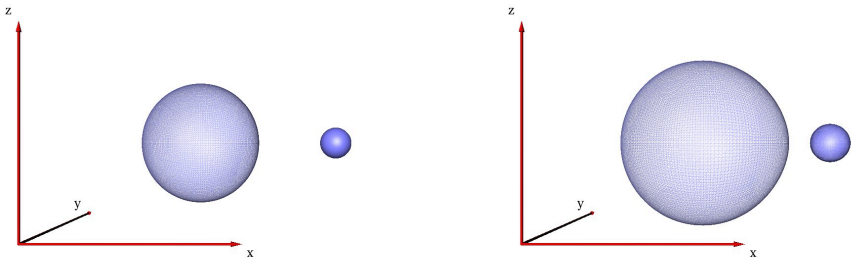

Figure 10.2: Coordinate shapes of both individual apparent horizons at times $t = 0.384M$ (left) and $t = 1.452M$ (right).

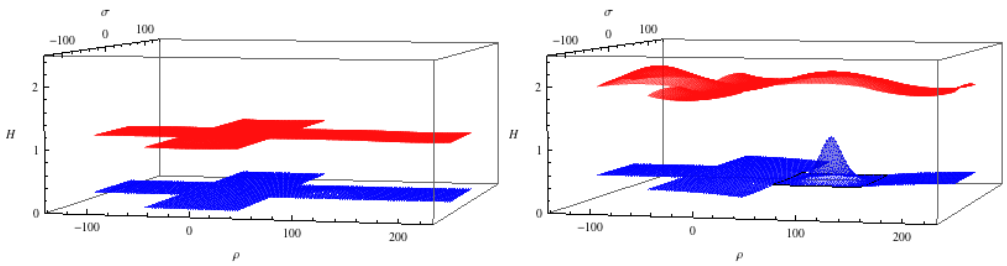

Figure 10.3: Mean curvature H of both individual apparent horizons at times $t = 0.384M$ (left) and $t = 1.452M$ (right) shown as a function of the 'laid-out' angular coordinates ρ and σ of the horizon finder.

Figure 10.4 provides surface plots of the determinant Q at times $0.384M$ and $1.452M$, for the two individual MOTS and the unstable inner branch of the common outer MOTS.

10.5 Exterior osculation of MOTS

At $t = 1.974M$ the front-sides of the approaching MOTS touch, as portrayed by their coordinate representations shown in figure 10.5. At this time, figure 10.6 shows surface plots of the mean curvatures of the individual MOTS. Now the tidal distortion has

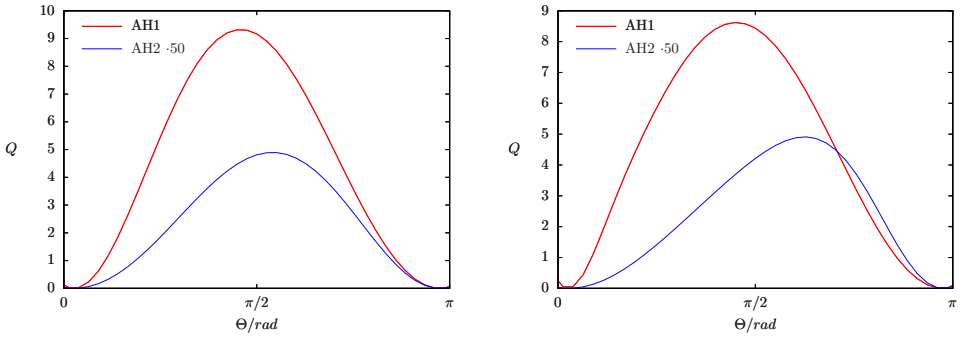

Figure 10.4: Determinant Q of both individual apparent horizons at times $t = 0.384M$ (left) and $t = 1.452M$ (right) shown as a function of Θ.

increased so that their mean curvatures are equal at their common point, as required by (10.19).

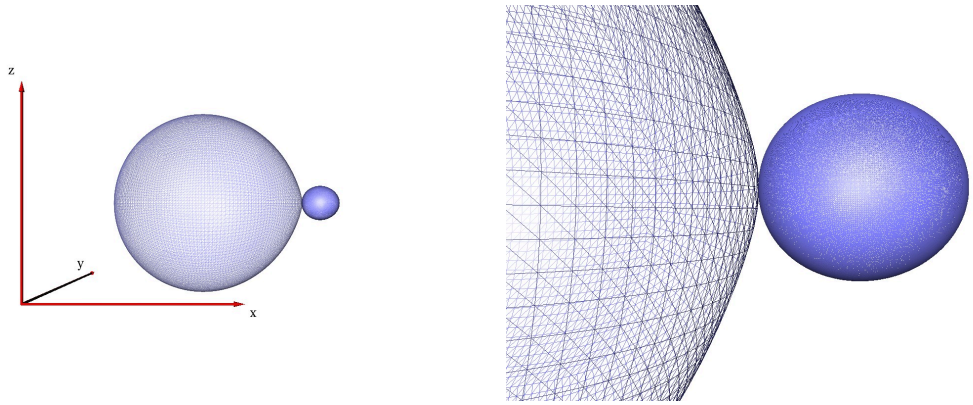

Figure 10.5: Default (left) and zoomed-in view (right) of the coordinate shapes of both individual apparent horizons at time $t = 1.974M$.

Figure 10.7 shows the determinant Q of the intrinsic two-metric induced on the horizon.

10.6 Con-penetration in the MOTS

As the MOTS continue to approach we continue to monitor the shapes of the two individual apparent horizons. Figure 10.8 shows the coordinate shapes of both individual MOTS as they start to overlap. The left panel of figure 10.8 shows the two individual MOTS at $t = 2.179M$. We clearly see a region of overlap and we observe the coordinate shape of the larger MOTS being affected by the smaller one penetrating. The right panel of figure 10.8 illustrates the coordinate shapes at a later time $t = 2.538M$.

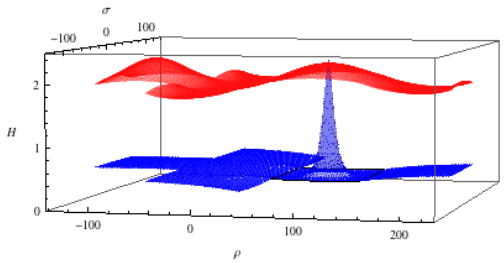

Figure 10.6: Mean curvature H shown as a function of the 'laid-out' angular coordinates ρ and σ of the horizon finder of both individual apparent horizons at time $t = 1.97384M$.

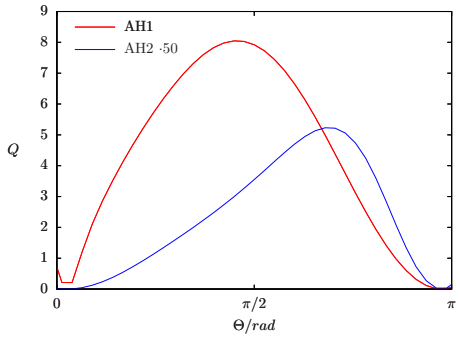

Figure 10.7: Determinant Q shown as a function of Θ for both individual apparent horizons at time $t = 1.97384M$.

At this time the smaller MOTS has entered half-way into the larger MOTS and the puncture of the smaller MOTS might interfere with the shape of the 2-surface of the larger MOTS. As our simulation progresses further we loose the larger MOTS. If this is due to the horizon finder breaking down for numerical reasons or simply the MOTS ceases to exist is only a matter of speculation. In addition to the coordinate shapes figure 10.9 shows surface-plots of the mean-curvature of both individual MOTS at the same times $t = 2.179M$ and $t = 2.538M$. In the left panel of figure 10.9 we see the mean curvature at the front end of the larger MOTS continuing to grow and actually obtain larger values then the mean curvature of the smaller MOTS. In the right panel of figure 10.9 we see the evolution of the mean curvature in the region located towards the smaller MOTS decrease in its value and show an oscillatory behavior. Again this easily could be attributed to the smaller MOTS puncture interfering with the results obtained on the larger MOTS' 2-surface. To highlight the effect the tidal-distortion on the larger MOTS caused by the smaller MOTS figure 10.11 now shows the mean

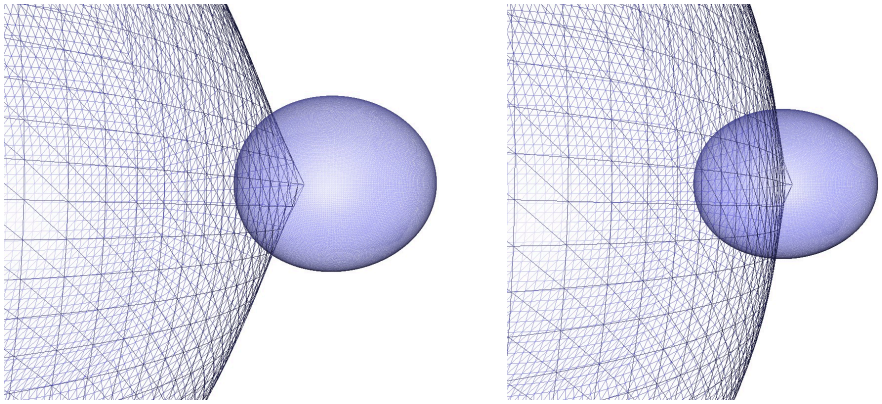

Figure 10.8: Zoomed-in view of the coordinate shapes of both individual apparent horizons at times $t = 2.179M$ (left) and $t = 2.538M$ (right).

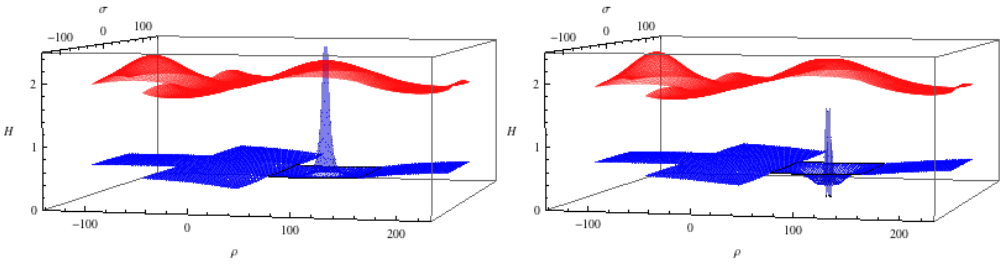

Figure 10.9: Mean curvature H shown as a function of the 'laid-out angular coordinates ρ and σ of the horizon finder of both individual apparent horizons at times $t = 2.1785M$ (left) and $t = 2.538M$ (right).

curvature only evaluated at the front-end points of both individual MOTS (front-end here being the closest point being located towards the other MOTS) as they approach each other. This provides a time-series of the interaction of the MOTS at the points where they first touch. While we see the mean curvature at the front-end of the smaller MOTS grow initially, it starts to settle down to a constant value as the solution adapts to the chosen gauge. In contrast to that the time evolution of the mean curvature at the front-end point of the larger MOTS shows a steep increase as the smaller MOTS approaches. At time $t = 2.179M$, and as already presented in figure 10.5, we see the values of both mean curvatures agree as expected from (10.19). After that the two MOTS begin to overlap, and the mean curvature at the front end point of the larger MOTS continues to grow before it suddenly shows a jump and drops to a much smaller value. This jump is not a result of our chosen spatial or time resolution (i.e. the time-

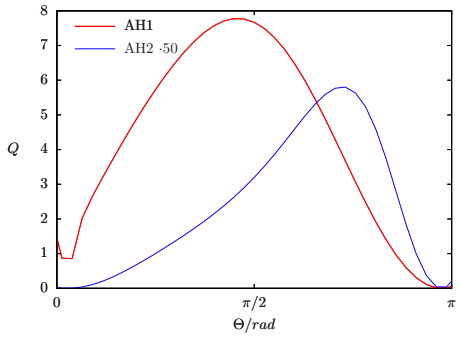

Figure 10.10: Determinant Q shown as a function of Θ for both individual apparent horizons at time $t = 2.1785M$.

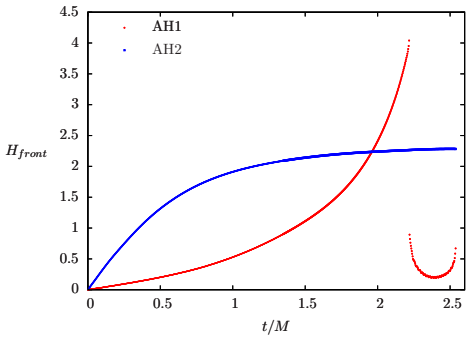

Figure 10.11: Mean curvature of the front end points of both apparent horizons H_{front} shown as a function of time.

step chosen in our simulations) as we can reproduce it by at different resolutions. It can be attributed to our chosen time-slicing intersecting with two MOTS and as the jump appears the horizon finder jumps from one surface to the other. This jump is also visible in figure 10.12, which shows the time evolution of the area A of both individual MOTS. Again, while we only see a minimal growth in the area of the smaller MOTS which is caused by numerical error, the larger MOTS shows a discontinuous jump in the area evolution.

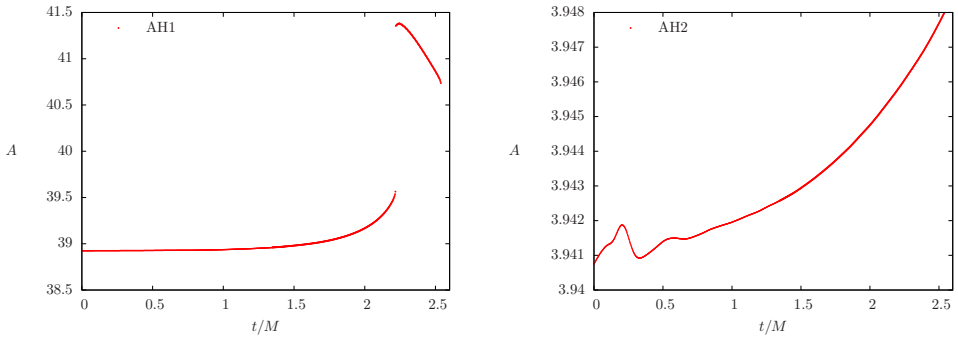

Figure 10.12: Area A of both apparent horizons shown as a function of time.

11

EM counterparts of binary black-hole mergers

In this chapter we present results from performing simulations of binary black-hole mergers immersed in a uniform magnetic field. Part of binary black-hole systems are expected to be formed as the consequence of galaxy mergers, where both galaxies are the host of supermassive black holes at their center. As those galaxies merge an accretion disc is formed for both black holes when still far apart. As the black holes get closer and closer in their separation eventually the time-scale of the gravitational wave energy loss will become shorter than the viscous time-scale. At this point most of the remnant gas will be ejected from the vicinity of the two black holes and a circumbinary disc will be formed [311, 312, 313]. In the final stage of coalescence the binary black-hole system will now be immersed in a low-density gas or plasma, and since most of the circumbinary discs are believed to be magnetized, a magnetic field anchored at the circumbinary disc at a radius of $100M - 1000M$ will also be present in the region containing the black-hole binary. Since the gas or plasma can now also radiate electromagnetically these systems form an ideal candidate for a detection of an EM counterpart signal accompanying the gravitational waves emitted. Detecting such an EM counterpart will benefit greatly the characterization of the source in both its parameters and sky localization and additionally provides an excellent verification for the detected gravitational wave signal.

As a first step towards a systematic modeling of the electromagnetic (EM) emission from an inspiraling and merging black hole binary we present results from a simple scenario in which the binary moves in a uniform magnetic field assumed to be anchored to a distant circumbinary disc. We study this system by solving the Einstein-Maxwell equations as detailed in chapter 5 in which the EM fields are chosen with strengths consistent with the values expected astrophysically and treated as test-fields. We study these systems in various approximations, first when the system is in an EV, i.e. no sources are present and only EM fields exits in our space-time. After presenting a number of tests performed for single black holes to assess the accuracy and validity of our simulations, we perform a set of spin-aligned or anti-aligned equal-mass binary

black-hole simulations and show that in this scenario the EM radiation in the lowest $\ell = 2, m = 2$ i multipole accurately reflects the gravitational one, with identical phase evolutions and amplitudes that differ only by a scaling factor. We also compute the efficiency of the energy emission in EM waves and find that it scales quadratically with the total spin and is given by $E^{\rm rad}_{\rm EM}/M \simeq 10^{-15} \left(M/10^8\ M_\odot\right)^2 \left(B/10^4\ {\rm G}\right)^2$, hence 13 orders of magnitude smaller than the gravitational energy for realistic magnetic fields. Although, unlikely to be detected *directly* and simultaneously with the gravitational-wave one, we propose the possibility that this radiation can be detected through indirect processes, driven by changes in the EM fields. If the accretion rate of the circumbinary disc is small and sufficiently stable over the timescale of the final inspiral, then the EM emission may be observable *indirectly* as it will alter the accretion rate through the magnetic torques exerted by the distorted magnetic field lines. In a second step we perform simulations in the force-approximation, i.e. the black holes are now immersed in a tenous plasma and we allow for electric currents to be present additionally to the EM fields itself (see section 11.4 for details). As the binary evolves it now not only interacts with the EM fields but also with the plasma, accelerating particles. Palenzuela and collaborators showed that a dual-jet structure will be formed in addition to an non-collimated emission [149, 314]. However it is not straight- forward in the modeling of these systems to determine genuine EM radiation because of the presence of the background magnetic field. We have therefor in detail investigated different measure for the EM luminosity. It is of great importance to use a proper measure to accurately determine the chances of observing the emission in both the jets and the non-collimated emission with realistic telescopes. We present a detailed assessment of the chances of detecting an EM counterpart from a binary black-hole system and accurately depict the structure of the emission in EM waves and the effect on the plasma in the vicinity of the black holes. In addition we present results on the treatment of the force-free equations. We compare different methods to enforce the system to stay in the force-free regime and show that by using a suitable Ohm's law prescription in combination with a suitable treatment of regions where current sheets can form (see chapter 4) we achieve lower violations of the force-free constraints and therefor more accurate simulations. The presentation in this chapter follows closely the work in [2, 3].

11.1 Physical and Astrophysical Setup

The astrophysical scenario we have in mind is motivated by the merger of supermassive black holes binaries resulting from galaxy mergers. More specifically, we consider the astrophysical conditions that would follow the merger of two supermassive black holes, each of which is surrounded by an accretion disc. As the merger between the two galaxies takes place and the black holes become close, a "circumbinary" accretion forms and reaches a stationary accretion phase. During this phase, the binary evolves on the timescale of the emission of gravitational radiation and its separation progressively decreases as gravitational waves carry away energy and angular momentum from the system. This radiation-reaction timescale is much longer than the (disc) accretion

timescale, which is regulated by the ability of the disc to transport outwards its angular momentum (either via viscous shear or magnetically-mediated instabilities). As a consequence, for most of the evolution the disc slowly follows the binary as its orbit shrinks. However, as the binary separation becomes of the order of $\sim 10^5 - 10^6\,M$, the radiation-reaction timescale reduces considerably and can become smaller than the disc accretion one. When this happens, the disc becomes disconnected from the binary, the mass accretion rate reduces substantially and the binary performs its final orbits in an "interior" region which is essentially devoid of gas [311, 312, 313]. This represents the astrophysical setup we place our simulations into.

We introduce a coupling between the binary and the disc via a large-scale magnetic field which we assume to be anchored to the disc, whose inner edge is assumed to be at a distance of $\sim 10^3\,M$ and is effectively outside of our computational domain, while the binary separation is only of $\sim 10\,M$, where M is the total gravitational mass of the binary. We note that although the large-scale magnetic field is poloidal, it will appear as essentially uniform within the "interior region" where the binary evolves and which we model here. As a result, the initially magnetic field adopted has Cartesian components given simply by $B^i = (0, 0, B_0)$ with $B_0\,M = 10^{-4}$ in geometric units or $B_0 \sim 10^8$ G for a binary with total mass $M = 10^8\,M_\odot$. We note that although astrophysically large, the initial magnetic field considered here has an associated EM energy which is several orders of magnitude smaller than the gravitational-field energy. As a result, any effect from the EM field dynamics on the space-time itself will be negligible and so the EM fields are treated here as test-fields. The case of stronger magnetic fields and their consequent impact on the space-time is an interesting aspect on its own but has not been investigated in this thesis.

11.2 Isolated Black Holes in EV

We first study isolated black holes, both as a check of our implementation and to analyze the interaction of the chosen external initial magnetic field with the space-time curvature generated by the black holes. The initial magnetic field in all simulations is uniform with strength B_0 and aligned with the z-axis, while the initial electric field is zero everywhere. Although this solution satisfies the Maxwell equations trivially, it is not a stationary solution of the coupled Einstein-Maxwell system for the chosen black hole initial data. The solution thus exhibits a transient behavior and evolves towards a time-independent state given by a solution first found by Wald [315]. One important feature of Wald's solution is that in the case of spinning black holes, a net charge (and hence a net electric field) will develop as a result of "selective accretion" and whose asymptotic value is simply given by $Q = 2B_0J$. Although this charge is astrophysically uninteresting, being limited to be $Q/M \leq 2B_0M \simeq 1.7 \times 10^{-20}\,B_0(M/M_\odot)$ G [315] for a Kerr black hole with $J/M^2 \leq 1$, it i represents an excellent testbed for our numerical setup.

To validate the ability of the code to recover this analytic solution we have performed several tests involving either a Schwarzschild black hole or Kerr black holes

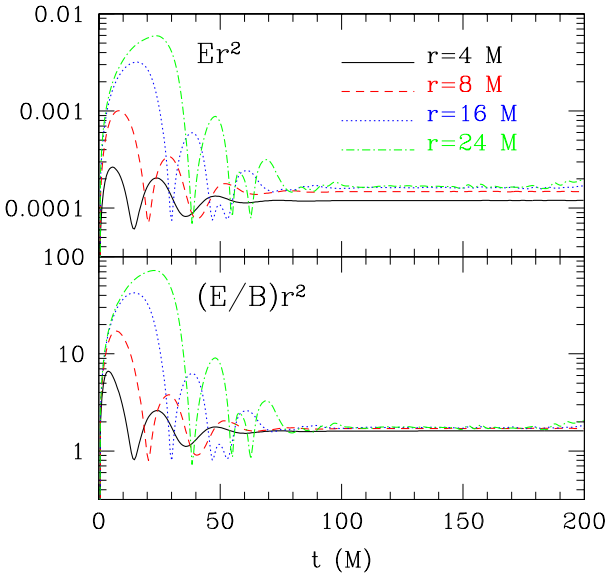

Figure 11.1: Recovery of Wald's solution for an isolated Kerr black hole with dimensionless spin $a = 0.7$. Shown in the top panel are the values of the electric field as measured at different distances from the origin; since $Er^2 \sim B_0 J$, the different lines should overlap at late times if the magnetic field is uniform which is evident in the figure. Shown in the bottom panel is the ratio of the electric and magnetic fields which is proportional to the black hole spin only. Note the transitory state until $t \approx 70M$, when the solution reaches a stationary state.

with dimensionless spin parameters $a = J/M^2 = 0.7$ (this value chosen as it is close to the final spin values resulting from the merger simulations covered in section 11.2). In this latter case, the spin vector was chosen to be either parallel to the background magnetic field, *i.e.,* with $J^i = (0, 0, J)$ or orthogonal to it, *i.e.,* with $J^i = (J, 0, 0)$. As expected, the early stages in the evolution reveal a transient behavior as the EM fields rearrange themselves and adapt to the curved space-time reaching a stationary configuration after about $\sim 70\,M$. The electric field, in particular, goes from being initially zero to being nonzero and decaying radially from the black hole.

Although the original solution found by Wald was expressed in Boyer-Lindquist coordinates, there is a simple way to validate that our gauge is sufficiently similar (at least at far distances) and that the numerical solution approaches Wald's one for an isolated black hole in a uniform magnetic field. This is shown in figure 11.1, which reports the time evolution of the EM fields E and B for a simulation of the Kerr black hole with spin $a = 0.7M$ aligned with the magnetic field. In particular, the top panel shows the time evolution of the electric field when the latter is rescaled by the radial positions where it is measured, *i.e.,* Er^2 with $r = 4\,M, 8\,M, 16\,M$ and $24\,M$. Because of $E \propto B_o J/r^2$, one expects the different lines to be on top of each other. This is clearly the case for the data extracted at $r = 16\,M$ and $24\,M$, but it ceases to be true for the

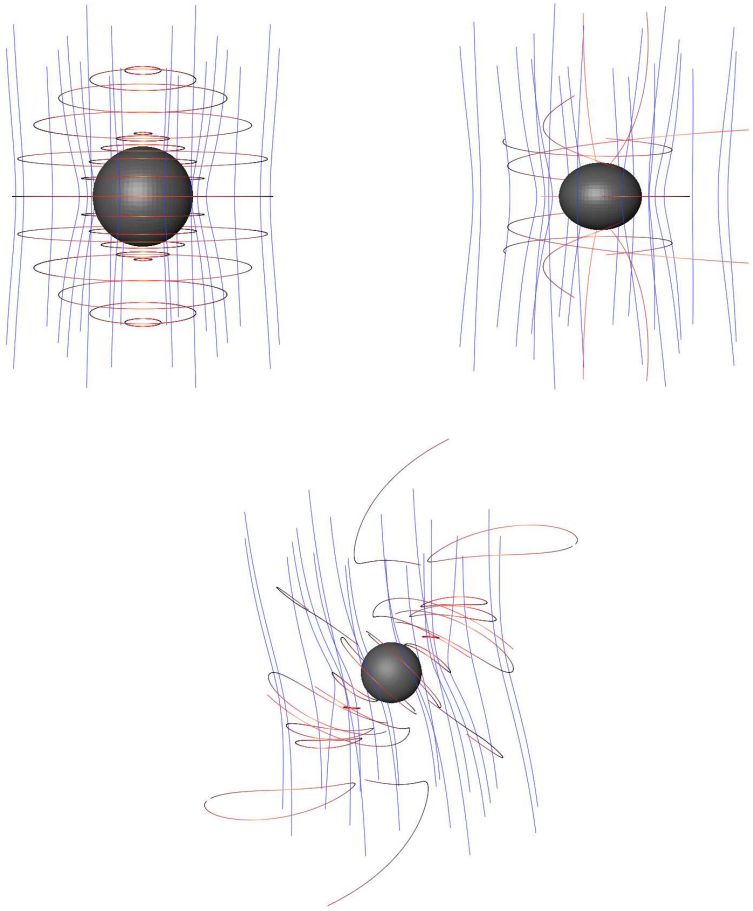

Figure 11.2: *Left panel:* Magnetic (blue) and electric field (red/magenta) field lines at $t = 200\,M$ for a Schwarzschild black hole. *Central panel:* the same as in the left panel but for a Kerr black hole with spin $a = J/M^2 = 0.7$ aligned with the magnetic field, *i.e.,* $J^i = \{0, 0, J\}$. *Right panel:* the same as in the center panel but for a Kerr black hole with spin $a = J/M^2 = 0.7$ which is orthogonal to the magnetic field, *i.e.,* $J^i = \{J, 0, 0\}$. Indicated with black surfaces are the apparent horizons.

data at $r = 4\,M, 8\,M$, for which the magnetic field and gauge structure are strongly influenced by the black-hole geometry. Interestingly, however, in this strong-field region near the black hole another scaling can be found and which is closely related to one expressed by Wald's solution. In particular, the radial dependence of the magnetic field can be factored out by considering the ratio of the electric and magnetic field which, in Wald's solution, should be proportional to the black-hole spin only. The bottom panel of figure 11.1 shows therefore the evolution of $(E/B)r^2 \sim J$ which is indeed a constant at all the radial positions as shown by the good overlap among the different curves. We find that this scaling can be used as an effective test which is valid at all

radial positions. These observations, together with the clear approach to a stationary configuration indicate the asymptotic (in time) behavior is indeed described by Wald's solution.

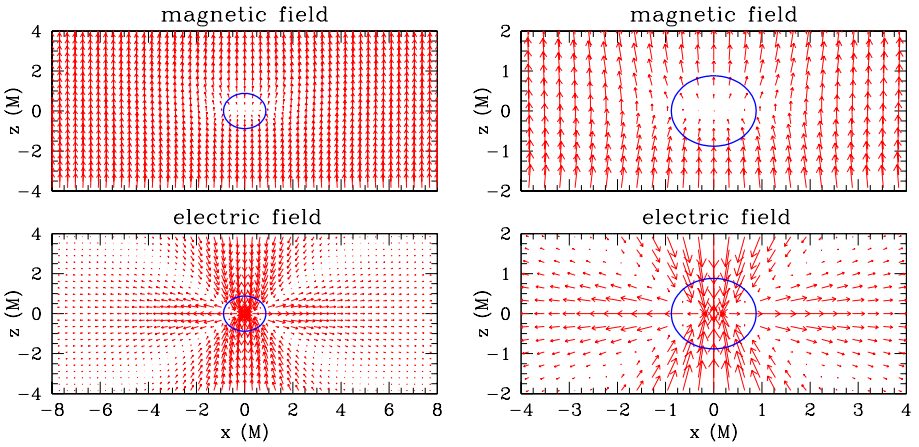

Figure 11.3: *Left panel:* Large-scale magnetic and electric field lines on the plane $y = 0$ and at $t = 200\,M$ for a Kerr black hole with spin $J/M^2 = 0.7$ aligned with the magnetic field, *i.e.,* along the z-axis. Indicated with blue circles are the apparent horizons. *Right panel:* The same as on the left panel but on a smaller scale to highlight the fields structure in the vicinity of the black hole.

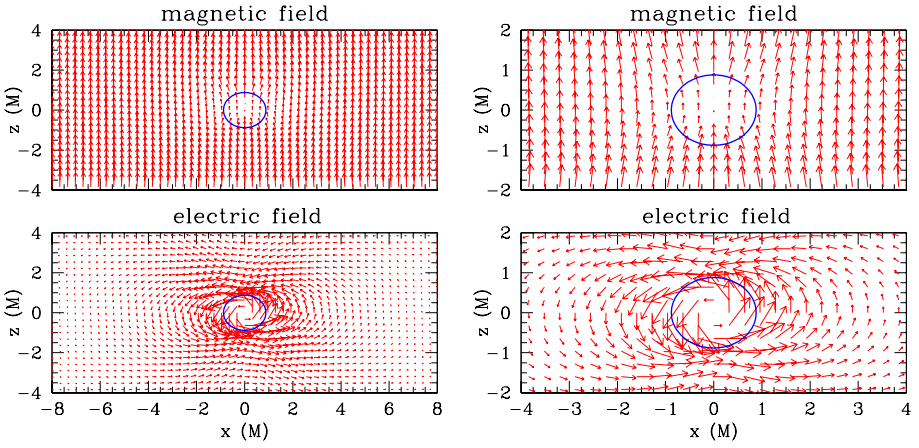

Figure 11.4: *Left panel:* Large-scale magnetic and electric field lines on the plane $y = 0$ and at $t = 200\,M$ for a Kerr black hole with spin $J/M^2 = 0.7$ orthogonal to the magnetic field, *i.e.,* along the x-axis. Indicated with blue circles are the apparent horizons. *Right panel:* The same as on the left panel but on a smaller scale to highlight the fields structure in the vicinity of the black hole.

In order to obtain a more intuitive picture of the different solutions for isolated black holes, we now turn our attention to the structure of the electric and magnetic fields

themselves. While those field lines are gauge-dependent, they can be used to determine the effect of the spin orientation of the black holes on the solution. Figure 11.2 shows therefore the three-dimensional (3D) EM field configurations at late simulation times when the solution has settled to a stationary state for either a Schwarzschild black hole (left panel), or for Kerr black holes with spin aligned (central panel) or orthogonal to the magnetic field (right panel). Note that in all of the panels, the magnetic field lines are bent by the black hole geometry. The appearance of toroidal electric field in the case of a non-spinning black hole does not contradict Wald's solution, for which it should be identically zero. It is due to the non-vanishing radial shift vector which, when coupled with the vertical magnetic field, leads to a toroidal magnetic field [316]. Finally, note that whenever the black hole is rotating, together with the gauge-induced toroidal electric field, there appears also a poloidal component which is induced by the gravitomagnetism (or frame-dragging) of the rotating black hole and whose detailed geometry depends on the relative orientation of the spin with respect to the background magnetic field. For compactness we do not report here the EM field configuration for a rotating black hole with spin anti-aligned with respect to the magnetic field. It is sufficient to remark that the solution shows the same behavior as the aligned case, with a simple reversal in the direction of the spin-induced effects.

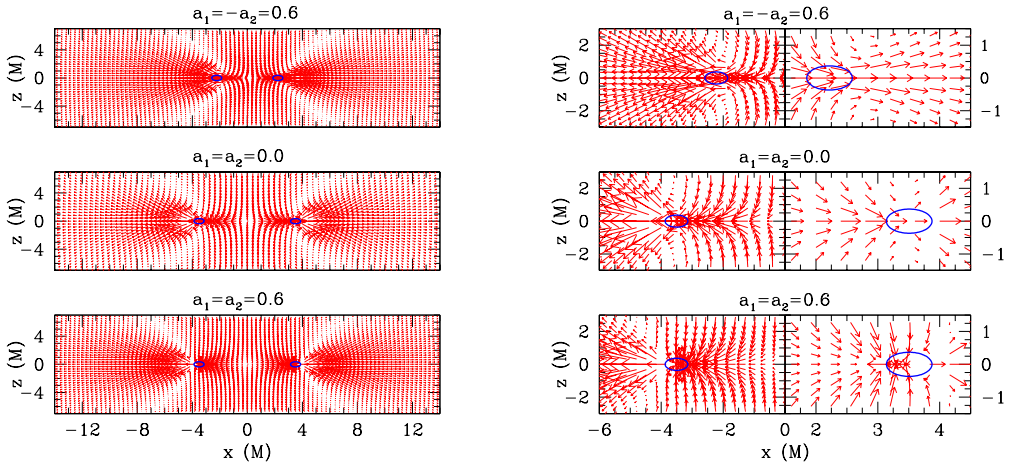

Figure 11.5: Electric field lines on the plane $y = 0$ for the r_0, s_0 and s_6 configurations at $t = 123, 155$ and $246\,M$, respectively. *Left panel:* Large-scale structure of the EM fields around the apparent horizons (blue circles). *Right panel:* The same as on the left but on a smaller scale to highlight the field structure in the vicinity of the black holes. Note that an additional magnification is applied to the black hole "on the right" so as to highlight the change of sign in the electric field near the horizon, *i.e.,* at $x \simeq 3\,M$.

To gain some insight on the influence of the black hole spin and orientation on the EM field lines, it is useful to exploit the phenomenological description offered by the "membrane paradigm" [267]. In such approach, the horizon of a rotating black hole is

seen as a one-way membrane with a net a surface charge distribution which, for the case of aligned spin and magnetic field, has negative values around the poles while positive ones around the equator. The resulting behavior is therefore the one shown in figure 11.3, where the magnetic and electric field lines for the Kerr black hole with spin aligned with the magnetic field are presented on the $y = 0$-plane. The left panel, in particular, offers a large-scale view of the EM fields, which is however magnified on the right panels to highlight the behavior of the fields near the apparent horizons. Finally, shown in figure 11.4 are the magnetic and electric-field lines on the $y = 0$-plane for the Kerr black hole with spin orthogonal to the the magnetic field, *i.e.,* along the x-axis. Note that while the differences in the magnetic field configurations in figure 11.3 and 11.4 are small and difficult to observe even in the zoomed-in version of the figures, the differences in the electric fields are instead significant and related to the different spin orientations.

11.3 Binary black-hole merger simulations in EV

We next extend the considerations made in the previous section to a series of black-hole binaries having equal masses and spins that are either aligned or anti-aligned with the orbital angular momentum.

11.3.1 Initial Data and Grid Setup

We construct consistent black-hole initial data via the "puncture" method (see chapter 3 for details) as described in [124]. We consider equal mass binaries with four different spin configurations belonging to the sequences labeled as *"r"* and *"s"* along straight lines in the (a_1, a_2) parameter space, also referred to as the "spin diagram" [317, 318]. These configurations allow us to cover the basic combinations for the alignment of the spin of the individuals black holes with respect to the magnetic field, while keeping the dimensionless spin parameter of the single black holes constant among the different binaries considered. Furthermore, it allows us to study the impact that the final black hole spin has on the late stages of the merger.

To obtain the orbital parameters of the black holes initially we perform PN evolutions following the scheme outlined in [125] and as described in detail in in section 3.5.4, which provides a straightforward prescription for initial-data parameters with small initial eccentricity, and which can be interpreted as part of the process of matching our numerical calculations to the inspiral described by the PN approximations. The free parameters of the puncture initial data we fix are: the puncture coordinate locations $\boldsymbol{C}_i$, the puncture bare mass parameters m_i, the linear momenta $\boldsymbol{p}_i$, and the individual spins $\boldsymbol{S}_i$. The initial parameters for all of the binaries considered are collected in Table 11.1. The initial separations are fixed at $D = 8\,M$ with the exception of the s_{-6} binary having an initial separation of $D = 10\,M$. Here M is the total initial black hole mass, chosen as $M = 1$ (note that the initial ADM mass of the space-time is not exactly 1 due to the binding energy of the black holes), while the individual asymptotic initial

Table 11.1: Binary sequences for which numerical simulations have been carried out, with various columns referring to the puncture initial location $\pm x/M$, the mass parameters m_i/M, the dimensionless spins a_i, the initial momenta and the normalized ADM mass $\widetilde{M}_{\rm ADM} \equiv M_{\rm ADM}/M$ measured at infinity. (See . [317, 318] for a discussion of the naming convention).

	$\pm x/M$	m_1/M	m_2/M	a_1	a_2	$(p_x,\ p_y)_1 = -(p_x,\ p_y)_2$	$\widetilde{M}_{\rm ADM}$
s_{-6}	5.0000	0.4000	0.4000	−0.600	−0.600	(0.001191, −0.100205)	0.9873
r_0	4.0000	0.4000	0.4000	−0.600	0.600	(0.001860, −0.107537)	0.9865
s_0	4.0000	0.4824	0.4824	0.000	0.000	(0.002088, −0.112349)	0.9877
s_6	4.0000	0.4000	0.4000	0.600	0.600	(0.001860, −0.107537)	0.9876

black hole masses are therefore $M_i = 1/2$. In addition, we choose the initial parameters for the EM fields to be $B^i = (0, 0, B_0)$ with $B_0 \sim 10^{-4}/M \sim 10^8(10^8 M_\odot/M)\,\mathrm{G}$ and $E^i = 0$. The setup for the numerical grids used in the simulations consists of 9 levels of mesh refinement with a fine-grid resolution of $\Delta x/M = 0.02$ together with fourth-order finite differencing. The wave-zone grid has a resolution of $\Delta x/M = 0.128$ and extends from $r = 24\,M$ to $r = 180\,M$, in which our wave extraction is carried out. The outer (coarsest) grid extends to a spatial position which is $819.2\,M$ in each coordinate direction.

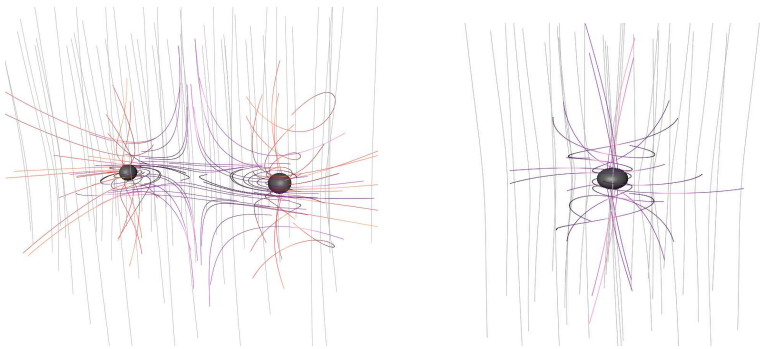

Figure 11.6: Electric (red/magenta) and magnetic field lines (gray) in 3D for the s_6 binary during inspiral when both black holes are still far separated at time $t = 328\,M$ (left panel), and after the merger at $t = 690\,M$ (right panel).

11.3.2 Binary Evolution and Spin Dependence

As mentioned in the previous subsection, we consider configurations where both black holes have equal mass and the individual black hole spins are either aligned or anti-aligned with the magnetic field (and orbital angular momentum). We thus consider a set of three different spinning binaries, as well as a non-spinning binary, which we take

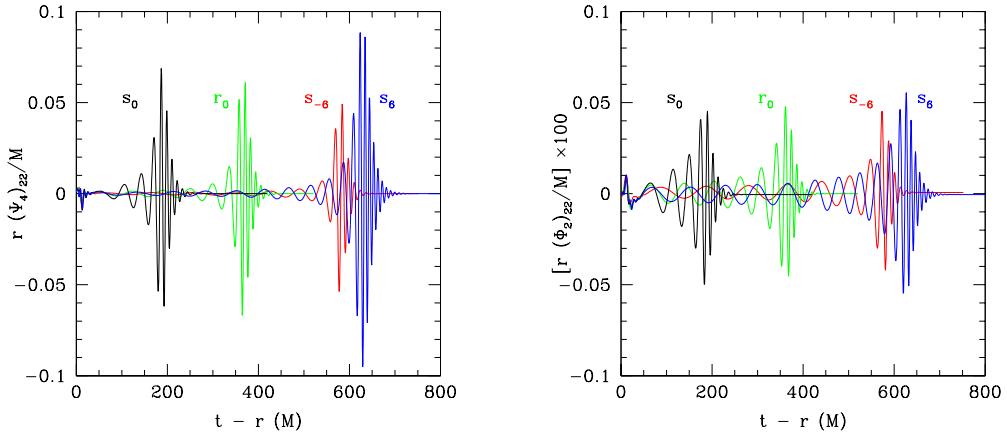

Figure 11.7: *Left panel:* gravitational waves as computed from the $(2,2)$ mode of Ψ_4 for the different binaries reported in Table 11.1. *Right panel:* The same as in the left panel but for the EM waveform as computed from Φ_2.

as a reference (*cf.* Table 11.1).

One feature of our simulations, that was already analyzed for single black holes in section 11.2, and is of even greater interest for binaries, is the structure of the EM field lines induced by the space-time dynamics around the black holes. The field line configurations, in fact, change considerably throughout the course of our simulations. When there is a large separation between the orbiting black holes, the electric field structure in both non-spinning and spinning binary systems is dominated by the orbital motion of the individual black holes. In particular, an inspection of the electric field vector along a line joining their centers indicates an outward radial dependence. This can be understood from the phenomenological interpretation suggested by the membrane paradigm and has been observed already in [316]. Namely, as the black holes move in a direction which is essentially orthogonal to the magnetic field, an effective quadrupolar charge separation develops on the horizons with effective positive charges at the poles and negative ones on the equator, thus inducing an electric field emanating from each black hole. This induced quadrupolar electric field is therefore reminiscent of the one produced by a conductor moving through a uniform magnetic field as the result of the Hall effect.

It is interesting to note that while the differences in the magnetic field lines among the various binaries considered are rather small, the differences in the electric fields show significant variation across the spin configurations. This is illustrated in figure 11.5, which shows the electric field lines at different scales of interest with respect to the black holes for two spinning binary black hole systems and the non-spinning binary on the $y = 0$-plane. Here we choose to concentrate on the configurations with the spins up/up (*i.e.*, s_6) and with the spin up/down (*i.e.*, r_0) since the configuration with the

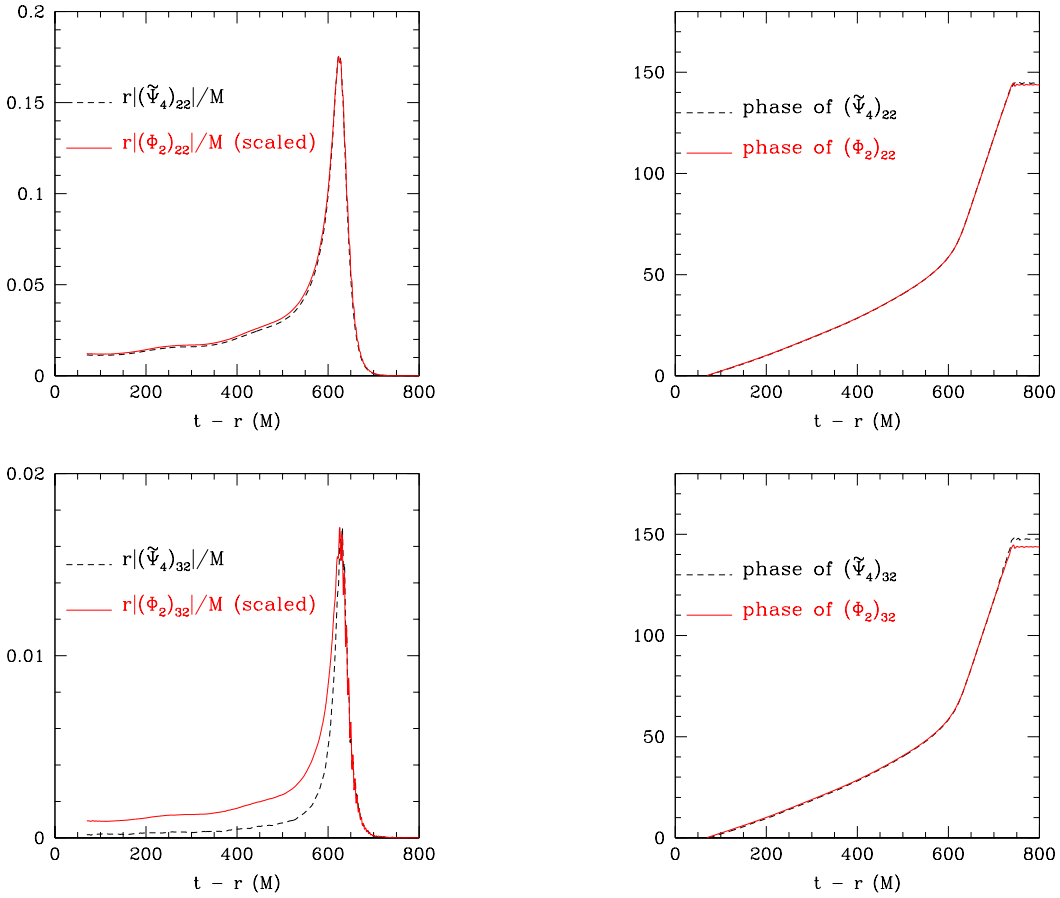

Figure 11.8: Amplitude and phase evolution of the main $\ell = m = 2$ modes for the Weyl scalar Φ_2 and the first time integral of Ψ_4 (*i.e.*, $\widetilde{\Psi}_4$), relative to the s_6 configuration. The plots show the data in retarded time $t - r$ for a detector located at $r = 100M$. While the $\ell = m = 2$ modes show the same amplitude (up to a scale factor) and phase evolution, this does not apply to modes with higher ℓ. For the $\ell = 3, m = 2$ and $\ell = 4, m = 2$ modes, the phase evolution is still identical but the amplitude no longer does not differ only by a constant scale factor.

spins down/down (*i.e.*, s_{-6}) shows the same field-line structure as the up/up case. In particular, the left panel of figure 11.5 reports the field-line structure on a scale which is much larger than that of the horizons and that clearly shows the quadrupolar nature of the field. At the same time, the right panel offers a magnified view of the same binaries on scales which is comparable with those of the horizons. In this way it is possible to find the properties of the electric field already discussed in sect 11.2 for isolated black holes also in case of binary black holes. Additionally the various spin configurations lead to different small-scale properties of the field. More specifically, while the field lines of the r_0 and s_0 configurations have a similar structure even in the magnified

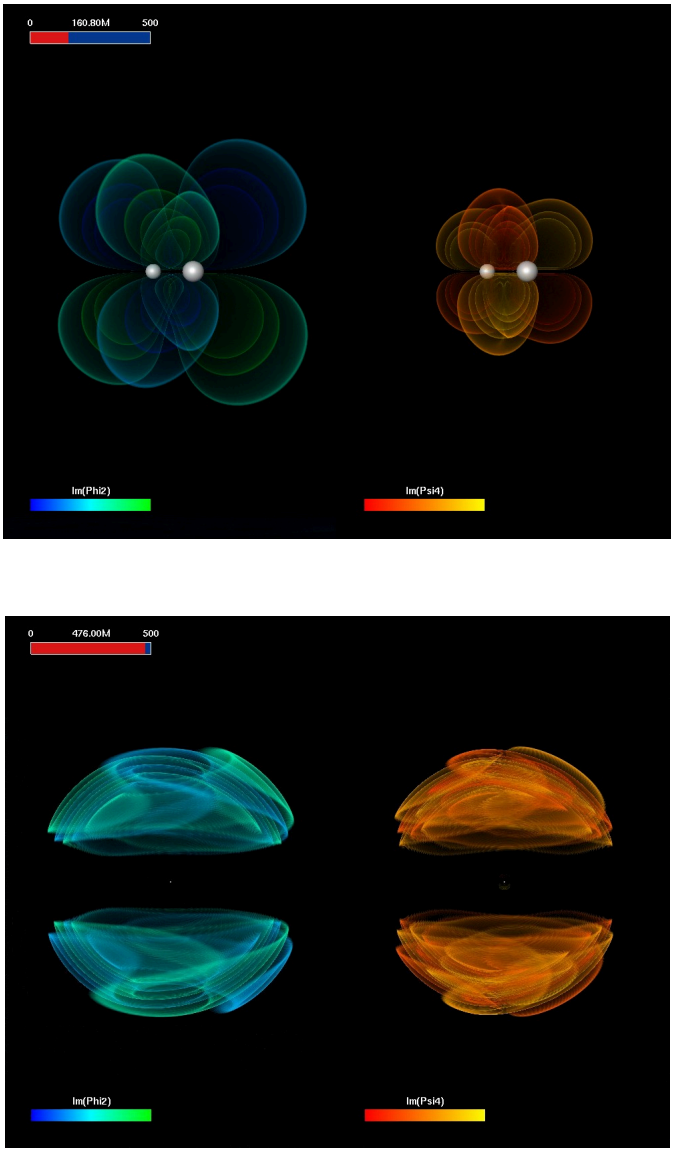

Figure 11.9: $\mathrm{Im}(\Phi_2)$ and $\mathrm{Im}(\Psi_4)$ shown as an iso-surface volume rendering for the s6-binary at two different snapshots in time. The top panel shows the binary during the early inspiral at $t = 160.8M$ while the bottom panel shows the time $t = 460.8M$, shortly after merger.

plot, the binary with the aligned spins s_6 shows a more complex structure in which the electric field changes sign near but outside the horizon, namely at $x \simeq 3\,M$ and which corresponds approximately to a distance $d \sim 2r_{\rm AH}$, with $r_{\rm AH}$ the mean radius of the apparent horizon. This additional property of the electric field could be related

to the location of the ergosphere (which has not been computed in these simulations) and may be seen as a response of the electric field to the additional charge separation induced on the black hole horizon and which leads to a greater distortion and twisting of the field lines in this region.

Although it is not trivial to disentangle how much of this behavior of the electric field depends on the gauges used, the complex structure of the electric fields, and which varies considerably through the late inspiral and the merger of the binary, may lead to interesting dynamics and to the extraction of energy via acceleration of particles along open magnetic field lines or via magnetic reconnection. To better illustrate the complex field structure, figure 11.6 offers 3D views of both the electric and magnetic fields for the s_6 binary. In particular, in the left panel of figure 11.6 we show the electric and magnetic field lines as well as the apparent horizons when the binary is inspiraling (*i.e.,* at $t = 328\,M$) and again observe the superposition of two effects: the overall orbital motion of the black holes causing the large scale structure of the electric field lines (highlighted in a magenta color); and the effect of the black hole spin (in red), which causes additional dragging in the electric field lines close to the apparent horizons. In the right panel, on the other hand, we present the late-time (*i.e.,* at $t = 690\,M$) state of the solution which, as expected, agrees well with the field line configurations presented for the Kerr black hole with spin aligned with the magnetic field in section 11.2.

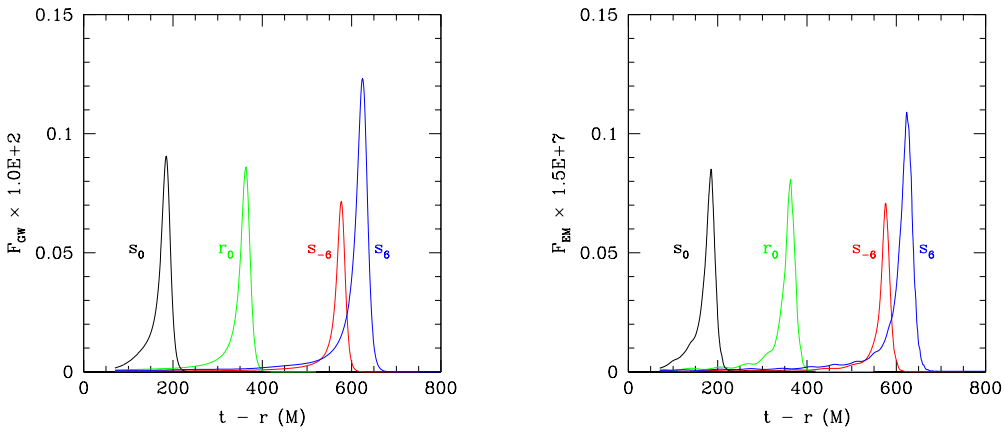

Figure 11.10: The total energy flux per unit solid angle in terms of gravitational wave waves (left panel) and of EM waves (right panel); clearly they differ only up to a scaling factor. The different lines refer to the different binaries reported in Table 11.1.

We next switch our attention to discussing how the different black-hole spin configurations affect the emission of EM radiation. This requires a careful analysis of the radiative properties of the solution in both the EM and gravitational channels. Figure 11.9 provides a qualitative picture of the emission in the two channels. It shows

3D volume renderings of the imaginary parts of both Ψ_4 and Φ_2 at two different times during the inspiral and after merger. The similarity of the two signals in their 3D structure is obvious. To quantify our analysis we first focus on the two types of waveforms and figure 11.7 illustrates the correlation between the two emissions by showing the time-retarded waveform of the principal mode, *i.e.,* the $\ell = m = 2$ of the spin-weighted spherical harmonic basis (note that Ψ_4 and Φ_2 have spin weight -2 and -1, respectively), for all different spin configurations to compare gravitational and EM waveforms directly. While both EM and gravitational wave radiation show the same characteristics in the dominant mode, we note that small differences arise when comparing the waveforms of the individual spin configurations more carefully with each other in the two channels. Note that the waveform for the binary s_{-6} has a larger number of cycles only because it merges very rapidly (the total angular momentum is smaller because the total spin is anti-parallel to the orbital angular i momentum) and thus it has been evolved from a larger initial separation $D = 10\,M$; all the other binaries have the same initial separation $D = 8\,M$. A closer inspection of figure 11.7 reveals that the amplitude evolution of the $\ell = m = 2$-mode for the different spin configurations differs when compared in the two channels. As an example, while in the gravitational wave channel the amplitude in the $\ell = 2, m = 2$-mode decreases when going from the r_0-configuration over to the s_0 and s_{-6} configurations, the amplitude remains nearly constant in the EM channel. This reveals that there are additional contributions in the EM emission coming from the higher-order modes (see figure 11.10 and the discussion below).

To further evaluate the correlation between the EM and the gravitational radiation, we now turn our attention to the amplitude and phase evolution of the main contributing spherical harmonic modes. Since radiated energy fluxes are given by Φ_2 and the time integral of Ψ_4 we here compare Φ_2 with $\widetilde{\Psi}_4 \equiv \int_\infty^t \Psi_4 dt'$. For briefness we only highlight the results obtained for the s_6 configuration, since this shows the highest amount of energy being radiated in both EM and gravitational waves, and because our remarks apply also to the other configurations. Since the main contributions to the radiated energy in the EM channel arise from the $\ell = 2, 3, 4,\ m = 2$-modes, we limit our analysis in this section to those modes only. In order to obtain a better understanding of the correlation in the radiation coming from the two channels, we analyze the amplitude and phase of the main contributing modes individually. Figure 11.8 shows the amplitude and phase evolution of the $\ell = 2, 3,\ m = 2$-modes in both channels. Clearly, the $\ell = m = 2$ modes show the same phase evolution (*cf.* the left panels) in the two forms of radiation, as expected given that the EM emission is essentially driven by the orbital motion of the binary. Furthermore, the amplitude evolution in the $\ell = 2, m = 2$ modes of both emissions are also simply related by a constant, time-independent, factor.

Although a simple scaling factor in the evolution of $\widetilde{\Psi_4}$ and Φ_2 appears for all of the different binary configurations considered here, this factor is not the same across different spin configurations. However, because the $\ell = m = 2$ represents by and large the most important contribution to the radiation emitted in the two channels and because the gravitational wave-emission from binaries with spins aligned/anti-aligned with the orbital angular momentum has been computed in a number of related

works [199, 231, 232, 233, 319, 320, 321, 322, 323, 324, 325, 326, 327, 328, 329], the results found here allow us to simply extend all of the phenomenology reported so far for the $\ell = 2, m = 2$ gravitational wave-emission from the above cited works also to the EM channel.

Unfortunately, the tight correlation found in the amplitude evolution of the lowest-order mode disappears for higher-order modes. This is reported in the bottom panels of figure 11.8, which indicate that while the phase amplitude remains the same (*cf.* the bottom right panel), the evolution of the amplitude in the two channels does not differ only by a simple constant scaling factor (*cf.* the bottom left panel). A similar behavior is found for lower-order modes such as the $\ell = 4, m = 2$ one but is not reported here for compactness. Overall, these results suggest that although the main (and lowest-order) contribution to the EM emission does indeed come as a result of the dragging of the EM fields by the orbital motion of the binary, additional contributions arise from higher-order modes which are not directly related to the orbital motions. These are likely to be the result of the complex interactions among the EM fields, discussed in figure 11.5 and whose investigation, although of great interest, goes beyond the scope of this paper.

Another interesting quantity to consider in our analysis is the energy carried away from the systems in the two emissions, which can be computed from the mode decomposition of the emission, where we have taken into account modes up to $\ell = 4$. Despite the differences between the EM and gravitational waves discussed already, when looking at the emission in the lowest-order modes that can be associated to the different multipolar decomposition of the two emissions (*cf.* figure 11.7), we find that the overall energy fluxes are extremely similar and differ essentially only by a constant (but large) factor. This is shown in figure 11.10 which reports both the gravitational wave (left panel) and the EM radiated energy fluxes (right panel) when integrated over a sphere located at $r = 100\,M$ for all the binary sequences considered here. Once again, the fact that $F_{\rm EM}$ basically mimics $F_{\rm GW}$, underlines that the emission in the EM channel is intimately tied to the emission in gravitational wave, so that the observation of one of the two would lead to interesting information also about the other one. As a final comment it is worth noting that although the energy fluxes from the binaries s_0 and r_0 show a different evolution, the total emitted energy, namely the area under the curves, is extremely similar and is reported in Table 11.2. This provides yet an additional confirmation of the results already presented in [231, 232, 233, 317, 329] for binaries with aligned spins and yields further support to the conjecture that when the initial spin vectors are equal and opposite and the masses are equal, the overall dynamics of the binary is the same that of the corresponding non-spinning binary.

11.3.3 Astrophysical Detectability

As discussed in the previous sections, the EM and gravitational radiation are tightly coupled and evolve on exactly the same timescales and with the same spectral distribution in frequency. The *rates* of loss of energy and angular momentum, however, are very different. This is summarized in Table 11.2 which reports the total energy radiated dur-

Table 11.2: Relative emitted energies in EM waves and gravitational waves ($E^{\rm rad}_{\rm EM}/M$, $E^{\rm rad}_{\rm GW}/M$, respectively), and emitted angular momentum in gravitational waves ($J^{\rm rad}_{\rm GW}/M^2$), for the magnetic field $B_0\,M = 10^{-4}$.

model	$E^{\rm rad}_{\rm EM}/M$	$E^{\rm rad}_{\rm GW}/M$	$J^{\rm rad}_{\rm GW}/M^2$
s_{-6}	$1.562\text{E}-7$	0.0243	0.216
r_0	$2.040\text{E}-7$	0.0357	0.213
s_0	$2.055\text{E}-7$	0.0354	0.243
s_6	$3.412\text{E}-7$	0.0590	0.380

ing the inspiral and merger in either EM waves or gravitational waves (*i.e.,* $E^{\rm rad}_{\rm EM}/M$, $E^{\rm rad}_{\rm GW}/M$) and the angular momenta radiated in gravitational waves (*i.e.,* $J^{\rm rad}_{\rm GW}/M^2$). From the values obtained, two interesting observations can be made. The first one is that the radiated EM energy is higher for binaries which lead to a more highly spinning final black hole. This is a consequence of these binaries merging with increasingly tighter orbits and at higher frequencies,which leads to stronger EM and gravitational wave fluxes. The second one has already been mentioned in the previous section and reflects the fact that the binaries r_0 and s_0 lead to the same energy emission (and to the same final black-hole spin [231, 232, 233, 329]) despite the s_0 binary has black holes with non-zero individual spins.

Note also that, in contrast with the losses in the gravitational wave emission, those in the EM one do not depend just on the masses and initial spins of the black holes but also on the strength of the initial magnetic field. This dependence must naturally scale quadratically with the magnetic field, so that we can write

$$\frac{E^{\rm rad}_{\rm EM}}{M} = k_1(a_1,a_2,M_1,M_2)B_0^2 \tag{11.1}$$

$$= 1.43\times 10^{-32} k_1 \left(\frac{M}{M_\odot}\right)^2 \left(\frac{B}{1\ \text{G}}\right)^2 , \tag{11.2}$$

where we have used the following relation

$$B\ [\text{G}] = 8.36\times 10^{19}\left(\frac{M_\odot}{M}\right) B\ [\text{geom. units}]\,. \tag{11.3}$$

to convert a magnetic field in geometric units (B [geom. units]) into a magnetic field expressed in Gauss (B [G]).

As discussed before, the EM emission is closely related via simple scaling factors to the gravitational wave one and whose efficiency has been discussed in detail in section VB of . [317]. In particular, it was shown there that the radiated gravitational wave energy depends quadratically on the total dimensionless spin (see equation. (24) in [317]) and the corresponding coefficients $\tilde{p}_i$ were presented in equation. (25) in the same reference. Hence, at least in the case of equal-mass binaries, it is trivial to express $k_1(a_1,a_2,M_1,M_2)$ in terms of the suitably rescaled coefficients $\tilde{p}_i$ in [317]. Here, however, because we are interested in much simpler order-of-magnitude estimates, we

will neglect the dependence of k_1 on the spins and simply assume that $k_1 \sim 10^{-7}$, so that

$$\frac{E^{\rm rad}_{\rm EM}}{M} \simeq 10^{-15} \left(\frac{M}{10^8\ M_\odot}\right)^2 \left(\frac{B}{10^4\ {\rm G}}\right)^2 , \tag{11.4}$$

where we have considered a total black hole mass of $10^8\,M_\odot$ and a magnetic field of 10^4 G as representative of the one possibly produced at the inner edges of the circumbinary disc [330] (see [331] for a recent discussion on the strength of magnetic fields in active galactic nuclei (AGN)).

It should be noted that only when an extremely strong magnetic field of $\sim 10^{11}$ G is considered, does the EM efficiency become as large as $E^{\rm rad}_{\rm EM}/M \simeq 10^{-1}$ and thus comparable with the gravitational wave one. For more realistic magnetic fields, however, and assuming for simplicity that $E^{\rm rad}_{\rm GW}/M \sim 10^{-2}$ for all possible spins, the ratio of the two losses is

$$\frac{E^{\rm rad}_{\rm GW}}{E^{\rm rad}_{\rm GW}} \simeq 10^{-13} \left(\frac{M}{10^8\ M_\odot}\right)^2 \left(\frac{B}{10^4\ {\rm G}}\right)^2 . \tag{11.5}$$

That is, for a realist value of the initial magnetic field, the gravitational wave emission is 13 orders of magnitude more efficient than the EM one. More importantly, however, the frequency of variation of the EM fields is of the order

$$f_{\rm B} \simeq (40\,M)^{-1} \simeq 10^{-4} \left(\frac{10^8\,M_\odot}{M}\right)\ {\rm Hz} \tag{11.6}$$

and therefore much lower than what is accessible via astronomical radio observations, which are lower-banded to frequencies of the order of ~ 30 MHz. As a result, it is very unlikely that a *direct* observation of the induced EM emission would be possible even from this simplified scenario.

Nevertheless, in the spirit of assessing whether this large release of EM radiation can lead to *indirect* observations of an EM counterpart, it is useful to compare $E^{\rm rad}_{\rm EM}$ with the typical luminosity of an AGN. To fix the ideas let us consider again a black hole of mass $M = 10^8\,M_\odot \simeq 10^{41}\,{\rm g} \simeq 10^{61}\,{\rm erg}$, so that the luminosity in EM waves for $B_0 = 10^4\,{\rm G}$ will be

$$\begin{aligned} L_{\rm EM} \equiv \frac{E^{\rm rad}_{\rm EM}}{\tau} &\simeq 10^{41} \left(\frac{B}{10^4\ {\rm G}}\right)^2 {\rm erg\ s^{-1}} \\ &\simeq 10^{8} \left(\frac{B}{10^4\ {\rm G}}\right)^2 L_\odot\,, \\ &\simeq 10^{-4} \left(\frac{B}{10^4\ {\rm G}}\right)^2 L_{\rm Edd}\,, \end{aligned} \tag{11.7}$$

where we have assumed a timescale $\tau \simeq 10^3\,M \simeq 10^5\,{\rm s} \simeq 1\,{\rm d}$ and where $L_\odot, L_{\rm Edd}$ are the total luminosity of the sun and the Eddington luminosity $L_{\rm Edd} = 3.3\times 10^4\,(M/M_\odot) L_\odot$, respectively. While this is a rather small luminosity (distant quasars are visible with much larger luminosities of the order $10^{47}\,{\rm erg\ s^{-1}}$), it is comparable with the luminosity

of nearby AGNs and that is of the order of $10^{41}\,\mathrm{erg\ s^{-1}}$. More important, however, is the comparison between the EM emitted by the merging binary and the one coming from the accretion disc. Using (11.7) it is straightforward to deduce that the binary EM luminosity is comparable with that of an AGN accreting at 10^{-4} the Eddington rate. Hence, unless the accretion rate is rather small (namely, much smaller than 10^{-4} the Eddington rate with the extreme case being the non-accreting scenario) the EM emission from the binary would be not only restricted to very low-frequencies but also just a small fraction of the total luminosity. Under these conditions it is unlikely that such emission could have an observable impact on the overall luminosity of the accreting system.

As a final consideration it is useful to estimate whether the inspiraling binary could nevertheless imprint a detectable effect on the disc via the perturbations in the magnetic field it can produce. To assess whether this is the case we first compare the frequency $f_{\rm B}$ with the typical plasma frequency

$$f_{\rm P} = \frac{\omega_{\rm P}}{2\pi} = \left(\frac{n_e e^2}{\pi m_e}\right)^{1/2} \simeq 10^{14}\left(\frac{n_e}{10^{21}\ \mathrm{cm^{-3}}}\right)\ \mathrm{Hz}\,, \tag{11.8}$$

where n_e is the electron number density, or with the electron cyclotron $f_{\rm C}$ frequency

$$f_{\rm C} = \frac{\omega_{\rm C}}{2\pi} = \frac{eB}{2\pi m_e c} \simeq 10^{10}\left(\frac{B}{10^4\ \mathrm{G}}\right)\ \mathrm{Hz}\,. \tag{11.9}$$

Clearly, the magnetic field varies with a frequency $f_{\rm B}$ that is is between 14 and 18 orders of magnitude smaller and hence that the electrons and protons in the disc are always able to "adjust" themselves to the changes in the magnetic fields, which are extremely slow when compared with the typical timescales in the plasma. Stated differently, the EM radiation produced by the inspiral cannot penetrate the disc and will be effectively reflected over a skin depth of $\lambda = c/\omega_e \simeq 8\times 10^{-6}$ cm.

Finally, we consider whether the perturbed magnetic magnetic field can have impact on the transport of angular momentum in the disc and hence modify its accretion rate in a detectable way. It is worth remarking, in fact, that there is considerably large EM energy flux reaching the accretion disc and that is $F_{\rm EM} \simeq L_{\rm EM}/r_{\rm in}^2 \sim 10^{11}(B/10^4\,\mathrm{G})^2\,\mathrm{erg\ s^{-1}\ cm^{-2}}$, where $r_{\rm in} \sim 10^2\, r_g$ is the inner radius of the disc and $r_g \simeq 10^{15}$ cm is the gravitational radius for a black hole of $10^8\ M_\odot$. A crude way to estimate the perturbation on the disc is by considering the ratio between the viscous transport timescale τ_V and the magnetic transport timescale induced by the oscillating magnetic field, τ_B. Should this ratio be of the order of unity (or larger), then the magnetic-field perturbation may be transmitted to the disc in the form of Alfvén waves. In practice we estimate this by considering the (inverse) ratio between the viscous and magnetic torques, with the first one being expressed in terms of the average pressure p and sound speed c_s as $f_{\phi,V} \simeq \alpha p \simeq \alpha\rho c_s^2$ and the second one as $f_{\phi,B} \simeq r\delta B^\phi B^z \alpha/(8\pi) \simeq r\beta B_0^2/(8\pi)$; here α is the standard alpha-disc viscosity parameter and β is a measure of the perturbation induced in the background magnetic

field (*i.e.,* $\delta B^{\phi} \sim \beta B_0,\ B^z \sim B_0$). We therefore obtain

$$\begin{aligned} \frac{\tau_V}{\tau_B} &= \frac{f_{\phi,B}}{f_{\phi,V}} \\ &\simeq 10\frac{\beta}{\alpha}\left(\frac{r}{10^{-2}\ r_g}\right)\left(\frac{10^{-2}\text{g cm}^{-3}}{\rho}\right)\left(\frac{B_0}{10^4\ \text{G}}\right)^2\left(\frac{c}{c_s}\right)^2 , \end{aligned} \tag{11.10}$$

where $10^{-2}\ r_g$ is the typical length scale over which magnetic torques could operate. Assuming now $\alpha \simeq 0.1 - 0.01$, $\beta \sim 10^{-2}$ and $c_s\ 0.1 - 0.01\, c$ as reference numbers, the rough estimate (11.10) suggests that it is indeed possible that $\tau_V > \tau_B$ and hence that the perturbations in the magnetic field, albeit small and rather slow, can induce a change in the viscous torque and hence induce a change in the accretion rate if the latter is sufficiently stable. Determining more precisely whether this modulation in the magnetic field can effectively leave an imprint on the accretion flow would require a more accurate modeling of the accretion disc and is clearly beyond the scope of this simple estimate. It is however interesting that this possibility is not obviously excluded.

In summary, the analysis carried out in this section shows that it is highly unlikely that the EM emission associated with the scenario considered in this paper can be detected *directly* and simultaneously with the gravitational wave one. This is essentially because the EM is too inefficient for realistic values of the magnetic fields and because it operates at frequencies which are well outside the ones accessible to astronomical radio observations. However, if the accretion rate of the circumbinary disc is sufficiently stable over the timescale of the final inspiral and merger of the black-hole binary, then it may be possible that the EM emission will be observable *indirectly* as it will alter the accretion rate through the magnetic torques exerted by the distorted magnetic field lines. A firmer conclusion of whether this can actually happen in practice will inevitably have to rely on a more realistic description of the accretion process.

As a final comment we stress that our analysis and discussions in this section have not included the role of gas or plasmas around the black hole(s) nor have we considered resistive scenarios. Both of these ingredients, when coupled to the EM fields behavior described here, could induce powerful emissions by accelerating charged particles via the strong fields produced (*e.g.,* in a manner similar to the Blandford-Znajek mechanism [332]) or by affecting the gas/plasma dynamics or via the reconnection of the complex EM fields produced during the inspiral and merger. We present results including the plasma effects in the next section where we perform binary black-hole merger simulations while the black holes are immersed in tenous plasma.

11.3.4 Concluding Remarks

We have analyzed the phenomenology that accompanies the inspiral and merger of black-hole binaries in a uniform magnetic field which is assumed to be anchored to a distant circumbinary disc. Our attention has been concentrated on binaries with equal masses and equal spins which are either aligned or anti-aligned with the orbital

angular momentum; in the case of supermassive black holes, these configurations are indeed expected to be the most common ones [333, 334]. Furthermore, this choice allows us to disentangle possible precession effects and concentrate on the EM fields dynamics as affected by the orbital motion of the binary. Overall, the simulations reveal several interesting aspects in the problem:

- The orbital motion of the black holes distorts the essentially uniform magnetic fields around the black holes and induces a quadrupolar electric field analogous to the one produced by the Hall effect for two conductors rotating in a uniform magnetic field. In addition, both electric and magnetic fields lines are dragged by the orbital dynamics of the binary. As a result, a time variability is induced in the EM fields, which is clearly correlated with the orbital behavior and ultimately with the gravitational wave-emission. The EM fields become, therefore, faithful tracers of the space-time evolution.

- As a result of the binary inspiral and merger, a net flux of electromagnetic energy is induced which, for the $\ell = 2, m \pm 2$ modes is intimately tied, via a constant scaling factor in amplitude, to the gravitational energy released in gravitational waves. This specular behavior in the amplitude evolution disappears for higher-order modes, even though the phase evolution remains the same for all modes.

- Because the tight correlation between the EM and the gravitational wave-emission has been found for all of the cases considered here, we expect it to extend to all possible binary configurations as long as the EM fields are playing the role of "test fields". Hence, the modeling of the gravitational wave emission does in practice provide information also on the EM one within the scenario considered here.

- Although the global *large-scale* structure of the EM fields is dictated by the orbital motion, the individual spins of the black holes further distort the EM field lines in their vicinities. These *small-scale* fields may lead to interesting dynamics and to the extraction of energy via acceleration of particles along open magnetic field lines or via magnetic reconnection.

- The energy emission in EM waves scales quadratically with the total spin and is given by $E^{\rm rad}_{\rm EM}/M \simeq 10^{-15} \left(M/10^8\ M_\odot\right)^2 \left(B/10^4\ {\rm G}\right)^2$, thus being 13 orders of magnitude smaller than the gravitational energy for realistic magnetic fields. This EM emission is at frequencies of $\sim 10^{-4}(10^8 M_\odot/M)$ Hz, which are well outside those accessible to astronomical radio observations. As a result, it is unlikely that the EM emission discussed here can be detected *directly* and simultaneously with the gravitational wave one.

- Processes driven by the changes in the EM fields could however yield observable events. In particular we argue that if the accretion rate of the circumbinary disc is small and sufficiently stable over the timescale of the final inspiral, then the EM emission may be observable *indirectly* as it will alter the accretion rate through the magnetic torques exerted by the distorted magnetic field lines.

All of these results indicate that the interplay of strong gravitational and EM fields represents a fertile ground for the development of interesting phenomena. Although our analysis is incomplete as the effects on plasmas are not taken into account, we believe that the main properties of the EM dynamics described above should hold as long as the energy in the black holes dominates the energy budget. A more precise estimate of the possible emissions and of the observational signatures calls for further studies which would necessarily have to include additional physics. This work, however, together with those in . [316, 335, 336, 337, 338, 339, 340], constitute interesting first steps in this direction. In the next section we will generalize our setup by including plasma effects into our evolutions and determine the impact on the radiation generated in our simulations.

11.4 Binary black-hole merger simulations in the force-free approximation

The inspiral and merger of supermassive black holes will represent a secure source for the planned space-borne gravitational-wave detectors. Together with the gravitational wave signal, this process is expected to be accompanied either before [341, 342] or after [343, 344] the merger by the emission of electromagnetic (EM) radiation, thus providing a perfect example of multi-messenger astronomy. Should a "simultaneous" detection take place, this would not only help to localize the gravitational wave source and provide its redshift, but also address a number questions in astrophysics and cosmology [345, 346].

As the merger between two galaxies takes place and the black holes get closer, a circumbinary accretion disc is expected to form. Because the radiation-reaction timescale over which the binary evolves is much longer than the accretion timescale, the disc will slowly follow the binary as its orbit shrinks. However, as the binary separation becomes $\sim 10^5\, M$, where M is the mass of the binary, the radiation-reaction timescale reduces considerably, becoming smaller than the accretion one. When this happens, the disc evolution disconnects from the binary, the accretion rate reduces, and the binary performs its final orbits in an inner region poor of gas [347, 348].

This basic picture represents the astrophysical backdrop of a simple model which has been used by a number of authors to model the EM emission from the black-hole binary. More specifically, assuming that the disc is threaded by a coherent and large-scale magnetic field which is anchored to the disc, this will also permeate the "evacuated" region where the binary is rapidly shrinking and provide an effective way of coupling the binary's orbital motion to the generation of an EM signal. This scenario has been considered both for space-times EV [316, 339, 349] and for space-times filled by a tenuous plasma in the force-free approximation [314, 350, 351]. In [349], in particular, has considered a series of spinning black-hole binaries and studied the dependence of the gravitational and EM signals with different spin configurations. All in all, it was found that EM radiation in the lowest $\ell = 2, m = 2$ multipole accurately reflects the gravitational one. Furthermore, the efficiency of the energy emission in EM waves was

found to scale quadratically with the total spin and to be ~ 13 orders of magnitude smaller than the one in gravitational waves for realistic magnetic fields. However, the prospects of detecting an EM counterpart have become larger when it was pointed out in [351] that during the inspiral in a force-free plasma, a *dual-jet* structure forms, as a generalization of the Blandford-Znajek process [332] to orbiting black holes, where the EM energy flux is concentrated along the magnetic-field lines. Under these conditions, the EM energy can accelerate electrons and lead to synchrotron radiation.

We extend here the investigations made in [349] by considering the evolution in a force-free regime and properly computing the EM emission as the net result of ingoing and outgoing radiation. We confirm in this way the presence of a dual-jet structure, but also find that this is energetically sub-dominant with respect to a non-collimated and predominantly *quadrupolar* emission. Hence, if the simplified scenario considered here is realized in astrophysical configurations, it will be difficult to reveal the emission from the dual jets, but it will also be easier that an EM counterpart to binary black-hole mergers can be detected.

11.4.1 Simulation setup

As mentioned above, we assume the magnetic field to be anchored to the disc, whose inner edge is at a distance of $\sim 10^3\,M$ and is effectively outside of our computational domain, while the initial binary separation is only $D = 8\,M$. Although the large-scale magnetic field is poloidal, it is set to be initially uniform within the computational domain, *i.e.,* $B^i = (0, 0, B_0)$ with $B_0 \sim 10^{-4}/M$. We note that although astrophysically large, such initial magnetic field has an EM energy which is several orders of magnitude smaller than the gravitational-field energy, so that the EM fields can be treated as test-fields and all the results can be scaled trivially with B_0. The electric field E^i is initially zero, but it rapidly reaches a consistent solution [349]. As black-hole initial data we consider binaries with equal masses but with two different spin configurations: namely, the s_0-binary (both black holes are non-spinning) and the s_6-binary (both black holes have spins aligned with the orbital angular momentum with $(J/M^2)_1 = a_1 = a_2 = 0.6$; see [233, 317] for details). These two configurations allow us to study both the contributions coming from the binary's orbital motion, but also those related to the spins of the two black holes. The setup for the numerical grids used in the simulations consists of 9 levels of mesh refinement with a fine resolution of $\Delta x/M = 0.02$. The wave-zone grid has a resolution of $\Delta x/M = 0.128$ and extends from $r = 24\,M$ to $r = 180\,M$, while the outer (coarsest) grid extends to $819.2\,M$. Our implementation of the force-free equations is based on a novel approach that is fully driven by evolution equations and does not require corrections "by-hand" to enforce the force-free condition or to avoid inconsistent EM fields; our approach will be presented in [152].

11.4.2 Luminosity measures

The calculation of the EM and gravitational radiation generated during the inspiral, merger and ringdown is arguably the most important aspect of this chapter as it allows

us to establish what are the characteristics of the emissions in two channels. For the gravitational wave sector, we compute the emission via the Newman-Penrose curvature scalar Ψ_4 as detailed in . [202, 349]. In practice, we define an orthonormal basis in the three space $(\hat{\boldsymbol{r}}, \hat{\boldsymbol{\theta}}, \hat{\boldsymbol{\phi}})$, with poles along $\hat{\boldsymbol{z}}$. Using the normal to the slice as time-like vector $\hat{\boldsymbol{t}}$, we construct the null orthonormal tetrad $\{\boldsymbol{l}, \boldsymbol{n}, \boldsymbol{m}, \overline{\boldsymbol{m}}\}$, with the bar indicating a complex conjugate

$$\boldsymbol{l} = \frac{1}{\sqrt{2}}(\hat{\boldsymbol{t}} + \hat{\boldsymbol{r}}), \quad \boldsymbol{n} = \frac{1}{\sqrt{2}}(\hat{\boldsymbol{t}} - \hat{\boldsymbol{r}}), \quad \boldsymbol{m} = \frac{1}{\sqrt{2}}(\hat{\boldsymbol{\theta}} + i\hat{\boldsymbol{\phi}})\,, \tag{11.11}$$

by means of which we project the Weyl curvature tensor $C_{\alpha\beta\gamma\delta}$ to obtain $\Psi_4 = C_{\alpha\beta\gamma\delta} n^\alpha \bar{m}^\beta n^\gamma \bar{m}^\delta$. For the EM sector, instead, we use two equivalent approaches to cross-validate our measures. The first one uses the Newman-Penrose scalars Φ_0 (for the ingoing EM radiation) and Φ_2 (for the outgoing EM radiation), defined using the same tetrad [352]

$$\Phi_0 \equiv F^{\mu\nu} l_\nu m_\mu\,, \qquad \Phi_2 \equiv F^{\mu\nu} \overline{m}_\mu n_\nu\,. \tag{11.12}$$

It is always useful to remark that by construction quantities such as Ψ_4, Φ_0, Φ_2 are well-defined only at very large distances from the sources. Any measure of these quantities in the strong-field region risks to be incorrect. As an example, the EM energy flux does not show the expected $1/r^2$ scaling when Φ_0, Φ_2 are measured at distances of $r \simeq 20\,M$ [314, 351], which is instead reached only for $r \gtrsim 100\,M$.

Since our choice of having a uniform magnetic field within the computational domain has a number of drawbacks (*e.g.,* nonzero initial $\Phi_2\,, \Phi_0$), great care has to be taken when measuring the EM radiation. Fortunately, we can exploit the linearity in the Maxwell equations to distinguish the genuine emission induced by the presence of the black hole(s) from the background one. Following [352], we compute the total EM luminosity as a surface integral across a 2-sphere at a large distance

$$L_{\rm EM} = \lim_{r\to\infty} \int r^2 \left(|\Phi_2 - \Phi_{2,\rm B}|^2 - |\Phi_0 - \Phi_{0,\rm B}|^2 \right) d\Omega\,, \tag{11.13}$$

where $\Phi_{2,\rm B}$ and $\Phi_{0,\rm B}$ are the values of the background scalars induced by the asymptotically uniform magnetic field solution in the time dependent space-time produced by the binary black-holes. The choice of $\Phi_{2,\rm B}$ and $\Phi_{0,\rm B}$ will be crucial to measure correctly the radiative EM emission.

The background values of the Newman-Penrose scalars $\Phi_{2,\rm B}, \Phi_{0,\rm B}$ to be used in (11.13) are themselves time dependent and cannot be distinguished, at least a-priori, from the purely radiative contributions. However, a first reasonable approximation can be made if we assume these background values to be time independent and to be those at the initial time, *i.e.,*

$$\Phi_{2,\rm B} = \Phi_2(t=0)\,, \qquad \Phi_{0,\rm B} = \Phi_0(t=0)\,. \tag{11.14}$$

A second prescription involves instead the removal of those multipole components of the Newman-Penrose scalars which are not expected to be radiative, namely all those associated with the $m = 0$ multipoles, *i.e.,*

$$\Phi_{2,\rm B} = (\Phi_2)_{\ell,m=0}\,, \qquad \Phi_{0,\rm B} = (\Phi_0)_{\ell,m=0}\,, \tag{11.15}$$

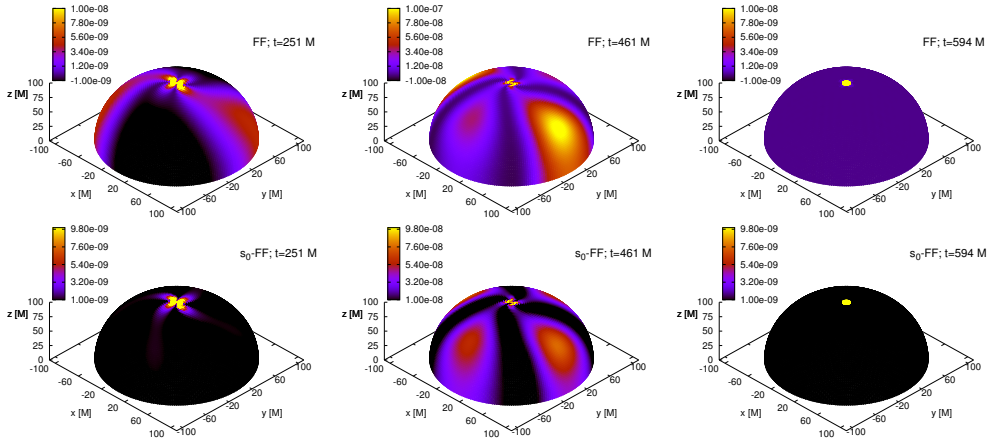

Figure 11.11: Snapshots of the EM energy flux during the inspiral and merger of the binary s_0. The two row shows the fluxes as measured with the expression (11.13) with (11.14) and (11.15), respectively. Note that (11.14) yields negative values which will cancel out when integrated over one orbit.

where $(\Phi_{2,0})_{\ell,m=0}$ refer to the $m = 0$ modes of the multipolar decomposition of $\Phi_{2,0}$ ($\ell \leq 8$ is sufficient to capture most of the background). Note that, because the $m = 0$ background is essentially time-independent (after the initial transient), the choice (11.15) is effectively equivalent to considering as background the final values of the Newman-Penrose scalars as computed in an EV calculation of the same binary system.

While apparently different, expressions (11.14) and (11.15) lead to very similar estimates and, more importantly they have a simple interpretation in terms of the corresponding measures made with. We recall, in fact, that the EM luminosity is customarily computed via the integral over a 2-sphere of the Poynting flux $S_i = \sqrt{\gamma}\epsilon_{ijk}E^j B^k$, which is again just the flux of the stress-energy tensor as measured now by observers on the spatial hypersurface. Of course also this measure is adequate only far from the binary and it suffers equally from a background non-radiative contribution. However, because of the linearity in the Maxwell equations, the non-radiative contributions can also be removed by introducing background values of the EM fields $E^j_{\rm B}, B^j_{\rm B}$ and computing the Poynting vector as $S_i = \sqrt{\gamma}\epsilon_{ijk}(E^j - E^j_{\rm B})(B^k - B^k_{\rm B})$. In this context, then, expressions (11.14) and (11.15) correspond respectively to setting $E^k_{\rm B} = 0, B^k_{\rm B} = B^k(t = 0)$ and $E^k_{\rm B} = E^k_{\ell,m=0}, B^k_{\rm B} = B^k_{\ell,m=0}$. We have verified that the measures of the EM luminosity obtained using (11.14) or (11.15) reproduce well the corresponding ones obtained with the Poynting flux. As a final remark we note that the EM flux in (11.13) is not always positive everywhere on the 2-sphere. The negative contributions, however, average to zero over one orbit and do not represent a radiative field. This point was remarked in [316], where a toy model within the membrane paradigm was used for the binary.

Using expression (11.13) with either the prescription (11.14) or (11.15) we find that the EM radiation generated during the late inspiral and merger does contain a dual-jet

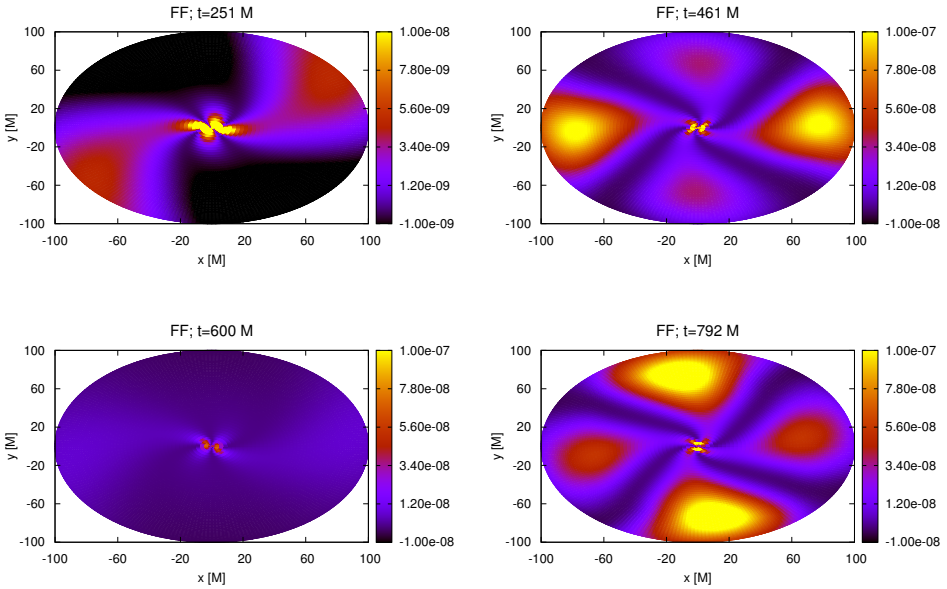

Figure 11.12: Map views of the EM energy flux computed using (11.13) with (11.15). The first row refers to the binary s_0, while the bottom one to the binary s_6 and has a larger emission from the dual jets.

structure, but also that the total energy flux is dominated by a non-collimated emission of quadrupolar nature. This is shown in figure 11.11, which reports snapshots at different times of the EM energy flux on a 2-sphere of radius $r = 100\,M$ for the s_0-binary. The first row shows the fluxes as computed with (11.14) and with a (non-radiative) component that enhances two lobes of the signal and decreases the other two. Although there are regions with negative values which will average to zero over one orbit, the corresponding EM fields could nevertheless induce motion in the plasma and secondary radiation which we cannot account for here. The second row refers to fluxes as computed with (11.15), where the time dependent background solution is almost completely subtracted, so that only the (positive) radiative part remains, showing a fairly symmetric four-lobe structure. Within both approaches, the extended quadrupolar distribution is accompanied by the presence of dual jets during the inspiral, and of a single jet from the spinning merged black hole. The energy flux in the jets is essentially the same in the two cases (both during the inspiral and after the merger), but that in the non-collimated part is different. In spite of this, the total luminosities are very similar, as most of the differences cancel when integrated over one orbit (*cf.* fig 11.14). However, because the Poynting-flux structure is different in the two measures [(11.14) has a non-radiative part missing in (11.15)], it could lead to a different secondary emission as the EM fields interact with the plasma; this is an aspect that cannot be investigated within our force-free approach but that deserves further study. Figure 11.13 finally provides a 3D volume rendering view of the mission for the $s0$-binary during shortly before merger during the inspiral at time $t = 300.8M$. The dual-jet structure is twisted

by the orbital motion of the black holes and the non-collimated emission is shown in terms of measure (11.13) with a background choice (11.14).

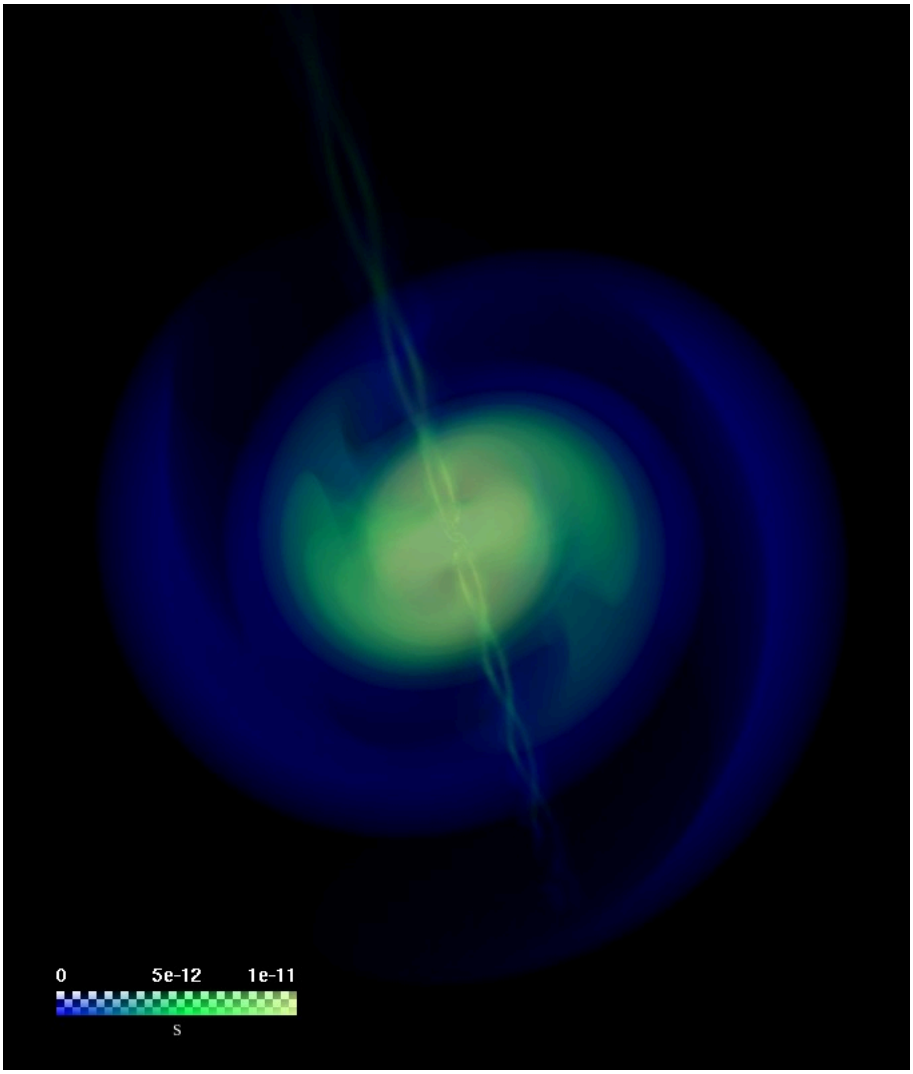

Figure 11.13: Poynting flux S shown as an iso-surface volume rendering for the s0-binary at time $t = 300.8M$ shortly before merger.

The corrections introduced by the spin of the black holes are shown in figure 11.12, which reports map views of the EM emission for the binaries s_0 and s_6 as computed through (11.15). Both the collimated and the non-collimated emission are very similar qualitatively, although there is a slight (*i.e.,* 50%) enhancement of the radiation in the spinning case, both in the total and in the collimated emission. This is not surprising since most of the radiation is produced by the interaction between the black-hole orbital

motion and the background magnetic field. Indeed we find the emission in the EV evolution to be comparable to the force-free one (this is different from what reported in [314, 351]).

A more quantitative assessment of the different contributions is shown in figure 11.14, which reports the evolution of the EM luminosity during the inspiral and merger of the binary s_0 (left panel) and of the spinning binary s_6 (right panel). Shown with (blue) solid lines is the total luminosity as computed through (11.15), while the (red) dashed lines refer to the luminosity integrated over a polar cap with an half-opening angle of 5° and thus representative of the emission from the two jets. Also shown with (magenta) dotted lines are the corresponding luminosities as computed through (11.14): the differences are small and hardly visible for the collimated part.

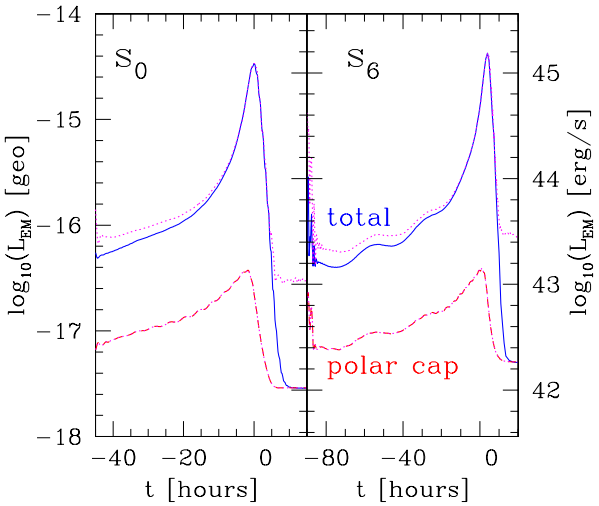

Figure 11.14: Evolution of the EM luminosity at $100\,M$ for the binary s_0 (left) and for the spinning binary s_6 (right), when $M = 10^8\,M_\odot$ and $B_0 = 10^4\,\mathrm{G}$. Using (11.15), (blue) solid lines show the total luminosity, while (red) dashed lines refer to the luminosity in a polar cap of 5°. Shown with (magenta) dotted lines are the measures with (11.14); note the presence of a small eccentricity for the binary s_6.

An accurate measure of the evolution of the collimated/non-collimated components is crucial to predict the properties of the system when the two black holes are widely separated. This, in turn, requires a reliable disentanglement of the collimated emission from the non-collimated one and from the background. The non-collimated emission measured with (11.15) matches well the growth expected if the EM emission is mostly quadrupolar and hence with a dependence that is the same as the gravitational wave one and, at the lowest order, scales as $L_{\rm EM}^{\rm non-coll} \approx \Omega^{10/3}$ [316, 349]. On the other hand, a smaller scaling is found when the approach (11.14) is adopted; at present it is difficult to determine which one is the most reliable scaling. At the same time, the frequency evolution for the collimated emission coincides in the two approaches, but it does not follow the scaling $L_{\rm EM}^{\rm coll} \approx \Omega^{2/3}$ suggested in [351] for boosted black holes; rather, it

scales as $L_{\rm EM}^{\rm coll} \lesssim \Omega^{5/3-6/3}$. We suspect the accelerated motion of the black holes to be behind this difference and longer simulations are needed to draw robust conclusions.

11.4.3 Impact on detectability

Assessing the detectability of the EM emission discussed above is of course of great importance and using the results of [314, 351], . [353] has estimated that the short timescales associated to the merger will limit the detectability in the radio band to less than one per year. As reported in figure 11.14, the peak of the collimated emission is ~ 100 times smaller than that of the total emission, making the detection of the dual jets at the merger unlikely. Unfortunately, even if the energy flux is $\sim 8-2$ times larger near the jets, the lack of knowledge about the Lorentz factor of the reprocessed plasma does not allow us to say whether the beaming in the jet will be larger than that in the extended emission and thus help its detection. That said, because the total luminosity at merger is ~ 100 times larger than in [351], the detection should be overall more likely if the assumptions in [353] are realized in practice. In addition, the dual jets emission could be dominant in the early inspiral (especially if the black holes are spinning). Assuming the scalings for the collimated and non-collimated emissions are different and go respectively like $\Omega^{10/3}$ and $\Omega^{6/3}$ ($\Omega^{5/3}$), the two components of the luminosity would become of the same order at a separation of ~ 16 (24) M, but obviously smaller (the collimated will be smaller of a factor ~ 10). Determining more precisely when and if this happens requires an accurate frequency scaling which is not available yet. As a note of caution we stress that luminosities $L_{\rm EM} \sim 10^{45}\,{\rm erg/s}$ are also typical of radio-loud galaxies, and the determination of an EM counterpart can be challenging if such sources are near the candidate event.

11.4.4 Conclusions

We have investigated the suggestion that dual jets can be produced during the inspiral and merger of supermassive black holes immersed in a force-free plasma threaded by a uniform magnetic field. We have found that the energy flux does have a dual-jet structure but is predominantly quadrupolar, with the non-collimated emission being about $10-100$ times larger than the collimated one. Our findings set restrictions on the detectability of dual jets from coalescing black-hole binaries, but also increase the chances of detecting an EM counterpart for astrophysical conditions similar to those in this simplified scenario.

Part IV

Gravitational wave data analysis

12

Binary coalescence search algorithms

The search for gravitational waves in detector output represents a major challenge due to the extremely small distortions that need to be detected. Since the possible signal we eventually want to detect is smallcompared to the many noise sources influencing the detector output, statiscal analysis methods need to be used to say with some certainty level that a gravitational wave has been detected. The method that has been used in this thesis is known as matched-filtering and is widely used for the search for gravitational waves from compact-binary coalescence. It uses an *a-priori* prediction of the signal that we expect to detect to compute the inner product between signal and detector noise, which normalized by the power spectral density (PSD) of the detector noise acts as our basic measure to decide whether a gravitational wave has been detected or not. In this chapter we will review the basics of probability theory to construct a matched-filter for the use in a binary inspiral search pipeline. The presentation follows closely [354]. For a more thorough discussion of the relevant concepts see [355, 356].

12.1 Searching for gravitational waves in detector output

We want to detect a gravitational wave embedded in the output of the interferometer $s(t)$. The output of the detector contains instrumental noise $n(t)$ and possibly a signal $h(t)$. The noise arising from random processes can be described by a probability distribution function and the detector output in the two cases can be describe as

$$s(t) = \begin{cases} n(t) + h(t), & \text{if a signal is present} \\ n(t), & \text{if no signal is present.} \end{cases} \tag{12.1}$$

The filter outputs a probability $P(h|s)$ that a signal $h(t)$ is present in the detector output $s(t)$ (the probability that no signal is present is $P(0|s) = 1 - P(h|s)$). To construct the filter we recall some basics of elementary probability theory. For two

events A and B the conditional probabilities can be related by

$$P(A|B) = \frac{P(A,B)}{P(B)} = \frac{P(A)P(B|A)}{P(B)}, \tag{12.2}$$

using $P(A,B) = P(A)P(B|A) = P(B)P(A|B)$, the probability for the two events to occur. Now given a set of mutually exclusive events $A_1, A_2, ..., A_K$, and an event B that can only occur if one of the A_k occurs, the probability that B occurs is

$$P(B) = \sum_{k=1}^{K} P(A_k)P(B|A_k). \tag{12.3}$$

Equation (12.3) is the *total probability formula*. The probability for an event A_k allowing B to happen now can be obtained as

$$P(A_k|B) = \frac{P(A_k)P(B|A_k)}{P(B)} = \frac{P(A_k)P(B|A_k)}{\sum_{j=1} KP(A_j)P(B|A_j)}, \tag{12.4}$$

known as *Bayes' theorem*. $P(A_k)$ is the *a-priori* probability of A_k occurring and $P(A_k|B)$ is the *a-posteriori* probability that A_k allowed the outcome of B happening. The conditional probability $P(B|A_k)$ is called the *likelihood*. Assuming that the set of events A_k contains only the two members, "signal present" or "signal not present" and for B being the output of the interferometer, the probability for the signal being present in the detector output is given by

$$P(h|s) = \frac{P(h)P(s|h)}{P(s)}. \tag{12.5}$$

Here

$$P(s) = \frac{P(s|h)/P(s|0)}{[P(s|h)/P(s|0)] + [P(0)/P(h)]} \tag{12.6}$$

is the probability of obtaining the detector output and $P(s|h)$ the likelihood function. Using the likelihood ratio

$$\Lambda = \frac{P(s|h)}{P(s|0)} \tag{12.7}$$

we can write equation (12.5) as

$$P(h|s) = \frac{\Lambda}{\Lambda + [P(0)/P(h)]}. \tag{12.8}$$

The probability for the signal not being present is

$$P(0|s) = \frac{P(0)/P(h)}{\Lambda + [P(0)/P(h)]}, \tag{12.9}$$

and we can express the ratio as

$$\frac{P(h|s)}{P(0|s)} = \Lambda \frac{P(h)}{P(0)}. \tag{12.10}$$

As a decision rule we can now conclude that if $P(h|s)$ is large (close to one) the signal is present, and if $P(h|s)$ is small (close to zero) the signal is not present. For making a decision in practice we can construct a threshold for making this decision:

$$\begin{aligned} P(h|s) &\geq P_T, \qquad \text{a signal is present} \\ P(h|s) &< P_T, \qquad \text{no signal is present} \end{aligned} \tag{12.11}$$

Given the decision rule (12.11), we can define the false alarm rate F and false dismissal rate F'. Equation (12.8) indicates that we need the a priori probabilities $P(h)$ and $P(0)$ to obtain $P(s|h)$. However since $P(h)/P(0)$ is constant and $P(h|s)$ a monotonically increasing function of the likelihood we can define or optimal filter to output the likelihood ratio given the detector output $s(t)$. To make our filter optimal we now maximize over the false alarm rate F. We now need to calculate Λ for real detector data $s(t)$ and signal $h(t)$. We assume the noise $n(t)$ to be Gaussian with zero mean value $\langle n(t)\rangle = 0$. The single-sided PSD $S_n(|f|)$ of the noise is given by

$$\langle \tilde{n}(f)\tilde{n}(f')\rangle = \frac{1}{2}S_n(|f|)\delta(f-f'), \tag{12.12}$$

with $\tilde{n}(f)$ being the Fourier transform of $n(t)$. We now re-express the likelihood-ratio by using probability densities

$$\Lambda = \frac{P(s|h)}{P(s|0)} = \frac{p(s|h)ds}{p(s|0)ds} = \frac{p(s|h)}{p(s|0)}. \tag{12.13}$$

The probability density for a specific configuration of detector noise is

$$p(n) = \kappa e^{-\frac{1}{2}(n|n)}, \tag{12.14}$$

with the inner product

$$(a|b) := \int_{-\infty}^{\infty} df \frac{\tilde{a}^*(f)\tilde{b}(f) + \tilde{a}(f)\tilde{b}(f)}{S_n(|f|)}. \tag{12.15}$$

The probability density of the interferometer output without any signal present is equivalently

$$p(s|0) = p(s) = \kappa e^{-\frac{1}{2}(s|s)}. \tag{12.16}$$

Finally

$$p(s|h) = p(s-h) = \kappa e^{-\frac{1}{2}(s-h|s-h)} \tag{12.17}$$

describes the probability density for obtaining $s(t)$ in case of a present signal $s(t) = n(t) + h(t)$. Using equations (12.16) and (12.17) we get the likelihood ratio as

$$\begin{aligned} \Lambda \quad &= \frac{p(s|h)}{p(s|0)} = \frac{e^{-1\frac{1}{2}(s-h|s-h)}}{e^{-\frac{1}{2}(s|s)}} \\ &= e^{(s|h)-\frac{1}{2}(h|h)}. \end{aligned} \tag{12.18}$$

Now we can set a threshold on $s(h)$ instead of on the probabilities directly, since the Λ is a monotonically increasing function of $(s|h)$:

$$\begin{aligned} (s|h) &\geq x_T, \qquad \text{signal is present} \\ (s|h) &< x_T, \qquad \text{signal is not present} \end{aligned} \tag{12.19}$$

We can use the fact that both the gravitational wave detector output $s(t)$ and the inspiral signals $h(t)$ are real functions, casting the inner product in equation (12.15) into the form

$$(a|b) = 4 \int_0^\infty df \mathrm{Re}[\frac{\tilde{a}(f)\tilde{b}^*(f)}{S_n(|f|)}]. \tag{12.20}$$

In the absence of a signal the mean of $(s|h)$ over an ensemble of detector outputs becomes

$$\langle (s|h) \rangle = \langle (n|h) \rangle = \int_{-\infty}^{\infty} \frac{\langle \tilde{n}(f) \rangle \tilde{h}^*(f)}{S_n(|f|)} = 0 \tag{12.21}$$

and using the PSD definition (12.12) we obtain its variance as

$$\langle (s|h)^2 \rangle = (h|h). \tag{12.22}$$

In the case of a signal being present we get

$$\langle (s|h) \rangle = \langle (n + h|h) \rangle = (\langle n \rangle + h|h) = (h|h), \tag{12.23}$$

and the variance

$$\langle (s|h)^2 \rangle = \langle [(s|h) - (h|h)]^2 \rangle = \langle [(n|h)]^2 \rangle = (h|h). \tag{12.24}$$

So $(h|h)$ is the output of the optimal filter $(s|h)$ and we define

$$\sigma^2 := (h|h). \tag{12.25}$$

The amplitude of the signal depends on the distance we are away from the source. While we assume the type of source by the choice of the waveform model $h(t)$ we do not *a-priori* know the distance from the source and therefore the expected amplitude of the signal. Thus in realistic situations we have to substitute in the above calculations $h(t) \rightarrow A\ h(t)$ to account for an arbitrary amplitude. In the analysis we can then extract a parameter for the distance to the source, the *effective distance*. Substituting $h(t) \rightarrow A\ h(t)$ leads to the expression for the likelihood ratio

$$\Lambda = e^{A(s|h) - \frac{1}{2}A^2(h|h)}, \tag{12.26}$$

which is still monotonic in $(s|h)$ and we can use the decision rules derived above. Now considering a gravitational wave signal of the form

$$h(t) = \frac{A(t)}{D} \cos(2\phi(t) - \theta), \tag{12.27}$$

with

$$A(t) = -\frac{2G\mu}{c^4}[\pi GMf(t)]^{\frac{2}{3}} \tag{12.28}$$

with the effective distance

$$D = \frac{r}{\sqrt{F_+^2(1+\cos^2 i)^2/4 + F_\times^2 \cos^2 i}}. \tag{12.29}$$

where i is the inclination angle of the source and the phase angle θ given by

$$\tan\theta = \frac{f_\times 2\cos i}{F_+(1+\cos^2 i)} \tag{12.30}$$

the likelihood ratio can be expressed as

$$\Lambda'(\theta) = p(\theta)\exp\left(D^{-1}(s|A(t)\cos[2\phi(t)-\theta]) - \frac{1}{2}D^{-2}(h|h)\right), \tag{12.31}$$

where $\phi(t)$ denotes the orbital phase of the signal. We can express the $(s|A(t)\cos[2\phi(t)-\theta])$ using $\cos(\phi-\theta) = \cos\theta\cos\phi + \sin\theta\sin\phi$ as

$$(s|A(t)\cos[2\phi(t)-\theta]) = |z|\cos(\phi-\theta), \tag{12.32}$$

with $x = |z|\cos\phi = (s|A(t)\cos(2\phi(t)))$, $y = |z|\sin\phi = (s|A(t)\sin(2\phi(t)))$ and $|z| = \sqrt{x^2+y^2}$. Assuming now the the unknown phase is uniformly distributed between 0 and 2π,

$$p(\theta) = \frac{1}{2\pi} \tag{12.33}$$

we can calculate the likelihood ratio as

$$\begin{aligned}\Lambda &= \int_0^{2\pi}\Lambda'(\theta)d\theta = \frac{1}{2\pi}\int_0^{2\pi}\exp\left(D^{-1}|z|\cos(\phi-\theta) - \frac{D^{-2}}{2}(h|h)\right)d\theta \\ &= I_0(D^{-1}|z|)e^{-D^{-2}\frac{1}{2}(h|h)}.\end{aligned} \tag{12.34}$$

Here I_0 is the modified Bessel function of the first kind at zero order. Since $I_0(D^{-1}|z|)$ is a monotonically increasing function of $|z|$ we can put our threshold on $|z|$. We can express the two different polarizations of the gravitational waveform by the orthogonal phases

$$h_c(t) = \frac{2}{c^2}\left(\frac{\mu}{M_\odot}\right)[\pi GMf(t)]^{\frac{2}{3}}\cos[2\phi(t)-2\phi_0], \tag{12.35}$$

$$h_s(t) = \frac{2}{c^2}\left(\frac{\mu}{M_\odot}\right)[\pi GMf(t)]^{\frac{2}{3}}\sin[2\phi(t)-2\phi_0] \tag{12.36}$$

and continue to calculate $|z|$ as

$$z = \sqrt{(s|h_c)^2 + (s|h_s)^2}. \tag{12.37}$$

In the absence of a signal $|z|^2$ is summing two squares of independent Gaussian random variables with zero mean and a variance of $\sigma^2 = (h_c|h_c) = (h_s|hs)$. Since x and y are independent random variables, we can introduce a normalized signal-to-noise ratio (SNR)

$$\rho^2 = \frac{|z|^2}{\sigma^2}. \tag{12.38}$$

ρ^2 is χ^2-distributed with the two degrees of freedom for Gaussian detector noise. In addition to determining whether a gravitational wave signal is present or not, in case it is present we also want to accurately determine its occurrence in time. The end-time parameter t_e of the waveform can used to determine the time of arrival. In the discussion above we have assumed to have $t_e = 0$, but allowing for an unknown end time t_e we can write $h(t - t_e)$ and get

$$(s|h_c)(t_e) = 2\int_{-\infty}^{\infty} df e^{2\pi i f t_e} \frac{\tilde{s}(f)\tilde{h}_c^*(f)}{S_n(|f|)}. \tag{12.39}$$

The SNR for a signal ending at time t now becomes

$$\rho(t) = \frac{1}{\sigma}\sqrt{(s|h_c(t))^2 + (s|h_s(t))^2} \tag{12.40}$$

and we can find $(s|h_c(t))$ and $(s|h_s(t))$ by inverse Fourier transforms. By allowing for a unknown end time t_e the statistic ρ has become a function of time $\rho(t)$. In the context of Newman-Pearson optimal detection we need to integrate our signal over all possible end times to apply the threshold for deciding if a signal is present or not. To also determine the arrival time of the signal we can maximize the likelihood [356] in time and use the value of maximum likelihood as the most probable value for the arrival time. So in case of a detection we can after maximizing over the likelihood conclude that we have detected a signal at the time, where the likelihood is maximal. We have in this section now described the basic strategy for detecting a gravitational wave signal in detector noise, and have constructed a optimal filter, which we commonly denote as a *matched filter*.

12.2 Digital matched filtering

In practice the output of the detector is a sampled quantity with discrete values and an sampling interval Δt. The digital matched filter works on a single segment of detector output data with N sampling points of the data $v_j = v(t_j)$. The length of a segment is $T = n\Delta t$ and we use the subscript $_j$ to denote discrete quantities in the time domain and $_k$ to denote discrete quantities in the frequency domain.

12.2.1 The discrete Fourier transform

For a discrete data set v_j with sampling interval Δt the sampling theorem says, that v_j is bandwidth limited to frequencies $-f_{Ny} \leq f \leq f_{Ny}$ with the *Nyquist frequency*

$f_{Ny} = \frac{1}{2\Delta t}$. To prevent power from frequencies above f_{Ny} affecting the signal in the range $-f_{Ny} \leq f \leq f_{Ny}$, we remove frequency above f_{Ny} by applying low-pass filters first and can approximate the Fourier transform of the band limited signal v_j by

$$\tilde{v}(f_k) \approx \sum_{j=0}^{n-1} \Delta t v(t_j) e^{-2\pi i f_a t_j} = \Delta t \sum_{j=0}^{n-1} v_b e^{-2\pi i l k/n}, \tag{12.41}$$

with $-(n/2+1) \leq l \leq N/2$ and $\approx$ describing the discretized version of the Fourier transform. In a similar way we can approximate the discrete inverse Fourier transform

$$v_j = \frac{1}{n\Delta t} \sum_{k=0}^{n-1} \tilde{v}_k e^{2\pi i j k/n}. \tag{12.42}$$

12.2.2 Discrete PSD

To obtain the discrete PSD we substitute $\tilde{n}(f_k)$ with the discrete quantity $\tilde{n}_k = \tilde{n}(f_k)$ leading to

$$\langle \tilde{n}_k \tilde{n}_k^* \rangle = \frac{n}{2\Delta t} S_n(|f_k|) \delta_{kk'}, \tag{12.43}$$

with $\delta_{kk'}$ being the discretized Kronecker δ-function. Equation (12.43) can be shown to be equivalent to

$$S_n(|f_k|) = \begin{cases} \frac{\Delta t}{n} \langle |\tilde{n}_0|^2 \rangle & k = 0, \\ \frac{\Delta t}{n} \langle |\tilde{n}_{N/2}|^2 \rangle & k = N/2 \\ \frac{\Delta t}{n} \langle |\tilde{n}_k|^2 + |\tilde{n}_{n-k}|^2 \rangle & \text{otherwise} \end{cases} \tag{12.44}$$

with the normalization satisfying

$$\Delta t \sum_{j=0}^{n-1} |v_j|^2 = \sum_{k=0}^{n/2} S_b(f_k). \tag{12.45}$$

As an example the power spectrum of white Gaussian noise is constant with value

$$S_n(|f_k|) = 2\Delta t \varsigma^2 \tag{12.46}$$

with ς being the variance of the noise.

12.2.3 Signal-to-noise ratio

Having obtained the discrete Fourier transform and the discrete PSDs we can now continue to calculate the SNR according to (12.17). To do so we need to calculate the time series

$$x(t) = 2 \int_{-\infty}^{\infty} df e^{2\pi i f t} \frac{\tilde{s}(f) \tilde{h}_c^*(f)}{S_n(|f|)} \tag{12.47}$$

$$y(t) = 2 \int_{-\infty}^{\infty} df e^{2\pi i f t} \frac{\tilde{s}(f) \tilde{h}_s^*(f)}{S_n(|f|)}, \tag{12.48}$$

and the normalization constant σ by

$$\sigma^2 = 2\int_{-\infty}^{\infty} df \frac{\tilde{h}_c^*(f)\tilde{h}_c(f)}{S_h(|f|)} = 2\int_{-\infty}^{\infty} df \frac{\tilde{h}_s^*(f)\tilde{h}_s(f)}{S_h(|f|)}. \tag{12.49}$$

The SNR is normalized according to [357] so that for Gaussian noise we have averaged over an ensemble of detectors

$$\langle \rho^2 \rangle = \frac{1}{\sigma^2}\langle x^2 + y^2 \rangle = 2. \tag{12.50}$$

12.3 Template banks and parameter estimation

In order to search for a inspiral signal in a matched filter algorithm we need to provide a target waveform. We call the target waveform a *template*. In practice we not only want to search for one template but for many different templates. To realize this we construct a *template bank*, a discrete subset of the waveform family that we want to search for and that covers the parameter space we are interested in. Ideally we would like to search for waveforms with any kind of parameters, but need to sample the parameters space with a set of discrete points. Choosing an appropriate spacing between the sample points is of one the key aspects in constructing a template bank. If we place the templates too far apart from each other in the parameter space we will loose a large percentage of signals as they do not match the parameters of the nearest template anymore accurately enough. At the same time we need to ensure that the choice of the template bank still leads to an efficient performance of the matched-filter. The spacing between templates is determined by the mismatch, the fractional loss in SNR when the template does not exactly match the inspiral signal. The mismatch $\mathcal{M}$ is defined as

$$\mathcal{M} = 1 - \mathcal{O} = 1 - \frac{(h|s)}{\sqrt{(h|h)(s|s)}}, \tag{12.51}$$

where $\mathcal{O} := \frac{(h|s)}{\sqrt{(h|h)(s|s)}}$ denotes the *overlap*. For a uniformly spaced template bank the number in events lost due to the mismatch is approximately $\mathcal{M}^3$. We commonly construct non-uniform template banks allowing for a mismatch of a maximum of 3%, leading to a loss in event of about 10%. The number of templates scales with the parameters of the bank and is also a function of the PSD of the interferometer since the sensitivity determines how many cycles of an inspiral signal can be potentially detected. Due to this we need to adjust the template bank to every individual data segment using its PSD profile.

We are interested in determining in an accurate fashion the parameters of a detected signal. The physical parameters of the signal are encoded into a parameter vector $\boldsymbol{\theta}$ and we attempt to determine those in terms the parameter vector of the template family $\boldsymbol{\lambda}$. In the construction of template banks two different concepts, a *physical template bank* or a *phenomenological template bank*, can be employed. While a physical bank is constructed from a well-motivated physical model, a phenomenological bank

is constructed *ad hoc*. In case of a physical bank $\boldsymbol{\theta}$ and $\boldsymbol{\lambda}$ consist of the same set of physical parameters, a phenomenological bank often uses a set of parameters $\boldsymbol{\lambda}$ that can be larger or smaller in number then the physical parameters. A mapping of the phenomenological parameters to the physical parameters is then introduced to determine the physical parameters of a signal. The detection efficiency of a template bank is typically measure by a threshold SNR that is larger than a certain minimum value while smaller than a desired value for the false-alarm rate (typically 1%). This threshold value depends on the number of independent templates and the *fitting factor* defined as

$$FF(h, \boldsymbol{\theta}) := \max_{\boldsymbol{\lambda}} \mathcal{M}(s(\boldsymbol{\theta}, h(\boldsymbol{\lambda})) = \mathcal{M}(s(\boldsymbol{\theta}, h(\boldsymbol{\theta}_{max})), \tag{12.52}$$

where $s(\boldsymbol{\theta})$ is a family of waveforms with parameter vector $\boldsymbol{\theta}$ and $h(\boldsymbol{\lambda})$ a family of templates. A template bank with a high fitting factor is called *effectual*. We associate every point $\boldsymbol{\theta} \epsilon \Theta$ in the physical space with the best-match point $\boldsymbol{\lambda}_{max} \epsilon \Lambda$, which results in the mapping $P : \Theta \to \Lambda$ defined as

$$P(\boldsymbol{\theta}) = \boldsymbol{\lambda}_{max}. \tag{12.53}$$

We will assume that this mapping is single-valued, and for a physical template bank we can identify the best-match parameter $\boldsymbol{\theta}_{max}$ as the estimation of the original parameter $\boldsymbol{\theta}$. This will result in the *bias*

$$\Delta\boldsymbol{\theta} = \boldsymbol{\theta}_{max} - \boldsymbol{\theta} = P(\boldsymbol{\theta}) - \boldsymbol{\theta}. \tag{12.54}$$

We call a bank with small bias *faithful*. As long as there is no uncertainty in the true waveforms, then as long as we require p o be invertible, we can always convert non-faithful bank into a faithful one by the reparametrization

$$h_{faithful}(\boldsymbol{\theta}) := h(P(\boldsymbol{\theta}). \tag{12.55}$$

For a physical bank it is quite intuitive, that if the bank does describe the physical parameters well, P is invertible. For a phenomenological bank this is in general not true as P can be a many-to-one map with $P(\boldsymbol{\theta}_1) = P(\boldsymbol{\theta}_2)$ for $\boldsymbol{\theta}_1 \neq \boldsymbol{\theta}_2$. In this case the set of parameters $P^{-1}(\boldsymbol{\lambda}_{max})$ is the best knowledge we can obtain about the physical parameters of the signal.

12.4 χ^2-veto

In the previous discussion we have assumed that the noise affecting the detector is Gaussian. In reality this condition does not hold as the various noise sources influence the detector in a different way. It is however crucial that we have a tool to decide if a signal is a true gravitational wave from an inspiral event since transient events in the detector data may lead to false alarms in our matched filter implementation. These transient events typically appear with a high SNR and we consequently need a different theoretical tool to distinguish true signals from transient events. We have found that a

time-frequency veto, the χ^2-veto, first suggested in [358] is very effective in performing this test. We briefly describe the key points of χ^2-veto in this section and refer the interested reader to [358] for more details. For u and v being two orthonormal time series describing the two phases of a inspiral signal $h_c(t_j)$ and $h_s(t_j)$ we divide u and v into p frequency intervals u_l and v_l with $l = 1...p$ such that

$$(u_l|u_m) = \frac{1}{p}\delta_{lm} \tag{12.56}$$

$$(v_l|v_m) = \frac{1}{p}\delta_{lm} \tag{12.57}$$

$$(u_l|v_m) = 0. \tag{12.58}$$

We can now obtain

$$x = \sum_{l=1}^{p} x_l = (h|u) \tag{12.59}$$

$$y = \sum_{l=1}^{p} y_l = (h|v), \tag{12.60}$$

using $x_l = (s|u_l)$ and $y_l = (s|v_l)$ with s being the detector output and imposing $\rho^2 = (x^2 + y^2)/\sigma^2$. For $\Delta x_l = x_l - \frac{x}{p}$ and $\Delta y_l = y_l - \frac{y}{p}$ we can define

$$\chi^2 = \frac{p}{\sigma^2}\sum_{l=1}^{p}[(\Delta x_l)^2 + (\Delta y_l)^2]. \tag{12.61}$$

In both cases of only Gaussian noise present in our detector output ($s = n$) or Gaussian noise plus an inspiral signal ($s = n + h$) χ^2 is χ^2-distributed, but a small value of χ^2 for a high SNR indicates it is a true inspiral signal while high values indicate a transient event. We therefore apply an additional χ^2 threshold on high SNR events. In principle we are interested in applying the χ^2-veto to all events, but in practice only apply the χ^2-veto to high SNR events to limit the computational cost of our algorithm.

12.5 Trigger recording and selection

The times when our matched filter tells us that an inspiral signal was detected are called inspiral triggers. For any trigger event, we record the time, mass and parameters of the template as well as the value of σ^2 of the data segment, the trigger was found in. However a trigger can be a false alarm, and as described in the previous section we perform an additional χ^2-test to distinguish between real inspiral triggers and transient events. For any trigger event the SNR must exceed the threshold value $\rho^2 > \rho_T^2$ and the χ^2-statistic must be below the threshold value $\chi_T^2/(p_\rho^2\delta^2)$. It may happen that multiple triggers are present in one data segment. Additionally, one inspiral event will likely have many sampling points corresponding to the full signal. To group triggers for one

event we require any trigger that belongs to a different template to have a difference in coalescence time that is different by at least the length of the template waveform. This algorithm is also called *maximizing over a chirp*. The final output of our matched filer search algorithm is a list of triggers and their parameters as well as the GPS time. After these lists have been generated and vetoed we can test for coincidence between different detectors and apply additional analysis. All of these steps combined constitute a data analysis pipeline and we will describe the pipeline used for the search for compact binary coalescence (CBC) in the next section.

12.6 Gravitational wave data analysis using the CBC pipeline

In the previous sections we have described the core functionality of a matched filter algorithm used to search for gravitational wave signals in detector output data. The basic features and equations have been described for a search in one segment of detector data. For current gravitational wave searches this functionality is embedded in a more complex data analysis pipeline that handles all the other tasks necessary to analyze a stream of detector data and perform additional analysis steps that go beyond the matched filtering algorithm. This includes generating a template bank, managing the analysis of all the detector output data segments, grouping triggers, determining the coincidence properties of triggers between independent detectors. In analysis pipelines operating on real detector output additional data quality cuts are applied to determine whether the data collected was obtained during stable operation of the interferometer. However since all the results presented in this dissertation were obtained with simulated noise instead, we neglect this aspect of analysis pipelines in the following and concentrate on the relevant core components. In this section we will briefly describe a modification of the standard CBC pipeline that allows for a more general filtering algorithm and that was developed to perform the analysis presented in chapter 13.

12.7 Signal injection and simulating detector noise

Beyond the search for real gravitational wave inspiral signals it may be useful to inject 'fake' signals into the detector noise output or even simulate detector noise output with injected signals. This becomes especially useful for testing new functionality of the analysis pipeline in a more limited and simple setting. There are various different noise profiles that can be easily generated, most commonly colored (i.e., the noise values are correlated in some fashion) Gaussian noise is used. While this is not comparable to realistic detector output it provides an excellent testing setup. In addition to the noise spectrum being generated we can inject signals from analytically modeled waveform families into the noise or detector output. The waveform families available range from simple PN inspiral only waveforms to the very advanced phenomenological waveform families that include spin effects and have been constructed using PN theory for the inspiral and data from Numerical Relativity simulations for merger and ring-down phase.

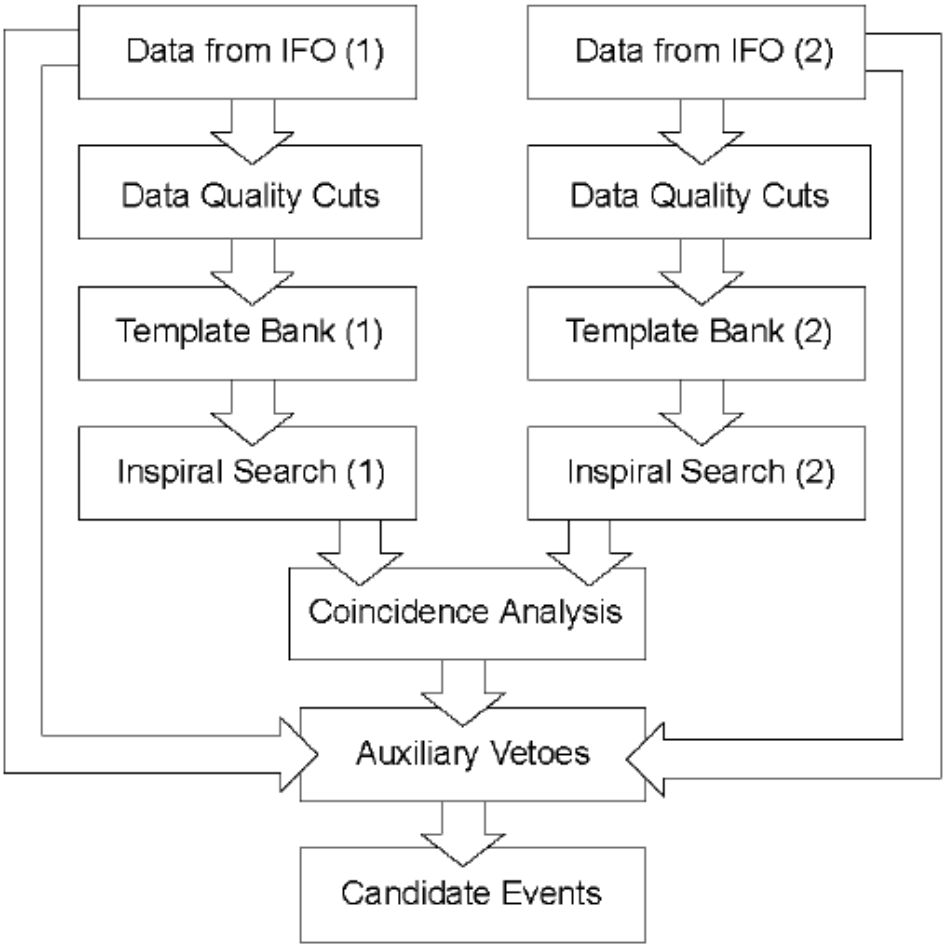

Figure 12.1: Schematic work-flow of a simple pipeline using input data from two detectors IFO 1 and IFO 2. Figure taken from [354].

12.8 Generation of inspiral triggers

For both the construction of the template bank and for the generation of the inspiral triggers several parameters can be tuned to achieve minimum false alarm and false dismissal rates. We require a calibrated PSD and the inspiral trigger generation is coupled to the length of the data segments in the analysis output. The parameters in the construction of the data segments that determine the characteristics of the PSD are tuned in a procedure called *data conditioning*. In the following we give a quick overview about these parameters. For a more detailed discussion we refer the reader to [359].

- The number of sample points in a data segment, n, determines the length of the segments and the overlap between data segments $n_{overlap} = n/2$.
- The number of data segments in a chunk of data $N_{segments}$ determines the number of segments in an analysis chunk.
- The sample rate is $1/\Delta t$.
- The number of non-zero points in the square root of the inverse power spectrum in the time domain, $N_{invspectrum}$.

Additionally the parameters that control cut-offs for the time and frequency domain filter used in the matched filtering algorithm are

- The high-pass filter cut-off frequency f_{high} applied to the analysis chunks before PSD estimation and inspiral trigger generation.
- The low-pass filter cut-off frequency f_{low} to exclude low frequencies in the matched filter and χ^2-analysis.

The parameters used in the generation of the inspiral triggers are

- The SNR threshold ρ_T.
- The χ^2 threshold χ^2.
- The number of bins used in the χ^2-analysis p.
- The parameter δ^2 used to describe the mismatch of signal and template in the χ^2-analysis as described in section 12.4.

These parameters are tuned to the specific search that is carried out.

12.9 Trigger coincidence

Detecting a trigger in coincidence in two or more independent detectors greatly decreases the chances of a false alarm. To say a trigger is in coincidence between two or more detectors we must define a time interval δt in which we say we have a coincidence detection. To determine δt we must take into account the accuracy in which we can measure the time of the trigger, which for current detectors is approximately 1ms. If the two detectors are not located in the same site we must also also allow for the difference in arrival time of the signal in the two different detectors. For the two LIGO detectors in Washington and Louisiana this accounts to 10ms so that we have in combination for a coincidence between LIGO Livingston Observatory (LLO) and LIGO Hanford Observatory (LHO) a $\delta t = 11$ms. If a trigger is present in both detectors within that time interval we have a coincident trigger. In addition to the temporal coincidence a inspiral signal detected in coincidence should also be recovered with the same signal parameters. However since detectors have different antenna patterns and

other specifics in the detector channels may influence the trigger generation, we must allow for a difference in the signal's parameters. For example we allow for a parameter coincidence in the two masses m_1 and m_2 for an interval δm. If we obtain the parameters between triggers in different detectors within δm we say we have parameter coincidence. Besides the time and parameters of the trigger, the amplitude and phase of a trigger will differ between different detectors due to the different antenna pattern. In extreme cases this can lead to a trigger generated in one of the detectors while not generated in the other. Thus we can use the effective distances and their differences between the two detectors not in alignment, to perform an amplitude cut.

13

Improving detection statistics for spinning phenomenological waveform templates

Currently, three major detectors are in operation (more specifically currently one of them is in an upgrade process and not performing scientific measurements). The GEO detector is a German-British effort with its detector being located close to Hanover, Germany. It has an arm-length of about 600m and tries to incorporate the latest detector hardware and techniques. The Virgo detector is operated in Italy has an arm-length of approximately 3km. The LIGO detectors are located in the U.S.A., one in state of Washington, and one in Louisiana. Both interferometers have an arm-length of 4km and to date have achieved the highest sensitivity in their respective noise curves. The basic principle of these detectors is simple: If a gravitational wave passes by, it will change the arm-length of the detectors. By construction the arms are oriented to each other with an angle of 90 degrees and taking into account the polarizations states of gravitational waves (see chapter 1), the photons traveling through one arm would need to travel a longer distance than the other, leading to an interference pattern in the detection screen. This interference pattern is measured and is the basic output of the detector. However, due to the many noise sources that influence the detector and due to the vanishingly small nature of a possible gravitational wave distortion changing the detectors arm-lengths, sophisticated techniques for filtering the expected signal from the detector noise are needed. For a certain class of gravitational wave sources we can accurately predict the signal, and we can use this in combination with data analysis techniques for statistically analyzing the detector output. There are many ways in which this analysis can be done but in this thesis the approach of matched-filtering was used to obtain the results presented in this chapter.

A gravitational wave signal from the merger of two compact objects provides an ideal candidate for detection. The most probable types of these systems are formed by two neutron stars or black holes. Mixed binary systems may also be detected but at the moment it is unclear how likely these source are and they play a minor role in

the effort of current gravitational wave data analysis. Binary systems consisting of two inspiraling black holes can be modeled analytically very well by the use of PN expansion theory for the inspiral phase and perturbation theory for the ring-down. Recently, also the gravitational wave signature of the merger can be predicted very well by Numerical Relativity simulations. Historically, the search for gravitational waves from CBC was carried out using templates in the matched filtering techniques that only consisted of the pre-merger part of the signal. But the radiated energy reaches its maximum during the merger and thus it is desirable to include the full waveform in constructing the templates for a matched-filtering pipeline. Recently, hybrid waveform models have been suggested [360, 361, 362] which combine PN theory and numerical relativity to construct waveforms covering the very long inspiral as well as the merger by stitching the two models together. The use of these inspiral-merger-ringdown (IMR) waveforms is currently the state-of the art in CBC detection pipelines.

Astrophysical binary black-hole systems can be characterized by the mass of the two black holes (or the mass-ratio) and the spin vectors of the two individual black holes (see section1.5 for more details). As we do not precisely know which systems we can expect to detect we need to in principle search every possible combination of the 7-dimensional parameter space. This however is too expensive to carry out in practice. In most searches up to now the spin of the black holes was mainly ignored and non-spinning waveform models were used as this greatly reduces the parameter space to sample as well as simplifies the modeling considerably. With the construction of IMR waveforms however models for including spin effects have been suggested.

In this chapter we first present the basic concepts and techniques used in modified version of the CBC pipeline. It has been extended to included phenomenological waveform models for the matched filter. We focus our presentation on the waveform models we use, the construction of a spinning template bank, and the heart of the detection pipeline, the matched-filtering algorithm. We provide first results on searching for CBC signals with templates constructed from IMR waveforms using aligned or anti-aligned spins with respect to the orbital angular momentum of the binary. We provide basic comparisons between non-spinning waveforms and waveforms including spin effects and determine the effect on the detection statistics of CBC signals. Finally we present results obtained using injected waveforms in simulated detector noise to estimate the improvement on detection statistics and parameter estimation for CBC sources. The presentation here follows closely [363].

13.1 Waveform models

Searches for CBC signals in data from ground-based detectors have long used PN approximate waveforms as templates (e.g. [364, 365]). However, these waveforms are only applicable in the pre-merger regime. Numerical Relativity simulations allow an exploration of the merger and ring-down regimes, but the computational resources needed to produce even short waveforms prohibit using Numerical Relativity waveforms for template searches. In recent years, there have therefore been several efforts to

develop full (semi-)analytic IMR waveforms, which can be computed quickly enough to be used for template searches, for example effective one-body/Numerical-Relativity (EOBNR) templates [366].

The first such phenomenological model was fitted using just mass and mass ratio to hybrids of non-spinning numerical waveforms and TaylorT1 2PN[360]. This model was extended to spinning waveforms in two separate studies, one carrying out the hybridization in the time domain[361] and one in the frequency domain [362]. These latter waveforms are used in this thesis. They were fitted to numerical waveforms from several groups, and made use of a 3.5PN expansion of the phase, including incomplete spin terms at 3PN and 3.5PN, and a 3PN expansion of the amplitude. They also depend on three intrinsic physical parameters, M, η and χ. We use these waveforms to investigate the effects of including and/or neglecting spin when using the findchirp search.

Phenomenological waveforms are produced by matching PN approximate waveforms to several Numerical Relativity waveforms. These hybrid waveforms are fitted with functions, dependent on several phenomenological parameters. These are, in turn, functions of the physical parameters characterizing the two black holes. The two black holes are characterized by their masses, m_i, and the magnitude of their spins,

$$S_i = |\chi_i| m_i^2, \;\; i = 1, 2. \tag{13.1}$$

The physical parameters that are used to create the waveforms are the total mass, $M = m_1 + m_2$, the symmetric mass ratio,

$$\eta = \frac{m_1 m_2}{(m_1 + m_2)^2}, \tag{13.2}$$

and the mass-weighted total spin of the system,

$$\chi = \frac{1+\delta}{2}\chi_1 + \frac{1-\delta}{2}\chi_2, \tag{13.3}$$

where $\delta = (m_1 - m_2)/M$. We integrate up to the Lorentzian ringdown (LRD) frequency, which is mass and mass-ratio dependent, but does not depend on the spin,

$$f_{LRD} = 1.2 \frac{1 - 0.63(1 - 3.4641016\eta + 2.9\eta^2)^{0.3}}{2\pi(1 - 0.057181\eta - 0.498\eta^2)M}. \tag{13.4}$$

13.2 Creating spinning template banks

In order to efficiently search the parameter space, template banks are created. In the case of a two-dimensional search (i.e. η-$\mathcal{M}_{\rm chirp}$) the optimal spacing is a hexagonal lattice, with the lattice determined using the metric. In fact, often the τ_0-τ_3 space is used, as the parameter space is flatter.

When we extend to a three-dimensional search, including the χ parameter, the simplest approach is to construct a two-dimensional lattice in η-$\mathcal{M}_{\rm chirp}$ or τ_0-τ_3 space,

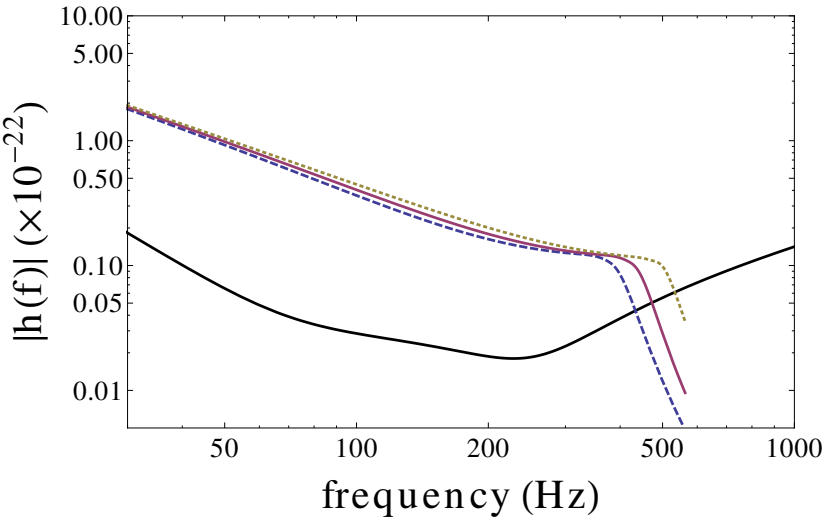

(a)

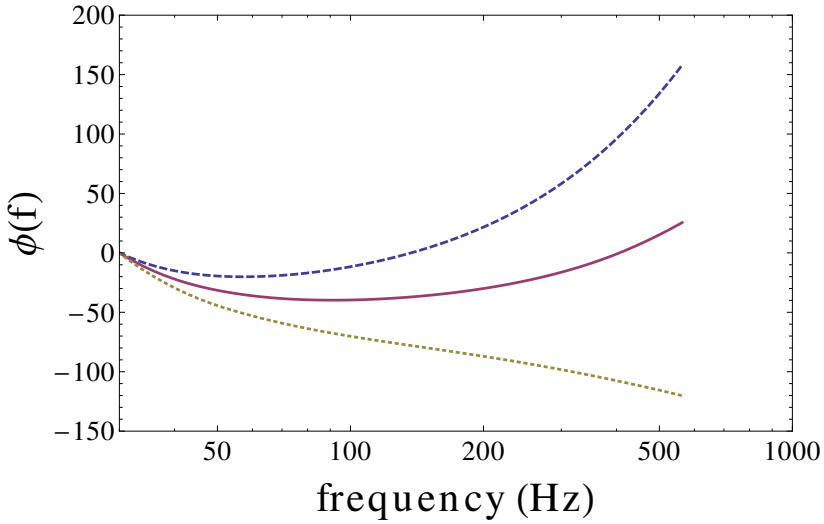

(b)

Figure 13.1: Plot showing the waveforms from a binary at 500 MPc, with "average" sky position. The waveforms have mass ratio $\eta = 0.25$ and total mass $M = 40M_{\odot}$. The solid line shows the waveform with spin $\chi = 0$, the dashed line has spin $\chi = -0.5$ and the dotted line has spine $\chi = 0.5$. The waveform stays in band for longer for higher spins. The upper cutoff is given by the LRD frequency, Equation (13.4). The solid black line shows the advanced LIGO spectrum for comparison.

then replicate this at regular intervals in χ space (we call this a *stacked* bank. This, has been used in some limited cases, however it does not allow for the possibility of

the metric varying significantly with χ. In order to construct an optimal template bank, we could choose to construct a lattice on the metric using an optimal spacing (e.g. body-centered cubic). However, this is not a trivial approach. It has been shown that, at low dimensionality, it is similarly efficient to construct a *stochastic* template bank [367]. We compare the use of a *stacked* bank with a *stochastic* bank, and show that the stochastic method is an efficient way to construct a template bank.

13.2.1 Approximation to the overlap using Fisher matrices

In order to form a template bank, we must place templates such that the minimum overlap between any waveform in the parameter space and any waveform in the bank is 0.97 (or whatever we choose). In order to do this efficiently, we use a metric constructed with Fisher matrices. The Fisher matrix has elements given by

$$\Gamma_{ij} = \left(\frac{\partial \tilde{h}(f;\boldsymbol{\theta})}{\partial \theta_i} \middle| \frac{\partial \tilde{h}(f;\boldsymbol{\theta})}{\partial \theta_j} \right), \tag{13.5}$$

where $\boldsymbol{\theta}$ is the parameter vector of the injected waveform. In order to approximate the ambiguity function, we must use the normalized Fisher matrix,

$$\hat{\Gamma}_{ij} = \frac{\Gamma_{ij}}{\left(\tilde{h}(f;\boldsymbol{\theta}) | \tilde{h}(f;\boldsymbol{\theta}) \right)}. \tag{13.6}$$

We approximate the overlap with a Gaussian function with a covariance matrix equal to the inverse of the Fisher matrix

$$\mathcal{A}(\boldsymbol{\theta}, \boldsymbol{\theta'}) = \max_{t_c', \phi_c'} \left[\exp\left(-\frac{1}{2} (\boldsymbol{\theta'} - \boldsymbol{\theta})^T \cdot \Gamma \cdot (\boldsymbol{\theta'} - \boldsymbol{\theta}) \right) \right], \tag{13.7}$$

Here $\boldsymbol{\theta'}$ is the vector of parameters of the search waveform, and the function is maximized over the extrinsic parameters – time and phase of coalescence – of the search waveform. The maximization of a Gaussian can be done analytically, and we find the maxima at

$$t_c = \frac{\sum_{i=\eta,\chi,M}^{3} (\Gamma_{it_c}\Gamma_{\phi_c\phi_c} - \Gamma_{i\phi_c}\Gamma_{t_ct_c})(\theta_i' - \theta_i)}{\Gamma_{\phi_ct_c}^2 - \Gamma_{\phi_c\phi_c}\Gamma_{t_ct_c}} \tag{13.8}$$

$$\phi_c = \frac{\sum_{i=\eta,\chi,M}^{3} (\Gamma_{i\phi_c}\Gamma_{t_ct_c} - \Gamma_{it_c}\Gamma_{\phi_ct_c})(\theta_i' - \theta_i)}{\Gamma_{\phi_ct_c}^2 - \Gamma_{\phi_c\phi_c}\Gamma_{t_ct_c}}. \tag{13.9}$$

Figure 13.2 shows the actual overlap and its approximation using Fisher matrices for a particular waveform. We see that the Fisher Matrix approximation is a little narrower that the actual overlap, so its use gives us a slightly overpopulated template bank.

The stacked bank contained 154 templates, while the stochastic bank contained only 89. This indicates that the stacked bank is intrinsically less efficient than a stochastic bank. If we plot the template points, we also see that the density of points depends on

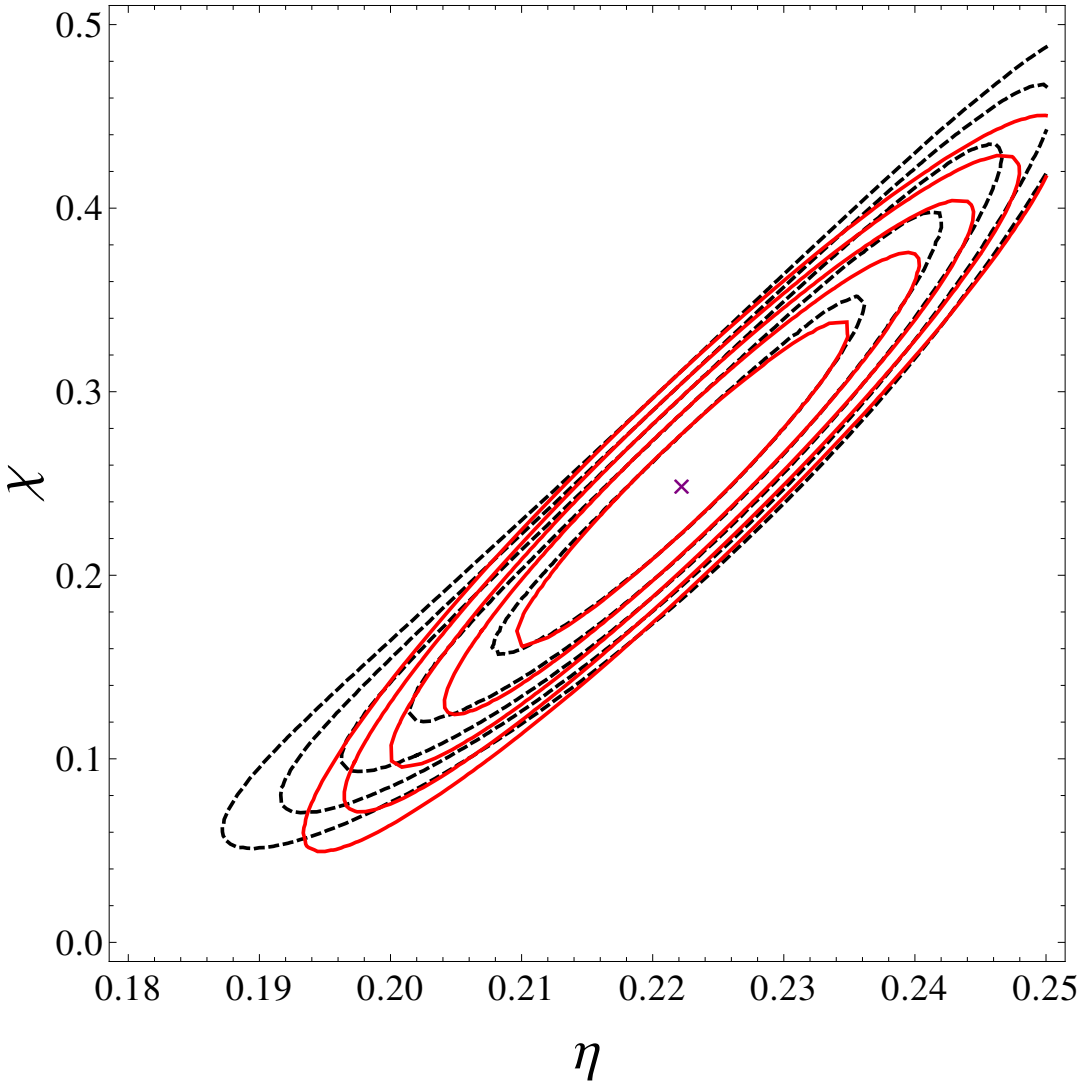

Figure 13.2: Plot of the 2d overlap contours using the (maximized) overlap and the Fisher Matrix approximation

the spin – higher values of χ seem to require higher densities of points. If we compare the biases obtained for the three parameters, we see that they are comparable for both banks. The stochastic bank is much more efficient, containing slightly over half the number of templates, but giving similar biases.

13.3 Effects of spin

Until now, it has been assumed that the use of non-spinning templates for a match-filtered search will decrease detection efficiency within acceptable limits (below 10%).

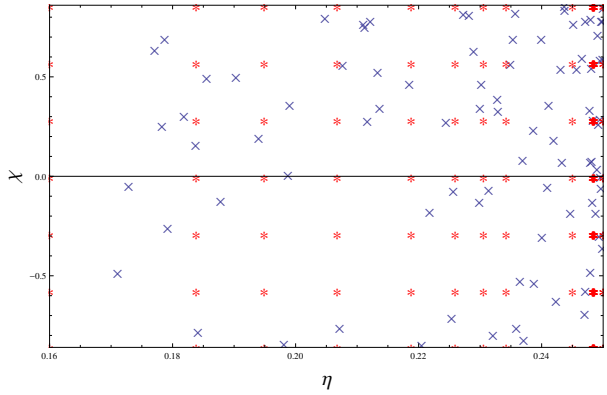

(a)

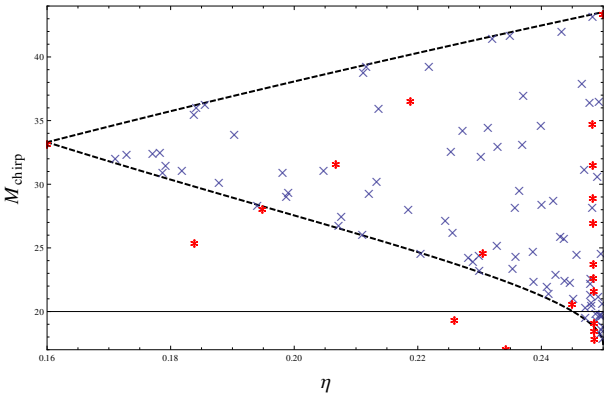

(b)

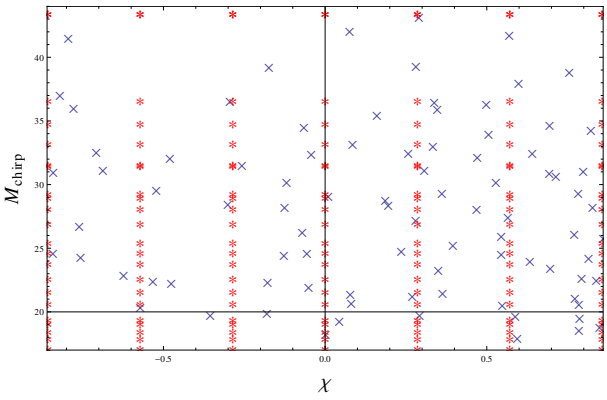

(c)

Figure 13.3: Plots showing the templates in two banks with minimal match 0.97. Red stars are the stacked bank, blue crosses the stochastic bank

We investigate the effect that introducing a spin contribution has on the detection efficiency of a search, along with the bias that it may introduce on the recovered parame-

ters. We use the full spinning IMR waveforms as our fiducial target waveform, and use the non-spinning versions (i.e. $\chi = 0$) as our search waveforms. The results presented in this section were obtained running in simulated detector output using data segments of a length of 4096. Signal were injected using waveforms of the phenomenological family including spin effects presented in 13.1. Filtering was first performed using waveforms modeled by inspiral only waveforms as a reference to what was previously used in data analysis pipelines. Next we present the improvements in the detection statistic when we in contrast filter with the same phenomenological templates as injected including spin effects. The results in terms of the detection statistics are presented in figures **??** and 13.5.

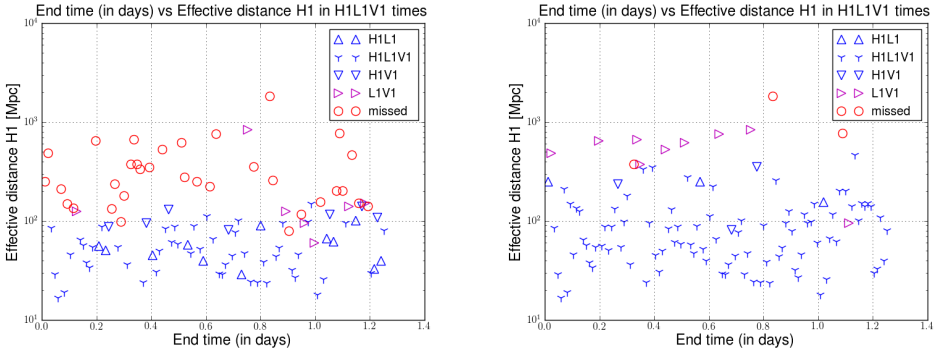

Figure 13.4: Detection statistics overview for injected signals in Gaussian detector noise. The left panel shows the results when filtering with non-spinning inspiral only templates, while the right panel presents results obtained when filtering with a templates constructed from a phenomenological waveform family including spin effects. Coincidence properties of the recovered triggers are indicated by the different symbols explained in the legend in the top-right corner of the respective plots. H1 represents the Hanford LIGO detector, L1 the Livingston LIGO detector, and V1 the Virgo detector.

Figure **??** shows an overview over the detection statistic achieved by filtering with non-spinning templates in contrast to filtering with phenomenological templates including spin. The top panel uses Schwarzschild ISCO waveforms used in typical searches in current pipelines. Shown is the effective distance as recovered in the H1 detector versus the end-time of the recovered signal. The missed signals are obvious and constitute a good portion of the total number of injected signals. In contrast in the lower panel of this figure we show the same plot but now in the case when we filter with templates including spin effects. We find that only a few signals are missed, indicating that the detection statistic is superior in its ability to efficiently detect spinning inspiral signals.

Figure 13.5 presents data illustrating the recovery of the degenerate spin parameter χ. In the top panel the recovered spin parameter χ is plotted against the injected one. It is evident that we use five point in sampling the range in χ and signals are recovered with these values. The lower panel shows a histogram version of the fractional error in χ including a fit to the data and the fit parameters.

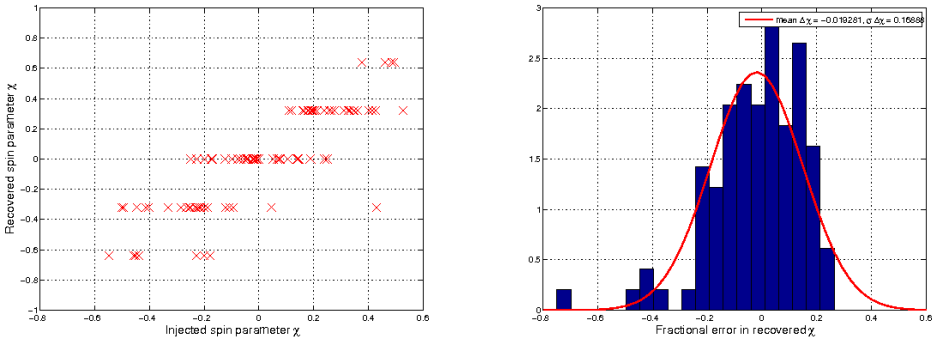

Figure 13.5: Injection and recovery in the degenerate spin parameter χ of the binary as obtained for the H1 LIGO detector. The left panel shows recovered versus injected χ. The right panel shows a histogram view of the fractional error (blue bars) in χ in the recovered signals when compared with the injected ones. In addition a Gaussian fit is included (red curve).

If we were to search with only non-spinning waveforms, this would severely reduce our detection efficiency. It would also introduce a bias on the value of η' and M' that maximize the overlap.

13.3.1 Bias on parameters

In addition to missing signals due to filtering with non-spinning waveform templates only, we will also introduce a bias for the parameters for the successfully recovered signals. To estimate the bias figure 13.6 shows the ambiguity function predicted bias on the parameter η of the recovered inspiral signal. We show the ambiguity function predicted bias in η for three choices of η corresponding to mass ratios $1:1$,$1:2$, and $1:3$. We clearly see a predicted bias on the spin parameter χ.

To make our analysis more quantitative we continue to compare the predicted bias on η with the bias obtained in simulated detector data. The data is colored with the LIGO spectrum and we first carry out a search using non-spinning templates. The top panel of figure 13.7 shows the predicted bias for different values of η as solid lines and the actual relative error in recovered versus injected signal parameters. The results from the simulation clearly follow the predicted trend with an additional statistical distribution around these curves. When in contrast performing the search with templates including spin effects, we do not see a trend following the predicted bias for non-spinning waveforms. This is illustrated in the bottom panel of figure 13.7, which again shows the relative error in η of recovered versus injected signals. It is evident that in this case we only see a statistical distribution of values around zero.

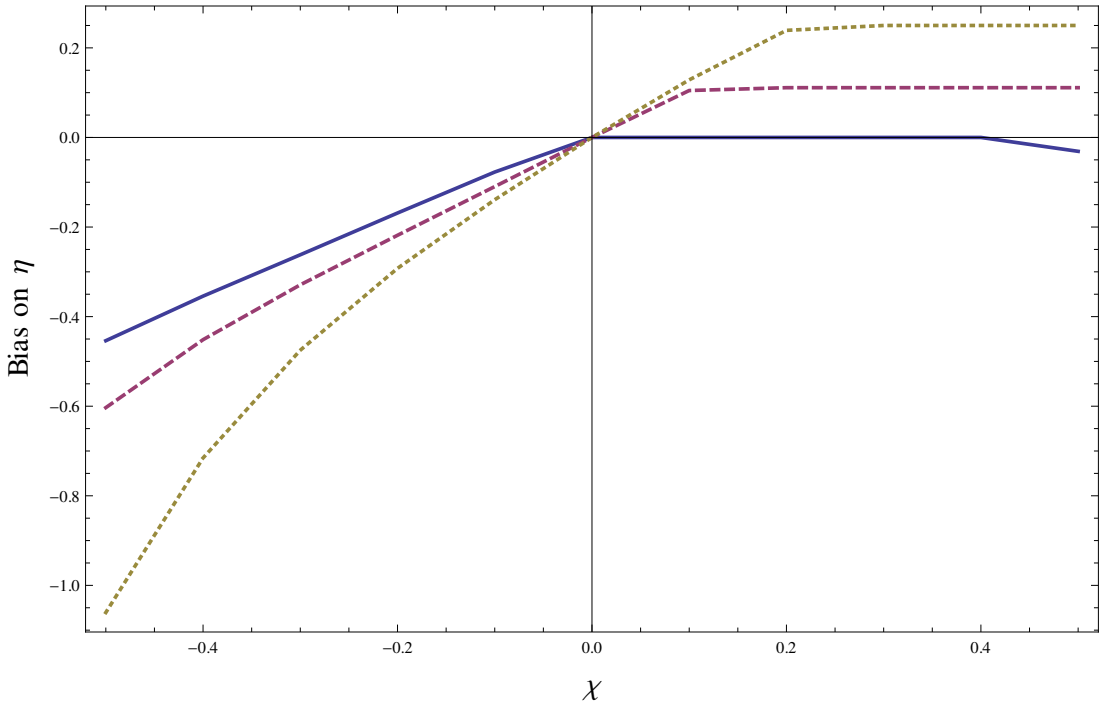

Figure 13.6: Plot showing the relative bias on η corresponding to the maxima of the (approximate) ambiguity function. The target waveforms have mass ratio 1:1 (solid), 2:1 (dashed) and 3:1 (dotted), and have total mass equal to $40M_{\odot}$. The line becomes horizontal for high spin as the symmetric mass ratio is constrained to be physical ($\eta \leq 0.25$).

13.4 Implications for future searches

We have taken the first steps in investigating the effects of using spinning waveform models in a matched-filtering based CBC analysis pipeline. We have found that by constructing spinning template banks and using phenomenological waveform models in the matched filter we can considerably increase the ability of our detection pipeline to detect injected spinning signals in simulated detector data. In addition we have analyzed the bias on recovered signal parameters and provide an example study of the mass-ratio parameter η. We have investigated how the predicted bias relates with the bias obtained from searches in simulated data and found good agreement. Additionally we have shown that this bias mostly vanishes when using spinning waveforms when filtering. In combination these results indicate that by the inclusion of spin effects in CBC pipelines we can expect to improve the detection statistics for spinning signals as well as reduce the bias in the recovered signal parameters when compared to searches using non-spinning templates. The inclusion of spin in the search for inspiral signal from CBC sources ensures a much better detection efficiency, as well as reduces bias on estimated parameters.

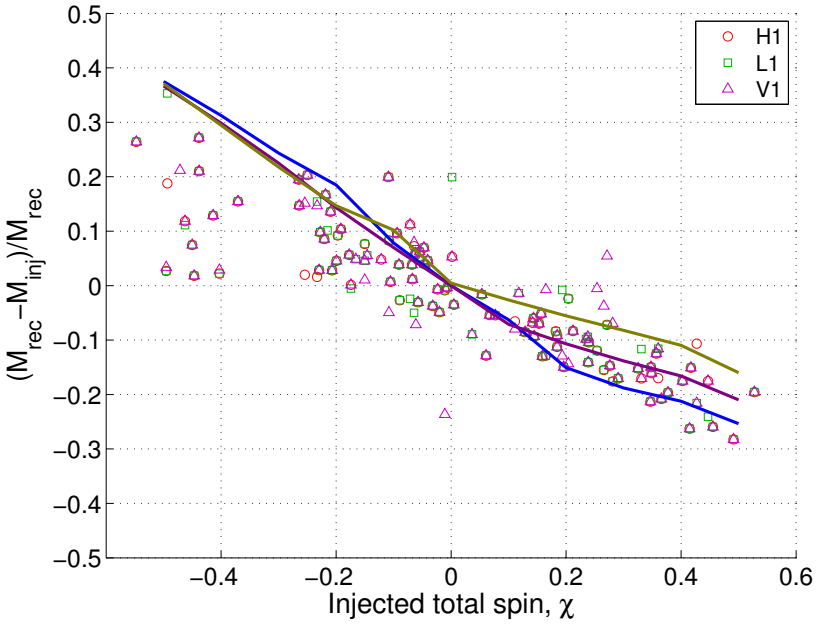

(a)

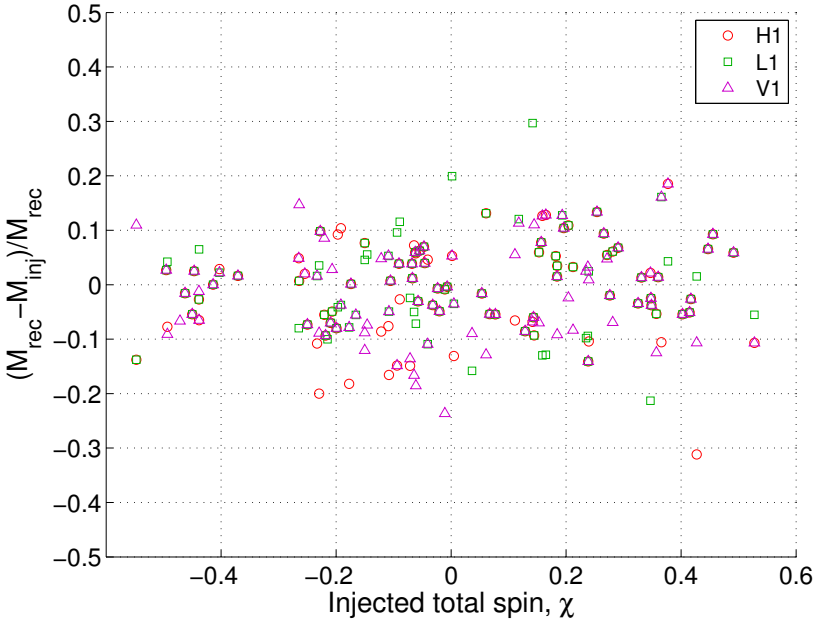

(b)

Figure 13.7: Plots showing the predicted relative bias on η corresponding to the maxima of the ambiguity function, for target waveforms with mass ratio 1:1 (blue), 2:1 (purple) and 3:1 (yellow). Also the bias obtained when carrying out a search in data colored with LIGO spectra, when the search was carried out with non-spinning templates (a) and with spinning templates (b).

13. IMPROVING DETECTION STATISTICS FOR SPINNING PHENOMENOLOGICAL WAVEFORM TEMPLATES

14

The big picture: Summary and conclusion

Binary black-hole mergers are undoubtedly one of the most exciting events in our universe. Observing such events would enable us to gain insight into gravity in a highly dynamical strong field regime. Furthermore, in the case of supermassive black holes these mergers will not take place in an isolated setting and their interaction with surrounding gas and matter will be a fertile ground for exciting new physics. More specifically, as the gravitational wave emission becomes the dominant mechanism of energy loss of the inspiraling black holes, the binary will probably be surrounded by a circumbinary, likely magnetized, accretion disk. The interior region then will be mostly devoid of matter, and the binary immersed in a low-density gas and a plasma. If the disk is magnetized, the magnetic field will also reach the region containing the black holes. This setting provides an exciting possibility of studying various observational signatures of binary black-hole mergers.

Gravitational waves from binary black-hole mergers are among the prime sources for current earth-based as well as planned future space-based detectors. In the case of supermassive black holes the possibility of detecting an EM counterpart to the gravitational wave signature is particularly important as it would allow for the measurement of the red-shift and would boost our understanding of the source by an enormous amount. In this way, we would be able to determine not only the sky position with much more accuracy, but also learn about the surrounding matter, the host galaxy and the cosmological setting.

Apart from the observational prospects binary black-hole mergers also provide an interesting setting to study the geometry and structure of space-time itself. By studying the geometry in this highly dynamical and non-linear setting we can learn a lot about the merger process and even connect geometric quantities to measurable ones, like the radiated angular momentum. This opens a completely new way of analyzing binary black-hole mergers in terms of quantities defined in the near-field region.

In this dissertation we have reported on our work towards modeling a variety of aspects regarding binary black-hole merger simulations and the closely connected analysis

of their gravitational wave signature. First, we have performed numerical simulations of head-on unequal mass binary black holes and shown a correlation between the effective curvature anisotropies and the radiated linear momentum in gravitational waves. Additionally we have introduced a number of geometric quantities constructed on dynamical and isolated horizons which may serve as valuable tools in the analysis of black-hole mergers. In a further step we have investigated the time evolution of the individual apparent horizons in an unequal-mass head-on collision of two black holes and provided the first systematic analysis of the evolution of these surfaces. In a second part of this thesis, we have investigated the possible EM signatures of supermassive binary black-hole mergers, when immersed in a magnetic field or plasma. We have carried out the first simulations of spinning black-hole mergers in a uniform magnetic field, determined the effect of the spin on the EM field and the radiation that is generated, and have assessed the relevance of the processes for astrophysical detectability. In a second step, we have extended our model to include plasma effects and have proposed a new way of measuring the radiation content of space-times when dealing with sources of non-compact support. We have shown an overall improved efficiency in the radiated energy but also have found restrictions on the visibility of the collimated emission. Third, we have investigated the effect of using spinning waveform templates in state-of-the-art data analysis pipelines for the search of gravitational waves from binary black-hole mergers. In this way we have demonstrated an overall improved detection statistics and reduced bias when recovering source parameters of spinning signals.

In the following we summarize the results found in this dissertation, draw quantitative and qualitative conclusions based on current knowledge and provide an outlook towards possible future research.

14.1 Explaining the anti-kick in binary black-hole mergers

We have demonstrated that qualitative and quantitative aspects of the post-merger recoil dynamics at infinity can be understood in terms of the evolution of the geometry of the common horizon of the resulting black hole. More importantly, we have shown that suitably-built quantities defined on inner and outer world-tubes can act as test screens responding to the space-time geometry in the bulk, thus opening the way to a precise cross-correlation approach to probe the dynamics of space-time. We have constructed a phenomenological vector $\tilde{K}_i^{\rm eff}(t)$ on the dynamical horizon sections, which captures the global properties of the flux of Bondi linear momentum $(dP_i^{\rm B}/dt)(t)$ at infinity, namely (proportional to) the acceleration of the black hole. At the same time, we have developed a cross-correlation methodology which is able to compensate for the gauge character of the time evolution on the two surfaces. The effective curvature vector reflects the properties of the black hole and in particular its exponentially damped ringing. The timescales associated with this process, which are inevitably imprinted in our geometric variables, provided also a natural connection with the approach discussed in [213], where the anti-kick is explained in terms of the spectral features of the signal at large distances. In the setting of a $3+1$ approach to the black-hole space-time

construction, the foliation uniqueness of dynamical horizons provides a rigid structure that confers a preferred character to these hypersurfaces as probes of the black-hole geometry. Employed as inner screens in the *cross-correlation* approach, this DH foliation uniqueness permits to introduce the preferred normalization of the null normals to apparent horizon sections and, consequently, a preferred angular scaling in the Weyl scalars on these horizons. We have linked the effective curvature vector $\tilde{K}_i^{\rm eff}(t)$ to the identification of the shear $\sigma_{ab}^{(h)}$, associated with the DH evolution vector h^a, as being proportional to a geometric DH news-like function $\mathcal{N}_{ab}^{(\mathcal{H})}$. This identification provides a (refined) geometric flux quantity $(dP^{(\mathcal{H})}/dv)_i(v)$ on DH sections to be correlated to the flux of Bondi linear momentum $(dP^{\rm B}/du)_i$ at $\mathcal{I}^+$. We have advocated the physical relevance of tracking the internal horizon in $3+1$ black-hole evolutions and from the perspective of a viscous-horizon analogy we have identified a dynamical decay time-scale τ associated with bulk viscosity and an oscillation time-scale T associated with the shear viscosity.

14.2 The merger of small and large black holes from a geometric perspective

We have given independent confirmation of the penetration of individual MOTS reported in [281] and furthermore presented the first detailed analysis of the time evolution and ultimate fate of the individual and common inner apparent horizons in a head-on unequal-mass binary black-hole merger. The larger apparent horizon produces a strong tidal effect in its mean curvature localized towards the line of approach of the two black holes. As the two horizons touch for the first time their mean curvatures match at the point of osculation. We have obtained a maximum overlap that accounts to about 1/2 of the coordinate area of the smaller apparent horizon. The time evolution of the area and of the determinant of the induced metric on the apparent horizon exhibits a discrete jump during the stage when both apparent horizons are overlapping.

14.3 Vacuum EM counterparts of binary black-hole mergers

We have analyzed the phenomenology that accompanies the inspiral and merger of black-hole binaries in a uniform magnetic field which is assumed to be anchored to a distant circumbinary disc. Our attention has been concentrated on binaries with equal masses and equal spins which are either aligned or anti-aligned with the orbital angular momentum; in the case of supermassive black holes, these configurations are indeed expected to be the most common ones [333, 334]. The simulations reveal several interesting aspects. The orbital motion of the black holes distorts the essentially uniform magnetic fields around the black holes and induces a quadrupolar electric field analogous to the one produced by the Hall effect for two conductors rotating in a uniform magnetic field. In addition, both electric and magnetic fields lines are dragged

by the orbital dynamics of the binary. As a result, a time variability is induced in the EM fields, which is clearly correlated with the orbital behavior and ultimately with the gravitational wave emission. The EM fields become, therefore, faithful tracers of the space-time evolution. As a result of the binary inspiral and merger, a net flux of EM energy is induced which, for the $\ell = 2, m \pm 2$ modes is intimately tied, via a constant scaling factors in phase and amplitude, to the gravitational energy released in gravitational waves. This specular behavior in the amplitude evolution disappears for higher-order modes, even though the phase evolution remains the same for all modes. Although the global *large-scale* structure of the EM fields is dictated by the orbital motion, the individual spins of the black holes further distort the EM field lines in their vicinities. These *small-scale* fields may lead to interesting dynamics and to the extraction of energy via acceleration of particles along open magnetic field lines or via magnetic reconnection. The energy emission in EM waves scales quadratically with the total spin and is given by $E^{\rm rad}_{\rm EM}/M \simeq 10^{-15} \left(M/10^8\ M_\odot\right)^2 \left(B/10^4\ {\rm G}\right)^2$, thus being 13 orders of magnitude smaller than the gravitational energy for realistic magnetic fields. This EM emission is at frequencies of $\sim 10^{-4}(10^8 M_\odot/M)$ Hz, which are well outside those accessible to astronomical radio observations. As a result, it is unlikely that the EM emission discussed here can be detected *directly* and simultaneously with the gravitational wave one. Processes driven by the changes in the EM fields could however yield observable events. In particular we argue that if the accretion rate of the circumbinary disc is small and sufficiently stable over the time-scale of the final inspiral, then the EM emission may be observable *indirectly* as it will alter the accretion rate through the magnetic torques exerted by the distorted magnetic field lines. All of these results indicate that the interplay of strong gravitational and EM fields represents a fertile ground for the development of interesting phenomena. The results presented in this dissertation, constitute interesting first steps in this direction.

14.4 On the detectability of dual jets from binary black-hole mergers

Dual jets are produced during the inspiral and merger of supermassive black holes immersed in a force-free plasma threaded by a uniform magnetic field. These dual jets are furthermore accompanied by a non-collimated emission. The energy per unit angle in the jets is dominant throughout the whole course of our simulation but the total energy flux is predominantly quadrupolar in nature, with the non-collimated emission being about $10-100$ times larger than the collimated one. The non-collimated emission is composed of two contributions. A truly EM radiation part arises due to perturbation in the electromagentic fields of the kind $d\vec{E} \times d\vec{B}$ in the Poynting flux. In addition, a contribution due to the presence of non-vanishing background EM fields needs to be properly accounted for as it does not correspond to genuine electromagentic radiation. Extrapolating the luminosity dependence back in time it may or may not be possible that in the earlier inspiral the jets become the dominant feature. On the whole, our findings set restrictions on the detectability of dual jets during the merger

stage of coalescing black-hole binaries due to the presence of a dominant non-collimated emission. However the strong non-collimated emission in combination with the dual jet structure makes it overall more likely to detect an EM counterpart to the gravitational wave signature of supermassive black-hole binaries if astrophysical conditions similar to those in this simplified scenario are realized.

14.5 Improving detection statistics for gravitational wave signals from binary black-hole mergers including spin-effects

By constructing spinning template banks and using phenomenological waveform models in a matched-filtering based data analysis pipeline we have considerably increased the ability of our pipeline to detect injected spinning signals in simulated detector data. In addition, the bias on recovered signal parameters is reduced. More specifically, a systematic bias in the evaluation of the mass ratio, that arises in searches with non-spinning template, is eliminated. The inclusion of spin effects ensures a much better detection efficiency, reduces drastically the number of missed signals due to inappropriate waveform templates and reduces the bias on estimated parameters of the source.

14.6 Conclusion and outlook

All of the material discussed above highlights the importance of binary black-hole mergers as a candidate for both observations and the geometric analysis of non-linear dynamics in the strong field regime of GR. With the advent of the advanced generation of detectors within the next five years, the scenarios considered in this thesis, may become reality.

In the future we plan to investigate in a deeper fashion the space-time geometry in binary black-hole mergers. We plan to extend our analysis to more generic situations by the inclusion of spin and allowing for inspiraling orbits. The modeling of EM signatures of binary black-hole mergers and assessing their detectability with current and future EM telescopes is of great importance. The models presented in this dissertation are very simple and provide only a first, although promising and exciting, step towards understanding the signatures of these events. We plan to extend our models and perform simulations including both matter and plasma effects in addition to the presence of EM fields. This results in a major redesign of the codes presented in this dissertation, but offers a fascinating opportunity to explore new physics.

Our future goal is to model each of the aspects explored in this thesis in a more realistic and accurate fashion capturing all the relevant physical effects in the problem.The space-time structure of binary black-hole mergers needs to be understood to unravel the driving mechanisms behind the signatures of the merger. In addition, binary black-hole merger simulations need to be extended to allow for the most realistic

modeling of their environment and we need to have a data analysis pipeline that covers the parameter space with accurate templates in an efficient way. The combination of all of these aspects will put us in the position to gain the maximum insight, once we start making observations of these systems. Furthermore, connecting gravitational wave signals with measurements of EM telescopes will boost significantly our understanding of black-hole coalescence and of their environments.

Appendix A

Constants and units

In General Relativity it is common to use geometric units, *i.e.*, $G = 1 = c$. The mass unit M in vacuum space-times can be chosen arbitrarily. This results in mass, time and spatial distance being measured in units of meters m. We here report the conversion factors to the CGS system. A solar mass can be expressed as

$$1M_{\odot} = 1.9891 \cdot 10^{30}\ kg = 1476.63m = 4.92549 \cdot 10^{-6}\ s. \tag{A.1}$$

The constants used in these conversions are $c = 299792458\ m/s$ and $G/c^2 = 7.4247 \cdot 10^{28}\ m/kg$. Table **??** shows a selection of quantities and their dimensions in the geometric and CGS unit systems.

Quantity	Symbol	Unit[Geom]	Unit[CGS]
Time	t	M	s
Distance	d	M	m
Mass	M	M	kg
Energy	E	M	J
Frequency	f	$1/M$	Hz
Angular momentum	J	M^2	Js

Table A.1: Geometric and CGS units of a selection of useful quantities.

Appendix B

Sensitivity curves

We here report the sensitivities profiles that can be used to compute PSDs and SNRs in the data analysis devoted part of this thesis. As the results were targeted at the ground-based detectors LIGO and Virgo, we restrict the presentation to these sensitivity curves only.

LIGO:

$$S_h(f) = S_0 \left[\left(\frac{4.49 f}{f_0} \right)^{-56} + 0.16 \left(\frac{f}{f_0} \right)^{-4.52} + 0.52 + 0.32 \left(\frac{f}{f_0} \right)^{2} \right], \tag{B.1}$$

with

$$S_0 = 9 \cdot 10^{-46} \qquad \text{and} \qquad f_0 = 150 Hz.$$

Virgo:

$$S_h(f) = S_0 \left[\left(\frac{7.87 f}{f_0} \right)^{-4.8} + \frac{6}{17} \left(\frac{f}{f_0} \right) + \left(1 + \left(\frac{f}{f_0} \right)^{2} \right) \right], \tag{B.2}$$

with

$$S_0 = 10.2 \cdot 10^{-46} \qquad \text{and} \qquad f_0 = 500 Hz.$$

List of related publications

[1] P. Mösta. Puncture Evolutions within the Harmonic Framework. *Diploma thesis*, Universität Kassel, 2008. x

[2] P. Mösta, C. Palenzuela, L. Rezzolla, L. Lehner, S. Yoshida and D. Pollney. Vacuum Electromagnetic Counterparts of Binary Black-Hole Mergers. *Phys. Rev. D* 81 064017, 2010, arXiv:0912.2330. x, 162

[3] P. Moesta, D. Alic, C. Palenzuela, L. Rezzolla, O. Zanotti and C. Palenzuela. On the detectability of dual jets from binary black holes. *submitted to Phys. Rev. Lett.*, 2011, arXiv:1109.1177. x, 162

[4] P. Moesta, L. Andersson, J. Metzger, B. Szilagyi and J. Winicour. The merger of small and large black holes. *in preparation*, 2011. x, 145

[5] E. Robinson, P. Moesta, F. Ohme, L. Santamaria and B. Krishnan. Searching for gravitational wave signals from non-precessing spinning black-hole binaries. *in preparation*, 2011. x

[6] J.L. Jaramillo, R.P. Macedo, P. Moesta, and L. Rezzolla. Black-hole horizons as probes of black-hole dynamics I: post-merger recoil in head-on collisions. *accepted for publication in Phys. Rev. D*, 2011, arXiv:1108.0060. x

[7] J.L. Jaramillo, R.P. Macedo, P. Moesta, and L. Rezzolla. Black-hole horizons as probes of black-hole dynamics II: geometrical insights. *accepted for publication in Phys. Rev. D*, 2011, arXiv:1108.0061. x

[8] D. Alic, L. Rezzolla, I. Hinder, P. Mösta. Dynamical damping terms for symmetry-seeking shift conditions. *Class. Quantum Grav.* 27,245023, 2010, arXiv:1008.2212. x

[9] L. Santamaria, F. Ohme, P. Ajith, B. Bruegmann, N. Dorband, M. Hannam, S. Husa, P. Moesta, D. Pollney, C. Reisswig, E. L. Robinson, J. Seiler, B. Krishnan Matching post-Newtonian and numerical relativity waveforms: systematic errors and a new phenomenological model for non-precessing black hole binaries. *Phys. Rev. D* 82 064016, 2010, arXiv:1005.3306.

[10] J. Abadie and others. Implementation and testing of the first prompt search for electromagnetic counterparts to gravitational wave transients. *ArXiv-preprint*, 2011, arXiv:1109.3498.

[11] J. Abadie and others. All-sky Search for Periodic Gravitational Waves in the Full S5 LIGO Data. *ArXiv-preprint*, 2011, arXiv:1110.0208.

[12] J. Abadie and others. Beating the spin-down limit on gravitational wave emission from the Vela pulsar. *Astrophys.J.* 737 93, 2011, arXiv:1104.2712.

[13] J. Abadie and others. Search for Gravitational Wave Bursts from Six Magnetars. *Astrophys.J.* 734 L35, 2011, arXiv:1011.4079.

LIST OF RELATED PUBLICATIONS

References

[1] A. Einstein, "Zur Elektrodynamik bewegter Körper," *Annalen der Physik*, vol. 322, pp. 891–921, 1905. 3

[2] A. Einstein, *Die Feldgleichungen der Gravitation.* Verlag der Königlichen Akademie der Wissenschaften, in Kommission bei Georg Reimer, 1915. 3

[3] A. Einstein, *Zur allgemeinen Relativitätstheorie.* Akademie der Wissenschaften, in Kommission bei W. de Gruyter, 1915. 3

[4] A. Einstein, *Über Gravitationswellen.* Verl. d. Königl. Akad. d. Wiss., 1918. 3

[5] R. P. Kerr, "Gravitational field of a spinning mass as an example of algebraically special metrics," *Phys.Rev.Lett.*, vol. 11, pp. 237–238, 1963. 3, 4

[6] K. Schwarzschild, "On the gravitational field of a mass point according to Einstein's theory," *Sitzungsber.Preuss.Akad.Wiss.Berlin (Math.Phys.)*, vol. 1916, pp. 189–196, 1916. Translated by S. Antoci and A. Loinger. 3, 4

[7] E. T. Newman, R. Couch, K. Chinnapared, A. Exton, A. Prakash, *et al.*, "Metric of a Rotating, Charged Mass," *J.Math.Phys.*, vol. 6, pp. 918–919, 1965. 4

[8] R. Penrose, "The cosmic censorship hypothesis.," *The Observatory*, vol. 96, pp. 138–+, Aug. 1976. 4, 15, 18

[9] S. Hawking, "Black holes in general relativity," *Commun.Math.Phys.*, vol. 25, pp. 152–166, 1972. 5, 40

[10] V. Kalogera, K. Belczynski, C. Kim, R. W. O'Shaughnessy, and B. Willems, "Formation of Double Compact Objects," *Phys.Rept.*, vol. 442, pp. 75–108, 2007. 5

[11] K. A. Postnov and L. R. Yungelson, "The evolution of compact binary star systems," *Living Reviews in Relativity*, vol. 9, no. 6, 2006. 5

[12] P. Amaro-Seoane, C. Eichhorn, E. Porter, and R. Spurzem, "Binaries of massive black holes in rotating clusters: Dynamics, gravitational waves, detection and the role of eccentricity," 2009. 5

[13] M. C. Miller and E. Colbert, "Intermediate - mass black holes," *Int.J.Mod.Phys.*, vol. D13, pp. 1–64, 2004. 5

[14] M. Begelman, R. Blandford, and M. Rees, "Massive black hole binaries in active galactic nuclei," *Nature*, vol. 287, pp. 307–309, 1980. 5

[15] A. Eckart and R. Genzel, "Observations of stellar proper motions near the Galactic Centre," *Nature*, vol. 383, pp. 415–417, 1996. 5

[16] D. Richstone, E. Ajhar, R. Bender, G. Bower, A. Dressler, *et al.*, "Supermassive black holes and the evolution of galaxies," *Nature*, vol. 395, pp. A14–A19, 1998. This is a near duplicate of the paper in Nature 395, A14, 1998 (Oct 1). 5

[17] A. King, "Black holes, galaxy formation, and the $M_B H - sigma relation,''$ *Astrophys.J.*, *vol.* 596, *pp.* $L27 - -L30$, 2003. 5

REFERENCES

[18] A. King, J. Pringle, and J. Hofmann, "The Evolution of Black Hole Mass and Spin in Active Galactic Nuclei," 2008. * Brief entry *. 5

[19] T. Tanaka and Z. Haiman, "The Assembly of Supermassive Black Holes at High Redshifts," *Astrophys.J.*, vol. 696, pp. 1798–1822, 2009. * Brief entry *. 5

[20] J. Yoo and J. Miralda-Escude, "Formation of the black holes in the highest redshift quasars," *Astrophys.J.*, vol. 614, pp. L25–L28, 2004. 5

[21] S. L. Detweiler, "Resonant oscillations of a rapidly rotating black hole," *Proc.Roy.Soc.Lond.*, vol. A352, pp. 381–395, 1977. 5

[22] K. D. Kokkotas and B. G. Schmidt, "Quasinormal modes of stars and black holes," *Living Rev.Rel.*, vol. 2, p. 2, 1999. 5

[23] C. Vishveshwara, "Scattering of Gravitational Radiation by a Schwarzschild Black-hole," *Nature*, vol. 227, pp. 936–938, 1970. 5

[24] E. Newman and R. Penrose, "An Approach to gravitational radiation by a method of spin coefficients," *J.Math.Phys.*, vol. 3, pp. 566–578, 1962. 6, 55, 58, 61

[25] R. Penrose, "Asymptotic properties of fields and space-times," *Phys.Rev.Lett.*, vol. 10, pp. 66–68, 1963. 6, 55, 56

[26] R. Penrose, "Zero rest mass fields including gravitation: Asymptotic behavior," *Proc.Roy.Soc.Lond.*, vol. A284, p. 159, 1965. 6, 55, 56, 61

[27] H. Bondi, "Plane gravitational waves in general relativity," *Nature*, vol. 179, pp. 1072–1073, 1957. 6

[28] H. Bondi, M. van der Burg, and A. Metzner, "Gravitational waves in general relativity. 7. Waves from axisymmetric isolated systems," *Proc.Roy.Soc.Lond.*, vol. A269, pp. 21–52, 1962. 6, 63

[29] R. Hulse and J. Taylor, "Discovery of a pulsar in a binary system," *Astrophys.J.*, vol. 195, pp. L51–L53, 1975. 7

[30] I. Stairs, S. Thorsett, J. Taylor, and A. Wolszczan, "Studies of the relativistic binary pulsar psr b1534+12: I. timing analysis," *Astrophys.J.*, vol. 581, pp. 501–508, 2002. * Brief entry *. 7

[31] B. Sathyaprakash and B. Schutz, "Physics, Astrophysics and Cosmology with Gravitational Waves," *Living Rev.Rel.*, vol. 12, p. 2, 2009. 7

[32] B. F. Schutz, J. Centrella, C. Cutler, and S. A. Hughes, "Will Einstein Have the Last Word on Gravity?," 2009. 7

[33] A. Abramovici, W. E. Althouse, R. W. Drever, Y. Gursel, S. Kawamura, *et al.*, "LIGO: The Laser interferometer gravitational wave observatory," *Science*, vol. 256, pp. 325–333, 1992. 9

[34] E. E. Flanagan and S. A. Hughes, "The Basics of gravitational wave theory," *New J.Phys.*, vol. 7, p. 204, 2005. 9, 62

[35] R. A. Isaacson, "Gravitational Radiation in the Limit of High Frequency. I. The Linear Approximation and Geometrical Optics," *Phys.Rev.*, vol. 166, pp. 1263–1271, 1967. 9, 10, 63

[36] R. A. Isaacson, "Gravitational Radiation in the Limit of High Frequency. II. Nonlinear Terms and the Ef fective Stress Tensor," *Phys.Rev.*, vol. 166, pp. 1272–1279, 1968. 9, 10, 63, 64

[37] K. Thorne, "Multipole Expansions of Gravitational Radiation," *Rev.Mod.Phys.*, vol. 52, pp. 299–339, 1980. 10, 64

[38] B. Abbott *et al.*, "LIGO: The Laser interferometer gravitational-wave observatory," *Rept.Prog.Phys.*, vol. 72, p. 076901, 2009. 11

[39] F. Acernese, P. Amico, M. Alshourbagy, S. Aoudia, S. Avino, *et al.*, "The Status of VIRGO," *Class.Quant.Grav.*, vol. 23, pp. S63–S70, 2006. 11

[40] S. A. Hughes, S. Marka, P. L. Bender, and C. J. Hogan, "New physics and astronomy with the new gravitational-wave observatories," 2001. 12

[41] P. Peters, "Gravitational Radiation and the Motion of Two Point Masses," *Phys.Rev.*, vol. 136, pp. B1224–B1232, 1964. 13

[42] A. Ashtekar, C. Beetle, and J. Lewandowski, "Geometry of generic isolated horizons," *Class.Quant.Grav.*, vol. 19, pp. 1195–1225, 2002. 13

[43] M. Campanelli, C. O. Lousto, and Y. Zlochower, "Algebraic Classification of Numerical Spacetimes and Black-Hole-Binary Remnants," *Phys.Rev.*, vol. D79, p. 084012, 2009. 13

[44] J. Lewandowski and T. Pawlowski, "Geometric characterizations of the Kerr isolated horizon," *Int.J.Mod.Phys.*, vol. D11, pp. 739–746, 2002. 13

[45] M. A. Scheel, M. Boyle, T. Chu, L. E. Kidder, K. D. Matthews, *et al.*, "High-accuracy waveforms for binary black hole inspiral, merger, and ringdown," *Phys.Rev.*, vol. D79, p. 024003, 2009. 13, 70

[46] M. Campanelli, C. O. Lousto, Y. Zlochower, and D. Merritt, "Maximum gravitational recoil," *Phys.Rev.Lett.*, vol. 98, p. 231102, 2007. 14

[47] A. Buonanno, L. E. Kidder, and L. Lehner, "Estimating the final spin of a binary black hole coalescence," *Phys.Rev.*, vol. D77, p. 026004, 2008. 14

[48] L. Rezzolla, P. Diener, E. N. Dorband, D. Pollney, C. Reisswig, *et al.*, "The Final spin from the coalescence of aligned-spin black-hole binaries," *Astrophys.J.*, vol. 674, pp. L29–L32, 2008. 14

[49] S. Hawking and G. Ellis, "The Large scale structure of space-time," 1973. 15, 16, 18, 21

[50] S. Hawking and R. Penrose, "The Singularities of gravitational collapse and cosmology," *Proc.Roy.Soc.Lond.*, vol. A314, pp. 529–548, 1970. 15, 18

[51] R. Penrose, "Gravitational collapse and space-time singularities," *Phys.Rev.Lett.*, vol. 14, pp. 57–59, 1965. 15, 18

[52] A. Ashtekar, C. Beetle, O. Dreyer, S. Fairhurst, B. Krishnan, *et al.*, "Isolated horizons and their applications," *Phys.Rev.Lett.*, vol. 85, pp. 3564–3567, 2000. 15, 19

[53] A. Ashtekar and B. Krishnan, "Dynamical horizons and their properties," *Phys.Rev.*, vol. D68, p. 104030, 2003. 15

[54] P. Diener, "A New general purpose event horizon finder for 3-D numerical space-times," *Class.Quant.Grav.*, vol. 20, pp. 4901–4918, 2003. 17

[55] J. Thornburg, "Event and apparent horizon finders for 3+1 numerical relativity," *Living Rev.Rel.*, vol. 10, p. 3, 2007. 17

[56] O. Dreyer, B. Krishnan, D. Shoemaker, and E. Schnetter, "Introduction to isolated horizons in numerical relativity," *Phys.Rev.*, vol. D67, p. 024018, 2003. 18, 20

[57] A. Ashtekar and B. Krishnan, "Dynamical horizons: Energy, angular momentum, fluxes and balance laws," *Phys.Rev.Lett.*, vol. 89, p. 261101, 2002. 19

[58] E. Schnetter, B. Krishnan, and F. Beyer, "Introduction to dynamical horizons in numerical relativity," *Phys.Rev.*, vol. D74, p. 024028, 2006. 19

[59] A. Ashtekar, C. Beetle, and J. Lewandowski, "Mechanics of rotating isolated horizons," *Phys.Rev.*, vol. D64, p. 044016, 2001. 19, 20

[60] A. Ashtekar, S. Fairhurst, and B. Krishnan, "Isolated horizons: Hamiltonian evolution and the first law," *Phys.Rev.*, vol. D62, p. 104025, 2000. 19, 20

[61] D. Christodoulou, "Reversible and irreversible transforations in black hole physics," *Phys.Rev.Lett.*, vol. 25, pp. 1596–1597, 1970. 20

[62] L. Smarr, "Mass formula for Kerr black holes," *Phys.Rev.Lett.*, vol. 30, pp. 71–73, 1973. 20

[63] J. Stewart, "Advanced general relativity," 1990. 21, 56, 60, 61

[64] C. Reisswig, *Binary Black Hole Mergers and Novel Approaches to Gravitational Wave Extraction in Numerical Relativity.* PhD thesis, Leibniz Universität Hannover, 2010. 22, 76, 86

[65] R. L. Arnowitt, S. Deser, and C. W. Misner, "The Dynamics of general relativity," 1962. Gravitation: an introduction to current research, Louis Witten ed. (Wilew 1962), chapter 7, pp 227-265. 21, 57

[66] L. Smarr, "Space-Time Generated by Computers: Black Holes with Gravitational Radiation," in *Eighth Texas Symposium on Relativistic Astrophysics* (M. D. Papagiannis, ed.), vol. 302 of *Annals of the New York Academy of Sciences*, pp. 569–+, Dec. 1977. 22

[67] L. L. Smarr, *The Structure of General Relativity with a Numerical Illustration: the Collision of Two Black Holes.* PhD thesis, THE UNIVERSITY OF TEXAS AT AUSTIN., 1975. 22

[68] P. Anninos, D. Hobill, E. Seidel, L. Smarr, and W.-M. Suen, "The Collision of two black holes," *Phys.Rev.Lett.*, vol. 71, pp. 2851–2854, 1993. 22, 33

[69] T. W. Baumgarte and S. L. Shapiro, "On the numerical integration of Einstein's field equations," *Phys.Rev.*, vol. D59, p. 024007, 1999. 23, 26

[70] T. Nakamura, K. Oohara, and Y. Kojima, "General Relativistic Collapse to Black Holes and Gravitational Waves from Black Holes," *Prog.Theor.Phys.Suppl.*, vol. 90, pp. 1–218, 1987. 23, 26

[71] M. Shibata and T. Nakamura, "Evolution of three-dimensional gravitational waves: Harmonic slicing case," *Phys.Rev.*, vol. D52, pp. 5428–5444, 1995. 23, 26

[72] H. Friedrich and A. D. Rendall, "The Cauchy problem for the Einstein equations," *Lect.Notes Phys.*, vol. 540, pp. 127–224, 2000. Einstein's Field Equations and their Physical Interpretation, ed. by B. G. Schmidt, Springer, Berlin, 2000. 23

[73] F. Pretorius, "Evolution of binary black hole spacetimes," *Phys.Rev.Lett.*, vol. 95, p. 121101, 2005. 23, 36

[74] F. Pretorius, "Numerical relativity using a generalized harmonic decomposition," *Class.Quant.Grav.*, vol. 22, pp. 425–452, 2005. 23, 36

[75] T. W. Baumgarte and S. L. Shapiro, "Numerical relativity and compact binaries," *Phys.Rept.*, vol. 376, pp. 41–131, 2003. 23

[76] H. Friedrich, "Hyperbolic reductions for Einstein's equations," *Class.Quant.Grav.*, vol. 13, pp. 1451–1469, 1996. 26

[77] M. Alcubierre, B. Bruegmann, M. A. Miller, and W.-M. Suen, "A Conformal hyperbolic formulation of the Einstein equations," *Phys.Rev.*, vol. D60, p. 064017, 1999. 26, 29

[78] M. Campanelli, C. Lousto, P. Marronetti, and Y. Zlochower, "Accurate evolutions of orbiting black-hole binaries without excision," *Phys.Rev.Lett.*, vol. 96, p. 111101, 2006. 26, 28, 29, 44, 45

[79] P. Marronetti, W. Tichy, B. Bruegmann, J. Gonzalez, M. Hannam, *et al.*, "Binary black holes on a budget: Simulations using workstations," *Class.Quant.Grav.*, vol. 24, pp. S43–S58, 2007. 26, 28, 29

[80] M. Alcubierre, G. Allen, B. Bruegmann, T. Dramlitsch, J. A. Font, *et al.*, "Towards a stable numerical evolution of strongly gravitating systems in general relativity: The Conformal treatments," *Phys.Rev.*, vol. D62, p. 044034, 2000. 26

[81] S. Frittelli and O. A. Reula, "Well posed forms of the (3+1) conformally decomposed Einstein equations," *J.Math.Phys.*, vol. 40, pp. 5143–5156, 1999. 26

[82] O. Sarbach, G. Calabrese, J. Pullin, and M. Tiglio, "Hyperbolicity of the BSSN system of Einstein evolution equations," *Phys.Rev.*, vol. D66, p. 064002, 2002. 26

[83] C. W. Misner, K. Thorne, and J. Wheeler, "Gravitation," 1974. 33, 62

[84] P. Anninos, K. Camarda, J. Masso, E. Seidel, W.-M. Suen, *et al.*, "Three-dimensional numerical relativity: The Evolution of black holes," *Phys.Rev.*, vol. D52, pp. 2059–2082, 1995. 33, 35

[85] P. Anninos, D. Hobill, E. Seidel, L. Smarr, and W.-M. Suen, "The Headon collision of two equal mass black holes," *Phys.Rev.*, vol. D52, pp. 2044–2058, 1995. 33

[86] D. M. Eardley and L. Smarr, "Time function in numerical relativity. Marginally bound dust collapse," *Phys.Rev.*, vol. D19, pp. 2239–2259, 1979. 33

[87] F. Estabrook, H. Wahlquist, S. Christensen, B. DeWitt, L. Smarr, *et al.*, "Maximally slicing a black hole," *Phys.Rev.*, vol. D7, pp. 2814–2817, 1973. 33

[88] L. Smarr and J. York, James W., "Kinematical conditions in the construction of space-time," *Phys.Rev.*, vol. D17, pp. 2529–2551, 1978. 33

[89] B. Bruegmann, "Binary black hole mergers in 3-d numerical relativity," *Int.J.Mod.Phys.*, vol. D8, p. 85, 1999. 33, 44

[90] P. Anninos, G. Daues, J. Masso, E. Seidel, and W.-M. Suen, "Horizon boundary condition for black hole space-times," *Phys.Rev.*, vol. D51, pp. 5562–5578, 1995. 34, 44

[91] J. Balakrishna, G. Daues, E. Seidel, W.-m. Suen, M. Tobias, *et al.*, "Coordinate conditions and their implementation in 3-D numerical relativity," *Class.Quant.Grav.*, vol. 13, pp. L135–L142, 1996. 34, 36

[92] C. Bona, J. Masso, E. Seidel, and J. Stela, "A New formalism for numerical relativity," *Phys.Rev.Lett.*, vol. 75, pp. 600–603, 1995. 34

[93] J. R. van Meter, J. G. Baker, M. Koppitz, and D.-I. Choi, "How to move a black hole without excision: Gauge conditions for the numerical evolution of a moving puncture," *Phys.Rev.*, vol. D73, p. 124011, 2006. 35, 36

[94] C. Bona, J. Masso, E. Seidel, and J. Stela, "First order hyperbolic formalism for numerical relativity," *Phys.Rev.*, vol. D56, pp. 3405–3415, 1997. 35

[95] M. Alcubierre, B. Bruegmann, P. Diener, M. Koppitz, D. Pollney, *et al.*, "Gauge conditions for long term numerical black hole evolutions without excision," *Phys.Rev.*, vol. D67, p. 084023, 2003. 35, 36

[96] M. Alcubierre, B. Bruegmann, D. Pollney, E. Seidel, and R. Takahashi, "Black hole excision for dynamic black holes," *Phys.Rev.*, vol. D64, p. 061501, 2001. 35, 36

[97] L. Smarr, A. Cadez, B. S. DeWitt, and K. Eppley, "Collision of Two Black Holes: Theoretical Framework," *Phys.Rev.*, vol. D14, pp. 2443–2452, 1976. 36

[98] D. Alic, L. Rezzolla, I. Hinder, and P. Mösta, "Dynamical damping terms for symmetry-seeking shift conditions," *Classical and Quantum Gravity*, vol. 27, pp. 245023–+, Dec. 2010. 36

[99] D. Müller and B. Brügmann, "Toward a dynamical shift condition for unequal mass black hole binary simulations," *Class. Quant. Grav.*, vol. 27, p. 114008, 2010. 36

[100] D. Müller, J. Grigsby, and B. Brügmann, "Dynamical shift condition for unequal mass black hole binaries," *Phys. Rev. D*, vol. 82, p. 064004, 2010. 36

[101] J. G. Baker, J. Centrella, D.-I. Choi, M. Koppitz, and J. van Meter, "Gravitational wave extraction from an inspiraling configuration of merging black holes," *Phys.Rev.Lett.*, vol. 96, p. 111102, 2006. 36, 44, 45

[102] L. Lindblom and B. Szilágyi, "Improved gauge driver for the generalized harmonic Einstein system," , vol. 80, pp. 084019–+, Oct. 2009. 36

[103] B. Szilagyi, L. Lindblom, and M. A. Scheel, "Simulations of Binary Black Hole Mergers Using Spectral Methods," vol. D80, p. 124010, 2009. 36, 70

[104] A. Einstein and N. Rosen, "The Particle Problem in the General Theory of Relativity," *Phys.Rev.*, vol. 48, pp. 73–77, 1935. 37

[105] D. R. Brill and R. W. Lindquist, "Interaction energy in geometrostatics," *Phys.Rev.*, vol. 131, pp. 471–476, 1963. 37, 41, 42

[106] C. W. Misner, "Wormhole Initial Conditions," *Phys.Rev.*, vol. 118, pp. 1110–1111, 1960. 37, 42

[107] C. W. Misner, "The method of images in geometrostatics," *Annals of Physics*, vol. 24, pp. 102–117, Oct. 1963. 37, 41, 42

[108] C. W. Misner and J. A. Wheeler, "Classical physics as geometry: Gravitation, electromagnetism, unquantized charge, and mass as properties of curved empty space," *Annals Phys.*, vol. 2, pp. 525–603, 1957. 37

[109] J. Wheeler, "Geons," *Phys.Rev.*, vol. 97, pp. 511–536, 1955. 37

[110] J. Bowen, J. Rauber, and J. W. York, Jr., "Two black holes with axisymmetric parallel spins - Initial data," *Classical and Quantum Gravity*, vol. 1, pp. 591–610, Sept. 1984. 37, 39

[111] J. M. Bowen, "General form for the longitudinal momentum of a spherically symmetric source.," *General Relativity and Gravitation*, vol. 11, pp. 227–231, Oct. 1979. 37, 39, 40

[112] J. M. Bowen, "General solution for flat-space longitudinal momentum," *General Relativity and Gravitation*, vol. 14, pp. 1183–1191, Dec. 1982. 37, 39

[113] J. M. Bowen and J. York, James W., "Time asymmetric initial data for black holes and black hole collisions," *Phys.Rev.*, vol. D21, pp. 2047–2056, 1980. 37, 39, 40

[114] G. B. Cook, "Initial data for axisymmetric black-hole collisions," , vol. 44, pp. 2983–3000, Nov. 1991. 37, 39

[115] A. D. Kulkarni, L. C. Shepley, and J. W. York, "Initial data for n black holes," *Physics Letters A*, vol. 96, pp. 228–230, July 1983. 37, 39

[116] R. Beig, "Generalized Bowen-York initial data," 2000. pp.55-59 in Spiros Cotsakis and Gary Gibbons, Eds., 'Mathematical and Quantum Aspects of Relativity and Cosmology', Springer Lecture Notes in Physics v. 537. 37

[117] R. Beig and N. Murchadha, "Trapped surfaces in vacuum space-times," *Class.Quant.Grav.*, vol. 11, pp. 419–430, 1994. 37

[118] S. Brandt and B. Bruegmann, "A Simple construction of initial data for multiple black holes," *Phys.Rev.Lett.*, vol. 78, pp. 3606–3609, 1997. 37, 40

[119] G. B. Cook, "Initial data for numerical relativity," *Living Rev.Rel.*, vol. 3, p. 5, 2000. 37, 38, 39

[120] J. York, James W., "Gravitational degrees of freedom and the initial-value problem," *Phys.Rev.Lett.*, vol. 26, pp. 1656–1658, 1971. 37, 38

[121] J. York, James W., "Role of conformal three geometry in the dynamics of gravitation," *Phys.Rev.Lett.*, vol. 28, pp. 1082–1085, 1972. 37, 38

[122] J. W. York, Jr., "Conformal "Thin-Sandwich" Data for the Initial-Value Problem of General Relativity," *Physical Review Letters*, vol. 82, pp. 1350–1353, Feb. 1999. 37

[123] H. P. Pfeiffer and J. York, James W., "Extrinsic curvature and the Einstein constraints," *Phys.Rev.*, vol. D67, p. 044022, 2003. 38

[124] M. Ansorg, B. Bruegmann, and W. Tichy, "A Single-domain spectral method for black hole puncture data," *Phys.Rev.*, vol. D70, p. 064011, 2004. 38, 42, 89, 91, 93, 94, 168

[125] S. Husa, M. Hannam, J. A. Gonzalez, U. Sperhake, and B. Bruegmann, "Reducing eccentricity in black-hole binary evolutions with initial parameters from post-Newtonian inspiral," *Phys.Rev.*, vol. D77, p. 044037, 2008. 38, 44, 168

[126] M. Alcubierre, *Introduction to 3+1 Numerical Relativity*. Oxford University Press, 2008. 39, 60, 71, 78

[127] A. Garat and R. H. Price, "Nonexistence of conformally flat slices of the Kerr spacetime," , vol. 61, pp. 124011–+, June 2000. 40

[128] R. A. Matzner, M. F. Huq, and D. Shoemaker, "Initial data and coordinates for multiple black hole systems," *Phys.Rev.*, vol. D59, p. 024015, 1999. 40

[129] W. Tichy, B. Bruegmann, and P. Laguna, "Gauge conditions for binary black hole puncture data based on an approximate helical Killing vector," *Phys.Rev.*, vol. D68, p. 064008, 2003. 43

[130] M. Hannam, S. Husa, D. Pollney, B. Bruegmann, and N. O'Murchadha, "Geometry and regularity of moving punctures," *Phys.Rev.Lett.*, vol. 99, p. 241102, 2007. 43, 45

[131] M. Hannam, S. Husa, and N. O. Murchadha, "Bowen-York trumpet data and black-hole simulations," *Phys.Rev.*, vol. D80, p. 124007, 2009. 43

[132] M. Hannam, S. Husa, F. Ohme, B. Bruegmann, and N. O'Murchadha, "Wormholes and trumpets: The Schwarzschild spacetime for the moving-puncture generation," *Phys.Rev.*, vol. D78, p. 064020, 2008. 43, 46

[133] A. Buonanno, Y. Chen, and T. Damour, "Transition from inspiral to plunge in precessing binaries of spinning black holes," *Phys.Rev.*, vol. D74, p. 104005, 2006. 43

[134] P. Jaranowski and G. Schaefer, "Third postNewtonian higher order ADM Hamilton dynamics for two-body point mass systems," *Phys.Rev.*, vol. D57, pp. 7274–7291, 1998. 43

[135] T. Damour, P. Jaranowski, and G. Schaefer, "Dimensional regularization of the gravitational interaction of point masses," *Phys.Lett.*, vol. B513, pp. 147–155, 2001. 43

[136] L. Blanchet and G. Faye, "General relativistic dynamics of compact binaries at the third postNewtonian order," *Phys.Rev.*, vol. D63, p. 062005, 2001. 44

[137] L. Blanchet and B. R. Iyer, "Third postNewtonian dynamics of compact binaries: Equations of motion in the center-of-mass frame," *Class.Quant.Grav.*, vol. 20, p. 755, 2003. 44

[138] L. Blanchet, B. R. Iyer, and B. Joguet, "Gravitational waves from inspiralling compact binaries: Energy flux to third postNewtonian order," *Phys.Rev.*, vol. D65, p. 064005, 2002. 44

[139] M. Boyle, D. A. Brown, L. E. Kidder, A. H. Mroue, H. P. Pfeiffer, *et al.*, "High-accuracy comparison of numerical relativity simulations with post-Newtonian expansions," *Phys.Rev.*, vol. D76, p. 124038, 2007. 44

[140] H. P. Pfeiffer, D. A. Brown, L. E. Kidder, L. Lindblom, G. Lovelace, *et al.*, "Reducing orbital eccentricity in binary black hole simulations," *Class.Quant.Grav.*, vol. 24, pp. S59–S82, 2007. 44

[141] M. Alcubierre, W. Benger, B. Bruegmann, G. Lanfermann, L. Nerger, *et al.*, "The 3-D grazing collision of two black holes," *Phys.Rev.Lett.*, vol. 87, p. 271103, 2001. 44

[142] B. Brügmann, W. Tichy, and N. Jansen, "Numerical Simulation of Orbiting Black Holes," *Physical Review Letters*, vol. 92, pp. 211101–+, May 2004. 44

[143] P. Diener, F. Herrmann, D. Pollney, E. Schnetter, E. Seidel, R. Takahashi, J. Thornburg, and J. Ventrella, "Accurate Evolution of Orbiting Binary Black Holes," *Physical Review Letters*, vol. 96, pp. 121101–+, Mar. 2006. 44

[144] J. Brown, "Puncture Evolution of Schwarzschild Black Holes," *Phys.Rev.*, vol. D77, p. 044018, 2008. 45

[145] J. Thornburg, P. Diener, D. Pollney, L. Rezzolla, E. Schnetter, E. Seidel, and R. Takahashi, "Are moving punctures equivalent to moving black holes?," *Classical and Quantum Gravity*, vol. 24, pp. 3911–3918, Aug. 2007. 45

[146] C. Bona, C. Palenzuela-Luque, and C. Bona-Casas, *Elements of Numerical Relativity and Relativistic Hydrodynamics: From Einstein' s Equations to Astrophysical Simulations*. Springer Publishing Company, Incorporated, 2009. 47

REFERENCES

[147] L. Baiotti, B. Giacomazzo, and L. Rezzolla, "Accurate evolutions of inspiralling neutron-star binaries: Prompt and delayed collapse to a black hole," *Phys. Rev. D*, vol. 78, p. 084033, Oct. 2008. 51

[148] S. Komissarov, "Multi-dimensional Numerical Scheme for Resistive Relativistic MHD," *Mon.Not.Roy.Astron.Soc.*, 2007. 53

[149] C. Palenzuela, L. Lehner, and S. L. Liebling, "Dual Jets from Binary Black Holes," *Science*, vol. 329, p. 927, 2010. 53, 162

[150] S. Komissarov, "Electrodynamics of black hole magnetospheres," *Mon.Not.Roy.Astron.Soc.*, vol. 350, p. 407, 2004. 53, 54

[151] S. Komissarov, "Observations of the Blandford-Znajek and the MHD Penrose processes in computer simulations of black hole magnetospheres," *Mon.Not.Roy.Astron.Soc.*, vol. 359, pp. 801–808, 2005. 54

[152] D. Alic and others *in preparation*, 2011. 54, 182

[153] e. Frauendiener, J. and e. Friedrich, H., "The conformal structure of space-time: Geometry, analysis, numerics," 2002. 56

[154] R. Penrose and W. Rindler, "SPINORS AND SPACE-TIME. VOL. 2: SPINOR AND TWISTOR METHODS IN SPACE-TIME GEOMETRY," 1986. 56, 61

[155] N. O Murchadha and J. W. York, "Gravitational energy," *Phys.Rev.*, vol. D10, pp. 2345–2357, 1974. 57

[156] R. Sachs, "Gravitational waves in general relativity. 6. The outgoing radiation condition," *Proc.Roy.Soc.Lond.*, vol. A264, pp. 309–338, 1961. 61

[157] R. Sachs, "Gravitational waves in general relativity. 8. Waves in asymptotically flat space-times," *Proc.Roy.Soc.Lond.*, vol. A270, pp. 103–126, 1962. 61

[158] I. Hinder, B. Wardell, and E. Bentivegna, "Falloff of the Weyl scalars in binary black hole spacetimes," *Phys.Rev.*, vol. D84, p. 024036, 2011. 61

[159] D. Pollney, C. Reisswig, N. Dorband, E. Schnetter, and P. Diener, "The Asymptotic Falloff of Local Waveform Measurements in Numerical Relativity," *Phys.Rev.*, vol. D80, p. 121502, 2009. 61, 106

[160] L. Gunnarsen, H. Shinkai, and K. Maeda, "A '3+1' method for finding principal null directions," *Class. Quantum Grav.*, vol. 12, pp. 133–140, 1995. 61

[161] S. A. Teukolsky, "Perturbations of a rotating black hole. 1. Fundamental equations for gravitational electromagnetic and neutrino field perturbations," *Astrophys.J.*, vol. 185, pp. 635–647, 1973. Ph.D. Thesis (Advisor: Kip S. Thorne). 62, 63, 65

[162] M. Ruiz, R. Takahashi, M. Alcubierre, and D. Nunez, "Multipole expansions for energy and momenta carried by gravitational waves," *Gen.Rel.Grav.*, vol. 40, p. 2467, 2008. 63, 64

[163] M. Favata, S. A. Hughes, and D. E. Holz, "How black holes get their kicks: Gravitational radiation recoil revisited," *Astrophys.J.*, vol. 607, pp. L5–L8, 2004. 64, 99

[164] J. S. Hesthaven and T. Warburton, *Nodal Discontinuous Galerkin Methods: Algorithms, Analysis, and Applications*. Springer Publishing Company, Incorporated, 1st ed., 2007. 70

[165] B. Fornberg, "Generation of Finite Difference Formulas on Arbitrarily Spaced Grids," *Mathematics of Computation*, vol. 51, no. 184, pp. 699–706, 1988. 71

[166] H. Kreiss and J. Oliger, *Methods for the approximate solution of time dependent problems: Global Atmospheric Research Programme (GARP) ; WMO-ICSU Joint Organizing Committee*. GARP publications series, Genf, 1973. 71

[167] B. Gustafsson, H. O. Kreiss, and J. Oliger, "Time dependent problems and difference methods," 1996. 72, 73, 74, 75

[168] J. G. Charney, R. Fjörtoft, and J. von Neumann, "Numerical Integration of the Barotropic Vorticity Equation," *Tellus*, vol. 2, pp. 237–+, Aug. 1950. 73, 75

[169] J. Crank, P. Nicolson, and D. R. Hartree, "A practical method for numerical evaluation of solutions of partial differential equations of the heat-conduction type," *Proceedings of the Cambridge Philosophical Society*, vol. 43, pp. 50–+, 1947. 73

[170] R. Courant, K. Friedrichs, and H. Lewy, "Über die partiellen Differenzengleichungen der mathematischen Physik," *Mathematische Annalen*, vol. 100, pp. 32–74, 1928. 73, 76

[171] O. A. Reula, "Hyperbolic methods for Einstein's equations," *Living Rev.Rel.*, vol. 1, p. 3, 1998. 76

[172] M. W. Choptuik, "Consistency of finite-difference solutions of Einstein's equations," , vol. 44, pp. 3124–3135, Nov. 1991. 79

[173] "`http://www.cactuscode.org`." 81, 82

[174] G. Allen, W. Benger, T. Goodale, H. christian Hege, G. Lanfermann, A. Merzky, T. Radke, E. Seidel, and J. Shalf, "The cactus code: A problem solving environment for the grid," pp. 253–260, IEEE Computer Society, 2000. 81, 82

[175] T. Goodale, G. Allen, G. Lanfermann, J. Mass, E. Seidel, and J. Shalf, "The cactus framework and toolkit: Design and applications," in *In Vector and Parallel Processing - VECPAR 2002, 5th International Conference*, Springer, 2003. 81, 82, 83

[176] "`http://www.carpetcode.org`." 81, 85

[177] E. Schnetter, S. H. Hawley, and I. Hawke, "Evolutions in 3-D numerical relativity using fixed mesh refinement," *Class.Quant.Grav.*, vol. 21, pp. 1465–1488, 2004. 81, 85, 87, 88

[178] "`www-unix.mcs.anl.gov/mpi/index.htm`." 84

[179] "`http://www.openmp.org/`." 84

[180] M. J. Berger and J. Oliger, "Adaptive Mesh Refinement for Hyperbolic Partial Differential Equations," *J.Comput.Phys.*, vol. 53, p. 484, 1984. 85, 86, 87

[181] M. J. Berger and P. Colella, "Local adaptive mesh refinement for shock hydrodynamics," *Journal of Computational Physics*, vol. 82, pp. 64–84, May 1989. 85

[182] T. Plewa and E. Müller, "AMRA: An Adaptive Mesh Refinement hydrodynamic code for astrophysics," *Computer Physics Communications*, vol. 138, pp. 101–127, Aug. 2001. 85

[183] S. Dain, "Initial data for two Kerr - like black holes," *Phys.Rev.Lett.*, vol. 87, p. 121102, 2001. 92, 93

[184] J. Thornburg, "A Fast apparent horizon finder for three-dimensional Cartesian grids in numerical relativity," *Class.Quant.Grav.*, vol. 21, pp. 743–766, 2004. 95, 96

[185] J. D. Bekenstein, "Gravitational-Radiation Recoil and Runaway Black Holes," *Astrophys. J.*, vol. 183, pp. 657–664, July 1973. 99

[186] A. Peres, "Classical radiation recoil," *Phys. Rev.*, vol. 128, pp. 2471–2475, 1962. 99

[187] M. J. Fitchett and S. Detweiler, "Linear momentum and gravitational waves – Circular orbits around a Schwarzschild black hole," *Mon. Not. R. Astron. Soc.*, vol. 211, pp. 933–942, Dec. 1984. 99

[188] T. Nakamura and M. P. Haugan, "Gravitational radiation from particles falling along the symmetry axis into a kerr black hole: The momentum radiated," *Astrophys. J.*, vol. 269, pp. 292–296, 1983. 99

[189] L. Blanchet, M. S. S. Qusailah, and C. M. Will, "Gravitational recoil of inspiralling black-hole binaries to second post-Newtonian order," *Astrophys. J.*, vol. 635, p. 508, 2005. 99

[190] T. Damour and A. Gopakumar, "Gravitational recoil during binary black hole coalescence using the effective one body approach," *Phys. Rev. D*, vol. 73, p. 124006, 2006. 99

[191] L. E. Kidder, "Coalescing binary systems of compact objects to post$^{5/2}$-Newtonian order. V. Spin effects," *Phys. Rev. D*, vol. 52, pp. 821–847, 1995. 99

[192] A. G. Wiseman, "Coalescing binary systems of compact objects to (post)5/2 newtonian order. 2. higher order wave forms and radiation recoil," *Phys. Rev. D*, vol. 46, pp. 1517–1539, 1992. 99

[193] Z. Andrade and R. H. Price, "Head-on collisions of unequal mass black holes: Close-limit predictions," *Phys. Rev. D*, vol. 56, pp. 6336–6350, 1997. 99

[194] C. F. Sopuerta, N. Yunes, and P. Laguna, "Gravitational recoil from binary black hole mergers: The close-limit approximation," *Phys. Rev. D*, vol. 74, p. 124010, 2006. 99

[195] J. G. Baker, J. Centrella, D.-I. Choi, M. Koppitz, J. van Meter, and M. C. Miller, "Getting a kick out of numerical relativity," *Astrophys. J.*, vol. 653, pp. L93–L96, 2006. 99

[196] M. Campanelli, C. O. Lousto, Y. Zlochower, and D. Merritt, "Maximum gravitational recoil," *Phys. Rev. Lett.*, vol. 98, p. 231102, 2007. 99

[197] J. A. Gonzalez, U. Sperhake, B. Bruegmann, M. Hannam, and S. Husa, "Total recoil: the maximum kick from nonspinning black-hole binary inspiral," *Phys. Rev. Lett.*, vol. 98, p. 091101, 2007. 99

[198] J. Healy *et al.*, "Superkicks in Hyperbolic Encounters of Binary Black Holes," *Phys. Rev. Lett.*, vol. 102, p. 041101, 2009. 99

[199] F. Herrmann, I. Hinder, D. Shoemaker, P. Laguna, and R. A. Matzner, "Gravitational Recoil from Spinning Binary Black Hole Mergers," *Astrophys. J.*, vol. 661, pp. 430–436, May 2007. 99, 175

[200] M. Koppitz and al., "Getting a kick from equal-mass binary black hole mergers," *Phys. Rev. Lett.*, vol. 99, p. 041102, 2007. 99

[201] C. O. Lousto and Y. Zlochower, "Further insight into gravitational recoil," *Phys. Rev. D*, vol. 77, p. 044028, 2008. 99

[202] D. Pollney *et al.*, "Recoil velocities from equal-mass binary black-hole mergers: a systematic investigation of spin-orbit aligned configurations," *Phys. Rev. D*, vol. 76, p. 124002, 2007. 99, 120, 121, 183

[203] M. Campanelli, C. O. Lousto, Y. Zlochower, and D. Merritt, "Large merger recoils and spin flips from generic black-hole binaries," *Astrophys. J.*, vol. 659, pp. L5–L8, 2007. 99

[204] J. A. Gonzalez, M. D. Hannam, U. Sperhake, B. Bruegmann, and S. Husa, "Supermassive kicks for spinning black holes," *Phys. Rev. Lett.*, vol. 98, p. 231101, 2007. 99

[205] L. Rezzolla, "Modelling the final state from binary black-hole coalescences," *Class. Quant. Grav.*, vol. 26, p. 094023, 2009. 99

[206] Y. Zlochower, M. Campanelli, and C. O. Lousto, "Modeling gravitational recoil from black-hole binaries using numerical relativity," *Classical and Quantum Gravity*, vol. 28, no. 11, p. 114015, 2011. 99

[207] A. Le Tiec, L. Blanchet, and C. M. Will, "Gravitational-Wave Recoil from the Ringdown Phase of Coalescing Black Hole Binaries," *Class. Quant. Grav.*, vol. 27, p. 012001, 2010. 99

[208] R. Hamerly and Y. Chen, "Event Horizon Deformations in Extreme Mass-Ratio Black Hole Mergers," *arXiv:1007.5387*, July 2010. 99

[209] Y. Mino and J. Brink, "Gravitational Radiation from Plunging Orbits - Perturbative Study -," *Phys. Rev. D*, vol. 78, p. 124015, 2008. 99

[210] D. A. Nichols and Y. Chen, "Hybrid method for understanding black-hole mergers: Head-on case," *Phys. Rev. D*, vol. 82, pp. 104020–+, Nov. 2010. 99

[211] J. D. Schnittman, A. Buonanno, J. R. van Meter, J. G. Baker, W. D. Boggs, J. Centrella, B. J. Kelly, and S. T. McWilliams, "Anatomy of the binary black hole recoil: A multipolar analysis," , vol. 77, p. 044031, Feb. 2008. 99

[212] U. Sperhake, E. Berti, V. Cardoso, F. Pretorius, and N. Yunes, "Superkicks in ultrarelativistic encounters of spinning black holes," *Phys. Rev. D*, vol. 83, p. 024037, 2011. 99, 122

[213] R. H. Price, G. Khanna, and S. A. Hughes, "Systematics of black hole binary inspiral kicks and the slowness approximation," *Phys. Rev. D*, vol. 83, pp. 124002–+, June 2011. 99, 118, 119, 120, 121, 122, 123, 141, 142, 143, 218

[214] L. Rezzolla, R. P. Macedo, and J. L. Jaramillo, "Understanding the 'anti-kick' in the merger of binary black holes," *Phys. Rev. Lett.*, vol. 104, p. 221101, 2010. 100, 101, 102, 118, 120, 121, 138, 139, 143

[215] M. M. D. Kramer, H. Stephani and E. Herlt, *Exact Solutions of Einstein's Field Equations*. Cambridge: Cambridge University Press, 1980. 100

[216] I. Robinson and A. Trautman, "Some spherical gravitational waves in general relativity," *Proc. Roy. Soc. Lond.*, vol. A265, pp. 463–473, 1962. 100

[217] J. L. Jaramillo, R. P. Macedo, o. P. Moesta, and L. Rezzolla, "Black-hole horizons as probes of black-hole dynamics II: geometrical insights," *accepted for publication in Phys. Rev. D*, 2011. 101

[218] J. L. Jaramillo, R. P. Macedo, P. Moesta, and L. Rezzolla, "Black-hole horizons as probes of black-hole dynamics I: post-merger recoil in head-on collisions," *accepted for publication in Phys. Rev. D*, 2011. 101

[219] A. Ashtekar, J. Engle, T. Pawlowski, and C. Van Den Broeck, "Multipole moments of isolated horizons," *Class. Quant. Grav.*, vol. 21, pp. 2549–2570, 2004. 102, 105, 106

[220] E. Schnetter, B. Krishnan, and F. Beyer, "Introduction to Dynamical Horizons in numerical relativity," *Phys. Rev. D*, vol. 74, p. 024028, 2006. 102, 105, 125

[221] A. Ashtekar and B. Krishnan, "Dynamical horizons and their properties," *Phys. Rev. D*, vol. 68, p. 104030, 2003. 104, 123, 127, 136

[222] A. Ashtekar and B. Krishnan, "Isolated and dynamical horizons and their applications," *Living Rev. Relativ.*, vol. 7, p. 10, 2004. 104, 123

[223] S. A. Hayward, "General laws of black hole dynamics," *Phys. Rev. D*, vol. 49, pp. 6467–6474, 15 June 1994. 104, 123

[224] D. Pollney, C. Reisswig, E. Schnetter, N. Dorband, and P. Diener, "High accuracy binary black hole simulations with an extended wave zone," *Phys. Rev. D*, vol. 83, p. 044045, Feb 2011. 106

[225] "`http://einsteintoolkit.org`." 106

[226] E. Schnetter, S. H. Hawley, and I. Hawke, "Evolutions in 3D numerical relativity using fixed mesh refinement," *Class. Quantum Grav.*, vol. 21, pp. 1465–1488, 21 March 2004. 106

[227] J. Thornburg, "A fast apparent-horizon finder for 3-dimensional Cartesian grids in numerical relativity," *Class. Quantum Grav.*, vol. 21, pp. 743–766, 21 January 2004. 106

[228] O. Dreyer, B. Krishnan, D. Shoemaker, and E. Schnetter, "Introduction to Isolated Horizons in Numerical Relativity," *Phys. Rev. D*, vol. 67, p. 024018, 2003. 106

[229] M. Alcubierre, *Introduction to* $3 + 1$ *Numerical Relativity*. Oxford, UK: Oxford University Press, 2008. 111

[230] E. Berti, V. Cardoso, and A. O. Starinets, "Quasinormal modes of black holes and black branes," *Class. Quant. Grav.*, vol. 26, p. 163001, 2009. 117, 120

[231] E. Barausse and L. Rezzolla, "Predicting the direction of the final spin from the coalescence of two black holes," *Astrophys. J. Lett.*, vol. 704, pp. L40–L44, 2009. 120, 175, 176

[232] L. Rezzolla, P. Diener, E. N. Dorband, D. Pollney, C. Reisswig, E. Schnetter, and J. Seiler, "The Final Spin from the Coalescence of Aligned-Spin Black Hole Binaries," *Astrophys. J.*, vol. 674, pp. L29–L32, Feb. 2008. 120, 175, 176

[233] L. Rezzolla, E. N. Dorband, C. Reisswig, P. Diener, D. Pollney, E. Schnetter, and B. Szilágyi, "Spin Diagrams for Equal-Mass Black-Hole Binaries with Aligned Spins," *Astrophys. J.*, vol. 679, p. 1422, Aug. 2008. 120, 175, 176, 182

[234] J. L. Jaramillo, R. P. Macedo, P. Moesta, and L. Rezzolla, "Black-hole horizons as probes of black-hole dynamics I: post-merger recoil in head-on collisions." 2011. 122, 123

[235] S. A. Hayward, "Quasi-localization of bondi-sachs energy loss," *Classical and Quantum Gravity*, vol. 11, no. 12, p. 3037, 1994. 123

[236] S. A. Hayward, "Spatial and null infinity via advanced and retarded conformal factors," *Phys. Rev. D*, vol. 68, p. 104015, Nov 2003. 123

[237] I. Booth and S. Fairhurst, "The first law for slowly evolving horizons," *Phys. Rev. Lett*, vol. 92, p. 011102, 2004. 124

[238] I. Booth, L. Brits, J. A. González, and C. Van Den Broeck, "Marginally trapped tubes and dynamical horizons," *Class. Quantum Grav.*, vol. 23, pp. 413–440, 2006. 125

[239] I. Booth and S. Fairhurst, "Extremality conditions for isolated and dynamical horizons," *Phys. Rev.*, vol. D77, p. 084005, 2008. 125

[240] J. L. Jaramillo, M. Ansorg, and N. Vasset, "Application of initial data sequences to the study of black hole dynamical trapping horizons," *AIP Conf. Proc.*, vol. 1122, pp. 308–311, 2009. 125, 154

[241] A. B. Nielsen and M. Visser, "Production and decay of evolving horizons," *Class.Quant.Grav.*, vol. 23, pp. 4637–4658, 2006. 125

[242] I. Booth and S. Fairhurst, "Isolated, slowly evolving, and dynamical trapping horizons: geometry and mechanics from surface deformations," *Phys. Rev. D*, vol. 75, p. 084019, 2007. 127

[243] A. Ashtekar and B. Krishnan, "Dynamical Horizons: Energy, angular momentum, fluxes, and balance laws," *Phys. Rev. Lett.*, vol. 89, p. 261101, 2002. 127

[244] S. Hawking, "Gravitational radiation from colliding black holes," *Phys. Rev. Lett.*, vol. 26, pp. 1344–1346, 1971. 127

[245] S. W. Hawking, "Black holes in general relativity," *Comm. Math. Phys.*, vol. 25, p. 152, 1972. 127

[246] A. Ashtekar and G. Galloway, "Some uniqueness results for dynamical horizons," *Advances in Theoretical and Mathematical Physics*, vol. 9, no. 1, pp. 1–30, 2005. 129, 130

[247] L. Andersson, M. Mars, and W. Simon, "Local existence of dynamical and trapping horizons," *Phys. Rev. Lett.*, vol. 95, p. 111102, 2005. 129

[248] L. Andersson, M. Mars, and W. Simon, "Stability of marginally outer trapped surfaces and existence of marginally outer trapped tubes," *Adv. Theor. Math. Phys.*, vol. 12, pp. 853–888, 2008. 129

[249] A. Ashtekar and B. Krishnan, "Dynamical Horizons: Energy, angular momentum, fluxes, and balance laws," *Phys. Rev. Lett.*, vol. 89, p. 261101, 2002. 136

[250] S. Hayward, "Energy conservation for dynamical black holes," vol. 93, p. 251101, 2004. 136

[251] S. A. Hayward, "Energy and entropy conservation for dynamical black holes," *Phys. Rev. D*, vol. 70, p. 104027, 2004. 136, 137

[252] J. L. Jaramillo, N. Vasset, and M. Ansorg, "A numerical study of Penrose-like inequalities in a family of axially symmetric initial data," 2007. 136

[253] B. C. Nolan, "Physical interpretation of gauge invariant perturbations of spherically symmetric space-times," *Phys. Rev. D*, vol. 70, p. 044004, Aug 2004. 136

[254] P. Szekeres, "The gravitational compass," *J. Math. Phys*, vol. 6, pp. 1387–1391, 1965. 136

[255] B. Krishnan, C. O. Lousto, and Y. Zlochower, "Quasi-Local Linear Momentum in Black-Hole Binaries," *Phys. Rev. D*, vol. 76, p. 081501, 2007. 137

[256] G. Lovelace *et al.*, "Momentum flow in black-hole binaries: II. Numerical simulations of equal-mass, head-on mergers with antiparallel spins," *Phys. Rev. D*, vol. 82, p. 064031, 2010. 137

[257] Y.-H. Wu, *Isolated Horizons, Dynamical Horizons and their quasi-local energy-momentum and flux*. PhD thesis, University of Southampton, Southampton, U.K., 2006. 137

[258] Y.-H. Wu and C.-H. Wang, "Gravitational radiation of generic isolated horizons," *arXiv:0807.2649*, 2008. 137

[259] Y.-H. Wu and C.-H. Wang, "Gravitational radiations of generic isolated horizons and non-rotating dynamical horizons from asymptotic expansions," *Phys. Rev. D*, vol. 80, p. 063002, 2009. 137

[260] Y.-H. Wu and C.-H. Wang, "Gravitational radiation and angular momentum flux from a slow rotating dynamical black hole," *Phys. Rev.*, vol. D83, p. 084044, 2011. 137

[261] B. Szilagyi, D. Pollney, L. Rezzolla, J. Thornburg, and J. Winicour, "An Explicit harmonic code for black-hole evolution using excision," *Class.Quant.Grav.*, vol. 24, pp. S275–S293, 2007. 138

[262] J. B. Hartle, "Tidal Friction in Slowly Rotating Black Holes," *Phys. Rev. D*, vol. 8, pp. 1010–1024, 1973. 139

[263] J. B. Hartle, "Tidal shapes and shifts on rotating black holes," *Phys. Rev. D*, vol. 9, pp. 2749–2759, 1974. 139

[264] S. W. Hawking and J. B. Hartle, "Energy and angular momentum flow into a black hole," *Commun. Math. Phys.*, vol. 27, pp. 283–290, 1972. 139

[265] T. Damour, *Quelques propriétés mécaniques, électromagnétiques, thermodynamiques et quantiques des trous noirs*. France: Thèse de doctorat dÉtat, Université Paris 6, 1979. 139

[266] T. Damour, "Surface effects in black hole physics," in *Proceedings of the Second Marcell Grossman Meeting on General Relativity* (R. Ruffini, ed.), p. 587, North Holland, 1982. 139

[267] R. Crowley, D. Macdonald, R. Price, I. Redmount, Suen, K. Thorne, and X.-H. Zhang, *Black Holes: The Membrane Paradigm*. Yale University Press, 1986. 139, 167

[268] R. H. Price and K. S. Thorne, "Membrane viewpoint on black holes: Properties and evolution of the stretched horizon," *Phys. Rev. D*, vol. 33, p. 915, 1986. 139

[269] T. Damour and M. Lilley, "String theory, gravity and experiment," *arXiv:0802.4169 [hep-th]*, 2008. 139

[270] N. Straumann, "The membrane model of black holes and applications," *arXiv:9711276 [astro-ph]*, 1997. 139

[271] E. Gourgoulhon, "A generalized Damour-Navier-Stokes equation applied to trapping horizons," *Phys. Rev. D*, vol. 72, p. 104007, 2005. 139, 140

[272] E. Gourgoulhon and J. L. Jaramillo, "A $3+1$ perspective on null hypersurfaces and isolated horizons," *Physics Reports*, vol. 423, pp. 159–294, February 2006. 139, 140

[273] E. Gourgoulhon and J. L. Jaramillo, "Area evolution, bulk viscosity and entropy principles for dynamical horizons," *Phys. Rev. D*, vol. 74, p. 087502, 2006. 139, 140

[274] E. Gourgoulhon and J. L. Jaramillo, "New theoretical approaches to black holes," *New Astron. Rev.*, vol. 51, pp. 791–798, 2008. 139, 140

[275] T. Padmanabhan, "Entropy density of spacetime and the navier-stokes fluid dynamics of null surfaces," *Phys. Rev. D*, vol. 83, p. 044048, Feb 2011. 140

[276] S. Bhattacharyya, V. E. Hubeny, R. Loganayagam, G. Mandal, S. Minwalla, T. Morita, M. Rangamani, and H. S. Reall, "Local fluid dynamical entropy from gravity," *Journal of High Energy Physics*, vol. 2008, no. 06, p. 055, 2008. 141

[277] S. Bhattacharyya, S. Minwalla, V. E. Hubeny, and M. Rangamani, "Nonlinear fluid dynamics from gravity," *Journal of High Energy Physics*, vol. 2008, no. 02, p. 045, 2008. 141

[278] I. Booth, M. P. Heller, G. Plewa, and M. Spaliński, "Apparent horizon in fluid-gravity duality," *Phys. Rev. D*, vol. 83, p. 106005, May 2011. 141

[279] I. Booth, M. P. Heller, and M. Spalinski, "Black Brane Entropy and Hydrodynamics," *Phys. Rev.*, vol. D83, p. 061901, 2011. 141

[280] R. Owen, J. Brink, Y. Chen, J. D. Kaplan, G. Lovelace, K. D. Matthews, D. A. Nichols, M. A. Scheel, F. Zhang, A. Zimmerman, and K. S. Thorne, "Frame-dragging vortexes and tidal tendexes attached to colliding black holes: Visualizing the curvature of spacetime," *Phys. Rev. Lett.*, vol. 106, p. 151101, Apr 2011. 142

[281] B. Szilágyi, D. Pollney, L. Rezzolla, J. Thornburg and J. Winicour, "An explicit harmonic code for black-hole evolution using excision", *Class. Quantum Grav.*, **24**, S275 2007. 145, 146, 147, 219

[282] V. Fock, *The Theory of Space, Time and Gravitation*, p. 392 (MacMillan, New York, 1964). 145

[283] M. C. Babiuc, B. Szilágyi and J. Winicour, *Phys.Rev.* **D73**, 064017 (2006). 31, 145

[284] M. C. Babiuc, H.-O. Kreiss and J. Winicour, *Phys. Rev.* **D75**, 044002 (2007). 145

[285] Cactus Computational Toolkit home page: `http://www.cactuscode.org`. 145

[286] S. Brandt and B. Brügmann, "A simple construction of initial data for multiple black holes", em Phys. Rev. Lett. **78**, 3606 (1997). 145

[287] M. Alcubierre Miguel Alcubierre, B. Brüegmann, D. Pollney, E. Seidel and R. Takahashi, "Black hole excision for dynamic black holes", *Phys.Rev. D* **64**, 061501 (2001). 145

[288] S. A. Hayward, "General laws of black hole dynamics", *Phys.Rev. D* **49**, 6467 (1994). 145

[289] A. Ashtekar and B. Krishnan, "Dynamical horizons and their properties", *Phys.Rev. D* **68**, 104030 (2003). 145

[290] A. Ashtekar and B. Krishnan, "Isolated and dynamical horizons and their applications", *Living Rev. Rel.* **7**, 10 (2004). 145

[291] E. Schnetter and B. Krishnan, "Non-symmetric trapped surfaces in the Vaidya and Schwarzschild spacetimes", *Phys.Rev. D* **73**, 021502 (2006). 146

[292] E. Schnetter, B. Krishnan and F. Beyer, "Introduction to dynamical horizons in numerical relativity", *Phys.Rev. D* **74**, 024028 (2006). 146, 147, 154

[293] H. Friedrich and A. Rendall, "The Cauchy Problem", in **Einstein's Field Equations and their Physical Interpretation**, ed. B. G Schmidt (Springer-Verlag, Berlin, 2000). 29, 30

[294] P. Mösta, "Puncture Evolutions within the Harmonic Framework", Diploma thesis, Universitt Kassel (2008). 30

[295] M. C. Babiuc, B. Szilágyi and J. Winicour, "Harmonic initial-boundary evolution in general relativity", *Phys.Rev.* **D73**, 064017 (2006). 30

[296] H.-O. Kreiss, O. Reula, O. Sarbach, and J. Winicour, "Boundary conditions for coupled quasilinear wave equations with application to isolated systems", *Commun.Math.Phys.* **289**, 1099 (2009) 30

[297] H. Friedrich, "Hyperbolic reductions for Einstein's equations." *Class. Quantum Grav.* **13** 1451-1469, (1996)

[298] E. Schnetter, S. H. Hawley and I. Hawke, "Evolutions in 3D numerical relativity using fixed mesh refinement", *Class. Qunatum Grav.* **21**, 1465 (2004).

[299] "Mesh refinement with Carpet", `http://www.carpet.code.org`.

[300] J. Thornburgh, "Finding apparent horizons in numerical relativity", *Phys. Rev. D* **54**, 4899 (1996). 152

[301] J. Thornburgh, "A fast apparent-horizon finder for 3-dimensional Cartesian grids in numerical relativity", *Class. Quantum Grav.* **21**, 743 (2004). 152

[302] L. Andersson, M. Mars, J. Metzger and W. Simon, "The time evolution of marginally trapped surfaces", *Classical Quantum Gravity* **26(8)**, 085018, 14 (2009). 146, 151, 153

[303] L. Andersson, M. Mars and W. Simon, "Local existence of dynamical and trapping horizons", *Phys. Rev. Lett.* **95(11)**, 11110 (2005). 146, 149, 150, 151

[304] L. Andersson, M. Mars and W. Simon, "Stability of marginally outer trapped surfaces and existence of marginally outer trapped tubes", *Adv. Theor. Math. Phys.* **12(4)**, 853–888 (2008). 146, 149

[305] L. Andersson and J. Metzger, "Curvature estimates for stable marginally trapped surfaces", arXiv.org:gr-qc/0512106 (2005). 149

[306] L. Andersson and J. Metzger, "The area of horizons and the trapped region", *Comm. Math. Phys.* **290(3)**, 941–972 (2009). 149

[307] A. Ashtekar and G. J. Galloway, "Some uniqueness results for dynamical horizons", *Adv. Theor. Math. Phys.* **9(1)**, 1–30 (2005). 146, 149

[308] M. Eichmair, "The plateau problem for marginally outer trapped surfaces", arXiv.org:0711.4139 (2007). 149

[309] M. Eichmair, "Existence, regularity, and properties of generalized apparent horizons", arXiv.org:0805.4454 (2008). 149

[310] G. J. Galloway, "Rigidity of marginally trapped surfaces and the topology of black holes", *Comm. Anal. Geom.* **16(1)**, 217–229 (2008). 149

[311] P. J. Armitage and P. Natarajan, "Accretion during the Merger of Supermassive Black Holes," , vol. 567, pp. L9–L12, Mar. 2002. 161, 163

[312] F. K. Liu, X.-B. Wu, and S. L. Cao, "Double-double radio galaxies: remnants of merged supermassive binary black holes," , vol. 340, pp. 411–416, Apr. 2003. 161, 163

[313] M. Milosavljevic and E. S. Phinney, "The Afterglow of Massive Black Hole Coalescence," *Astrophys. J.*, vol. 622, pp. L93–L96, 2005. 161, 163

[314] C. Palenzuela, T. Garrett, L. Lehner, and S. L. Liebling, "Magnetospheres of black hole systems in force-free plasma," *Phys. Rev. D*, vol. 82, pp. 044045–+, Aug. 2010. 162, 181, 183, 187, 188

[315] R. M. Wald, "Black hole in a uniform magnetic field," *Phys. Rev. D*, vol. 10, pp. 1680–1685, Sept. 1974. 163

[316] C. Palenzuela, L. Lehner, and S. Yoshida, "Understanding possible electromagnetic counterparts to loud gravitational wave events: Binary black hole effects on electromagnetic fields," *Phys. Rev. D*, vol. 81, p. 084007, 2010. 167, 170, 181, 184, 187

[317] C. Reisswig, S. Husa, L. Rezzolla, E. N. Dorband, D. Pollney, and J. Seiler, "Gravitational-wave detectability of equal-mass black-hole binaries with aligned spins," *Phys. Rev. D*, vol. 80, p. 124026, Dec. 2009. 168, 169, 175, 176, 182

[318] L. Rezzolla *et al.*, "Spin Diagrams for Equal-Mass Black-Hole Binaries with Aligned Spins," *Astrophys. J*, vol. 679, pp. 1422–1426, 2008. 168, 169

[319] L. Boyle and M. Kesden, "The spin expansion for binary black hole merger: new predictions and future directions," *Phys. Rev. D*, vol. 78, p. 024017, 2008. 175

[320] L. Boyle, M. Kesden, and S. Nissanke, "Binary-Black-Hole Merger: Symmetry and the Spin Expansion," *Phys. Rev. Lett.*, vol. 100, p. 151101, Apr. 2008. 175

[321] A. Buonanno, L. E. Kidder, and L. Lehner, "Estimating the final spin of a binary black hole coalescence," *Phys. Rev. D*, vol. 77, p. 026004, Jan. 2008. 175

[322] M. Campanelli, C. O. Lousto, and Y. Zlochower, "Gravitational radiation from spinning-black-hole binaries: The orbital hang up," *Phys. Rev. D*, vol. 74, p. 041501, 2006. 175

[323] M. Campanelli, C. O. Lousto, and Y. Zlochower, "The last orbit of binary black holes," *Phys. Rev. D*, vol. 73, p. 061501, 2006. 175

[324] M. Campanelli, C. O. Lousto, and Y. Zlochower, "Spin-orbit interactions in black-hole binaries," *Phys. Rev. D*, vol. 74, p. 084023, 2006. 175

[325] F. Herrmann, I. Hinder, D. M. Shoemaker, P. Laguna, and R. A. Matzner, "Binary black holes: Spin dynamics and gravitational recoil," *Phys. Rev. D*, vol. 76, p. 084032, Oct. 2007. 175

[326] M. Koppitz, D. Pollney, C. Reisswig, L. Rezzolla, J. Thornburg, P. Diener, and E. Schnetter, "Getting a kick from equal-mass binary black hole mergers," *Phys. Rev. Lett.*, vol. 99, p. 041102, 2007. 175

[327] P. Marronetti, W. Tichy, B. Bruegmann, J. Gonzalez, and U. Sperhake, "High-spin binary black hole mergers," *Phys. Rev. D*, vol. 77, p. 064010, 2008. 175

[328] D. Pollney, C. Reisswig, L. Rezzolla, B. Szilágyi, M. Ansorg, B. Deris, P. Diener, E. N. Dorband, M. Koppitz, A. Nagar, and E. Schnetter, "Recoil velocities from equal-mass binary black-hole mergers: a systematic investigation of spin-orbit aligned configurations," *Phys. Rev. D*, vol. 76, p. 124002, 2007. 175

[329] L. Rezzolla, E. Barausse, E. N. Dorband, D. Pollney, C. Reisswig, J. Seiler, and S. Husa, "Final spin from the coalescence of two black holes," *Phys. Rev. D*, vol. 78, p. 044002, Aug. 2008. 175, 176

[330] M. Milosavljević and E. S. Phinney, "The afterglow of massive black hole coalescence," *Astrophys. J.*, vol. 622, p. L93, 2005. 177

[331] N. A. Silant'ev, M. Y. Piotrovich, Y. N. Gnedin, and T. M. Natsvlishvili, "The Black Hole Mass and Magnetic Field Correlation in AGN: Testing by Optical Polarimetry," *ArXiv e-prints*, Aug. 2009. 177

[332] R. D. Blandford and R. L. Znajek, "Electromagnetic extraction of energy from Kerr black holes," *Mon. Not. R. Astron. Soc.*, vol. 179, pp. 433–456, May 1977. 179, 182

[333] T. Bogdanović, C. S. Reynolds, and M. C. Miller, "Alignment of the Spins of Supermassive Black Holes Prior to Coalescence," *Astrophys. J.*, vol. 661, pp. L147–L150, June 2007. 180, 219

[334] M. Dotti, M. Volonteri, A. Perego, M. Colpi, M. Ruszkowski, and F. Haardt, "Dual black holes in merger remnants - II. Spin evolution and gravitational recoil," *Mon. Not. R. Astron. Soc.*, p. 1795, Nov. 2009. 180, 219

[335] T. Bode, R. Haas, T. Bogdanovic, P. Laguna, and D. Shoemaker, "Relativistic Mergers of Supermassive Black Holes and their Electromagnetic Signatures," 2009. 181

[336] P. Chang, L. E. Strubbe, K. Menou, and E. Quataert, "Fossil Gas and the Electromagnetic Precursor of Supermassive Binary Black Hole Mergers," 2009. 181

[337] L. R. Corrales, Z. Haiman, and A. MacFadyen, "Hydrodynamical Response of a Circumbinary Gas Disk to Black Hole Recoil and Mass Loss," 2009. 181

[338] A. I. MacFadyen and M. Milosavljević, "An Eccentric Circumbinary Accretion Disk and the Detection of Binary Massive Black Holes," , vol. 672, pp. 83–93, Jan. 2008. 181

[339] C. Palenzuela, M. Anderson, L. Lehner, S. L. Liebling, and D. Neilsen, "Stirring, not shaking: binary black holes' effects on electromagnetic fields," *Phys. Rev. Lett.*, vol. 103, p. 081101, 2009. 181

[340] J. R. van Meter *et al.*, "Modeling Flows Around Merging Black Hole Binaries," 2009. 181

[341] T. Bode, T. Bogdanovic, R. Haas, J. Healy, P. Laguna, and D. Shoemaker, "Mergers of Supermassive Black Holes in Astrophysical Environments," *arXiv:1101.4684*, Jan. 2011. 181

[342] B. D. Farris, Y. T. Liu, and S. L. Shapiro, "Binary black hole mergers in gaseous disks: Simulations in general relativity," *arXiv:1105.2821*, May 2011. 181

[343] E. M. Rossi, G. Lodato, P. J. Armitage, J. E. Pringle, and A. R. King, "Black hole mergers: the first light," *Mon. Not. R. Astron. Soc.*, vol. 401, pp. 2021–2035, Jan. 2010. 181

[344] O. Zanotti, L. Rezzolla, L. Del Zanna, and C. Palenzuela, "Electromagnetic counterparts of recoiling black holes: general relativistic simulations of non-Keplerian discs," *Astron. Astrophys.*, vol. 523, pp. A8+, Nov. 2010. 181

[345] Z. Haiman, B. Kocsis, K. Menou, Z. Lippai, and Z. Frei, "Identifying decaying supermassive black hole binaries from their variable electromagnetic emission," *Classical and Quantum Gravity*, vol. 26, p. 094032, May 2009. 181

[346] A. Sesana, J. Gair, E. Berti, and M. Volonteri, "Reconstructing the massive black hole cosmic history through gravitational waves," , vol. 83, p. 044036, Feb. 2011. 181

[347] P. J. Armitage and P. Natarajan, "Accretion during the Merger of Supermassive Black Holes," *Astrophys. J.*, vol. 567, pp. L9–L12, Mar. 2002. 181

[348] F. Liu, X. Wu, and S. Cao, "Double-double radio galaxies: remnants of merger of supermassive binary black holes," *Mon. Not. R. Astron. Soc.*, vol. 340, p. 411, 2003. 181

[349] P. Mösta, C. Palenzuela, L. Rezzolla, L. Lehner, S. Yoshida, and D. Pollney, "Vacuum Electromagnetic Counterparts of Binary Black-Hole Mergers," *Phys. Rev. D*, vol. 81, p. 064017, 2010. 181, 182, 183, 187

[350] D. Neilsen, L. Lehner, C. Palenzuela, E. W. Hirschmann, S. L. Liebling, P. M. Motl, and T. Garrett, "Boosting jet power in black hole spacetimes," *arxiv:1012.5661*, Dec. 2010. 181

[351] C. Palenzuela, L. Lehner, and S. L. Liebling, "Dual Jets from Binary Black Holes," *Science*, vol. 329, pp. 927–930, Aug. 2010. 181, 182, 183, 187, 188

[352] S. A. Teukolsky, "Perturbations of a rotating black hole. I. fundamental equations for gravitational, electromagnetic, and neutrino-field perturbations," *Astrophys. J.*, vol. 185, pp. 635–647, 1973. 183

[353] D. L. Kaplan, R. O'Shaughnessy, A. Sesana, and M. Volonteri, "Blindly Detecting Merging Supermassive Black Holes with Radio Surveys," *Astrophys. J.*, vol. 734, p. L37, June 2011. 188

[354] D. A. Brown, "Searching for Gravitational Radiation from Binary Black Hole MACHOs in the Galactic Halo," 2004. 191, 202

[355] C. Helstrom, *Statistical theory of signal detection.* International series of monographs on electronics and instrumentation, Pergamon Press, 1960. 191

[356] C. W. Helstrom, *Elements of signal detection and estimation.* Upper Saddle River, NJ, USA: Prentice-Hall, Inc., 1995. 191, 196

[357] C. Cutler and E. E. Flanagan, "Gravitational waves from merging compact binaries: How accurately can one extract the binary's parameters from the inspiral wave form?," *Phys. Rev.*, vol. D49, pp. 2658–2697, 1994. 198

[358] B. Allen, "A chi**2 time-frequency discriminator for gravitational wave detection," *Phys. Rev.*, vol. D71, p. 062001, 2005. 200

[359] B. Allen, W. G. Anderson, P. R. Brady, D. A. Brown, and J. D. E. Creighton, "FINDCHIRP: an algorithm for detection of gravitational waves from inspiraling compact binaries," 2005. 202

[360] P. Ajith *et al.*, "Phenomenological template family for black-hole coalescence waveforms," *Class. Quant. Grav.*, vol. 24, pp. S689–S700, 2007. 206, 207

[361] P. Ajith, M. Hannam, S. Husa, Y. Chen, B. Bruegmann, *et al.*, "Inspiral-merger-ringdown waveforms for black-hole binaries with non-precessing spins," *Phys.Rev.Lett.*, vol. 106, p. 241101, 2011. 206, 207

[362] L. Santamaria, F. Ohme, P. Ajith, B. Bruegmann, N. Dorband, *et al.*, "Matching post-Newtonian and numerical relativity waveforms: systematic errors and a new phenomenological model for non-precessing black hole binaries," *Phys.Rev.*, vol. D82, p. 064016, 2010. 206, 207

[363] E. Robinson, P. Moesta, F. Ohme, L. Santamaria, and B. Krishnan 206

[364] J. Abadie *et al.*, "Search for Gravitational Waves from Compact Binary Coalescence in LIGO and Virgo Data from S5 and VSR1," *Phys.Rev.*, vol. D82, p. 102001, 2010. 206

[365] B. Abbott *et al.*, "Search for gravitational waves from binary inspirals in S3 and S4 LIGO data," *Phys. Rev.*, vol. D77, p. 062002, 2008. 206

[366] A. Buonanno, B. Iyer, E. Ochsner, Y. Pan, and B. S. Sathyaprakash, "Comparison of post-Newtonian templates for compact binary inspiral signals in gravitational-wave detectors," *Phys. Rev.*, vol. D80, p. 084043, 2009. 207

[367] I. W. Harry, B. Allen, and B. S. Sathyaprakash, "A stochastic template placement algorithm for gravitational wave data analysis," *Phys. Rev.*, vol. D80, p. 104014, 2009. 209

Erklärung

Ich versichere hiermit, dass ich diese Dissertation eigenständig und nur unter Verwendung der angegebenen Hilfsmittel angefertigt habe.

Diese Dissertation wurde unter Anleitung von Prof. Bernard Schutz, Dr. Luciano Rezzolla und Dr. Badri Krishnan am Albert-Einstein-Institut, Potsdam angefertigt.

Potsdam, den 30. Oktober 2011